Title: On the nature of the earliest known lifeforms

Dheeraj Kanaparthi[1,2&3*], Marko Lampe[4], Baoli Zhu[2&5], Thomas Boesen[6], Andreas Klingl[7], Petra Schwille[1] & Tillmann Lueders[2&3*]

Affiliations:

[1]Max-Planck Institute for Biochemistry, Munich, Germany
[2]Chair of Ecological Microbiology, BayCeer, University of Bayreuth, Germany.
[3]Helmholtz Zentrum Munich, Germany
[4]Advanced Light Microscopy Facility, European Molecular Biology Laboratory, Heidelberg, Germany.
[5]Key Laboratory of Agro-ecological Processes in Subtropical Regions, Taoyuan Agroecosystem Research Station, Institute of Subtropical Agriculture, Chinese Academy of Sciences, Changsha, China.

[6]Department of Biosciences, Center for Electromicrobiology, Aarhus, Denmark.
[7]Department of Biology, LMU, Planegg-Martinsried, Germany.
*Corresponding authors

Lead contact: kanaparthi@biochem.mpg.de

Abstract:

Oldest known microfossils were known to have the most complex of morphologies among prokaryotes. Given the morphology of an organism is governed by information encoded in its genome, it was proposed that these primitive organisms most likely possessed complex molecular biological processes. Here we worked with bacterial protoplasts under environmental conditions of Archaean earth and reproduced morphologies of every known microfossil and associated structures. Contrary to the current presumption, our work suggest that complex morphologies of these microfossils could be explained not by presence but by complete absence of molecular biological mechanisms. Environmental conditions and

architecture of the cell membrane are the only factors that determined the morphology of these organisms. Based on our observations we present a case for reinterpretation of Archaean microfossils as protocells that were devoid of complex molecular biological processes rather than annotating them to a particular phylogenetic group of extant bacteria.

One Sentence Summary: Microfossils reported from Archaean BIF's most likely were liposome like protocells, which had evolved mechanisms for energy conservation, but not for regulating cell morphology and replication.

Main Text: Pilbara iron formation (PIF), Western Australia (1) and Barberton greenstone belt (BGB)(2), South Africa are the oldest known rock formations, which haven't been subjected to significant metamorphic alterations (1, 2). Hence, these rock formations have been a subject of numerous scientific investigations that were focused on understanding biology and biogeochemistry of Archaean Earth (1–6). These studies led to the discovery of organic structures within these rock formations, that resemble microorganisms in their morphology with $\delta^{13}C$ composition consistent with biologically derived organic carbon (5, 7). Although these observations suggest that these structures were fossil remnants of Archaean microorganisms, any such interpretation along with their physiology and biological origin has been a serious point of contention among researcher (8–12). Two factors currently limit wider acceptance of their biological origin – absence of truly analogous morphologies among extant prokaryotes and absence of an indication for a distinctively biological process like cell-replication (except for Swartkopie formations) (6). Decades of back and forth arguments led to general consensus, that reconstructing the lifecycles of Archaean Eon organisms, however improbable it appeared to be, is the only way of understanding the nature of these microfossils (13).

In our previous work we demonstrated the simplest of all reproductive processes, that were entirely dependent on the physicochemical properties of cell constituents, environmental conditions, and architecture of cell membrane (Under review). Given the likely possibility that such primitive cells could only had been native to early earth (prior to the origin of prokaryotes); Here, we studies the morphology and growth cycles of a Gram-positive (*Exiguobacterium Strain-Molly*) and a Gram-negative (*Rhodobacter sphaeroides*) bacteria into their protoplast state (*EM-P* and *RS-P* respectively) under presumed environmental conditions of Archaean Eon earth (*14*). We then compared *EM-P* and *RS-P* morphologies with that of Achaean Eon microfossils (3800-2500 million years old). As physio-chemical mechanisms behind complex morphologies were explained in the accompanying manuscript, we restrict the scope of current manuscript to drawing parallels between bacteria from our study and Archaean eon microfossils, in-terms of their morphologies, elemental, and carbon isotopic composition. Like the previous studies we grew *EM-P* and *RS-P* under static conditions at 30°C in half-strength tryptic soya broth nutrient broth amended with 5-10% Dead Sea salt (DSS) respectively.

In the first two sections of the manuscript, we present such an in-depth morphological comparison. In the later section, we present our case for reinterpretation of these microfossils as proto-Gram-positive and proto-Gram-negative bacteria.

Morphological similarities between 3.5 - 2.4-billion-year-old spherical microfossils with protoplasts of Gram-positive bacteria

Spherical microfossils of different morphologies were discovered from sites within PIF (*1*, *15*, *16*) and BGB (*4*, *6*, *17*). *EM-P* reproduced either by forming external or internal daughter cells (discussed in detail in accompanying manuscript). Over the course of its lifecycle *EM-P* exhibited morphologies similar to all known spherical microfossils reported from these sites.

The first step in reproduction by forming intracellular daughter cells is the formation of intracellular vesicles (ICV's), by a process similar to endocytosis (fig. S1A). Over time, size and number of ICV's within a cell gradually increased (Fig. 1E&F). No uniformity was observed in the morphology or number of ICV's within (Fig. 1E&F) or among different cell (fig. S2). *EM-P* with such ICV's, resemble microfossils reported from Apex chert (1) (Fig. 1 & S3). Like the Apex-chert microfossils, intracellular vesicles of *EM-P* were hollow and presence of organic carbon (cytoplasm) in these cells was restricted to spaces in-between ICV's (Fig. 1A-F). Microfossils reported from other sites like Strelley Pool Formation (SPF) formations (*18*) (Fig. 1G & fig. S4-S6), Farrel Quarzite (*19*)(fig. S7), Turee creek (*20*)(fig. S8), Fig tree (3)(fig. S9), and Hooggenoeg formations (*17*)(fig. S10), likely are morphological variants of *EM-P* and Apex-chert microfossils. For instance, *EM-P* with a large number of relatively smaller ICV's resemble Fig tree microfossils, both in size and shape (fig. S8). On the other hand, *EM-P* with a relatively larger number of ICV's squeezed within the cell, resemble SPF, Fig tree and Turee creek microfossils with polygonal alveolar structures (*18*)(Fig. 1G-I & S4-S9). Given the uncanny morphological resemblance between *EM-P* and SPF microfossils (fig. S4-S6), we presume that polygonal surface depressions could have formed by rupture of individual vesicles below the cell surface, similar to what was observed in *EM-P* (Fig. 1D-I & S6) (*18*)

The second stage of reproduction involves formation of daughter cells (fig. S1 D-H). Daughter cells were formed by blebbing of vesicle membrane (fig. S1D), leading to formation of either individual or a string of daughter cells (fig. S1E). Based on number of ICV's, two cell morphologies were observed. Cells with a single large (fig. S2E) or multiple smaller ICV's (fig. S2E). Gradual transfer of cytoplasm from parent to daughter cells led to a gradual reduction of cytoplasmic volume of the cell and a corresponding increase in vesicle size and number of daughter cell, within the ICV's (fig. S1H). Over time, we noticed cells with a single large ICV appeared as hollow vesicle with tiny daughter cells (fig. S11-S13). Morphology of these cells resemble microfossils reported from SPF (fig. S11&S12) (*21*, *22*)

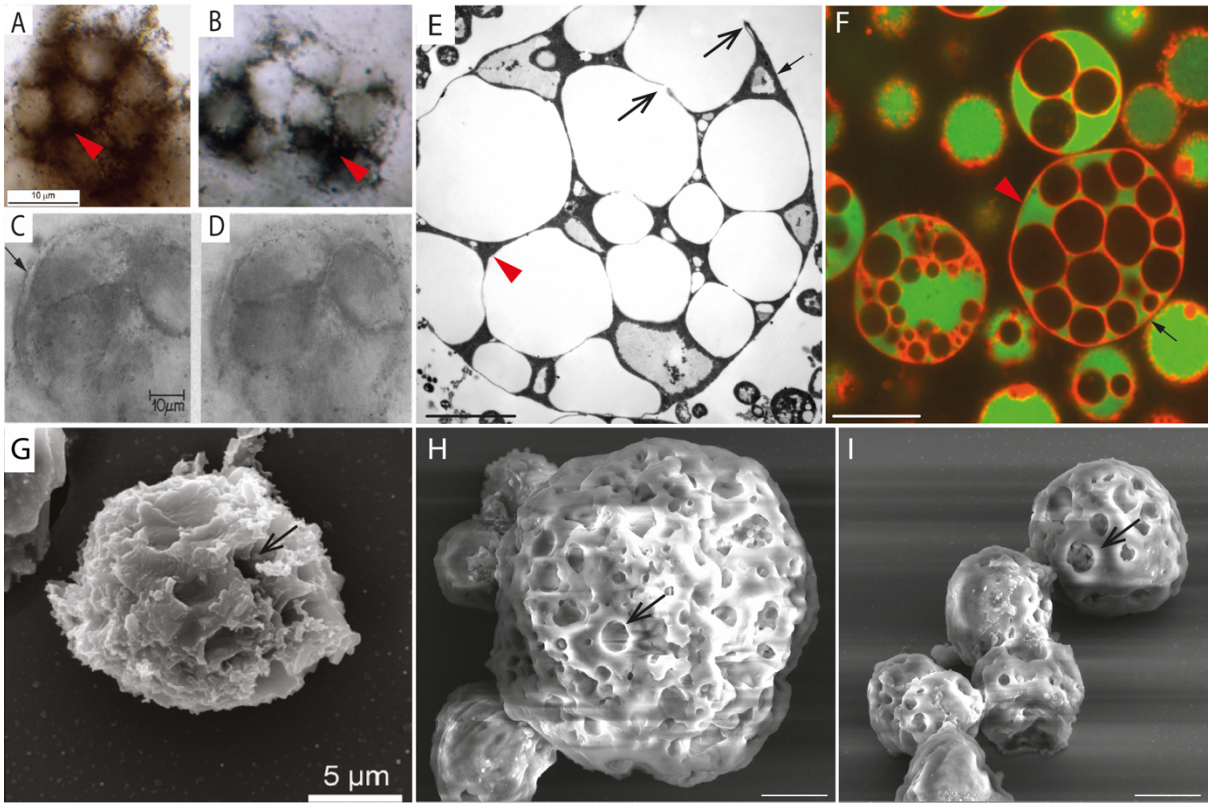

Fig 1. Morphological comparison of Apex chert & SPF microfossils with *EM-P*. Images A-D are spherical microfossils reported from Apex chert (originally published by Schopf et al., 1987) (*23*). Images E & F are TEM and confocal images of morphologically

analogous *EM-P* cells. Cells in image F were stained with universal membrane stain, FM™5-95 (red) and DNA stain, PicoGreen (green). Red arrows in images A-F points to cytoplasm sandwiched in-between large hollow vesicles. Black arrows in images C-F points to appearance of duel outer membrane due to the presence of ICV's (fig. S3). Open arrows point to ruptures in vesicle membrane, which led to formation of polygonal depressions on cell surface (H&I). Image G show microfossil reported from SPF site (originally published by Delarue *et al.,* 2020) (*18*). Images H & I are SEM images of morphologically analogous *EM-P* cells. Arrows in images G-I points to depressions formed on cell surface due to rupture of vesicle membrane (fig. S5-S6). Scale bars: 0.5µm (E), 5 µm (F) and 1µm (H&I).

and Goldsworth formation (fig. S13)(*24*). In case of cells with a multiple ICV's, cells underwent lysis to release ICV's with daughter cells (Movie S1-3 & fig. S12D-I). During the early logarithmic growth phase (at low cell densities), these ICV's aggregations gradually got separated from one another (fig. S14). Microfossils reported from SPF (*15*, *22*)(fig. S14-S16), Turee creek (fig. S17)(*20*) and Goldsworth formations (*13*, *24*)(fig. 2 & S18) bare close morphological similarities with the all the intermediate morphotypes of *EM-P* undergoing cell lysis, release and dispersion of ICV's.

During the late logarithmic growth phase (at high cell densities), expelled vesicles did not undergo subsequent separation (fig. S19). These vesicles remained as aggregates and formed mat like structures at the bottom of the culture bottles (fig. S19-20). Moreover, gradual

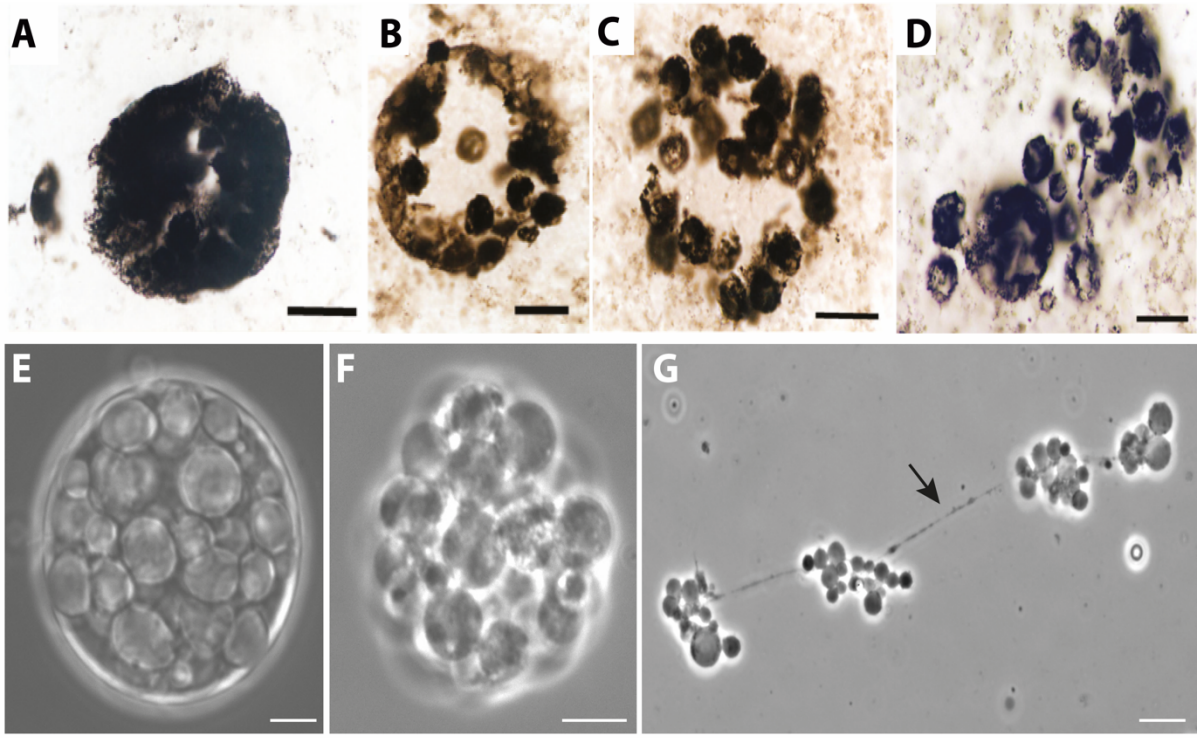

Fig 2. Morphological comparison between *EM-P* and Goldsworth microfossils. Images A-D shows spherical microfossils reported from Goldsworth formation (originally published by Sugitani et al., 2009) (13). Images E-G are images of *EM-P* cell undergoing lysis (E) and dispersion (F) of intracellular vacuoles. Arrows in these images points to interlinks between the released vesicles. Scale bars: 20µm (A) 2µm (E&F) and 5µm (G).

compression of vesicle, led to transformation of spherical vesicles into polygonal shapes, leading to the formation of honeycomb shaped mats (fig. S20-25). Organic structures resembling both the above discussed morphologies were reported from several microfossil sites. Large aggregations of spherical cells devoid of internal organic carbon reported from North-Pole formation (NPF) (fig. S21)(*16*) bare remarkably close resemblance to the above described morphotypes of *EM-P*. Like observed in *EM-P*, distribution of organic carbon in NPF restricted to periphery of the spherical cells (fig. S21). Along with the morphological and organizational similarities with NPF microfossils, *EM-P* also exhibited all the accessory structures observed in NPF formations like the filamentous structures originating from the

spherical cells and clots of organic carbon (fig. S21D). We presume that filamentous structures could have formed during the release of ICV's, like observed in *EM-P* (Movie S3). Large clots of organic carbon should have been the membrane debris that was formed during the process of lysis, that led to the release of ICV's (Movie S3). Honeycomb shaped mats formed by *EM-P* bare uncanny morphological resemblance with organic structures reported from Nuga, BRC, Mt. Grant, SPF and Turee creek formations (fig. S23-26)(*20*, *25–28*).

In the last growth stage, vacuole membrane underwent rupture to release of daughter cells (Movie S4 & fig. S12). We observed formation of three distinct types of daughter cells – individual spherical daughter cells (Movie S4 & fig. S12), string of daughter cells (fig. S27) and daughter cells that were still attached to the membrane debris of parent cell (Movie S5, fig. S28 & S29). All these daughter cell morphotypes were reported from microfossil sites like – SPF (fig. S12), Moodies and Sulphur spring formations (fig. S27-S29)(*28–30*). Lysis and release of either ICV's or daughter cells led to collapse or deflation of large spherical cell or Vesicles (Movie S4 & fig. S30E). Such deflated cells were often observed during the late-growth stages of *EM-P* and bare morphological resemblance with Kromberg formation microfossils (fig. S30)(*31*).

The second method of reproduction observed in *EM-P* is by formation of external daughter cells. Cells reproducing by this process bares morphological resemblance to microfossils reported from Swartkopie (6), Cleverville (*32*) and Sheba formations (*33*) along with rest of the spherical microfossils from above discussed sites like NPF and Sulphur spring formations (fig. S31-S36) (*16*, *34*). First stage in such a mode of reproduction involves formation of a bud like structure out of the cell (fig. S31), which resemble NPF microfossils with pustular protuberances (*16*) (fig. S31). Subsequently, these buds either grew in size and detached from

the parent cell or they transformed gradually into a string of daughter cells (fig. S34D,E & S35C). All cellular morphotypes observed in former type of reproduction (fig. S32) like, individual spherical cells, hourglass shaped cells undergoing fission and cells in dyads, all bares close morphological similarities with microfossils reported from Swartkopie formations (6) (fig. S32). In subsequent growth stages, we observed cells that were separated from one another with remnants of this process like membrane overhangs that resemble microfossils reported from Sheba formations (fig. S33)(*33*).

In addition to above discussed "binary division-like" cell replication, in some cases protuberances grew into string of daughter cell. *EM-P* during this growth stage resemble microfossils reported from Cleverville (*32*)(fig. S34) and Sulphur spring formations (fig. S35 & S36)(*34*). Based on the morphological similarities, we propose that hollow spherules arranged in a zig-zag manner reported from Onverwacht (Fig. 3)(*17*), spherical cells attached to one another resembling a beaded string that were reported from Moodies (fig. S27)(*29*) could also have formed by *EM-P* like cells fossilized at different growth stages.

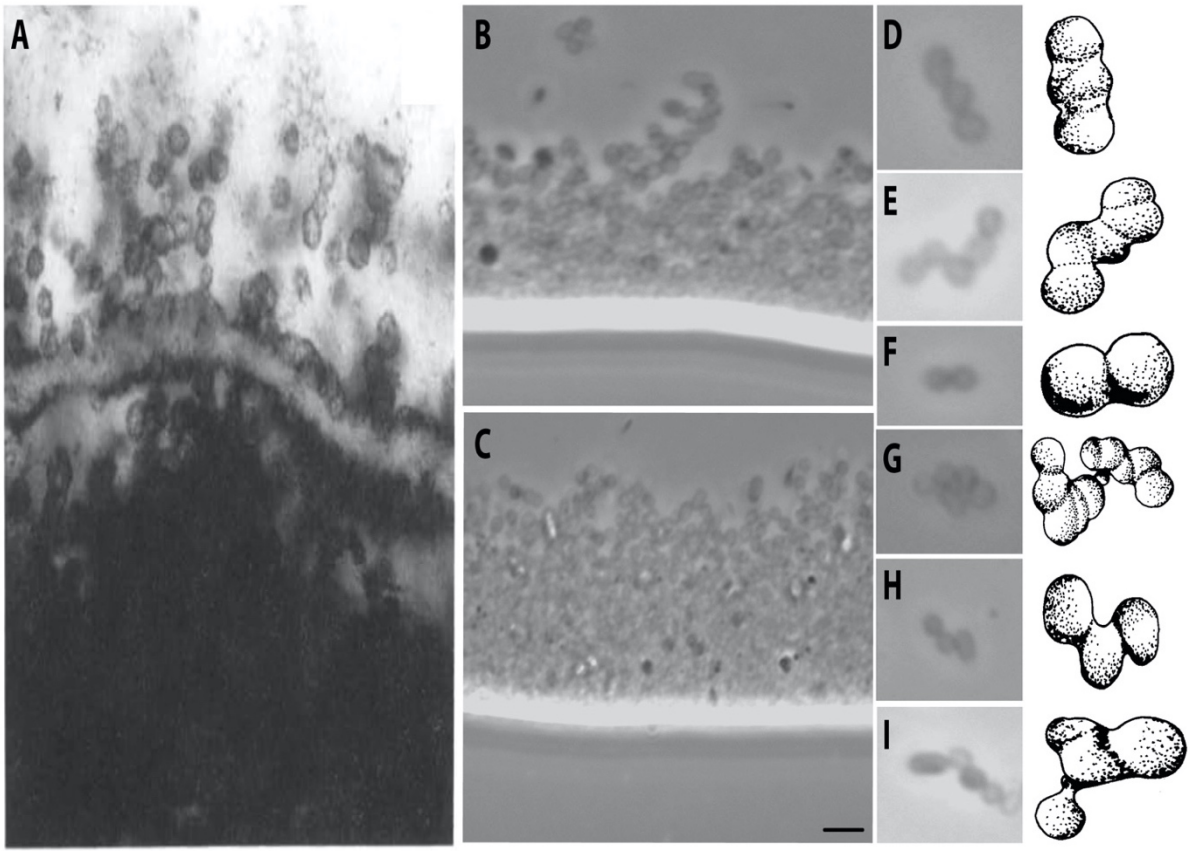

Fig 3. Comparison of Onverwacht group microfossils with *EM-P*.

Image A shows Onverwacht microfossils (5)(originally published by Walsh et al., 1992). Images C&D show sub micrometer size cells *EM-P*, exhibiting morphological similarities with Onverwacht microfossils. Images D-I show cluster of *EM-P* cells organized in different configurations along with interpretive drawings of morphologically similar Onverwacht microfossil (originally published by Westall et al., 2001)(*17*). Scale bars: 5µm.

Most microfossils from PIF and BGB were discovered within parallel layers of organic carbon, termed laminations (*26*, *35–37*). In-case of spherical microfossils, they were almost always discovered in close association with such laminations (*15*). During the late growth stages, *EM-P* formed very similar structures. These structures were formed by a three-step process. First, *EM-P* grew as multiple layers of cells (fig. S37). Second, lysis of these cells

led to the formation of considerable amount of membrane debris (fig. S38). In the third step, different types of membrane debris coalesced to form large fabric like structures, slightly differing in their morphology (fig. S39-48). Morphologically similar fabric-like structures were reported from several microfossil sites (fig. S39-48) (*12*, *15*, *18*, *19*, *28*, *38–40*). Over time these structures grew in area to form a continuous layer of membrane enclosing large cell population of cells, resembling different types of laminated structures reported from microfossil sites (*26*) (Fig. 4, S49-59, Movie S6).

All distinctive features of such lamination like raised mounds, swrils (fig. S60 & S61) (*37*, *41*), bifurcating layers and lenticular gaps (Fig. 4, fig. S50-53 & Movie S6&7) (*26*) were all observed in batch cultures of *EM-P*. Based on our observations, we propose that lenticular gaps within otherwise uniformly parallel laminations were formed due to un-uniform lysis or deflation of multi-layered *EM-P* cells (Fig. 4 & fig. S50-52). In support of this proposition, we noticed these lenticular gaps with an intact *EM-P* cells that didn't underwent complete lysis or remnants of lysed cells within these gaps (Fig. 4 & fig. S50-53). Subsequent lysis of cells within these lenticular structures should have led to formation of hollow gaps, like the ones reported from Moodies formations (*41*)(fig. S50).

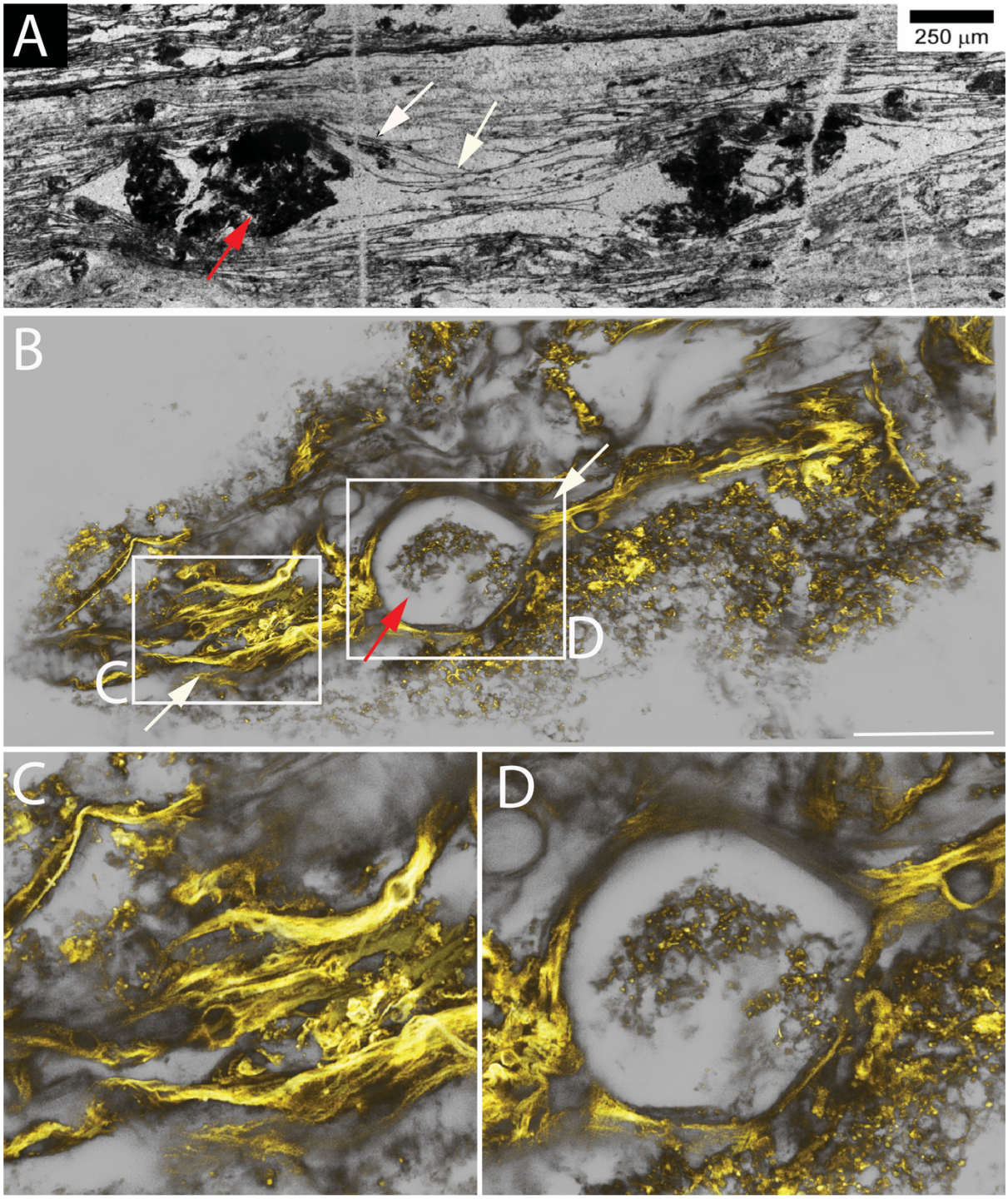

Fig 4. Morphological comparison of BRC laminations with *EM-P*'s membrane debris. Image A shows α-type laminations reported from BRC (originally published by Tice et al., 2009) (30). Images B-D is a 3D-rendered STED microscope image of *EM-P*'s membrane debris exhibiting similar lenticular gaps. White arrows in both the images points to individual layers within the laminations. Red arrows point to the organic structures within the lenticular

gaps (cells in image B). Images C & D are magnified regions of image B, highlighting the multi-layered nature of membrane debris and presence of *EM-P* cell aggregations within the lenticular gaps. Scale bar:20µm (B).

Morphological similarities between 3.8-3-billion-year-old filamentous microfossils with protoplasts of Gram-negative bacteria

Filamentous microfossils enclosed within clasts of organic carbon were reported from both PIF (*1*, *42*, *43*) and BGB sites (4, 5). On the basis of their morphology and discovery site, these microfossils were classified into different taxonomic groups (1). For instance, filamentous microfossils from Apex chert alone are classified into 11 different phylogenetic groups (1). *RS-P* alone exhibited uncanny morphological similarity with all these microfossils (fig. S64-S71). Our observations suggest that all the distinctive morphological features of these microfossils that formed the basis for their phylogenetic segregation, like the hollow spherical vacuoles in case of *Primaevifilum amoenum* (fig. S64-67), comparatively thinner filaments exhibiting a banded pattern in case of *Eoleptonema apex* (Fig. 5H&G) and even thinner filaments with rounded ends and sparsely distributed organic carbon in case of *Archaeotrichion septatum* (Fig. 5A-F), all represent different stages within the life-cycle of *RS-P* like cells (accompanying manuscript). Morphological comparison of *RS-P* with other filamentous Apex chert microfossils (1) and similar microfossils reported from North-pole (*42*) and Sulphur springs (*44*) is presented as fig. S68-S72.

SPF filamentous microfossils were among the well-studied in terms of their morphology, elemental and isotope composition (*24*). Two types of filamentous morphotypes were reported from this site - thin filamentous and thick tubular microfossils with scantly

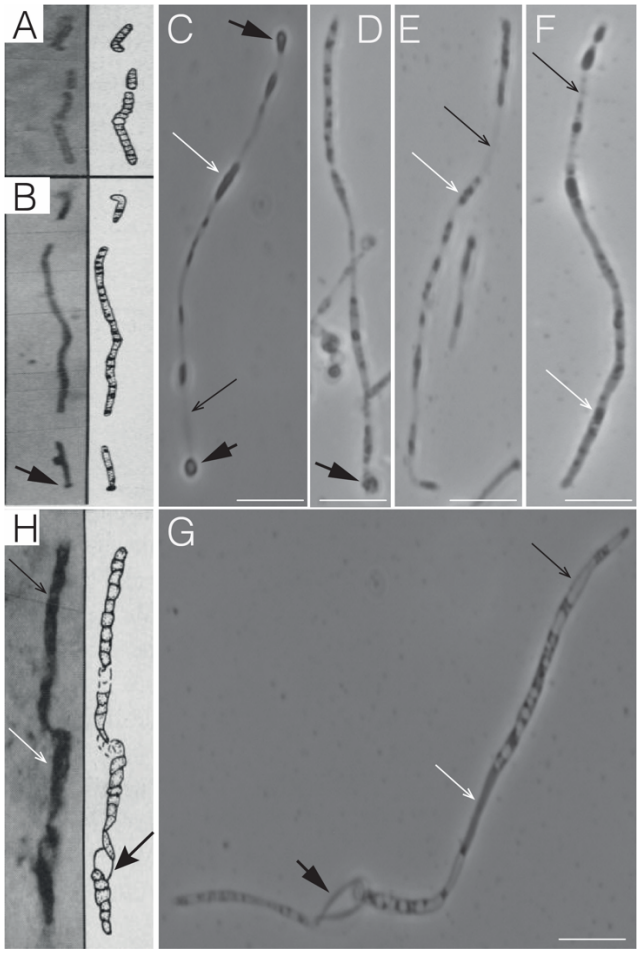

Fig 5. Morphological comparison of *A.septatum* and *E.apex* with *RS-P*.

Images A, B and H are *A.septatum* and *E.apex* respectively (originally published by Schopf et al., 1993) (1). Images C-F and G show *RS-P* cells that are morphologically analogous to *A.septatum* and *E.apex*. The distinctive features of A.septatum like thin filamentous cells with a banding pattern (mostly hollow with intermittently distributed organic carbon) (A & B) and rounded ends (B-black arrow) were also exhibited by *RS-P* (rounded ends indicated by black arrows in C & D and hollow filament in C&D). Image G is filamentous cells of *RS-P* exhibiting morphological similarity with *E.apex*. The white arrows in G and H points to characteristic twisting of hollow regions of cells. Scale bar 5µm (C-F & G).

distributed organic matter (*15*). The description of thin thread like microfossils with clots of organic carbon (blistered appearance) resemble morphotypes of *RS-P* observed during early stages of growth (fig. S73). *RS-P* morphotypes that were similar to tubular SPF microfossils were most frequently observed after 7 days of incubation (fig. S74). All distinctive morphological features of these microfossils like presence of spherical inclusions within tubular cells (fig. S74, Movie S8), characteristic twisting and bending of these filaments, were also exhibited by *RS-P* (fig. S74-S76 &)(*15*). Such internal spherical inclusions in *RS-P* were rarely noticed to be static (barely visible in fig. S74E but can be clearly seen in Movie S8). Spherical structures with and devoid of internal organic carbon were observed in close proximity to the tubular SPF microfossils (fig. S74). Similar spherical structures were also observed in batch cultures of *RS-P* (discussed in-detail in sections below) (fig. S74).

One of the morphologically distinct group of microfossils reported from both BGB and PIF are the lenticular microfossils (*4*, *5*, *15*, *24*). *RS-P* exhibited morphologies that were very similar to all known lenticular microfossils – individual lenticular cells (Fig. 6&7), chain-like structures composed of lenticular cells (Fig. 7G & fig. S77) and lenticular cells with internal voids (Fig. 6). Lenticular structures of *RS-P* were formed by further swelling of blister-like structures within filamentous cells, discussed above (fig. S73). Lenticular microfossils reported from Overwacht formations (5), cells with a defined cell boundary and dense interior with organic carbon resemble an early growth-stage *RS-P* cells (Fig. 6). In-comparison, microfossils reported from SPF having a fussy cell boundary and reticulate interiors resemble late growth-stage *RS-P* cells (Fig. 7) (*28*).

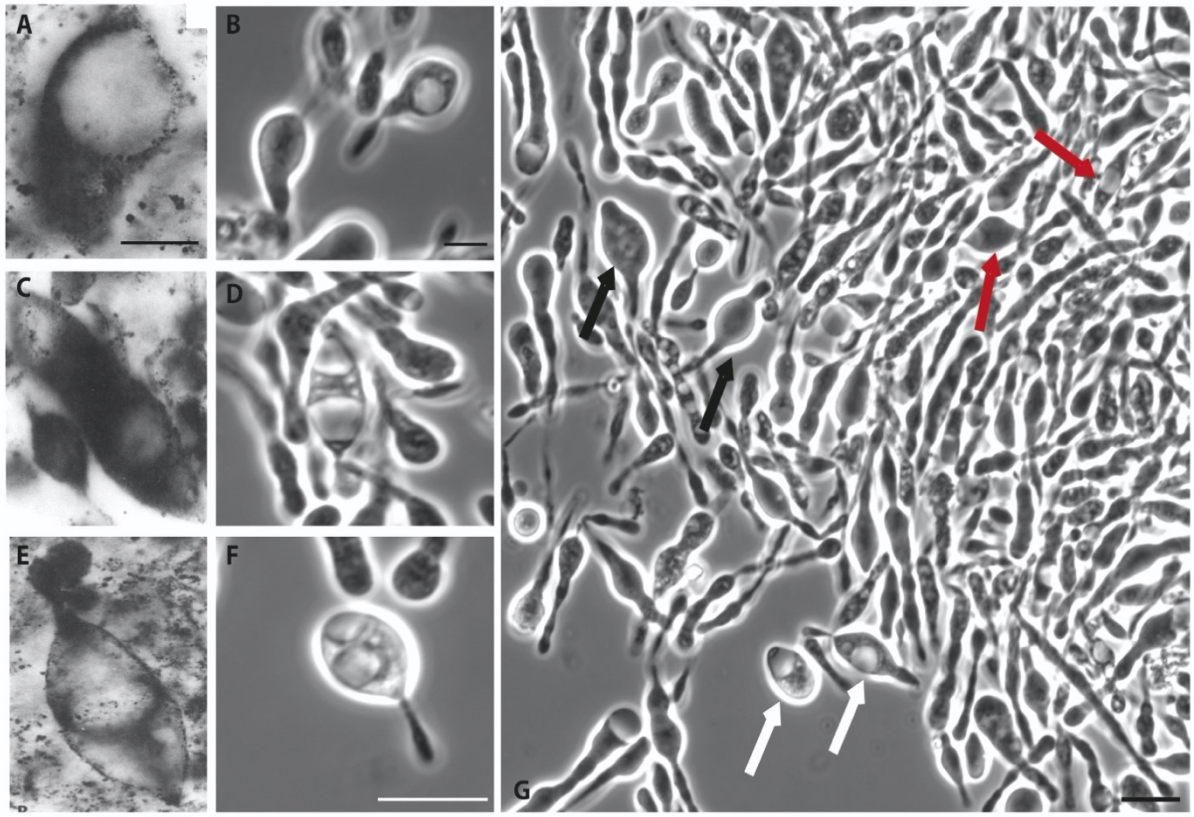

Fig 6. Comparison of Overwacht lenticular microfossils with *RS-P*.

Images A, C & E are lenticular microfossils reported from Overwacht region (originally published by Walsh et al., 1992) (5). Images B, D, F & G are images of *RS-P*. Scale bar in images A is10 µm (also applies for C&E). A&B shows lenticular Overwacht and *RS-P* cells exhibiting one vacuole. C&D shows lenticular Overwacht and *RS-P* cells exhibiting two terminal vacuoles. E&F shows lenticular Overwacht and *RS-P* cells exhibiting three vacuoles. Image G shows brightfield image of three-day old *RS-P*. Scale bar: 10 µm (A, C & E), 2 µm (B, D & F) and 10 µm (G).

A recent study reported microfossils from Nuvvuagittuq ferruginous rock formations (NMF) (~4.2-3.7Ga), which were considered to be the oldest known traces of life on Earth (*45*). These microfossils bares no close resemblance to any extant prokaryotes including *R.sphaeroides* (*RS*); nevertheless, protoplasts of *R.sphaeroides* (*RS-P*) exhibited uncanny

morphological similarities to NMF microfossils (Fig. 8). All distinctive features of these microfossils like large spherical cells with one or two filamentous arms (Fig. 8 & S78), presence of an inner filamentous structure within these arms (TEM cross sections in Fig. 8C); spherical or filamentous outer membrane vesicles (OMV) being formed by blebbing of outer membrane (Fig. 8, S79 and Movie S9); were also observed in *RS-P*.

Like *EM-P*, during the last growth- stage *RS-P* underwent lysis that led to formation of membrane debris (fig. S80 & S81). Two types of membrane debris were observed in *RS-P* incubations – film-like (fig. S80) and filamentous (fig. S81). Membrane debris of

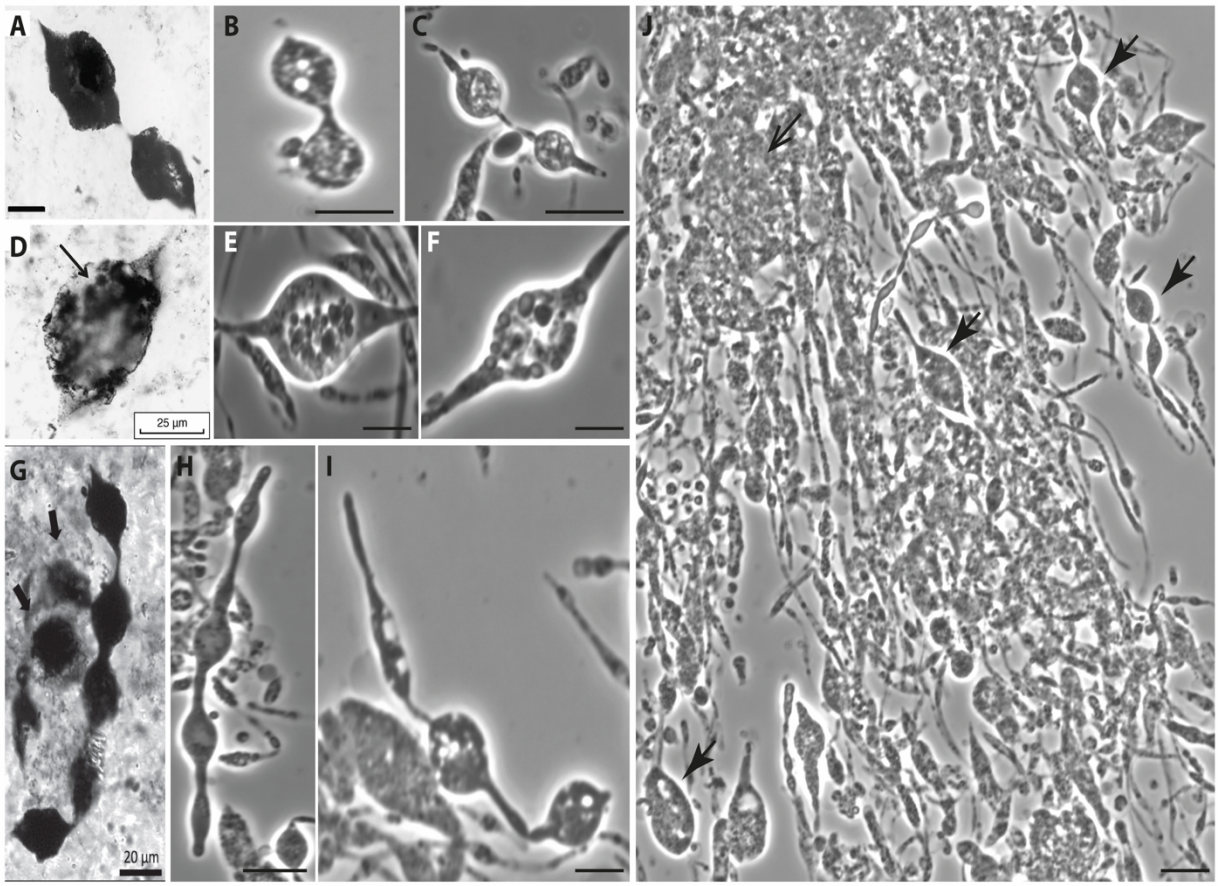

Fig 7. Morphological comparison of SPF lenticular microfossils with *RS-P*.

Images A, D&G are lenticular microfossils reported from Pilbara region, WA (originally published by Sugitani et al., 2007) (*28*). Images B, C, E, F, H, I &K are images of 10-18 days

old *RS-P* cells. The scale bars in images B, C, E, F, H & I are 5µm & in image J is 10µm. Images A-C shows lenticular WA microfossils and *RS-P* cells in pairs, probably undergoing cell separation. D-F shows lenticular WA microfossils and *RS-P* cells with overhangs probably formed by separation of cells from chains (G&H) and spherical intracellular structures. Images G-I shows lenticular WA microfossils and *RS-P* cells arranges as chains of lenticular cells. Image J shows wide filed image of 10-15 days old *RS-P* colony. Black arrows point to cells with internal reticulate structures.

RS-P bare close morphological resemblance to filamentous organic structures reported from Kitty's Gap Chert (fig. S81) (*46*) and film-like structures reported from BGB (fig. S81) (*17*, *47*). Like observed in BGB, *RS-P* formed biofilms with morphologically analogous rice grain-like cells (fig. S82).

Implications for taxonomy and ecophysiology of Archaean Eon microfossils

Advances in both microscopic (FIB-SEM) and analytical (NanoSIMS) techniques over the past few decades have facilitated precise determination of chemical and isotopic compositions of microfossils (*11*, *48*). Nevertheless, there is a considerable disagreement among researchers regarding the interpretation of this information (11). Decades of back-and-forth arguments led to general consensus, that reconstructing the life cycles of Archaean Eon organisms, is considered the only way for understanding the nature of

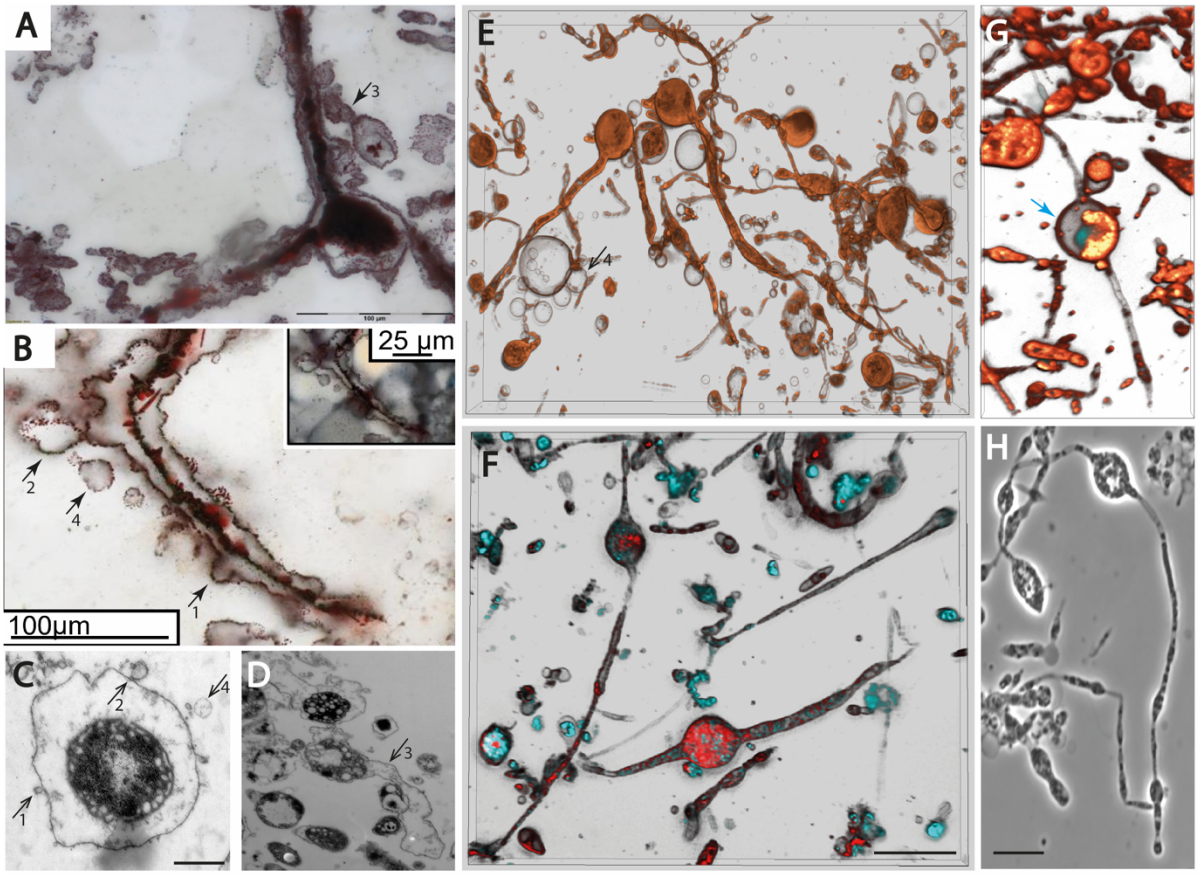

Fig 8. Morphological comparison of *RS-P* with NMF.

A & B are images of NMF (originally published by Dodd et al., 2017) (*45*). C-H are morphologically analogous *RS-P* with one or two filamentous extensions. C&D are the TEM cross sections of such filamentous cells exhibiting large periplasmic space (C), similar to NMF microfossils (B). Arrows in the images A-E points to the spherical (C) and filamentous (D) OMV's being formed by membrane blebbing. Numbers on arrows depicts sequential stages involved in formation of these vesicles. E-H are 3D-STED and phase-contrast images of *RS-P* with one or two filamentous extensions, that were similar to NMF microfossils (A&B). Movie S9 show *RS-P* with similar OMV's. Scale bars in images C & D are 0.5µm and in images E-H are 10µm.

these microfossils (13). To the best of our knowledge, ours is the first study to reproduce all known microfossil morphologies and their lifecycles from extant bacteria. In the following sections of this manuscript, we attempt to answer some long-standing questions like – Were these organic structures are of biological origin? How did microfossils reported from far-flung sites like Western Australia and South Africa exhibited very similar morphologies? Are they or are they not Cyanobacteria? along with likely explanation behind their δ^{13}C-biomass values.

Biological origin of several organic structures was questioned by previous studies as morphologies of these structures resemble mineral aggregates formed by abiotic processes (9–12). Much of the criticism was devoted to Apex Chert microfossils (*9*). Presence of organic carbon only at the periphery of the cell; absence of internal cell constituents; random pattern in cell length and width (fig. S68); twisting (fig. S75-S76 & S83) and branching (Fig. 9) of cells, which is inconsistent with morphologies of known filamentous bacteria; presence of silicate minerals inside the filaments; were argued as claims for their abiotic origin (11). Justifiably, such structures were never before observed in any living organism. Nevertheless, we observed all these morphological features in *RS-P*, suggesting these features were within the realm of possible bacterial morphologies. Here we also showed that cells could exhibit such morphologies when bacteria are exposed to environmental conditions, similar to the ones experienced by cells at the time of their fossilisation (*14*) (discussed below). Several of the above highlighted features like presence of inorganic salts within the microfossils and inconsistencies in dimension of individual cells within a filament are not restricted to Apex chert microfossils (*49*). Such discrepancies were reported from several bona-fide microfossil from other sites (*49*). Our observations suggest, inorganic minerals should have entered the cell during the formation of membrane vesicles extending into the cell (fig. S84), taking with

them the inorganic minerals from the surroundings. Moreover, morphologies of Apex chert organic structures were also in continuity with the microfossil morphologies from other sites, all of which represent different growth stages of *RS-P* or *EM-P*, corroborating biological nature of these microfossils.

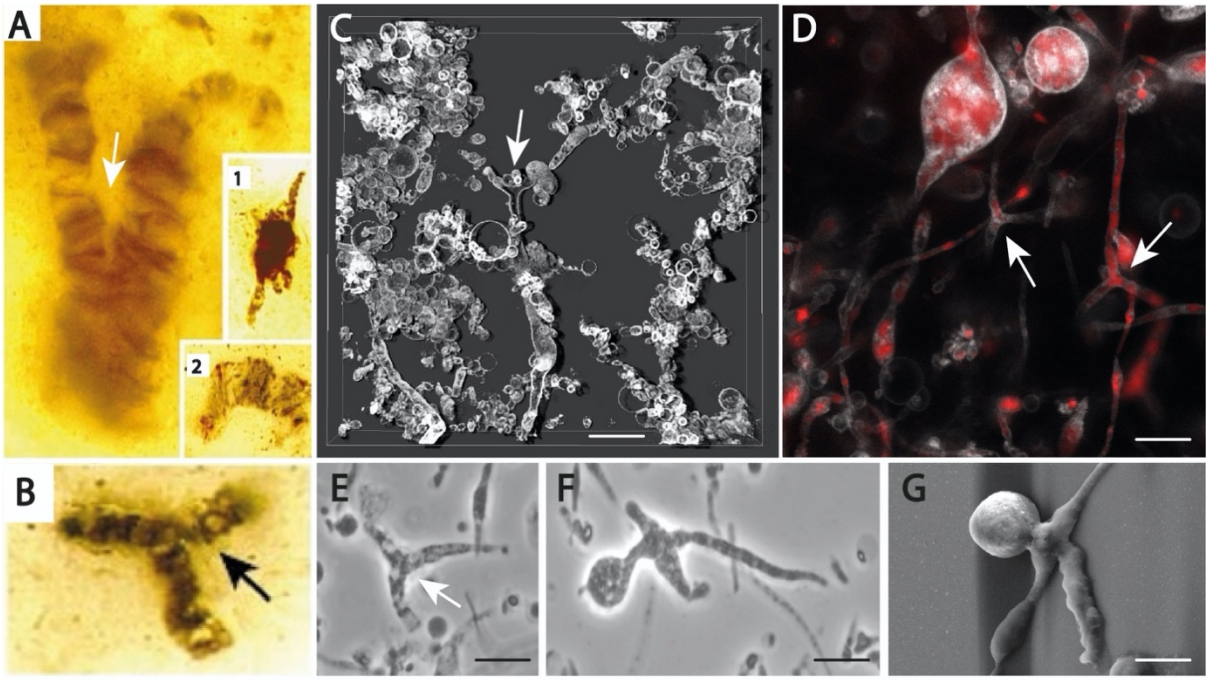

Fig 9. Comparison of filamentous *RS-P* cells with Apex chert microfossils.

Image A & B show microfossils reported from Apex chert, exhibiting branching (originally published by Brasier et al., 2002)(9). Images C-G are STED (C & D), phase-contrast (E & F) and SEM (G) *RS-P* cells exhibiting a similar branching pattern. Cells in image C&D are stained with DNA stain PicoGreen (red) and membrane stain FM^{TM}5-95 (white). Arrows in Images points to the branching of filaments observed in both Apex chert microfossils and *RS-P*. Images A1 shows a lenticular cell with filamentous overhangs, morphologically similar cell can be seen in image D. Scale bar in images C-F is 5μm and G is 1μm.

Along with Apex chert organic structures, recent studies contested biological origin of organic structures from Dresser (10), SPF and Moodie's formation (12). Like the above discussion, argument for re-classification of these organic structures as mineral aggregates is also based on the absence of analogous morphological features among extant organisms (10, 12). One of the most important criteria for establishing biogenicity of a microfossil is either to present a convincing morphological analogue among extant bacteria or to establish the biogenic process by which they are formed. The biogenicity of Swartkoppoie formation microfossils (fig. S32) was widely accepted among scientific community due to the discovery of microfossil morphologies in different stages of their cell-division (6). To date, a sequential process by which Archean organic structures might have formed, has never been presented before. In the supplementary section of this manuscript, we present exact morphological reproductions of organic structures reported from Dresser, SPF and Moodie's formations, whose biological origin is being contested (*10*, *37*, *48*). Along with reproducing their morphologies, we also describe the sequential steps leading to their formation. To the best of our knowledge, such extensive proof of biogenicity for Achaean microfossil was never presented before.

RS-P and *EM-P* when grown in the presence of 5-10% w/v DSS exhibited complex morphologies and lifecycles involving substantial morphological transformations. Only inherent property of these organisms that influenced the morphology is the architecture of the cell membrane. No morphological overlap was observed between *EM-P* and *RS-P*. Different morphologies observed within these two groups are interchangeable. They either represent differences in their growth stages or environmental conditions. Based on this property we classify microfossils into proto-Gram-positive, cells having a single bilayer membrane and

proto-Gram-negative, cells having a dual bilayer membrane. All reported Archean microfossils resemble one of *EM-P* (fig. S1-S63) or *RS-P* (fig. S64-S83) morphotypes. For example, all the filamentous and lenticular microfossils reported from PIF, BGB and NMF sites, were likely remains of a proto-Gram-negative (like *RS-P*) bacteria fossilised at different growth stages. Similarly, we classify all the spherical microfossils of different sizes exhibiting internal compartmentalisation, in dyads or organised as strands of pearls as likely remains of a proto-Gram-positive (like *EM-P*) bacteria fossilised at different growth stages. What was assumed to be fossilised EPS (*17*), most likely was the membrane debris produced by these organisms (Fig.4 & fig. S38-S63). Our results suggest, unlike extant bacteria which evolved mechanisms to regulate their morphology and mediate cell division, these primitive Archaean organisms most likely were dependent on physicochemical forces of the environment to mediate these processes. This phenomenon could also explain the similarities in the microfossil morphologies reported from far-flung sites like BGB in South Africa and PIF in Australia (3, 12).

Culture conditions employed in our experiments are presumably similar to the environmental conditions faced by Archaean organisms. All sites from which microfossils were reported are shallow intertidal regions. Evidence for periodic evaporation and flooding with sea water was presented from both BGB and PIF sites (*5*, *43*), indicating all microfossils experienced high salinities. Given the 1.5 to 2 times higher salinities of Achaean oceans (*14*), we presume the salinities of the sea water could be similar to the ones used in our experiments (5-10% w\v). To the best of our knowledge, the exact salt composition of the Archaean Ocean has not been elucidated. Hence, in our experiments we used complex mixture of salts (DSS) as a proxy to reproduce these salinities. Salts like Mg^{+2}, Ca^{+2}, Na^{+} and K^{+} salts or their oxides were reported to be present and constitute 1-5% by weight in both Pilbara and BGB microfossil

sites (*5*, *43*). Moreover, these salts were shown to be closely associated with microfossils from Apex chert. The pattern of spatial distribution of these salts seems to resemble the special distribution pattern of organic carbon, possibly indicating chelation of these salts to cell membrane, which is in agreement with our observations (*11*). Presence of potassium phyllosilicates and NaCl crystals within lenticular microfossils (*43*) is also in agreement with our hypothesis that internal structures of the microfossils should have formed by invagination of cell-membrane taking in salt rich water (fig. S84). Like observed in microfossils, presence of salt crystals on the cell membrane, within the membrane invaginations or cell-debris was often observed in *EM-P* (fig. S84), also supporting our hypothesis.

The most important criteria for establishing biogenicity and taxonomic classification of microfossils has always been their morphology and carbon isotopic composition. Given the consistency of morphology with phylogeny in extant bacteria (*51*), filamentous nature of microfossils (*1*, *15*) and δ^{13}C-MF-biomass values (*52*), arguably suggesting their autotrophic physiology; this led to annotating most of the above discussed microfossils as Cyanobacteria (*1*, *31*). Justifiably, colony characteristics of microfossils like formation of multi-layered stromatolite like structures and mechanisms of reproduction observed in some of these microfossils were similar to Cyanobacteria belonging to genus *Pleurocapsa* (*53*). But, more recent studies on both microfossil morphologies (≥10nm resolution)(11) and genome analysis of extant Cyanobacteria were not in-tune with this claim (*54*, *55*). For instance, Cyanobacteria have a cell-wall that is thicker than other Gram-negative bacteria (*56*). The cell-walls of both heterocysts and akinete spores are considerably thicker (51, 52). Neither indications of a thicker cell-wall nor the presence of internal structures consistent with the morphology of a heterocysts or akinete's were reported from PIF microfossils (11). The

periphery of Apex chert microfossils is marked by 5 nm carbon layer, matching the thickness of a lipid bilayer like observed in *RS-P*, rather than a cell-wall (Fig. 10).

Analyses of cyanobacterial genomes also concluded that they first evolved in fresh-water habitats and then evolved mechanisms to colonize marine habitats (*54*). Given the high salinities of microfossil sites and Precambrian oceans (*14*), we do not assume that this happened long before the great oxidation event (*58*). Early cyanobacterial morphologies were also considered to be restricted to simpler unicellular cocci. The filamentous forms exhibiting cell differentiation and large spherical baeocyte forming morphotypes are not thought to have evolved until 2.5 Ga (*55*), contradicting the annotation of filamentous PIF microfossils as Cyanobacteria. Upon long-term incubation (30 months) *EM-P* cells got encrusted with salts from the culture media to form stromatolite like structures, resembling Cyanobacteria, microfossils from BGB (fig. S85 & S86), North Pole (fig. S87) and SPF formation (fig. S88)(*15–17*). Based on uncanny morphological similarities between bacterial protoplasts from our study and Archaean microfossils, we propose that these microfossils were primitive cells yet to evolve a cell-wall rather than Cyanobacteria.

Discovery of microfossils in Archaean BIF's and δ^{13}C-biomass values, contributed to the wider acceptance of the proposition that these microfossils were Cyanobacteria. Although, presence of isotopically lighter carbon of microfossil biomass in-comparison to surrounding rock carbonates suggests their biological nature. In our opinion, further interpretation of their physiology solely based on one time-point δ^{13}C-biomass is fraught with errors. Moreover, drawing parallels between δ^{13}C-biomass of extant bacteria belonging to a particular physiological group and 3.8 Ga microfossils, involves subscribing to the idea that both these organisms used the same physiological pathways with identical enzymes. Such assumptions

are not in-tune either with the principles of Darwinian evolution or with the phylogenetic diversity and isotope discrimination properties of enzymes within a carbon fixation process (*59–61*). As an example, key enzyme of Calvin-Benson-Basham (CBB) cycle, RubisCO, was known to have diversified into several phylogenetic classes over time (*59*, *60*). These isoforms differ from each other not only in their carbon isotope fractionation values (*62*) but also in their substrate specificity (*61*), reaction kinetics (*61*), and even in their function (*63*, *64*). Existence of different isoforms of RubisCO's suggests existence of a proto-RubisCO, an evolutionary ancestor to all known RubisCO and RubisCO like proteins. The structure, function and isotope fractionation properties of such proto-RubisCO is presently unknown.

Even in case of extant Cyanobacteria, whose C-isotope fractionation properties were well determined, their δ^{13}C-biomass values in natural environments are known to fluctuate between -34.4% to -5.9% (*65*), indicating δ^{13}C-biomass values are prone to exhibit huge variations in natural environments. These reported values (-34.4% to -5.9%) overlap with other known C-fixation processes like methanogenesis, homoacetogenesis and methanotrophy (*66–70*), which further complicates the distinction between different physiological pathways.

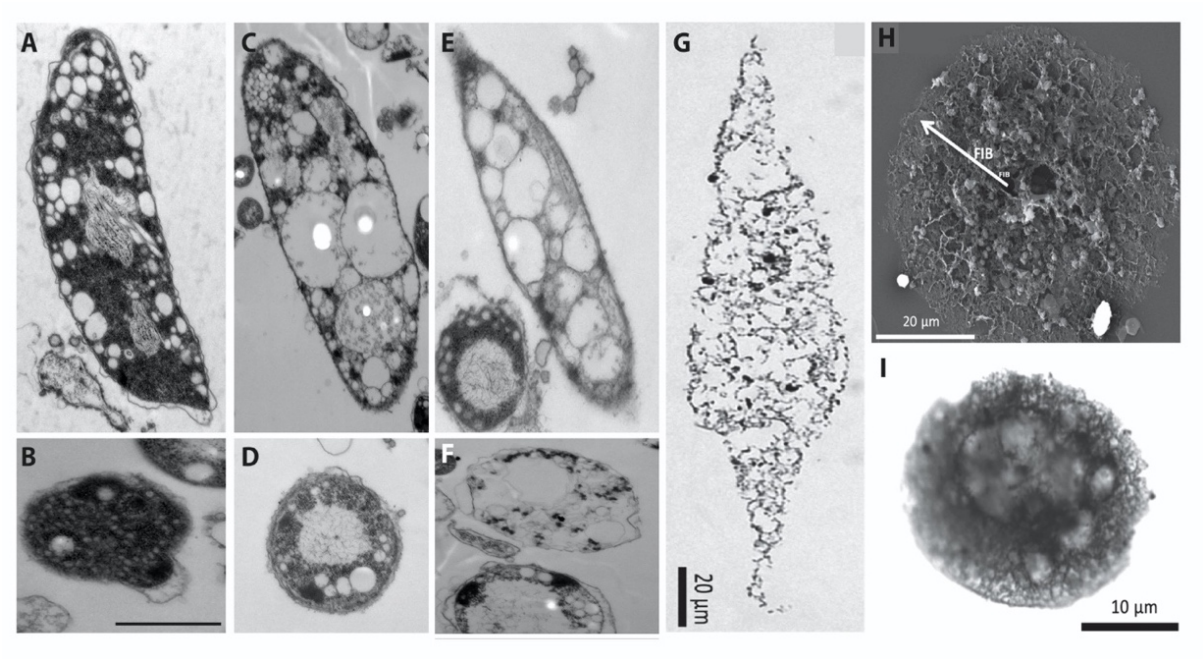

Fig 10. Morphological comparison of *RS-P* with SPF microfossils.

Images A-F are horizontal (A-E) and lateral (B-F) cross section TEM images of *RS-P* (Scale bar in B is 1µm) and G-I are TEM (G) and FIB-SEM (H&I) images of lenticular microfossils from Glodsworth locality (originally published by Sugitani et al., 2016) (*71*). Images A-E, shows sequential depletion of *RS-P*'s cytoplasm and simultaneous increase of intracellular vesicles, leading to a reticulate appearance. Tiny spherical inclusions can be seen in microfossil image H.

Lenticular microfossils with cytological differences were reported from Water fall region (*24*). Type-1 lenticular microfossils with uniformly distributed cytoplasm and δ^{13}C-biomass of -27.4% resemble early growth stage of *RS-P* cells (Fig. 6). Whereas Type-2 & 3 lenticular morphotypes with reticulate interiors, clots of organic carbon and lower δ^{13}C-biomass (-30 to -32% and -40%) resemble late growth stage of *RS-P* cells (Fig. 7). Such a gradual decrease in the cytoplasmic content together with an increase in intracellular membrane (reticulate) structures, was observed in *RS-P* (fig. S78). The gradual depletion in δ^{13}C-biomass values of microfossils could be due to the lower δ^{13}C-fatty acids compared to that of the δ^{13}C-biomass

(*72*). The lowest $\delta^{13}C$-values of spherical organic carbon clots could be explained by differences in $\delta^{13}C$-values of individual fatty acids. It was reported that unsaturated fatty acids were -4 to -17% depleted in $\delta^{13}C$-values compared to saturated fatty acids (*72*). When stained with dyes specific for lipids and liquid-disordered (L_d – mostly composed of unsaturated lipids) regions of the membrane, spherical internal vesicles were preferentially stained with L_d stains (fig. S89). This indicate that these internal vesicles were largely composed of unsaturated fatty acids, which could explain lower $\delta^{13}C$-values of these spherical clots. A similar pattern of differences was observed between $\delta^{13}C$ values of saturated and unsaturated FA in *RS-P* (Tab. S1 & 2). Morphological comparison of *RS-P* with lenticular microfossils also suggests most of the microfossil biomass could composed of fatty acids (Fig. 10). We presume, this variable nature of $\delta^{13}C$-fatty acids further adds to the complexities in conclusively determining the C-incorporation pathways of these microfossils. Due to these uncertainties, we refrain from predicting either phylogeny or C-fixation pathways of these microfossils, solely based on their morphology or $\delta^{13}C$-biomass of microfossils. Nevertheless, spatial distribution and isotopic composition of iron associated with microfossils seems to suggest their iron-oxidizing and iron-reducing physiology.

Our assumption that these microfossils were proto-iron cycling bacteria rather than Cyanobacteria is supported by the fact that most microfossils were discovered in BIF's and are closely associated with iron minerals (*73*). In NMF's, hematite is associated with outer and inner membrane of the microfossils (Fig. 9, red spots on inner filament). This suggests Fe(II)-oxidation took place in periplasmic space, like reported in phototrophic Fe(II)-oxidising bacteria (*74*). If Fe(II)-oxidation was mediated by an abiotic process, with O_2 produced by Cyanobacteria, we expect Fe(III)-hydroxides to be localised to cell surface, rather than in the periplasmic space. The pattern of Fe(III) distribution in several BIF's

resemble the morphologies observed in *RS-P* (incidentally, a genus well studied for phototrophic Fe(II)-oxidation). Some Archaean BIF's were reported to have magnetite/hematite precipitated as granules, enclosed in a lenticular structure (*75*) – Granular iron formations (fig. S90). These structures were morphologically similar to the ones observed in *RS-P*. Based on these similarities, we propose the following sequence of events that could have led to their formation – Oxidation of Fe(II) to Fe(III) could have happened in the periplasmic space (*74*) of lenticular microfossils, following this Fe(III) cation could have adsorbed to the anionic cell-membrane, this chelation could have led to the invagination and formation of spherical intracellular vesicles with Fe(III)-mineral coating around them. This phenomenon of vesicle formation by electrostatic interaction between cations and phospholipid membranes is a well-studied phenomenon (*76*). The δ^{56}Fe values of Archaean eon BIF's are also in agreement with anaerobic Fe(II)-oxidation processes and inconsistent with abiotic Fe(II)-oxidation coupled with oxygen produced by Cyanobacteria (*77*, *78*), which is also in accordance with our hypothesis that these microfossils could be proto-iron cycling bacteria rather than Cyanobacteria.

Instead of annotating Archaean Eon microfossils to a particular phylogenetic group of extant bacteria, we hypothesise that these microfossils are Protocells proposed by theory of chemical evolution (*79*). This theory proposed the existence of protocells, as an evolutionary intermediate between abiotic chemical reactions happening on early Earth and evolution of prokaryotes. These cells were hypothesised to be primitive and devoid of all molecular biological processes regulating either their morphology or cell-division.

Most of our current understanding of protocells and their mode of cell-division was largely either a result of studying lipid vesicles, termed bottom-up approach (*80*) or from studying cells whose genome was sequentially reduced to its bare minimum (*81*), termed top-down

approach. Morphologies and mode of cell-division observed in *RS-P* and *EM-P* is in accordance with theories proposed by both top-down (fig. S91) and bottom-up approaches (*82*). Moreover, morphologies of *EM-P* and microfossils, very much resemble the simulated morphologies of protocells generated by numerical modelling approaches (83)(fig. S92). As our hypothesis is in perfect accordance with results from above-described approaches, we argue for reinterpretation of these microfossils as protocells (proto-Gram-negative & proto-Gram-positive cells) and discourage use of microfossil morphology as a basis for systemic palaeontology.

To date, our understanding of early life on earth resulted from advances in several fields of biology: palaeontology, which deals with morphology and isotopic signatures of microfossils; phylogeny, which addresses genomic changes that happened over time; and a bottom-up approach of studying lipid vesicles. However, these fields were seldom integrated with one other to form coherent conclusions. Here we provide a missing link connecting these studies. We propose that microfossils observed in Archaean BIFs were most likely liposome like protocells, which had evolved mechanisms for energy conservation, but not for regulating cell morphology and replication. To the best of our knowledge, ours is the first study to provide paleontological evidence of the existence of protocells on Precambrian Earth.

References and Notes:

1. J. W. Schopf, Microfossils of the Early Archean Apex chert: new evidence of the antiquity of life. *Science (80-.).* **260**, 640–646 (1993).
2. M. M. Walsh, D. R. Lowe, Filamentous microfossils from the 3,500-Myr-old Onverwacht Group, Barberton Mountain Land, South Africa. *Nature*. **314**, 530 (1985).
3. J. W. Schopf, E. S. Barghoorn, Alga-like fossils from the early Precambrian of South Africa. *Science (80-.).* **156**, 508–512 (1967).
4. D. Z. Oehler, M. M. Walsh, K. Sugitani, M.-C. Liu, C. H. House, Large and robust lenticular microorganisms on the young Earth. *Precambrian Res.* **296**, 112–119 (2017).
5. M. W. Walsh, Microfossils and possible microfossils from the early archean onverwacht group, barberton mountain land, South Africa. *Precambrian Res.* **54**, 271–293 (1992).
6. A. H. Knoll, E. S. Barghoorn, Archean microfossils showing cell division from the Swaziland System of South Africa. *Science (80-.).* **198**, 396–398 (1977).
7. J. W. Schopf, K. Kitajima, M. J. Spicuzza, A. B. Kudryavtsev, J. W. Valley, SIMS analyses of the oldest known assemblage of microfossils document their taxon-correlated carbon isotope compositions. *Proc. Natl. Acad. Sci.* **115**, 53–58 (2018).
8. H. Gee, That's life? *Nature*. **416**, 28 (2002).
9. M. D. Brasier, O. R. Green, A. P. Jephcoat, A. K. Kleppe, M. J. Van Kranendonk, J. F. Lindsay, A. Steele, N. V. Grassineau, Questioning the evidence for Earth's oldest fossils. *Nature* (2002), doi:10.1038/416076a.
10. D. Wacey, N. Noffke, M. Saunders, P. Guagliardo, D. M. Pyle, Volcanogenic Pseudo-

Fossils from the ~3.48 Ga Dresser Formation, Pilbara, Western Australia. *Astrobiology* (2018), doi:10.1089/ast.2017.1734.

11. D. Wacey, M. Saunders, C. Kong, A. Brasier, M. Brasier, 3.46 Ga Apex chert 'microfossils' reinterpreted as mineral artefacts produced during phyllosilicate exfoliation. *Gondwana Res.* **36**, 296–313 (2016).

12. I. Köhler, C. Heubeck, Microbial-mat-associated tephra of the Archean Moodies Group, Barberton Greenstone Belt (BGB), South Africa: Resemblance to potential biostructures and ecological implications. *South African J. Geol.* (2019), doi:10.25131/sajg.122.0015.

13. K. Sugitani, K. Grey, T. Nagaoka, K. Mimura, M. R. Walter, Taxonomy and biogenicity of Archaean spheroidal microfossils (ca. 3.0 Ga) from the Mount Goldsworthy–Mount Grant area in the northeastern Pilbara Craton, Western Australia. *Precambrian Res.* **173**, 50–59 (2009).

14. L. P. Knauth, Salinity history of the Earth's early ocean. *Nature*. **395**, 554 (1998).

15. K. Sugitani, K. Mimura, T. Nagaoka, K. Lepot, M. Takeuchi, Microfossil assemblage from the 3400 Ma Strelley Pool Formation in the Pilbara Craton, Western Australia: results form a new locality. *Precambrian Res.* **226**, 59–74 (2013).

16. R. Buick, Microfossil Recognition in Archean Rocks: An Appraisal of Spheroids and Filaments from a 3500 M.Y. Old Chert-Barite Unit at North Pole, Western Australia. *Palaios* (1990), doi:10.2307/3514837.

17. F. Westall, M. J. de Wit, J. Dann, S. van der Gaast, C. E. J. de Ronde, D. Gerneke, Early Archean fossil bacteria and biofilms in hydrothermally-influenced sediments from the Barberton greenstone belt, South Africa. *Precambrian Res.* **106**, 93–116 (2001).

18. F. Delarue, F. Robert, S. Derenne, R. Tartèse, C. Jauvion, S. Bernard, S. Pont, A.

Gonzalez-Cano, R. Duhamel, K. Sugitani, Out of rock: a new look at the morphological and geochemical preservation of microfossils from the 3.46 Gyr-old Strelley Pool Formation. *Precambrian Res.* (2019), doi:10.1016/j.precamres.2019.105472.

19. G. J. Retallack, D. H. Krinsley, R. Fischer, J. J. Razink, K. A. Langworthy, Archean coastal-plain paleosols and life on land. *Gondwana Res.* (2016), doi:10.1016/j.gr.2016.08.003.

20. E. V. Barlow, M. J. Van Kranendonk, Snapshot of an early Paleoproterozoic ecosystem: Two diverse microfossil communities from the Turee Creek Group, Western Australia. *Geobiology* (2018), doi:10.1111/gbi.12304.

21. D. Wacey, M. R. Kilburn, M. Saunders, J. Cliff, M. D. Brasier, Microfossils of sulphur-metabolizing cells in 3.4-billion-year-old rocks of Western Australia. *Nat. Geosci.* **4**, 698–702 (2011).

22. K. Sugitani, K. Mimura, M. Takeuchi, T. Yamaguchi, K. Suzuki, R. Senda, Y. Asahara, S. Wallis, M. J. Van Kranendonk, A Paleoarchean coastal hydrothermal field inhabited by diverse microbial communities: the Strelley Pool Formation, Pilbara Craton, Western Australia. *Geobiology*. **13**, 522–545 (2015).

23. J. W. Schopf, B. M. Packer, Early Archean (3.3-billion to 3.5-billion-year-old) microfossils from Warrawoona Group, Australia. *Science (80-.).* **237**, 70–73 (1987).

24. K. Lepot, K. H. Williford, T. Ushikubo, K. Sugitani, K. Mimura, M. J. Spicuzza, J. W. Valley, Texture-specific isotopic compositions in 3.4 Gyr old organic matter support selective preservation in cell-like structures. *Geochim. Cosmochim. Acta*. **112**, 66–86 (2013).

25. J. Kazmierczak, W. Altermann, B. Kremer, S. Kempe, P. G. Eriksson, Mass occurrence of benthic coccoid cyanobacteria and their role in the production of

Neoarchean carbonates of South Africa. *Precambrian Res.* **173**, 79–92 (2009).

26. M. M. Tice, Environmental controls on photosynthetic microbial mat distribution and morphogenesis on a 3.42 Ga clastic-starved platform. *Astrobiology* (2009), doi:10.1089/ast.2008.0330.

27. J. W. Schopf, A. B. Kudryavtsev, J. T. Osterhout, K. H. Williford, K. Kitajima, J. W. Valley, K. Sugitani, An anaerobic ∼3400 Ma shallow-water microbial consortium: Presumptive evidence of Earth's Paleoarchean anoxic atmosphere. *Precambrian Res.* (2017), doi:10.1016/j.precamres.2017.07.021.

28. K. Sugitani, K. Grey, A. Allwood, T. Nagaoka, K. Mimura, M. Minami, C. P. Marshall, M. J. Van Kranendonk, M. R. Walter, Diverse microstructures from Archaean chert from the Mount Goldsworthy–Mount Grant area, Pilbara Craton, Western Australia: microfossils, dubiofossils, or pseudofossils? *Precambrian Res.* **158**, 228–262 (2007).

29. E. J. Javaux, C. P. Marshall, A. Bekker, Organic-walled microfossils in 3.2-billion-year-old shallow-marine siliciclastic deposits. *Nature*. **463**, 934 (2010).

30. L. J. Duck, M. Glikson, S. D. Golding, R. E. Webb, Microbial remains and other carbonaceous forms from the 3.24 Ga Sulphur Springs black smoker deposit, Western Australia. *Precambrian Res.* **154**, 205–220 (2007).

31. J. Kaźmierczak, B. Kremer, Pattern of cell division in∼ 3.4 Ga-old microbes from South Africa. *Precambrian Res.*, 105357 (2019).

32. Y. Ueno, Y. Isozaki, K. J. McNamara, Coccoid-like microstructures in a 3.0 Ga chert from Western Australia. *Int. Geol. Rev.* **48**, 78–88 (2006).

33. K. Hickman-Lewis, F. Westall, B. Cavalazzi, in *Earth's Oldest Rocks* (2019).

34. D. Wacey, M. Saunders, J. Cliff, M. R. Kilburn, C. Kong, M. E. Barley, M. D. Brasier, Geochemistry and nano-structure of a putative∼ 3240 million-year-old black smoker

biota, Sulphur Springs Group, Western Australia. *Precambrian Res.* **249**, 1–12 (2014).

35. M. M. Tice, D. R. Lowe, The origin of carbonaceous matter in pre-3.0 Ga greenstone terrains: A review and new evidence from the 3.42 Ga Buck Reef Chert. *Earth-Science Rev.* (2006), doi:10.1016/j.earscirev.2006.03.003.

36. M. M. Tice, D. R. Lowe, Photosynthetic microbial mats in the 3,416-Myr-old ocean. *Nature* (2004), doi:10.1038/nature02888.

37. M. Homann, C. Heubeck, A. Airo, M. M. Tice, Morphological adaptations of 3.22 Ga-old tufted microbial mats to Archean coastal habitats (Moodies Group, Barberton Greenstone Belt, South Africa). *Precambrian Res.* (2015), doi:10.1016/j.precamres.2015.04.018.

38. F. Westall, C. E. J. De Ronde, G. Southam, N. Grassineau, M. Colas, C. Cockell, H. Lammer, in *Philosophical Transactions of the Royal Society B: Biological Sciences* (2006).

39. M. D. Brasier, O. R. Green, J. F. Lindsay, N. McLoughlin, A. Steele, C. Stoakes, Critical testing of Earth's oldest putative fossil assemblage from the ~3.5 Ga Apex chert, Chinaman Creek, Western Australia. *Precambrian Res.* (2005), doi:10.1016/j.precamres.2005.06.008.

40. K. Hickman-Lewis, R. J. Garwood, M. D. Brasier, T. Goral, H. Jiang, N. McLoughlin, D. Wacey, Carbonaceous microstructures from sedimentary laminated chert within the 3.46 Ga Apex Basalt, Chinaman Creek locality, Pilbara, Western Australia. *Precambrian Res.* (2016), doi:10.1016/j.precamres.2016.03.013.

41. M. Homann, P. Sansjofre, M. Van Zuilen, C. Heubeck, J. Gong, B. Killingsworth, I. S. Foster, A. Airo, M. J. Van Kranendonk, M. Ader, S. V. Lalonde, Microbial life and biogeochemical cycling on land 3,220 million years ago. *Nat. Geosci.* (2018), doi:10.1038/s41561-018-0190-9.

42. Y. Ueno, Early Archean (ca. 3.5 Ga) microfossils and^< 13> C-depleted carbonaceous matter in the North Pole area, Western Australia: Field occurrence and geochemistry. *Geochemistry Orig. Life*, 203–236 (2001).

43. J. Alleon, S. Bernard, C. Le Guillou, O. Beyssac, K. Sugitani, F. Robert, Chemical nature of the 3.4 Ga Strelley Pool microfossils. *Geochemical Perspect. Lett.* **7**, 37–42 (2018).

44. B. Rasmusssn, Filamentous microfossils in a 3,235-million-year-old volcanogenic massive sulphide deposit. *Nature* (2000), doi:10.1038/35015063.

45. M. S. Dodd, D. Papineau, T. Grenne, J. F. Slack, M. Rittner, F. Pirajno, J. O'Neil, C. T. S. Little, Evidence for early life in Earth's oldest hydrothermal vent precipitates. *Nature*. **543**, 60–64 (2017).

46. F. Westall, S. T. De Vries, W. Nijman, V. Rouchon, B. Orberger, V. Pearson, J. Watson, A. Verchovsky, I. Wright, J. N. Rouzaud, D. Marchesini, A. Severine, The 3.466 Ga "Kitty's Gap Chert," an early Archean microbial ecosystem. *Spec. Pap. Geol. Soc. Am.* (2006), doi:10.1130/2006.2405(07).

47. K. Hickman-Lewis, B. Cavalazzi, F. Foucher, F. Westall, Most ancient evidence for life in the Barberton greenstone belt: Microbial mats and biofabrics of the ~3.47 Ga Middle Marker horizon. *Precambrian Res.* **312**, 45–67 (2018).

48. D. Wacey, M. Saunders, C. Kong, Remarkably preserved tephra from the 3430 Ma Strelley Pool Formation, Western Australia: Implications for the interpretation of Precambrian microfossils. *Earth Planet. Sci. Lett.* (2018), doi:10.1016/j.epsl.2018.01.021.

49. K. Lepot, A. Addad, A. H. Knoll, J. Wang, D. Troadec, A. Béché, E. J. Javaux, Iron minerals within specific microfossil morphospecies of the 1.88 Ga Gunflint Formation. *Nat. Commun.* **8**, 14890 (2017).

50. K. Sugitani, K. Mimura, M. Takeuchi, K. Lepot, S. Ito, E. J. Javaux, Early evolution of large micro-organisms with cytological complexity revealed by microanalyses of 3.4 Ga organic-walled microfossils. *Geobiology*. **13**, 507–521 (2015).

51. J. L. Siefert't, G. E. Fox, Phylogenetic mapping of bacterial morphology. *Microbiology*. **144**, 2803–2808 (1998).

52. J. W. Schopf, A. B. Kudryavtsev, Biogenicity of Earth's earliest fossils: a resolution of the controversy. *Gondwana Res.* **22**, 761–771 (2012).

53. J. B. Waterbury, R. Y. Stanier, Patterns of growth and development in pleurocapsalean cyanobacteria. *Microbiol. Rev.* **42**, 2 (1978).

54. P. Sánchez-Baracaldo, J. A. Raven, D. Pisani, A. H. Knoll, Early photosynthetic eukaryotes inhabited low-salinity habitats. *Proc. Natl. Acad. Sci.*, 201620089 (2017).

55. J. C. Uyeda, L. J. Harmon, C. E. Blank, A comprehensive study of cyanobacterial morphological and ecological evolutionary dynamics through deep geologic time. *PLoS One*. **11**, e0162539 (2016).

56. D. G. ADAMS, P. S. DUGGAN, Tansley Review No. 107. Heterocyst and akinete differentiation in cyanobacteria. *New Phytol.* **144**, 3–33 (1999).

57. S. P. Singh, B. L. Montgomery, Determining cell shape: adaptive regulation of cyanobacterial cellular differentiation and morphology. *Trends Microbiol.* **19**, 278–285 (2011).

58. A. D. Anbar, A. H. Knoll, Proterozoic ocean chemistry and evolution: a bioinorganic bridge? *Science (80-.).* **297**, 1137–1142 (2002).

59. F. R. Tabita, T. E. Hanson, H. Li, S. Satagopan, J. Singh, S. Chan, Function, structure, and evolution of the RubisCO-like proteins and their RubisCO homologs. *Microbiol. Mol. Biol. Rev.* **71**, 576–599 (2007).

60. F. R. Tabita, T. E. Hanson, S. Satagopan, B. H. Witte, N. E. Kreel, Phylogenetic and

evolutionary relationships of RubisCO and the RubisCO-like proteins and the functional lessons provided by diverse molecular forms. *Philos. Trans. R. Soc. Lond. B. Biol. Sci.* **363**, 2629–2640 (2008).

61. G. G. B. Tcherkez, G. D. Farquhar, T. J. Andrews, Despite slow catalysis and confused substrate specificity, all ribulose bisphosphate carboxylases may be nearly perfectly optimized. *Proc. Natl. Acad. Sci.* **103**, 7246–7251 (2006).

62. G. D. Farquhar, J. R. Ehleringer, K. T. Hubick, Carbon isotope discrimination and photosynthesis. *Annu. Rev. Plant Biol.* **40**, 503–537 (1989).

63. H. Ashida, Y. Saito, C. Kojima, K. Kobayashi, N. Ogasawara, A. Yokota, A functional link between RuBisCO-like protein of Bacillus and photosynthetic RuBisCO. *Science (80-.).* **302**, 286–290 (2003).

64. T. Kono, S. Mehrotra, C. Endo, N. Kizu, M. Matusda, H. Kimura, E. Mizohata, T. Inoue, T. Hasunuma, A. Yokota, A RuBisCO-mediated carbon metabolic pathway in methanogenic archaea. *Nat. Commun.* **8**, 14007 (2017).

65. K. Vuorio, M. Meili, J. Sarvala, Taxon-specific variation in the stable isotopic signatures (δ13C and δ15N) of lake phytoplankton. *Freshw. Biol.* **51**, 807–822 (2006).

66. H. Penning, C. M. Plugge, P. E. Galand, R. Conrad, Variation of carbon isotope fractionation in hydrogenotrophic methanogenic microbial cultures and environmental samples at different energy status. *Glob. Chang. Biol.* **11**, 2103–2113 (2005).

67. D. Goevert, R. Conrad, Effect of Substrate Concentration on Carbon Isotope Fractionation during Acetoclastic Methanogenesis by Methanosarcina barkeri and M. acetivorans and in Rice Field Soil. *Appl. Environ. Microbiol.* **75**, 2605–2612 (2009).

68. L. L. Jahnke, R. E. Summons, J. M. Hope, D. J. Des Marais, Carbon isotopic fractionation in lipids from methanotrophic bacteria II: The effects of physiology and

environmental parameters on the biosynthesis and isotopic signatures of biomarkers. *Geochim. Cosmochim. Acta*. **63**, 79–93 (1999).

69. R. D. Guy, M. L. Fogel, J. A. Berry, Photosynthetic Fractionation of the Stable Isotopes of Oxygen and Carbon. *Plant Physiol.* **101**, 37–47 (1993).

70. J. A. Raven, A. M. Johnston, J. E. Kübler, R. Korb, S. G. McInroy, L. L. Handley, C. M. Scrimgeour, D. I. Walker, J. Beardall, M. Vanderklift, S. Fredriksen, K. H. Dunton, Mechanistic interpretation of carbon isotope discrimination by marine macroalgae and seagrasses. *Funct. Plant Biol.* **29**, 355–378 (2002).

71. K. Sugitani, K. Mimura, M. Takeuchi, K. Lepot, S. Ito, E. J. Javaux, Early evolution of large micro-organisms with cytological complexity revealed by microanalyses of 3.4 Ga organic-walled microfossils. *Geobiology* (2015), doi:10.1111/gbi.12148.

72. K. L. Londry, L. L. Jahnke, D. J. Des Marais, Stable Carbon Isotope Ratios of Lipid Biomarkers of Sulfate-Reducing Bacteria. *Appl. Environ. Microbiol.* **70**, 745–751 (2004).

73. J. W. Schopf, in *Ecology of cyanobacteria II* (Springer, 2012), pp. 15–36.

74. Y. Jiao, D. K. Newman, The pio operon is essential for phototrophic Fe (II) oxidation in Rhodopseudomonas palustris TIE-1. *J. Bacteriol.* **189**, 1765–1773 (2007).

75. M. S. Dodd, D. Papineau, Z. She, M. L. Fogel, S. Nederbragt, F. Pirajno, Organic remains in late Palaeoproterozoic granular iron formations and implications for the origin of granules. *Precambrian Res.* **310**, 133–152 (2018).

76. A. Reddy, E. V Caler, N. W. Andrews, Plasma membrane repair is mediated by Ca2+-regulated exocytosis of lysosomes. *Cell*. **106**, 157–169 (2001).

77. N. Dauphas, M. Van Zuilen, M. Wadhwa, A. M. Davis, B. Marty, P. E. Janney, Clues from Fe isotope variations on the origin of early Archean BIFs from Greenland. *Science (80-.).* **306**, 2077–2080 (2004).

78. N. Planavsky, O. Rouxel, A. Bekker, R. Shapiro, P. Fralick, A. Knudsen, Iron-oxidizing microbial ecosystems thrived in late Paleoproterozoic redox-stratified oceans. *Earth Planet. Sci. Lett.* **286**, 230–242 (2009).

79. A. I. Oparin, Chemistry and the origin of life. *R. Inst. Chem. Rev.* (1969), doi:10.1039/rr9690200001.

80. I. Budin, J. W. Szostak, Physical effects underlying the transition from primitive to modern cell membranes. *Proc. Natl. Acad. Sci.* **108**, 5249–5254 (2011).

81. C. A. Hutchison, R. Y. Chuang, V. N. Noskov, N. Assad-Garcia, T. J. Deerinck, M. H. Ellisman, J. Gill, K. Kannan, B. J. Karas, L. Ma, J. F. Pelletier, Z. Q. Qi, R. A. Richter, E. A. Strychalski, L. Sun, Y. Suzuki, B. Tsvetanova, K. S. Wise, H. O. Smith, J. I. Glass, C. Merryman, D. G. Gibson, J. C. Venter, Design and synthesis of a minimal bacterial genome. *Science (80-.).* (2016), doi:10.1126/science.aad6253.

82. T. F. Zhu, J. W. Szostak, Coupled growth and division of model protocell membranes. *J. Am. Chem. Soc.* (2009), doi:10.1021/ja900919c.

83. T. Ruiz-Herrero, T. G. Fai, L. Mahadevan, Dynamics of growth and form in prebiotic vesicles. *arXiv Prepr. arXiv1901.04406* (2019).

84. M. R. Cerri, Q. Wang, P. Stolz, J. Folgmann, L. Frances, K. Katzer, X. Li, A. B. Heckmann, T. L. Wang, J. A. Downie, A. Klingl, F. de Carvalho-Niebel, F. Xie, M. Parniske, The ERN1 transcription factor gene is a target of the CCaMK/CYCLOPS complex and controls rhizobial infection in Lotus japonicus. *New Phytol.* **215** (2017), doi:10.1111/nph.14547.

85. R. Cornelissen, A. Bøggild, R. Thiruvallur Eachambadi, R. I. Koning, A. Kremer, S. Hidalgo-Martinez, E.-M. Zetsche, L. R. Damgaard, R. Bonné, J. Drijkoningen, J. S. Geelhoed, T. Boesen, H. T. S. Boschker, R. Valcke, L. P. Nielsen, J. D'Haen, J. V. Manca, F. J. R. Meysman, The Cell Envelope Structure of Cable Bacteria. *Front. Microbiol.* **9**

(2018), doi:10.3389/fmicb.2018.03044.

Acknowledgments: We gratefully acknowledge Ralf Conrad for his input throughout the work. We would also like to thank Diane Newman for insightful discussion. We would like to thank Gabriella Berthal for excellent technical support, members of ALMF, EMBL and rest of Ecological microbiology lab for their support throughout the work.

Author contributions: DK conceived the work with input from TL. DK performed laboratory experiments. AK & TB did SEM and TEM imaging. DK & ML did confocal imaging. DK coordinated work between the authors. DK wrote the manuscript with input from TL, BZ, ML, AK, & TB. This research was funded by the European Research Council (ERC), grant agreement 616644 (POLLOX) to TL.

Supplementary Materials for

Title: On the nature of the earliest known lifeforms

Dheeraj Kanaparthi[1,2&3*], Marko Lampe[4], Baoli Zhu[2&5], Thomas Boesen[6], Andreas Klingl[7], Petra Schwille[1] & Tillmann Lueders[2&3*]

Affiliations:

[1]Max-Planck Institute for Biochemistry, Munich, Germany

[2]Chair of Ecological Microbiology, BayCeer, University of Bayreuth, Germany.

[3]Helmholtz Zentrum Munich, Germany

[4]Advanced Light Microscopy Facility, European Molecular Biology Laboratory, Heidelberg, Germany.

[5]Key Laboratory of Agro-ecological Processes in Subtropical Regions, Taoyuan Agroecosystem Research Station, Institute of Subtropical Agriculture, Chinese Academy of Sciences, Changsha, China.

[6]Department of Biosciences, Center for Electromicrobiology, Aarhus, Denmark.

[7]Department of Biology, LMU, Planegg-Martinsried, Germany.

*Corresponding authors

Lead contact: kanaparthi@biochem.mpg.de

This PDF file includes:

Materials and Methods

Supplementary Text

figs. S1 to S112

Tables S1 to S2

Captions for Movies S1 to S9

Other Supplementary Materials for this manuscript include the following:

Movies S1 to S9

Materials and Methods

Exiguobacterium strain-Molly was isolated from submerged biofilms in The Dead Sea (84). This isolate was chosen because of its ability to grow in different types of salts (NaCl, KCl, $MgCl_2$ & Dead Sea salt) and concentrations up to 20% w/v. *Rhodobacter sphaeroides* (DSM159) was obtained from DMSZ (Braunschweig, Germany).

Protoplasts were generated from *Exiguobacterium Strain-Molly* (*EM-P*) by inoculating overnight cultures into half strength tryptic soya broth (TSB) containing 5% DSS (5%DSS-TSB), 80 µg/ml Lysozyme and 200µg/ml Penicillin G (all reagents were obtained from Sigma Aldrich, Germany) at 30°C. Protoplasts of *R. sphaeroides* (*RS-P*) were generated using the same procedure with exception of using NB amended with 5%-DSS (6%DSS-NB). Transformation to their protoplast state was confirmed by change in cell morphology. Over the next 3-4 weeks the cells were repeatedly sub-cultured into fresh media with pencillin G and lysozyme as described above. The stability of these protoplasts (*EM-P* & *RS-P*) was determined after ten sub-cultures by transferring cells to their respective media without Pencillin G or Lysozyme. As both *EM-P* & *RS-P* did not revert to their native morphology under salt stress, use of both Lysozyme and Penicillin G was discontinued for subsequent experiments. For subsequent experiments both bacteria are grown in their respective media with DSS concentrations ranging between 5-10%.

Morphology of both *EM-P* under different growth conditions was determined using Carl Zeiss Axioskop 2plus microscope equipped with Axiocam HRm (Carl Zeiss, Germany) or

Leica DSF9000 (Leica, Germany) cameras. TEM was carried out using a Zeiss EM 912 with an integrated OMEGA-filter as described before (84). Scanning electron microscopy of *RS-L* and *EM-L* cells was done using Versa 3D dual beam SEM microscope as described before (85) .

STED microscopy was performed with an inverted TCS SP8 STED 3X microscope (Leica Microsystems, Mannheim Germany) using an 86x/1.2 NA water immersion objective (Leica HC PL APO CS2 - STED White). Fluorophores were excited with either 488, 561nm, 594nm or 633m laser light derived from 80 MHz pulsed White Light Laser (Leica Microsystems, Mannheim Germany). For stimulated emission, either a pulsed 775 nm laser or a 592nm CW laser (Leica Microsystems, Mannheim Germany) was used depended on the fluorophore. The emitted fluorescence light was collected with Hybrid Detectors (HyD, Leica Microsystems, Mannheim Germany) using appropriate emission band pass-filter setting and typically a gate of 0.3ns-6.0ns for depletion with the 775nm laser or 1.0-6.0ns with the 592nm laser. Images were recorded in photon counting mode and line accumulation. Image deconvolution was performed on selected images and movies with Huygens Professional (version 16.10.1p2, Scientific Volume Imaging, Hilversum, The Netherlands).

Spinning Disk Microscopy was performed using an Olympus SpinSR10 spinning disk confocal microscope (Olympus, Tokyo, Japan) equipped with an 100x/NA1.35 silicone oil immersion objective (Olympus UPLSAPO100XS, Tokyo, Japan), a CSU-W1-Spinning Disk-Unit (Yokogawa, Tokyo, Japan) and ORCA-Flash 4.0 V3 Digital CMOS Camera (Hamamatsu, Hamamatsu City, Japan).

To study lysis and disintegration of cells, we conducted long term incubation of *EM-P* and *RS-P* - 3-6 months for the formation of membrane debris and its transformation into laminated structures and 36 months for the slow encrustation of cells biofilms by cations in the growth media. Both structures were imaged either using phase-contrast or STED microscope at regular intervals of time between 3-6 months. After 3 years of undisturbed incubations, biofilm of *EM-P* turned into crispy wafer. These wafers were carefully scratched from the bottom of the cultivation flask, dried at 45°C and imaged under a scanning electron microscope coupled with a EDX detector for elemental analysis as described above.

Supplementary Text

Biogenicity of organic structures from SPF, Moodie's and Dresser formations

Recent reports argue that, elliptical and spherical organic structures (microfossils) reported from several Archaean rock formations like SPF (49), Dresser (10) and Moodies formations (12) are abiotic mineral aggregates, rather than fossilised Archaean Eon microorganisms. Underlying argument for this proposition was that these structures bare greater morphological resemblance to inorganic mineral structures and lack true morphological analogues within extant prokaryotes. Nevertheless, we observed considerable morphological similarities between these structures and bacteria protoplasts from our study. In-case of elliptical organic structures reported from SPF site, all distinctive morphological features, that were being argued as indications for their abiotic origin like presence of granular interiors (fig. S93 & S94), lath like structures (fig. S95 & S96) within the cell and clasts of organic carbon layer enclosing the cell (fig. S97), were also exhibited by *RS-P*. Like observed in *RS-P*, granular interiors in these microfossils could have formed by invagination followed by vesiculation of

cell membrane (fig. S98). Intracellular lath-like structures should have formed by a similar process. Morphological differences observed within these two types of membrane vesicles could be due to the differences observed in their lipid composition. Staining with combination of membrane dyes, one specific form L_d membrane and a universal membrane dye, these lath-like structures remained unstained with the former dye (fig. S94). This indicates that these structures were largely composed of L_o membrane (saturated fatty acids). In-contrast, intracellular granules were stained with L_o-dyes suggesting that they mostly composed of un-saturated fatty acids (fig. S94). These differences in their composition could possibly explain the differences observed in their morphology. Based on these similarities, we hypothesis that these structures most likely were fossil remnants of proto Gram-negative bacteria, possibly involved in Fe(II)-oxidation.

Our presumption that these microorganisms were involved in Fe(II)-oxidation is based on the fact that these microfossils were discovered from Fe(III) rich rock formations and granular structures within the cell were uniformly coated with Fe(III)-minerals (*10*). We propose the following sequence of events that should have led to the formation of these intracellular granules. Like the extant Fe(II)-oxidising bacteria, we presume that oxidation of iron in Archaean microorganisms should have taken place in the periplasmic space (*74*). Following this Fe(III) should have chelated to phospholipid membrane due to their opposing charges. Chelation of charged cations to membrane should have led to invagination and membrane vesicle formation. This process of vesicle formation under the influence of chelating cations is a well studies process and was known to happen in many living cells (77). Presence of thin layer of organic carbon surrounding Fe(III)-mineral granules (5nm in thickness) (10) is in agreement with above proposed mechanism of their formation along with the isotopic composition of iron (77). Apart from SPF microfossils, this phenomenon of close association

between Fe(III)-minerals and cell membranes is observed in several microfossils. In Nuvvuagittuq microfossils (45), Fe(III)-chelated cell membranes along with the process of vesiculation could be seen among the published images of these microfossils (Fig 8). Similar to Nuvvuagittuq microfossils, several elliptical microfossils reported from SPF formation have spherical structures with or devoid of internal organic carbon, attached to their surfaces. Morphology of both these structures significantly resemble OMV's of *RS-P* (Fig 9 and Fig S93).

Clast of organic carbon enclosing elliptical microfossils was reported from both SPF and Moodies formations (fig. S97). We observed very similar structures in late stationary growth phase of *RS-P* incubations. These structures were formed when large quantities of membrane debris, formed from lysis of *RS-P* (fig. S99-S101) engulfed lenticular morphotypes of *RS-P* with granular interiors (fig. S97). This membrane debris also underwent a series of morphological transformations leading to the formation of structures that were being argued volcanic glass (fig. S102 – S104) or pumices (fig. S105 & S106). Such sequential morphological transformation of membrane debris is presented as Fig S101 to S105. In-brief, entanglement of long filamentous *RS-P* cells led to the formation of Over the course of its lifecycle, cells within the clumps formed OMV's and underwent lysis (during the last growth stage). This process led to the formation of large amounts of membrane debris (fig. S99 & S100). Compression of cells within the clumps led to the fusion of membrane debris into a continuous film-like structure that extends over the cells (fig. S99& S100). Structures that were similar to clasts of organic carbon reported from Dresser (49) and Moodies formations (12) should have formed by this process (fig. S97). Similarly, structures that were being argued as shreds of volcanic glass could have formed from linear clumps of membrane debris (fig. S102-S104). In support of our proposition, all the intermediary morphologies observed

in the transformation of lenticular cells into linear strands of organic carbon were discovered from these microfossil sites (Fig. 2A in Wacey et al.,2018) (49). Small spherical granules that were bound to the linear strands of organic carbon could also be intracellular granules reported from elliptical microfossils, like observed in *RS-P* (fig. S103 & S104). Pumice like structures reported from these microfossil sites could have formed by intercalation of hollow OMV's within filamentous membrane debris similar to what was observed in *RS-P* (fig. S105 & S106).

Spherical microfossils were reported from Dresser formation (10) with hollow silica filled vacuoles and a thick discontinuous wall (fig. S107-S109). TEM images showed that these cell-walls are pours structures with quartz and pyrite inclusions (fig. S109). In most cases, cell-wall is discontinuous structure with uneven thickness (fig. S108-S109). Moreover, interiors of these organic structures were mostly devoid of organic carbon (fig. S108-S109). All these observations were in sharp contrast to any known living cells. Nevertheless, *EM-P* exhibited all these morphological features (fig. S107-S109). What were assumed to be hollow spherical cells resemble vacuoles of *EM-P,* with daughter cells. Similarly, what was assumed to be a cell-wall most likely is the cytoplasm sandwiched between hollow cell vacuole and cell-membrane (fig. S109). The sequential morphological transformation of *EM-P* leading to the formation of such structures was depicted in fig. S110.

The structures exhibiting a wavy lamellar pattern are likely the membrane debris formed after lysis and release of daughter cells (fig. S112). This membrane debris underwent further morphological transformation leading to the formation of laminated structures (Fig 3, 4 & fig. S50-S58). Given these considerable morphological similarities between Moodies, Dresser formation organic structures and *EM-P*, we hypothesise that these organic structures are the

fossil remnants of *EM-P* like proto Gram-positive bacteria, possible mediating Fe(III)-reduction process. This assumption is based on the fact that all spherical microfossils were discovered from pyrite rich laminations (Wacey et al., 2018). Moreover, most of the pyrite was present in the cell interiors indicating that these cells metabolised/reduced Fe(III) (Wacey et al., 2018). The reason behind the presence of Fe(III) within the cells could be the same as discussed for elliptical microfossils – invagination of iron mineral coated membranes. Based on these similarities we argue that elliptical and spherical structures reported from Moodies, Dresser and SPF formations (*10, 41, 12*) were of biological origin and most likely were the fossil remnants of *RS-P* like proto-Gram-negative bacteria and *EM-P* like proto-Gram-positive bacteria.

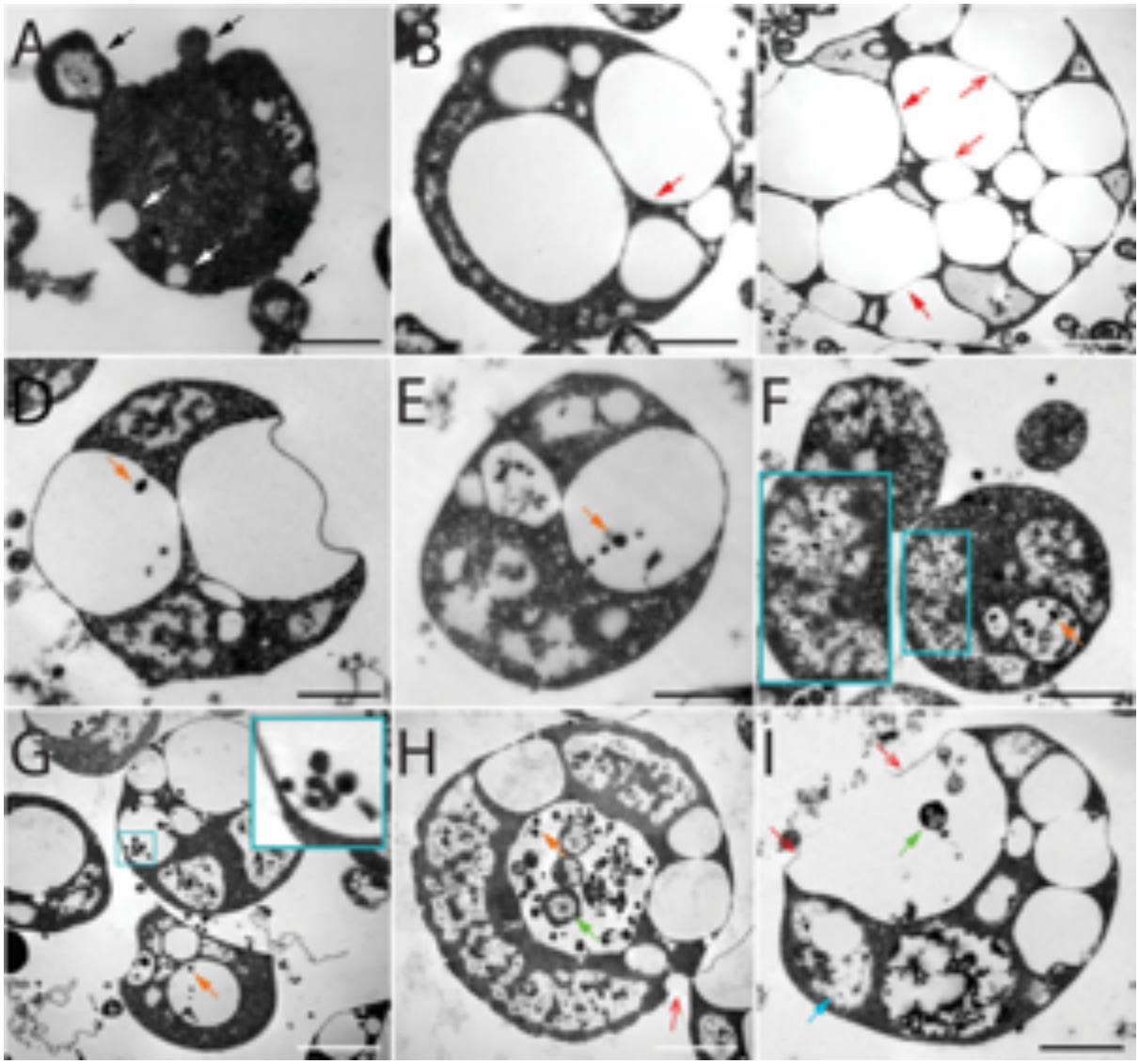

Fig. S1. Life cycle of *EM-P* reproducing via formation of intracellular daughter cells. Images A-I are TEM images showing sequential morphological transformation of *EM-P* reproducing by formation of intracellular daughter cells. Image A shows the ongoing formation of intracellular vesicles (white arrows). Images B& C show increase in volume or numbers of intracellular vesicles within the cell. Closed red arrows points to cytoplasmic region of the cell and open red arrows points to the ruptured regions of vesicle membrane. Images D-F show the formation and growth of intracellular daughter cells (orange arrows). Images G&E show *EM-P* cells with a mix tiny spherical daughter cells (orange arrows and boxed region) and daughter cells with intracellular vesicles (green arrows), like the parent

cells shown in image A. Image I show the process of daughter cell release by rupture of vesicle membrane (open red arrows). Boxed regions of image F and cyan arrows in image I points to reticulate structures within the cell. Scale bars: 1μm.

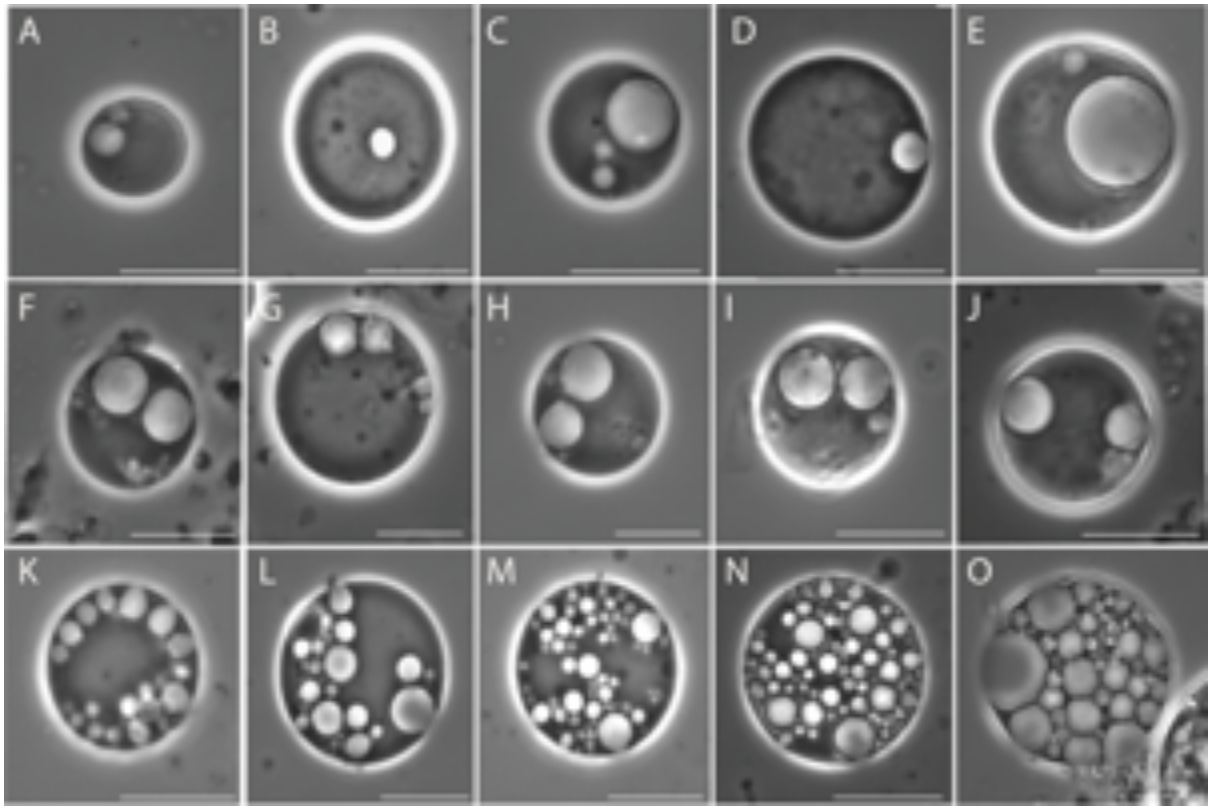

Fig. S2. *EM-P* cells with intracellular vacuoles.

Images A-O are different morphotypes of *EM-P* cells that differ in the number and morphology of intracellular vacuoles. Increase in size and number of vacuoles led to squeezing and formation of polygonal vacuoles like the ones shown in fig. S4. Scale bar: 10μm.

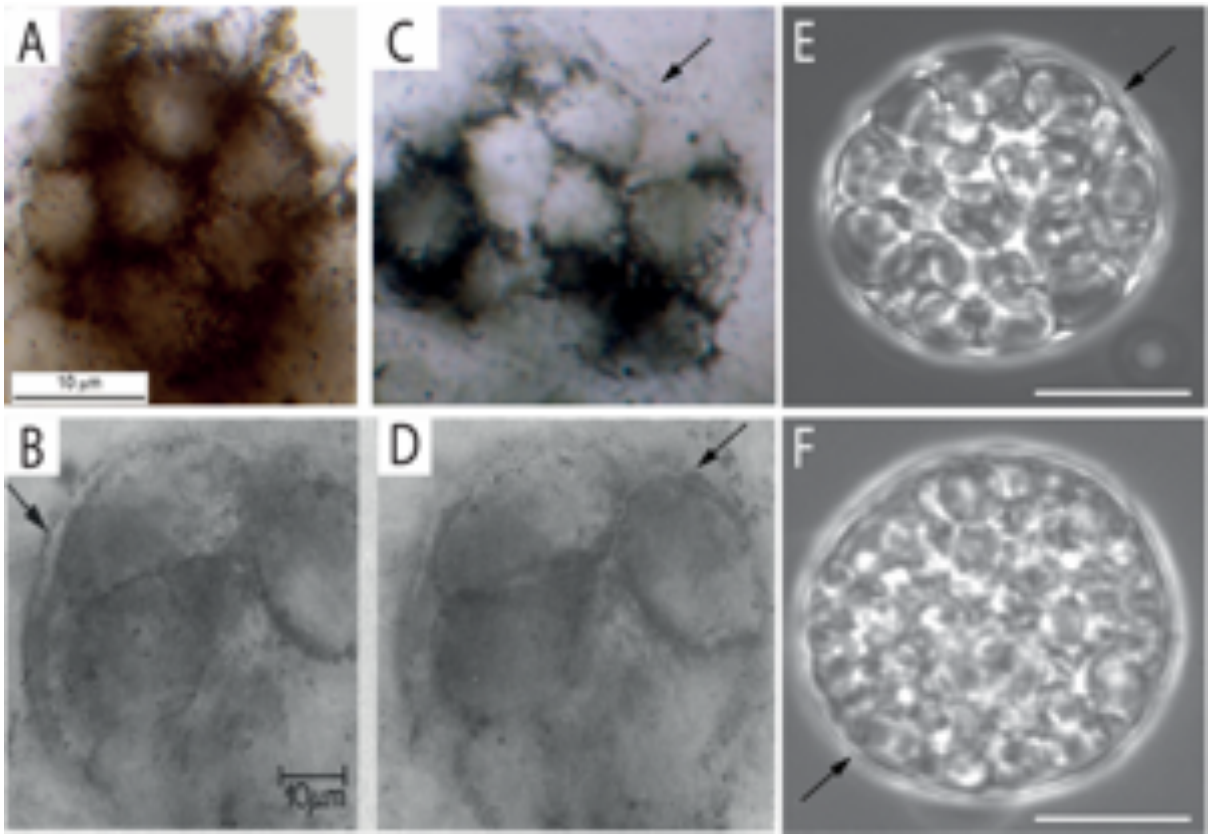

Fig. S3. Morphological comparison of Apex chert microfossils with *EM-P*.

Images A-D show spherical microfossils with hollow intracellular compartments and two layers of outer cell membrane (arrows) (originally published by Schopf *et al.,* 1987) (16). Images E&F are morphologically analogous *EM-P* cell with hollow intracellular compartments. Like microfossils *EM-P* cells also appear to have a duel outer membrane due to juxtaposition of vesicle membrane against cell membrane (arrows). Scale bar: 10µm (E&F).

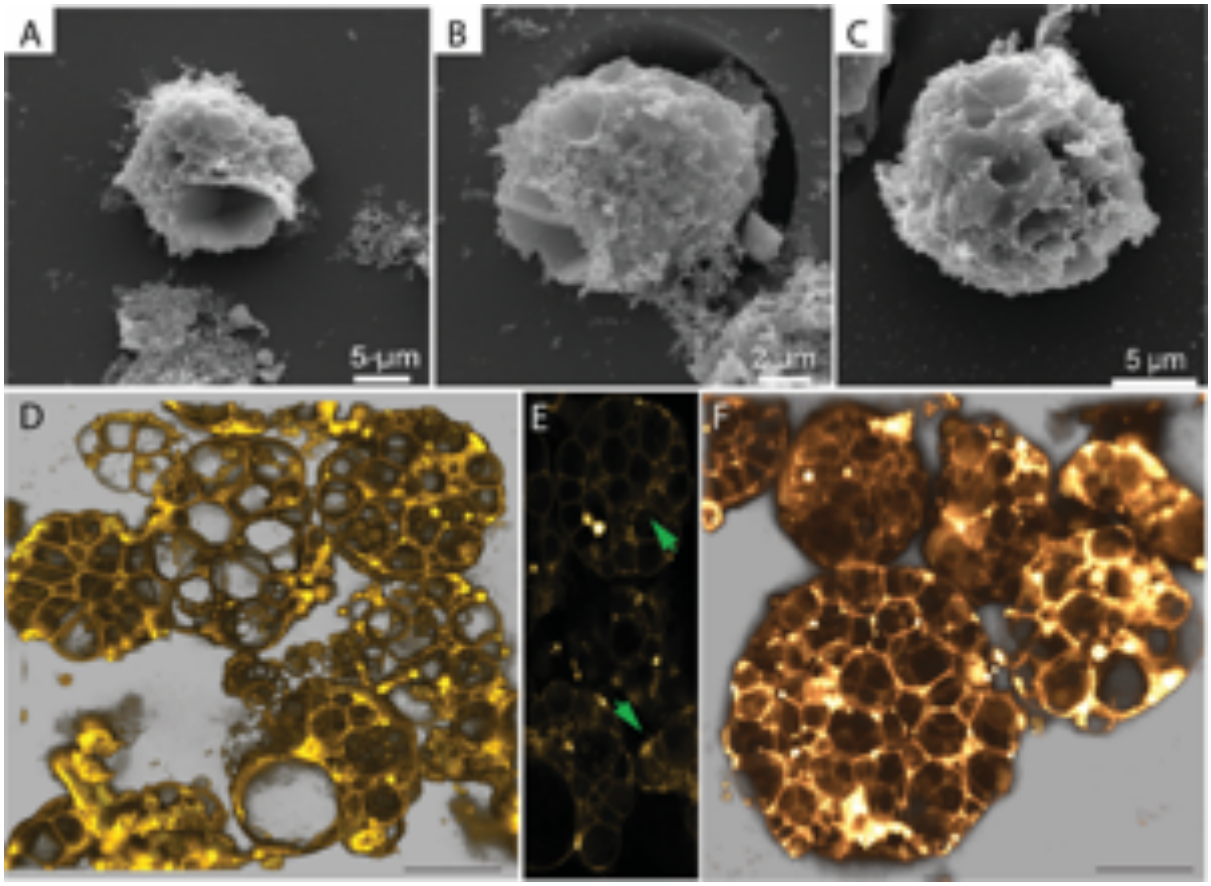

Fig. S4. Morphological comparison between *EM-P* and SPF microfossils.

Images A-C are SEM images of spherical microfossils reported from SPF site (originally published by Delarue *et al*., 2020) (17). Images D & F are 3D rendered STED microscope images of similar *EM-P* cells with hexagonal internal vacuoles. Image E is the individual Z-stack image of cells shown in image D. Arrows in this image points to regions of cells with large and small polygonal vacuoles. Cells in images D-F were stained with membrane stain, FM^{TM}5-95. Comparison of SPF microfossils with *EM-P* was also shown in fig. S5 & S6. Scale bar: 10µm (D&F).

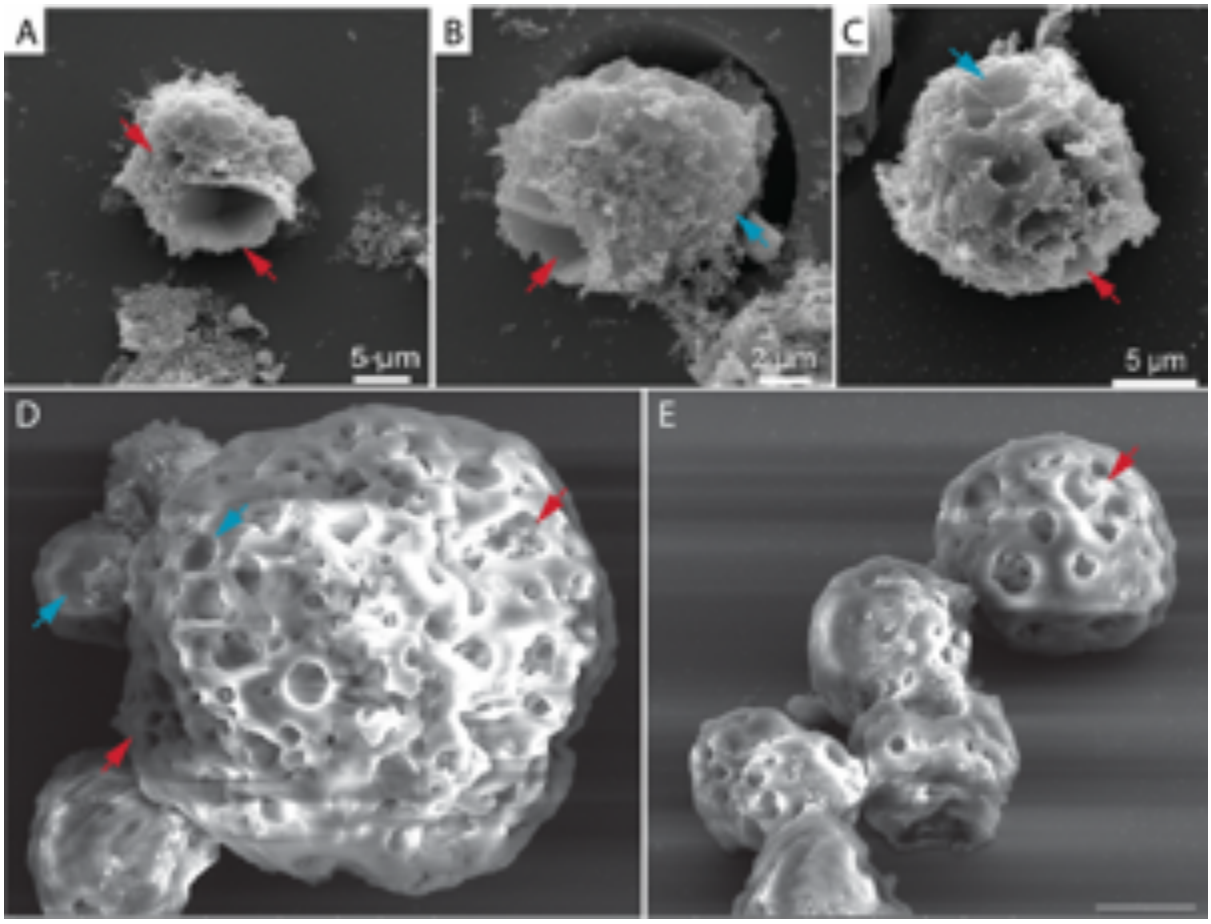

Fig. S5. Morphological comparison between *EM-P* and SPF microfossils.

Images A-C are SEM images of spherical microfossils reported from SPF site (originally published by Delarue *et al*., 2020) (17). Images D & E are SEM images of morphologically analogous *EM-P* cells with hexagonal internal vacuoles. Red and cyan arrows in all image's points to either surface depressions or inward bending of cell membrane in both SPF microfossils and *EM-P* cells. We assume these structures are formed either from complete lysis or invagination of individual vacuole membrane, like shown in fig. S6D&E. Scale bar: 0.5µm (E).

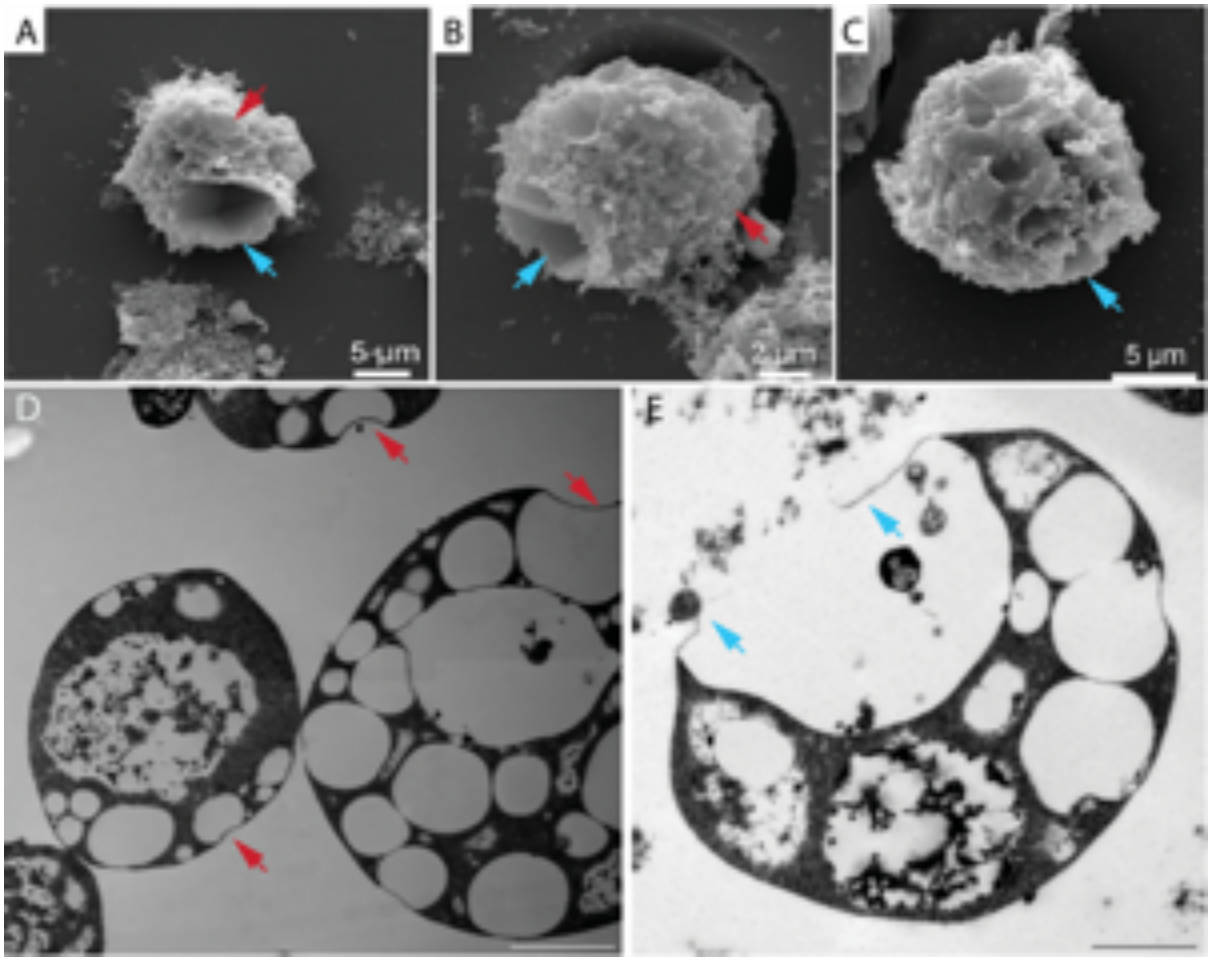

Fig. S6. Morphological comparison between *EM-P* and SPF microfossils.

Images A-C are SEM images of SPF spherical microfossils with spherical/polygonal surface depressions (originally published by Delarue *et al*., 2020) (17). Images D & E are TEM images of morphologically analogous *EM-P* cells. Red arrows in these images points to surface depressions formed by partial collapse of vacuole membrane. Blue arrows in these images points to surface depressions formed by complete collapse of vacuole membrane. Scale bar: 200nm (E).

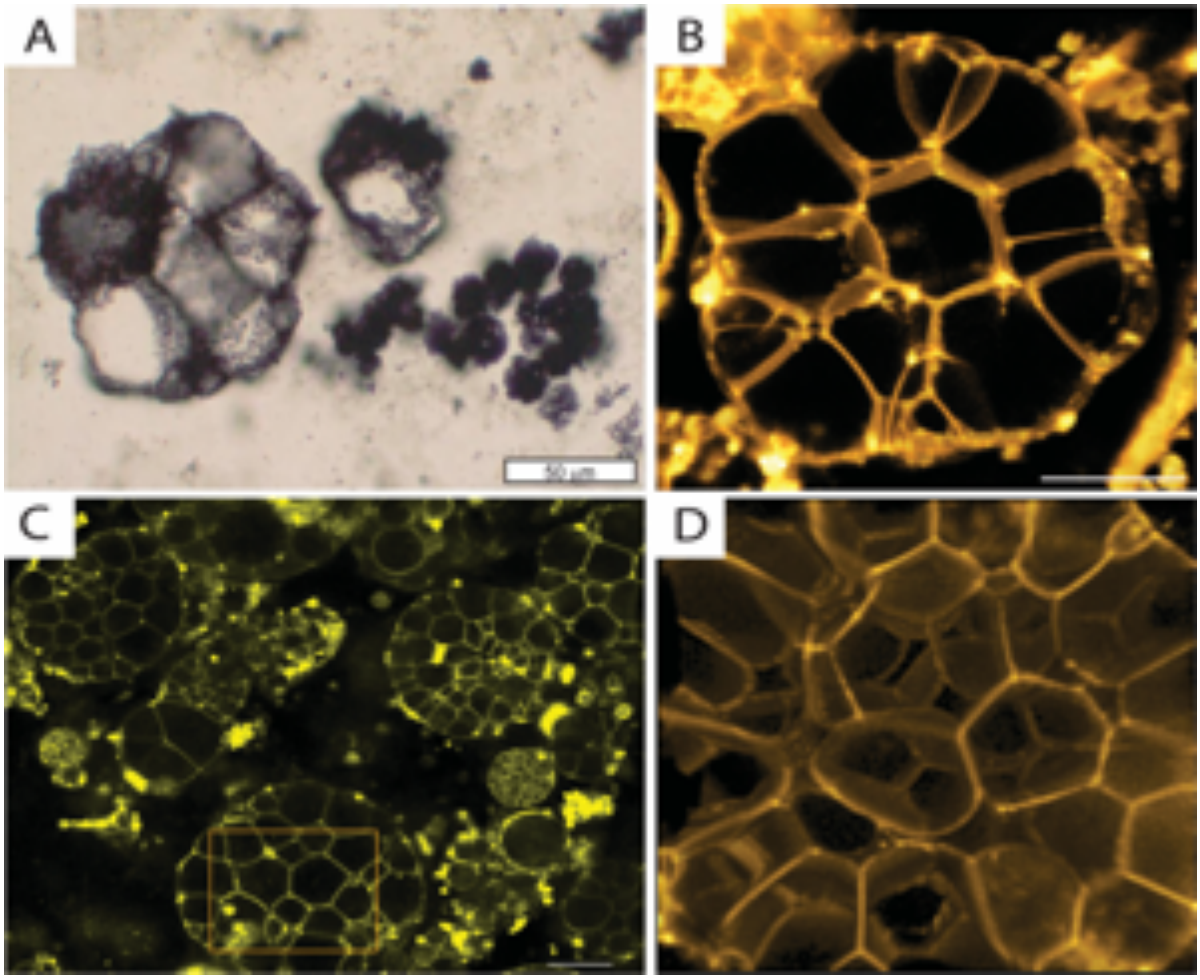

Fig. S7. Morphological comparison between *EM-P* and Farrel quarzite microfossils. Image A show microfossils with hollow polygonal vacuoles from Farrel quarzite formation (originally published by Retallack *et al*., 2016) (21). Images B-D are images of morphological analogous *EM-P* cells with polygonal vacuoles. Cells in images B-D were stained with membrane stain, FM™5-95. Polygonal vacuoles in these images could have formed by confinement of large number of vacuoles within a cell. Cytoplasm in these cells was restricted to narrow spaces in-between the vacuoles, like shown in Fig. 1E&F. Phase contrast images of such *EM-P* cells with hexagonal vacuoles can be seen in fig. S1C. Scale bar: 10µm (B) and 20µm (C).

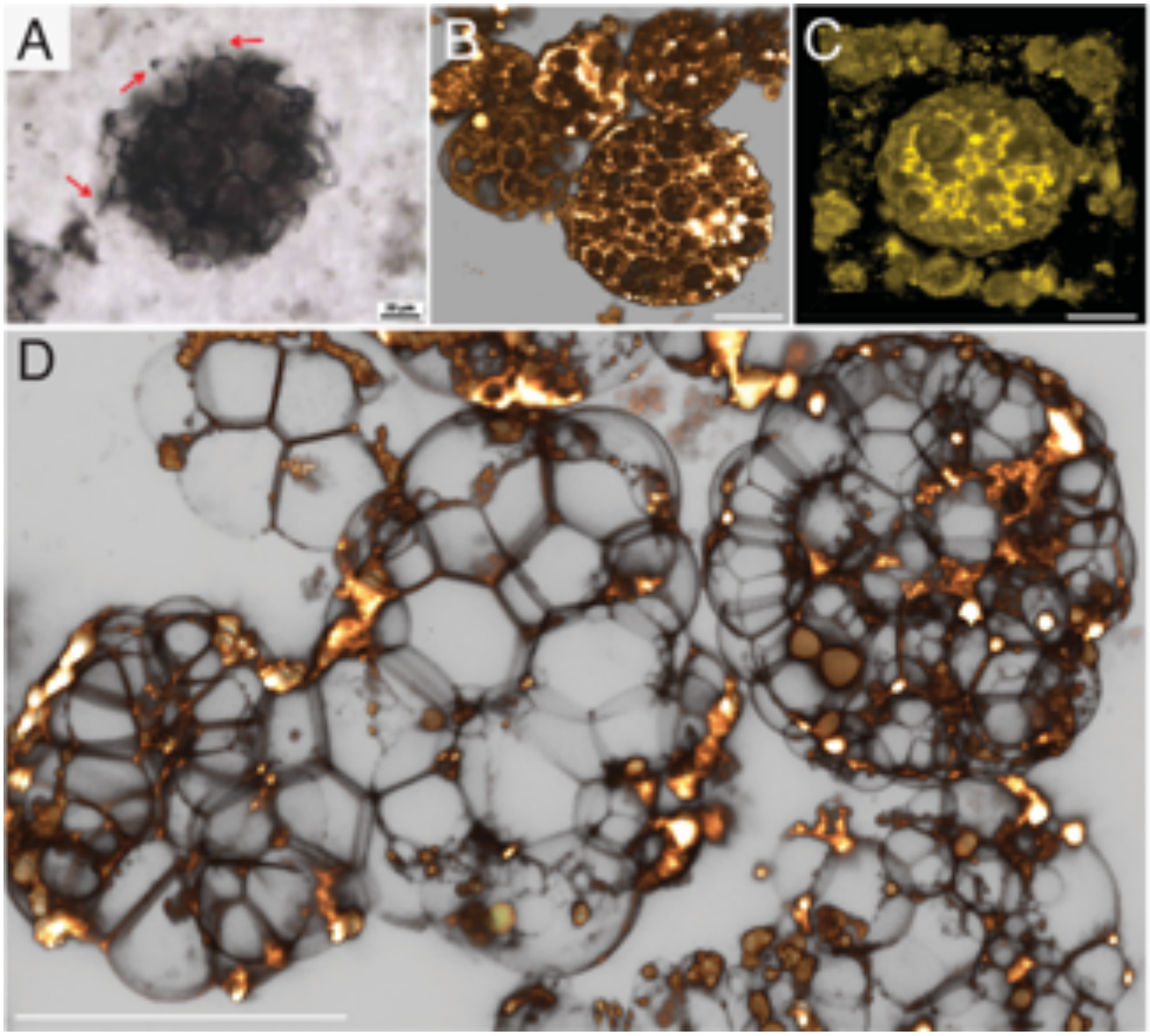

Fig. S8. Morphological comparison between honeycomb structures reported from Turee creek formations and *EM-P*.

Image A show spherical microfossil reported from Turee creek formation (originally published by Barlow *et al*., 2018) (22). Scale bar in images A is 20µm. Images B-D are morphologically analogous *EM-P* cells. Cells in these images were stained with membrane stain, FM™5-95. Scale bar: 20µm (B-D).

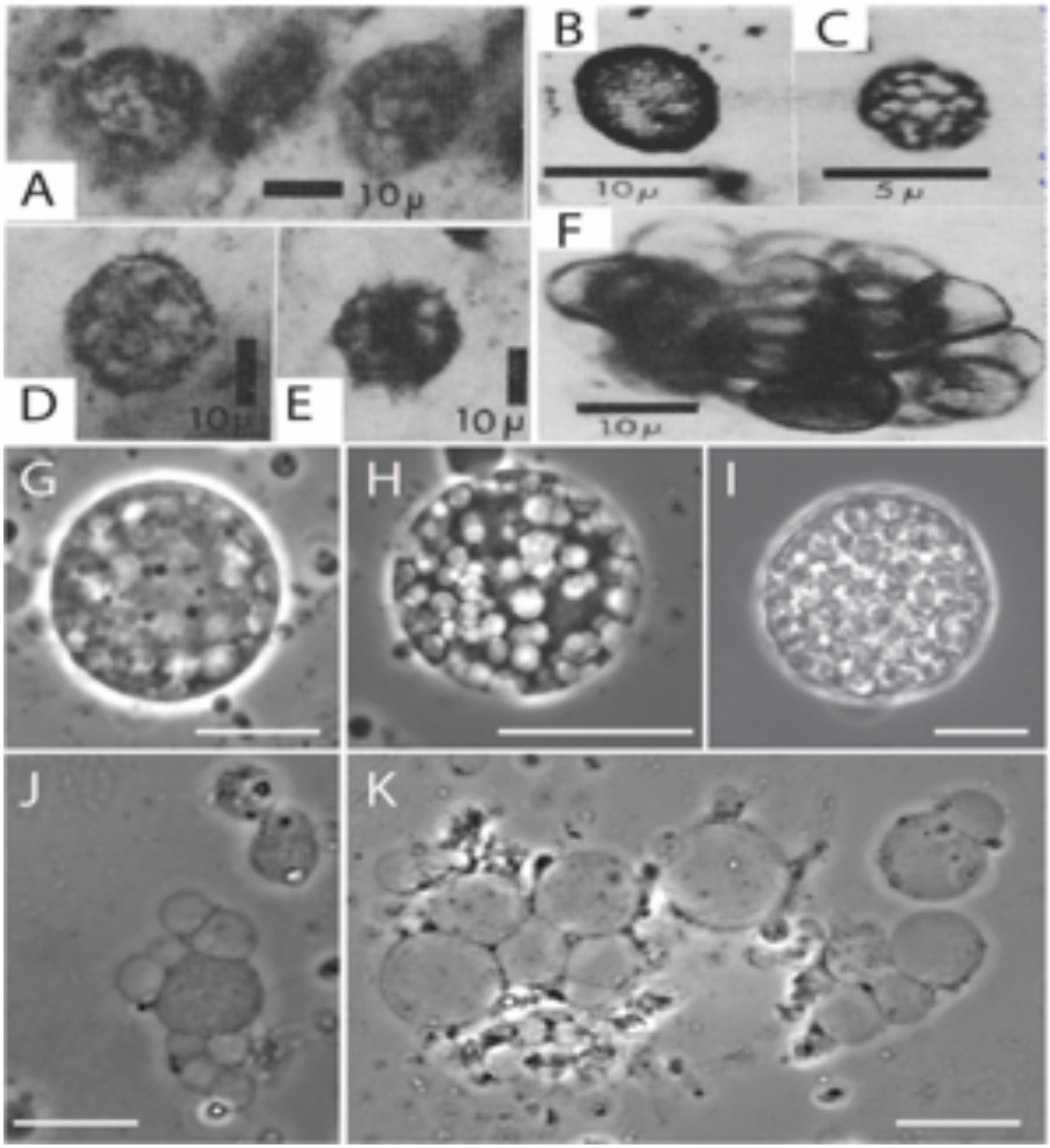

Fig. S9. Morphological comparison between *EM-P* and Fig tree formation microfossils. Images A-F show spherical microfossils reported from Fig tree formation (originally published by Schopf *et al*., 1967) (3). Images G-I are morphological analogues of Fig tree microfossils shown in images A-E. Presence of regions with and without organic carbon can be seen in microfossil images A-E and *EM-P* cell shown in image G. Distinctive spherical vacuoles devoid of organic carbon can be seen in microfossil images B&C and *EM-P* cell

shown in image H. Image F show hollow structures morphologically similar to hollow ICV's that were released by lysis of *EM-P*. Scale bar: 10μm (G-K).

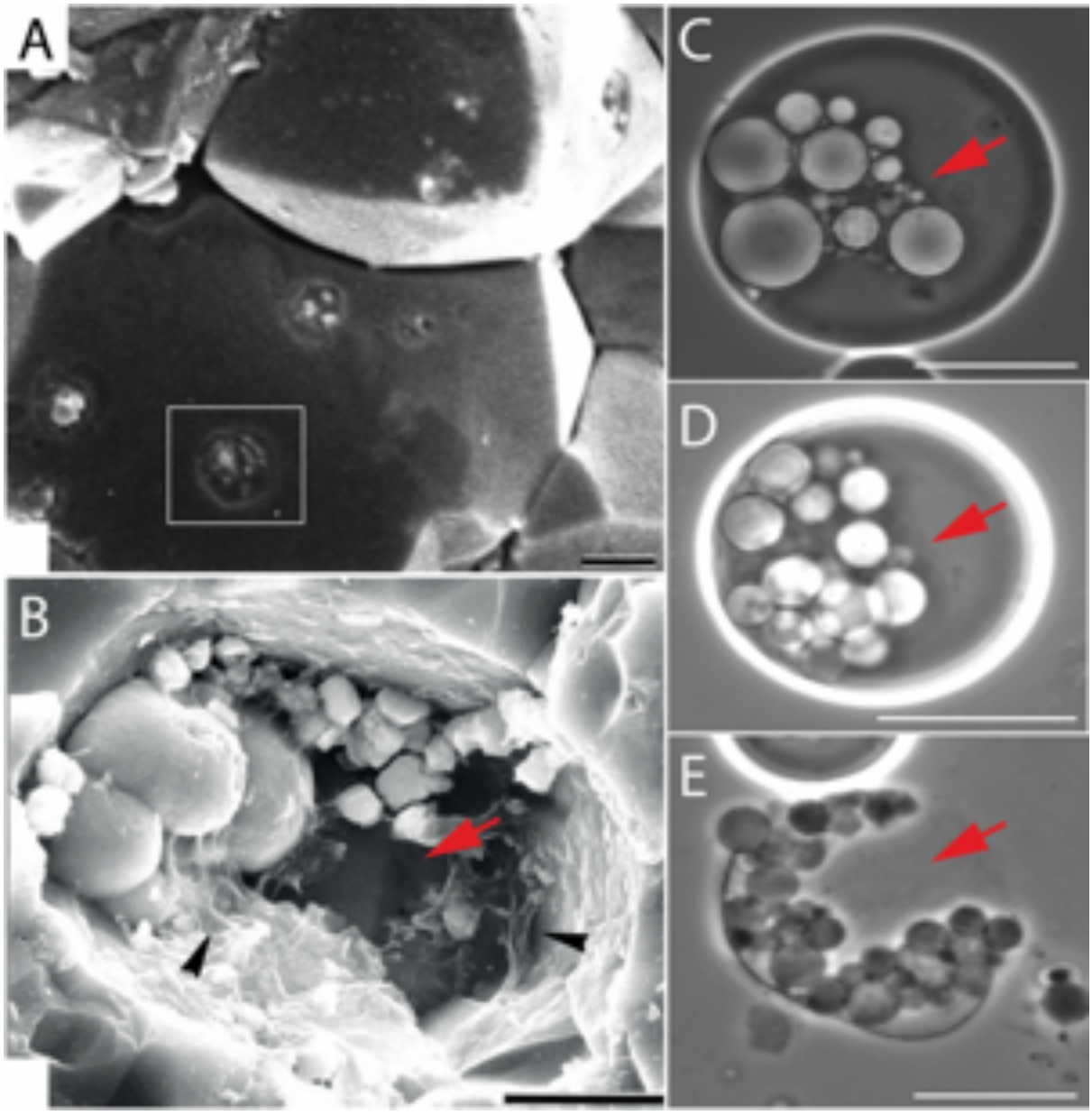

Fig. S10. Morphological comparison between *EM-P* and Hooggenoeg formation microfossils.

Images A&B are SEM images of hollow spherical structures covered in pyrite and embedded in quartz matrix (originally published by Westall *et al*., 2001) (20). Images C-E are phase-

contrast images of morphologically analogous *EM-P* cells. Based on the morphological similarities we propose the spherical structures of different sizes in image B could be the hollow spherical vacuoles of *EM-P* cells (C-E). Hollow structures (red arrows), in these microfossils could also have been formed by a process similar to what was observed in-case of *EM-P* (red arrows), by lysis of cells (E). Interconnected nature of the spherical structures was also similar to what was observed in *EM-P* (Movie S5). Scale bars: 1µm (A) 5µm (B) and 10µm (C-E).

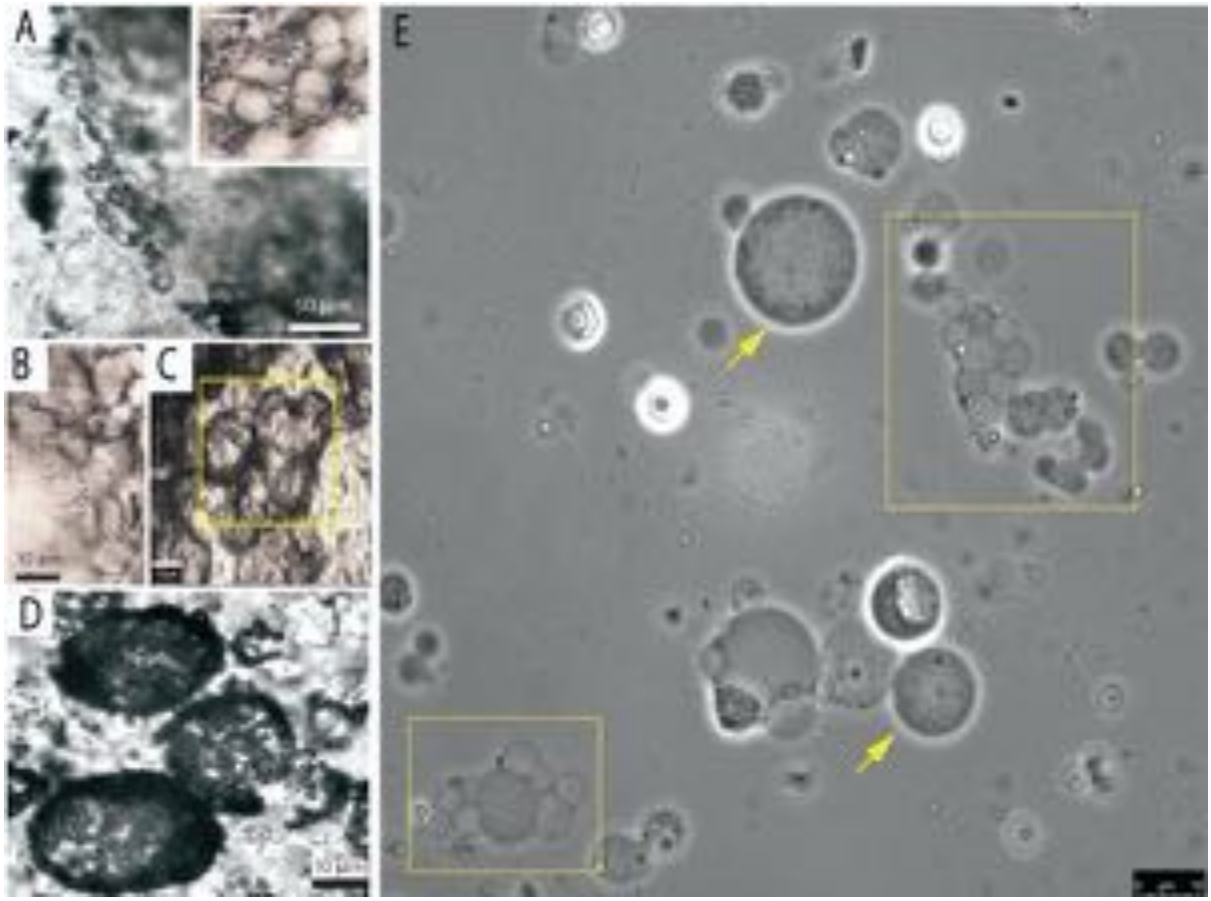

Fig. S11. Morphological comparison between *EM-P* and SPF microfossils.

Images A-D depicts SPF microfossils with intracellular organic inclusions (originally published by Wacey *et al*., 2011) (23). Images E shows morphologically analogous *EM-P*

cells. Images A-C shows chains and clumps of cells. Similar cluster of cells can be seen in image E (boxed regions). Image D is shows spherical microfossils with intracellular spherical inclusions. Similar *EM-P* cells with intracellular daughter cells can be seen in image E (yellow arrows). Lysis and release of daughter cells can be seen in Movie S10 & fig. S12.

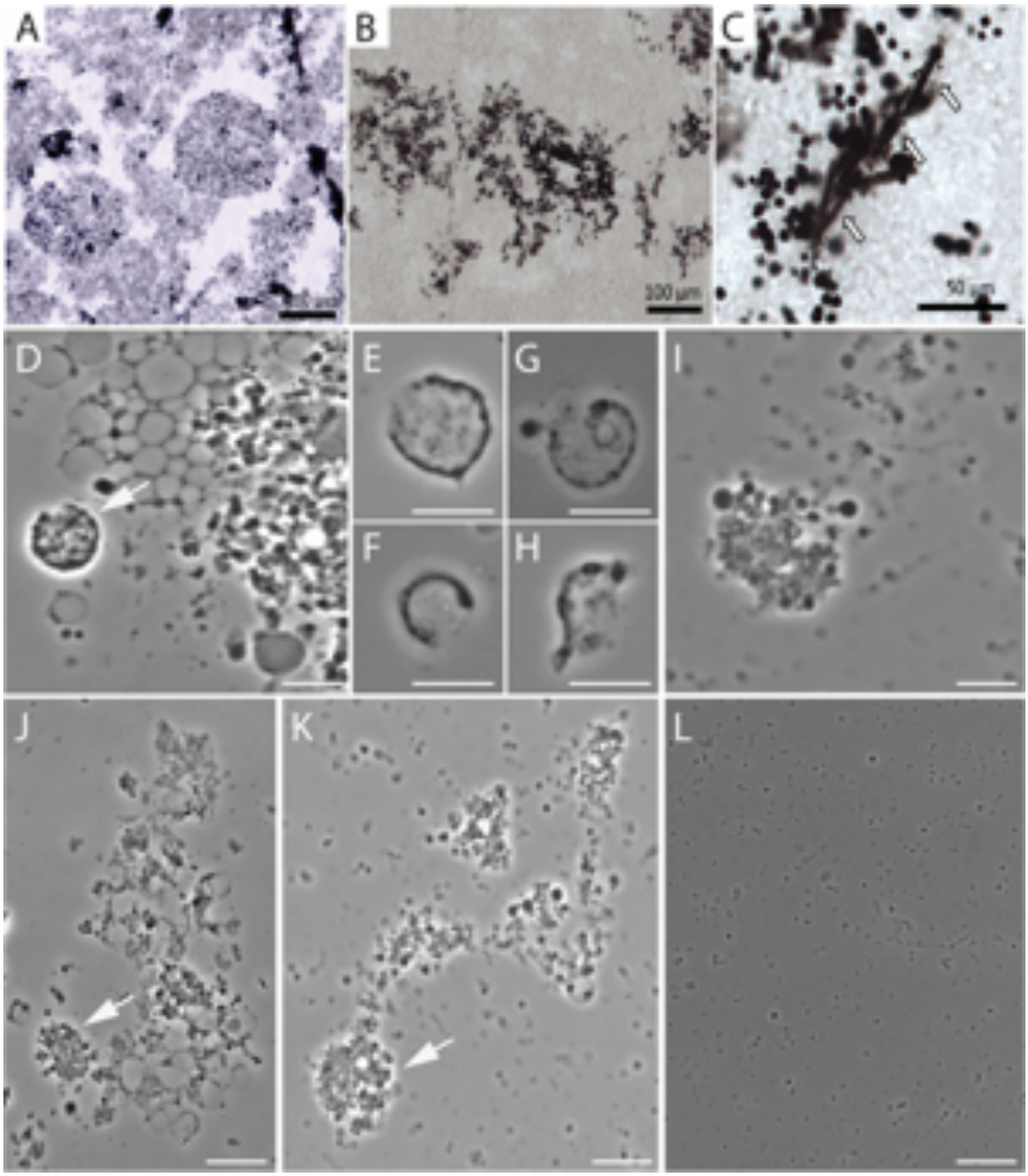

Fig. S12. Morphological comparison between *EM-P* and SPF microfossils.

Images A-C show clusters of faint and dark spherical microfossils reported from SPF (originally published by Sugitani *et al*., 2015) (24). Images D-L show sequential stages that led to formation of similar cells in *EM-P*. Scale bars: 10µm (A-E). Image D shows vacuoles with daughter cells undergoing lysis (arrow). Images E-H show leftover vacuole membrane after lysis and release of daughter cells. In some cases, daughter cells were initially clustered together like shown in images I & J (pointed by arrows). Subsequently these cells dispersed into individual daughter cells, like shown in images K & L. Lysis of cells or vacuoles was often observed to produce filamentous membrane debris, like seen in image C. Images of such thread-like membrane debris was shown in fig. S14 & S40.

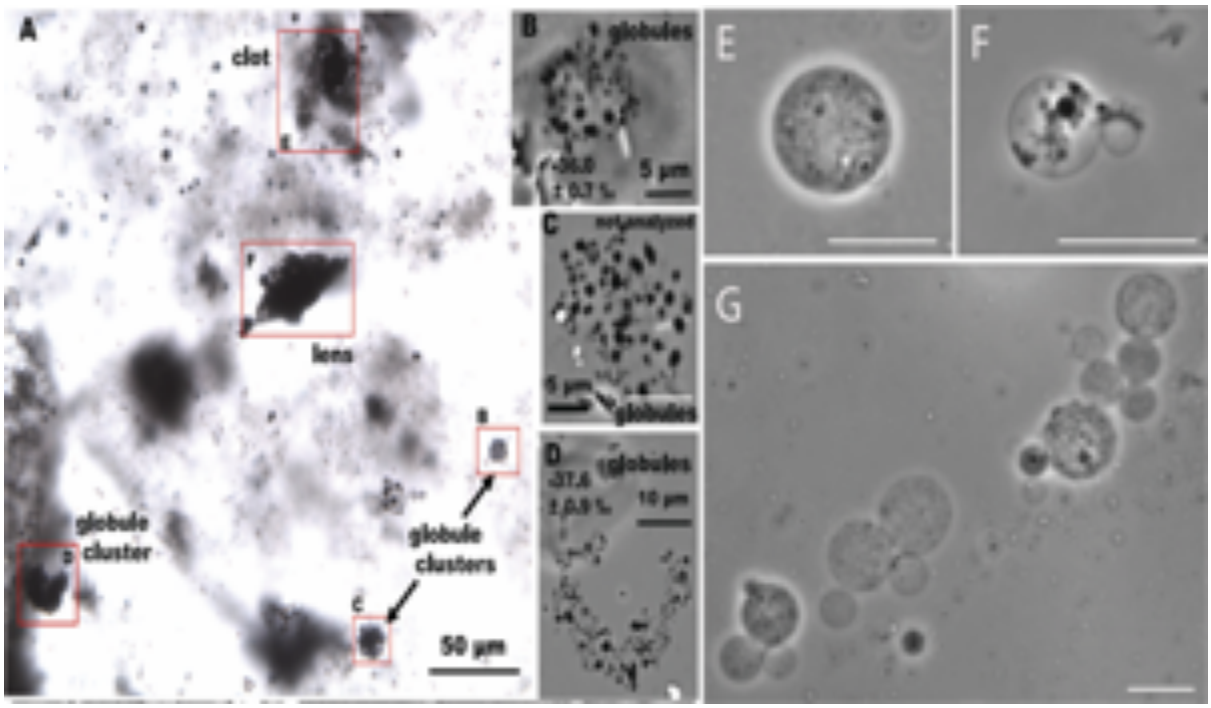

Fig. S13. Morphological comparison between *EM-P* and Goldsworth microfossils.

Images A-D depicts Goldsworth microfossils with intracellular organic inclusions (originally published by Lepot *et al*., 2013) (25). B-D are magnified images of boxed regions within image A. Images E-G shows morphologically analogous *EM-P* cells. Spherical globules reported from Goldsworth site were described as tiny spherical cells with filamentous extensions, very similar in morphology to daughter cells of *EM-P*. TEM images of such daughter cells can be seen in fig. S19. Scale bars: 10 µm (E-G).

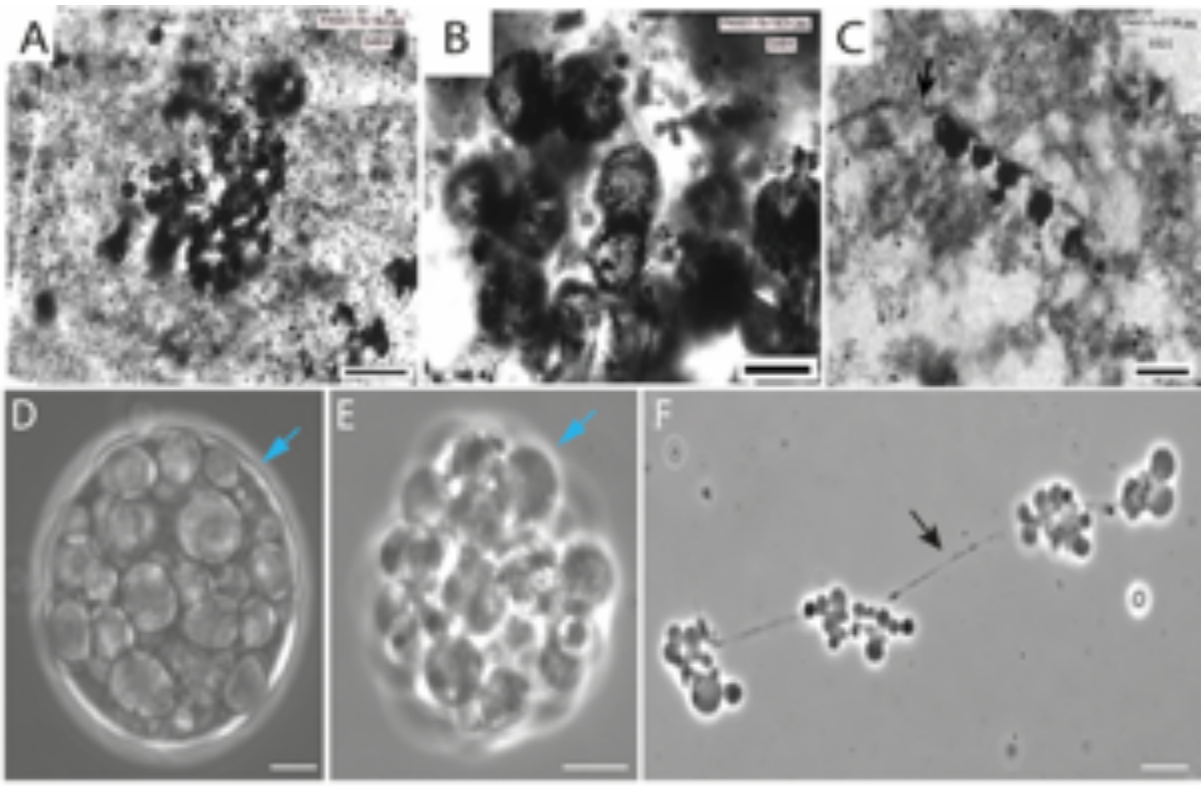

Fig. S14. Morphological comparison between SPF microfossils and *EM-P*.

Images A-D are hollow spherical SPF microfossils with internal inclusions (originally published by Sugitani *et al*., 2013) (18). Scale bars in Images A, B and C are 50µm, 20µm and 20µm respectively. Images D-F are images of *EM-P* cell undergoing lysis (E) and dispersion (F) of intracellular vacuoles. Cyan arrows in images D and E, points to presence

and absence of outer cell-membrane. Black arrows in images C & F points to filamentous structure interlinking spherical structures. Scale bar: 2µm (D&E) and 5µm (F).

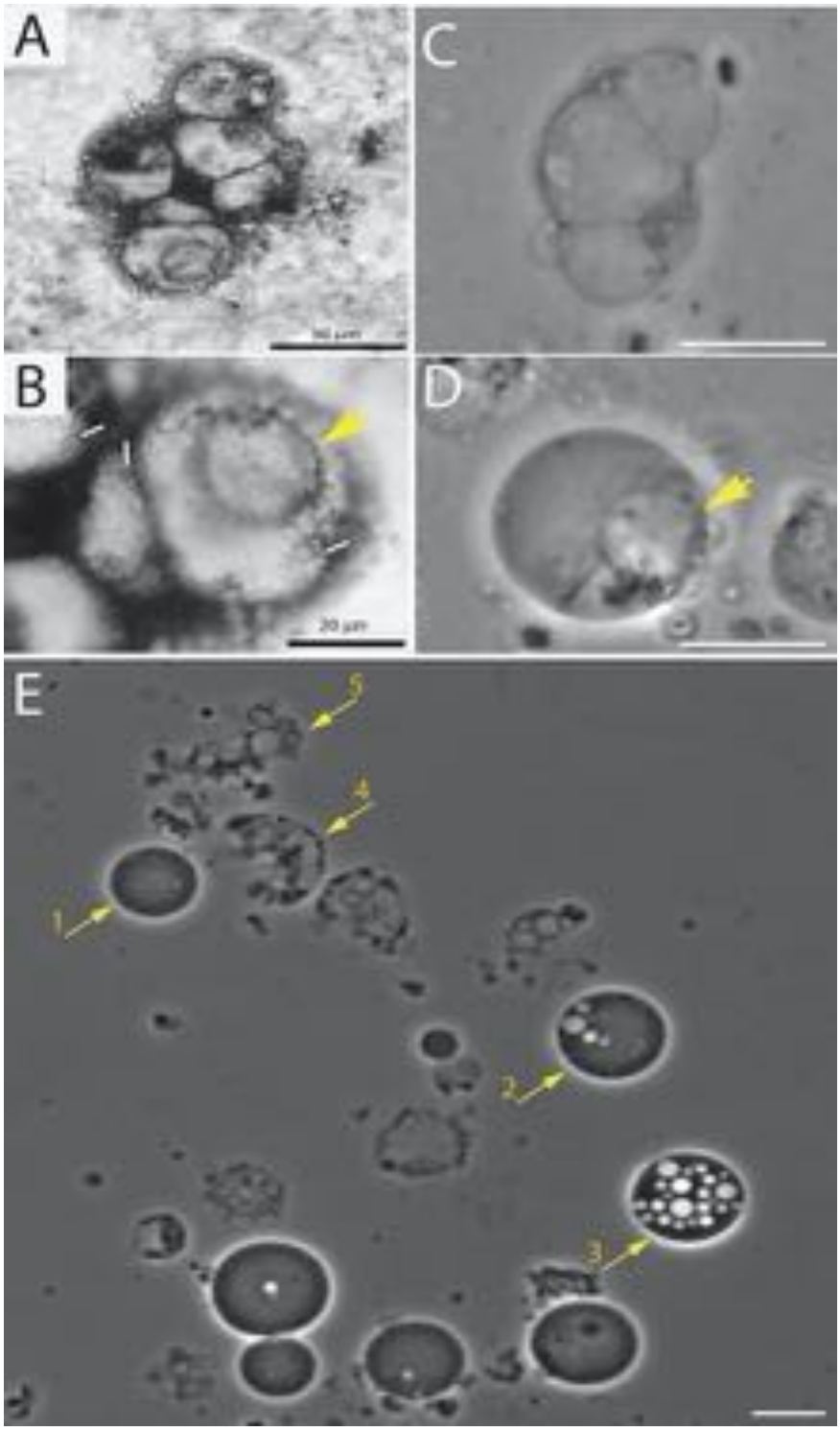

Fig. S15. Morphological comparison between *EM-P* and Waterfall microfossils.

Images A&B are microfossils reported from waterfall locality within SPF (originally published by Sugitani *et al*., 2015) (24). Image C&D shows morphologically analogous *EM-P* cells. Arrows in images B&D points to spherical intracellular vacuoles within the cell. Image E show sequential stages involved in formation of structures shown in images A&B. Sequential steps are indicated by numbers next to the arrows. White arrows in images A&B points to reticulate structures. Such structures were also observed in *EM-P* (fig. S4E & S7C). Scale bars: 10μm (C-E).

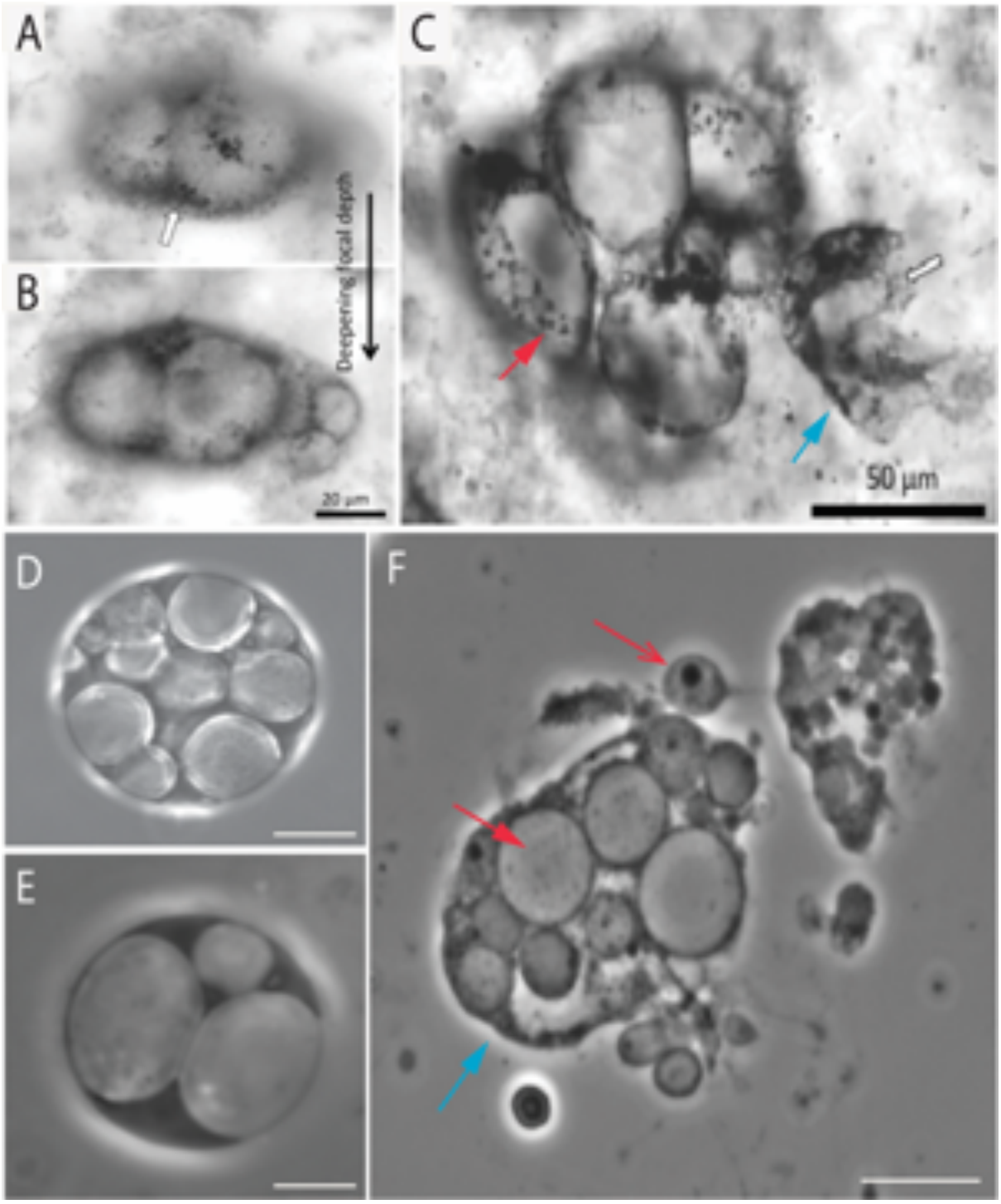

Fig. S16. Morphological comparison between *EM-P* and Waterfall microfossils. Images A, B & C are microfossils reported from waterfall locality within SPF (originally published by Sugitani *et al*., 2015) (24). Image D-F are phase-contrast images of morphologically analogous structures formed by *EM-P's*. Closed arrows in these images'

points to intracellular vacuoles with daughter cells. Cyan arrow in image F points to intact outer membrane. Rupture of cell membrane and release of vacuoles can be seen at the other end of the cell. Open red arrows points to a vacuole with relatively large daughter cell. Scale bars: 10μm (D-F).

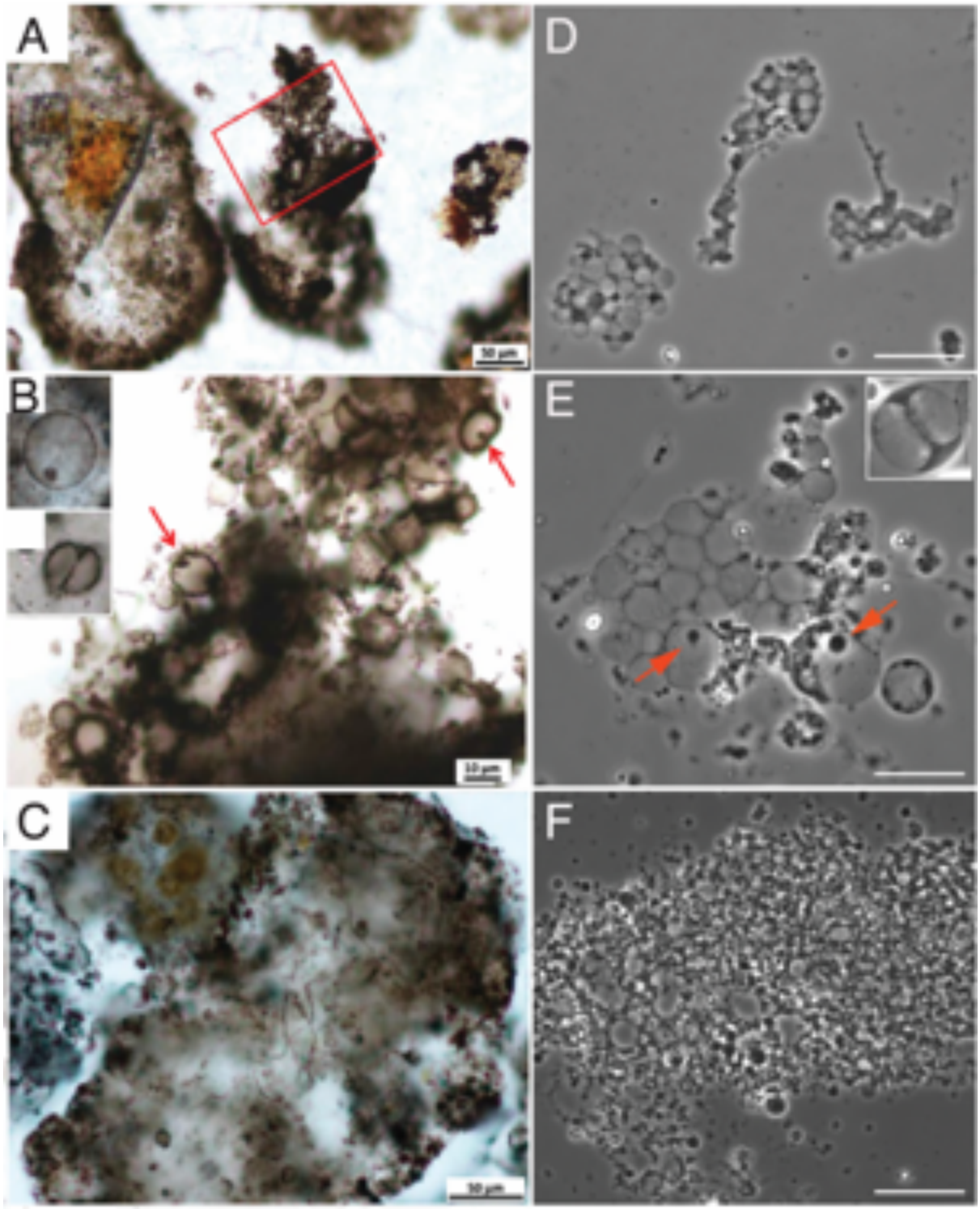

Fig. S17. Morphological comparison between honeycomb structures reported from Turee Creek formations and *EM-P*.

Images A, B & C are microfossils reported from Turee Creek locality within SPF (originally published by Barlow *et al*., 2018) (22). Image D-F are phase-contrast images of

morphologically analogous structures formed by *EM-P's*. Boxed region in image A resemble the lysed cells of *EM-P* (D). Arrows in images B&E point to the similar organic carbon inclusions within a hollow spherical cell. Insert in images B&E show spherical cell with two intracellular vesicles or nearly equal volume. Scale bars: 10µm (D-F).

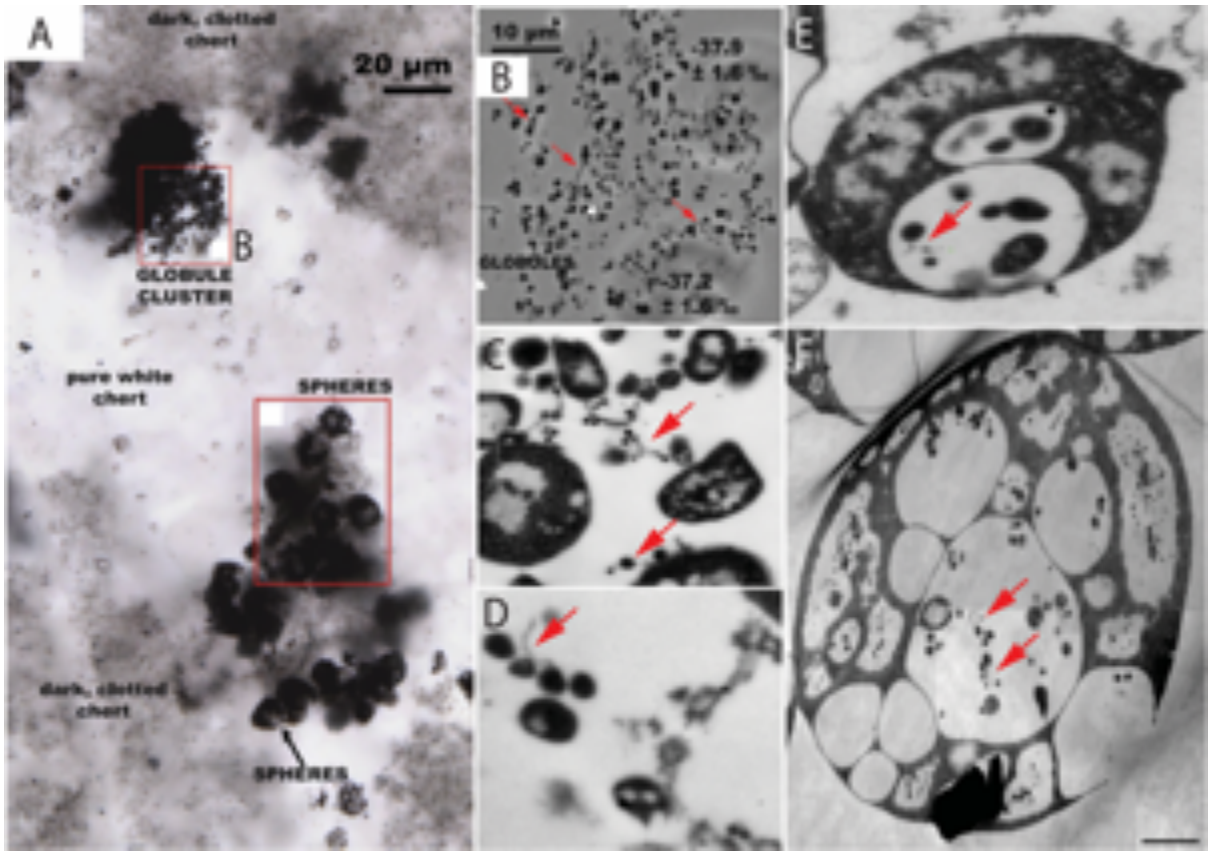

Fig. S18. Morphological comparison between *EM-P* and Goldsworth formation microfossils.

Images A & B are Goldsworth formation microfossils with intracellular organic inclusions (originally published by Lepot *et al*., 2013) (25). Images A shows clumps of spherical microfossils reported from Goldsworth site. Image B shows cluster of daughter cells with filamentous extensions. Images C-F shows morphologically analogous *EM-P* cells. Arrows in images B-F points to daughter cells with filamentous extensions. Scale bar: 500nm(E-G).

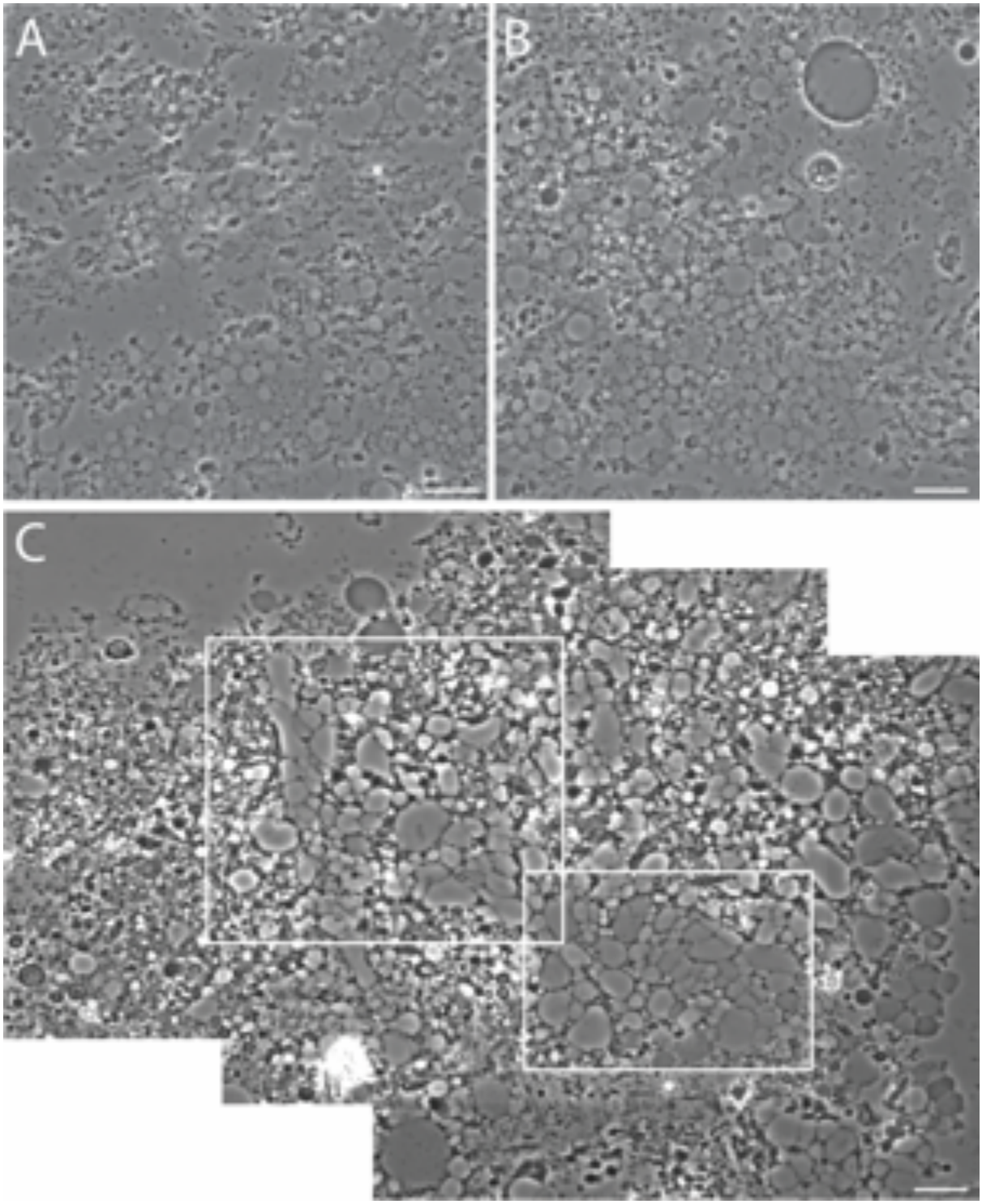

Fig. S19. Sequential stages involved in formation of honeycomb structures.

Images A-C are phase-contrast images of *EM-P's* vacuoles. Increase in number of vacuoles and tighter packing of these vacuoles can be seen from images A to C. Framed regions in image C shows deformation of spherical vacuoles into polygonal shapes due to compression of vacuoles within the interior of the mat. Scale bars: 10µm (A-C).

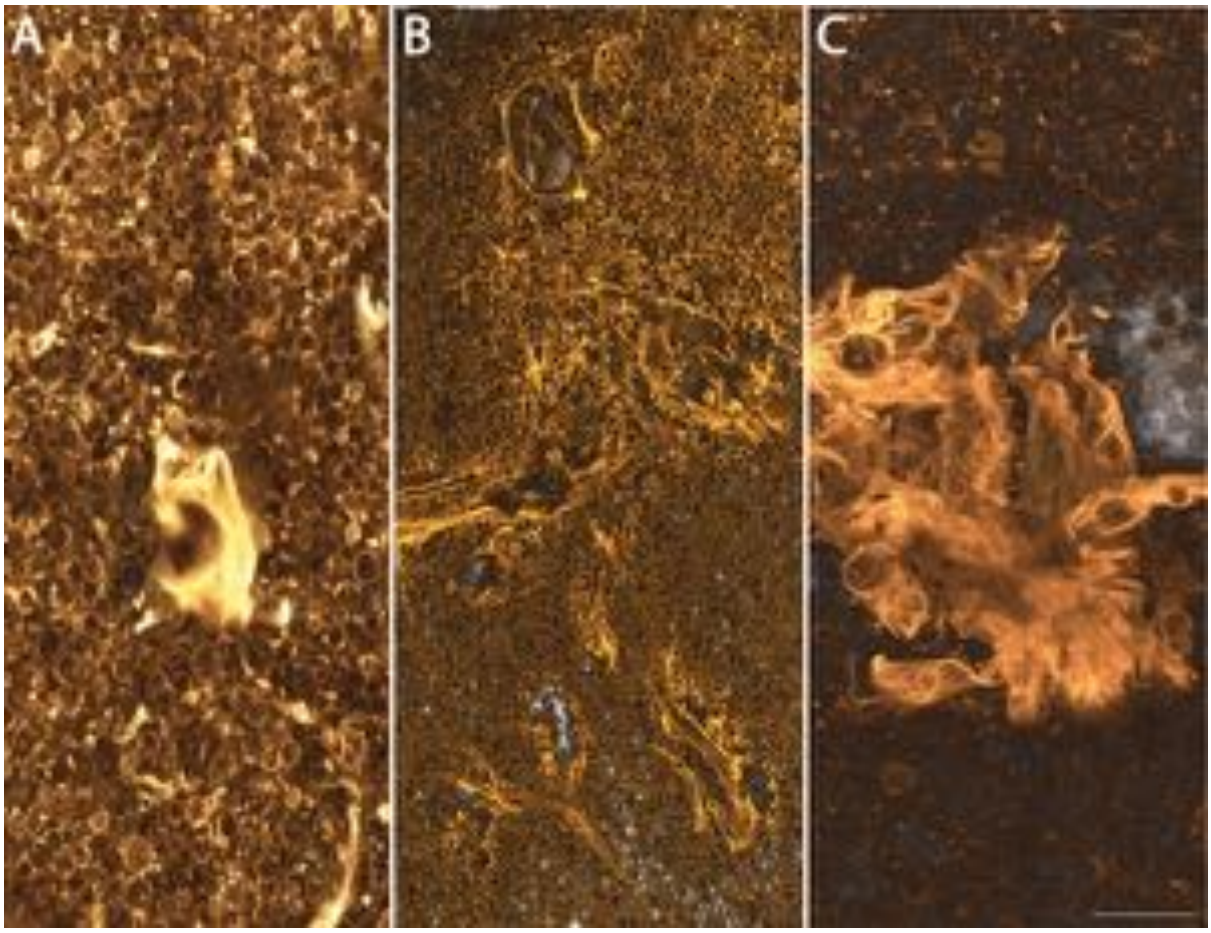

Fig. S20. Lysis and formation of membrane debris within multilayered *EM-P* cells. Images A, B & C shows mat-like structures formed by *EM-P*, and its subsequent transformation of these mats either to honeycomb-like structures (B) or undergoing lysis and formation of membrane debris (C). Cells in images D-F were stained with membrane stain, FM^{TM}5-95. Scale bar: 20µm (C).

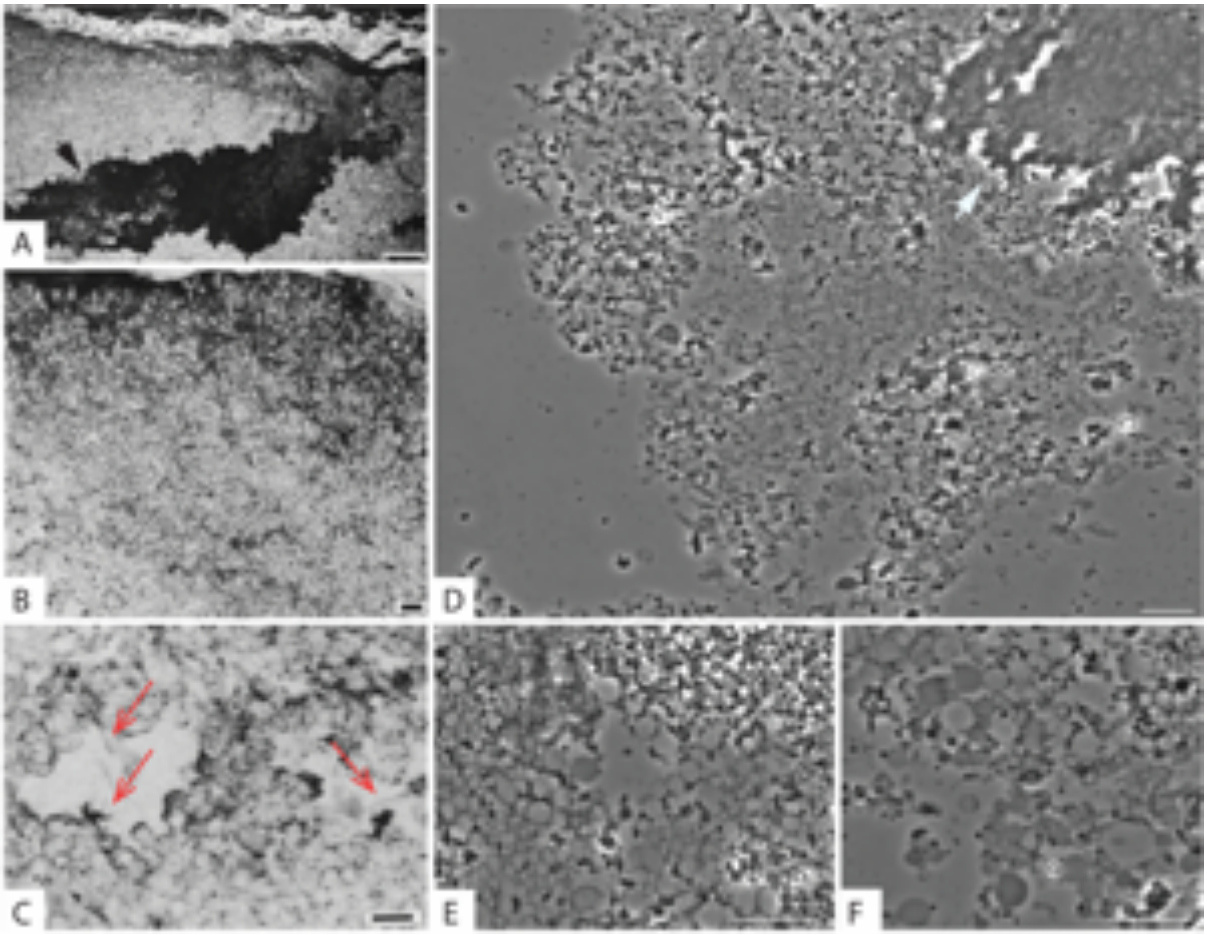

Fig. S21. Morphological comparison between *EM-P* and NPF microfossils.

Images A, B & C are organic structures reported from North-pole region (originally published by Buick *et al*., 1990) (19). The scale bar in image A is 1mm and in images B&C are 0.1mm. Images D, E and F are images of morphologically analogous structures observed in *EM-P* incubations. The scale bar in these images are 10µm. Arrows in images A & D points to the membrane debris in-between the cell aggregates. Images B & C and E & F are magnified regions of similar cell aggregates depicting individual spherical cell or the regions within the mats, that were devoid of cells. Red arrows in image C points to filamentous structures within the spherical structures. Formation of these structures can be seen in Movie S6-S8.

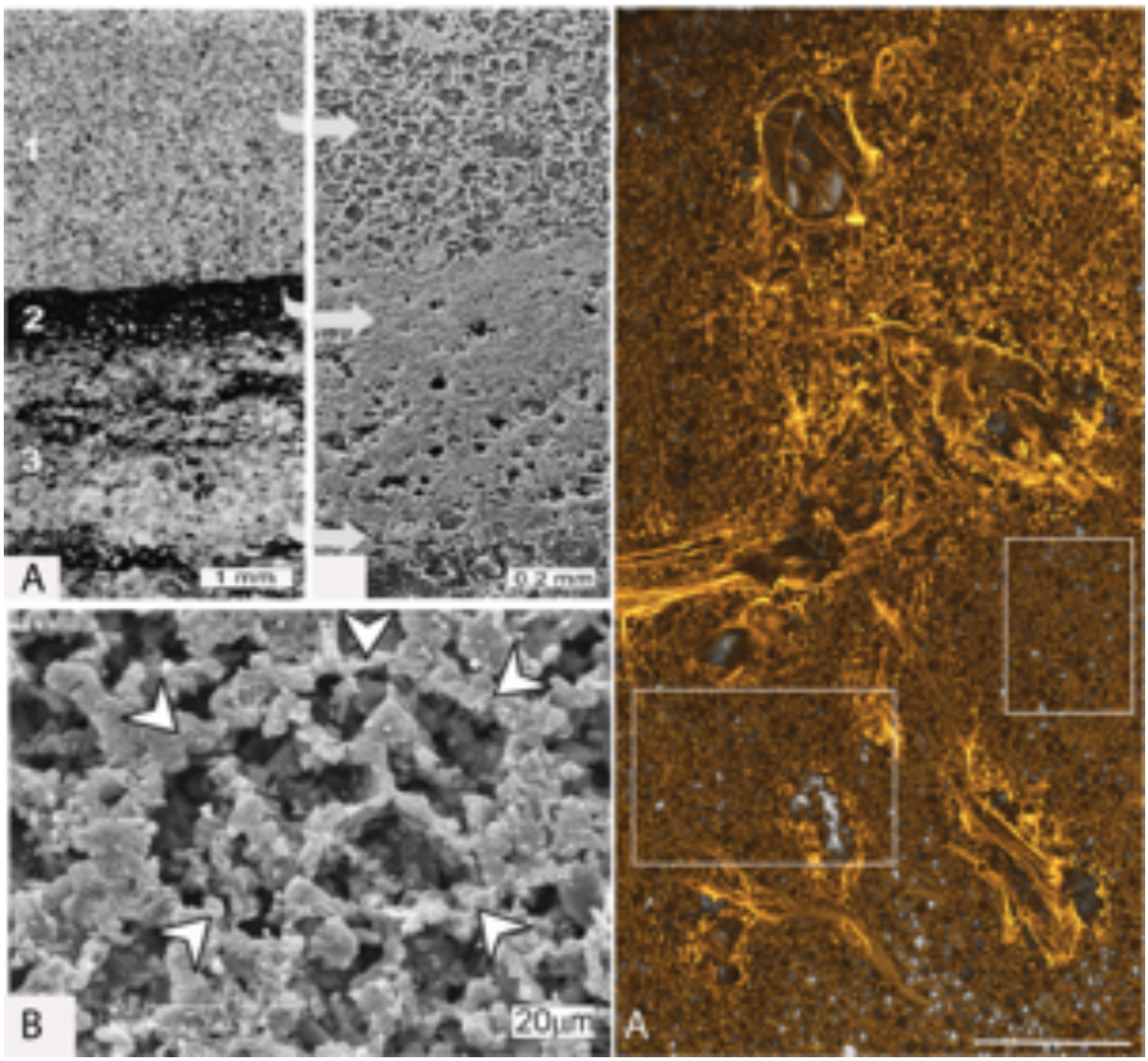

Fig. S22. Morphological comparison between organic structures reported from Nuga formation and honeycomb structures of *EM-P*.

Images A & B are honeycomb shaped organic structures reported from Nauga formation (originally published by Kazmierczak *et al*., 2009) (26). Image D shows morphologically analogous structures formed by *EM-P's*. Cells in images D-F were stained with membrane stain, FM™5-95 (yellow). Boxed regions within image C shows polygonal structures that were similar in their morphology to organic structures shown in Image B. Magnified image of similar hexagonal structures was shown in fig. S23D. Scale bar: 20µm (C).

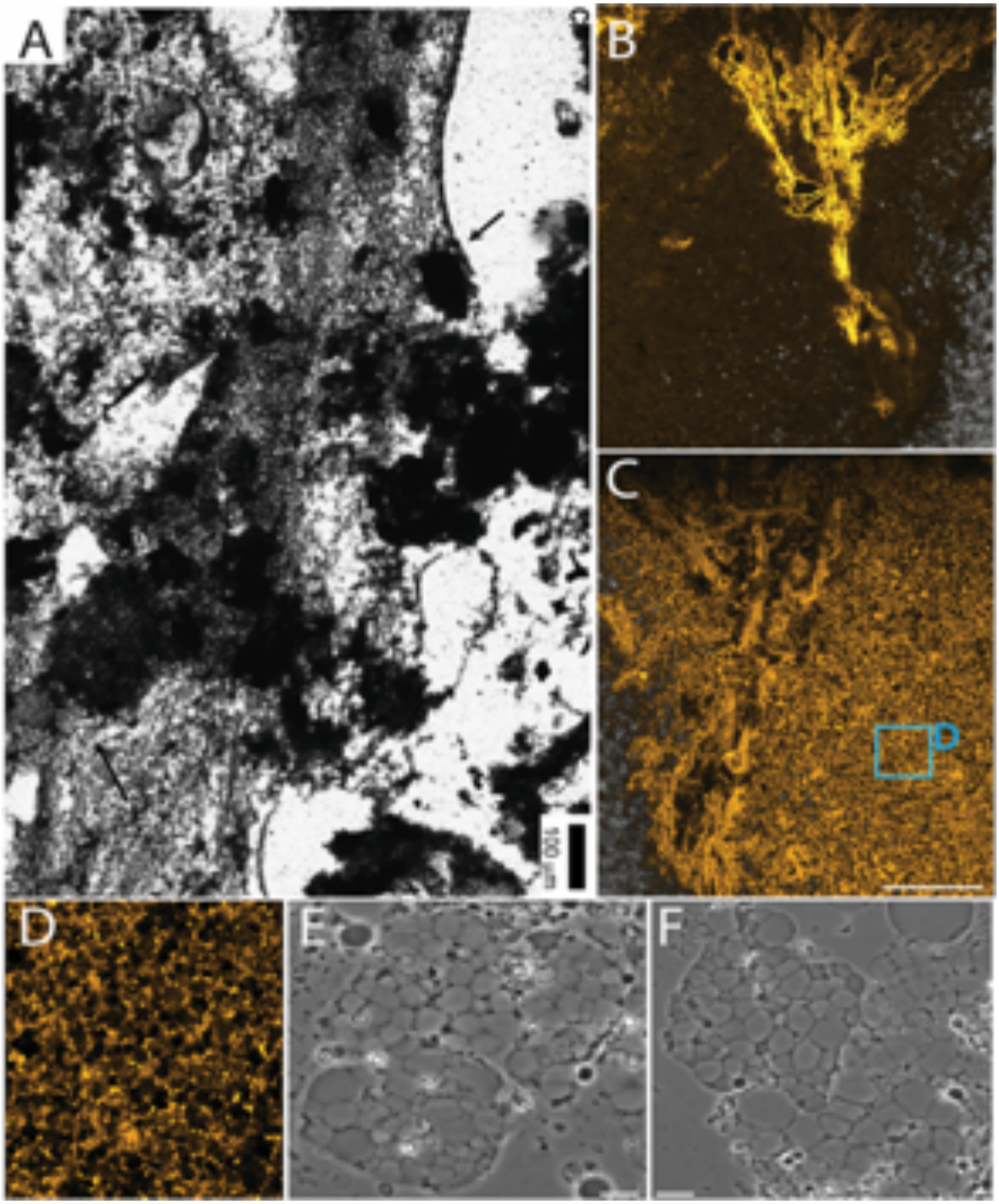

Fig. S23. Morphological comparison between organic structures reported from BRC formation and honeycomb structures of *EM-P*.

Images A is honeycomb shaped organic structures reported from BRC (originally published by Tice *et al*., 2009) (27). Images B&C are anterior and posterior view of morphologically analogous *EM-P's* membrane debris. Cells in images D-F were stained with membrane stain, FM^{TM}5-95 (yellow). Image D is the magnified region of the biofilm showing honeycomb

structures. Scale bar in images C is 100µm. Images E&F are phase-contrast images of large spherical *EM-P* cells with polygonal vacuoles undergoing clumping to form large honeycomb shaped mat. Scale bars: 10µm.

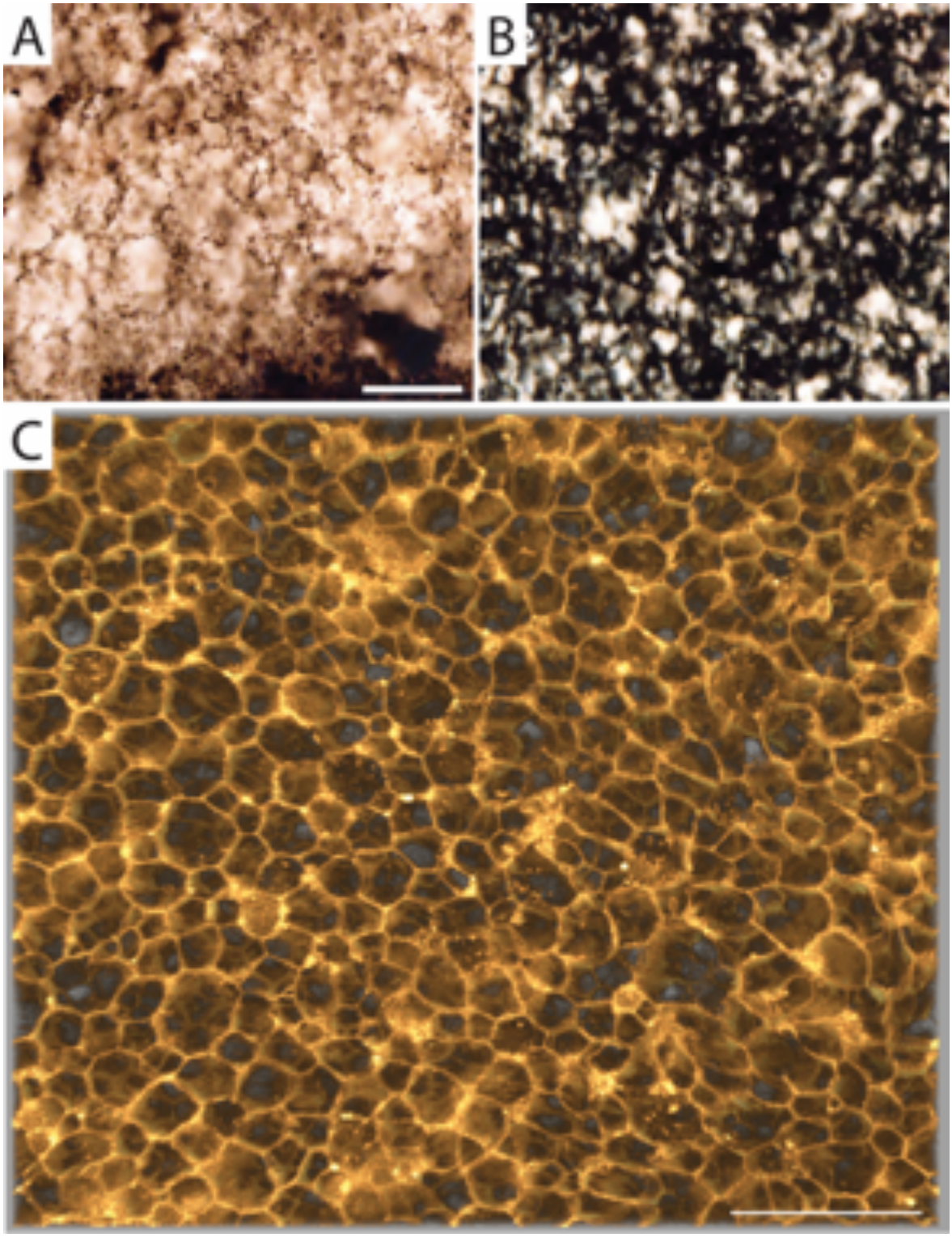

Fig. S24. Morphological comparison between *EM-P* and Mount Grant microfossils. Images A&B are honeycomb shaped organic structures reported from Mount Grant formation (originally published by Sugitani *et al*., 2007) (29). Image C is morphologically analogous

EM-P's membrane debris. Cells in images C were stained with membrane stain, FM™5-95 (yellow). Scale bars: 20µm.

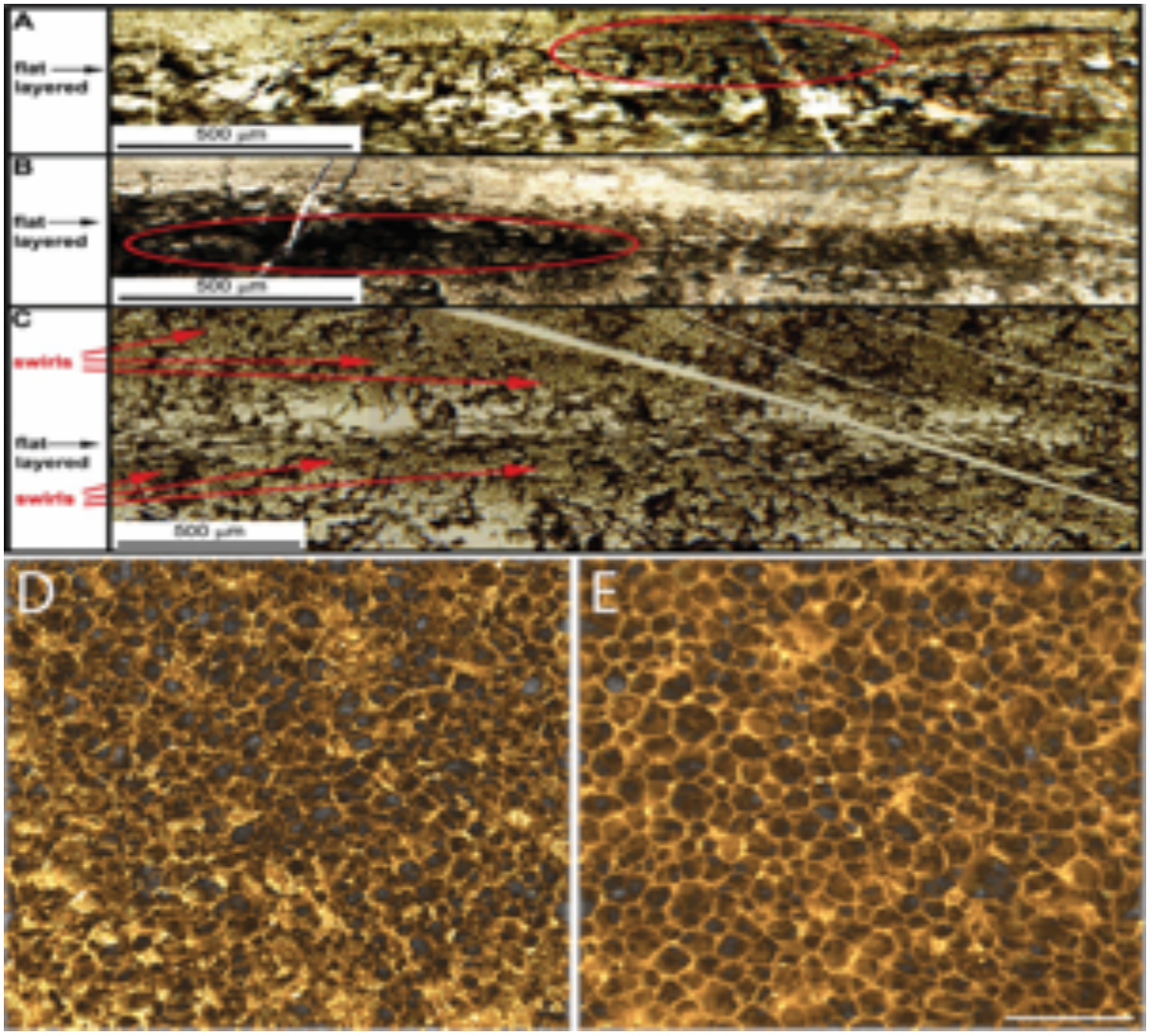

Fig. S25. Morphological comparison between honeycomb structures of *EM-P* organic structures reported from SPF.

Images A-C are honeycomb shaped organic structures reported from SPF (originally published by Schopf *et al*., 2017) (28). Images D&E shows morphologically analogous *EM-P's* membrane debris. Cells in images D-F were stained with membrane stain, FM™5-95. Circled region in image B points to flattened honeycomb structures. Morphologically analogous structures were shown in fig. S20. Scale bar: 20µm (E).

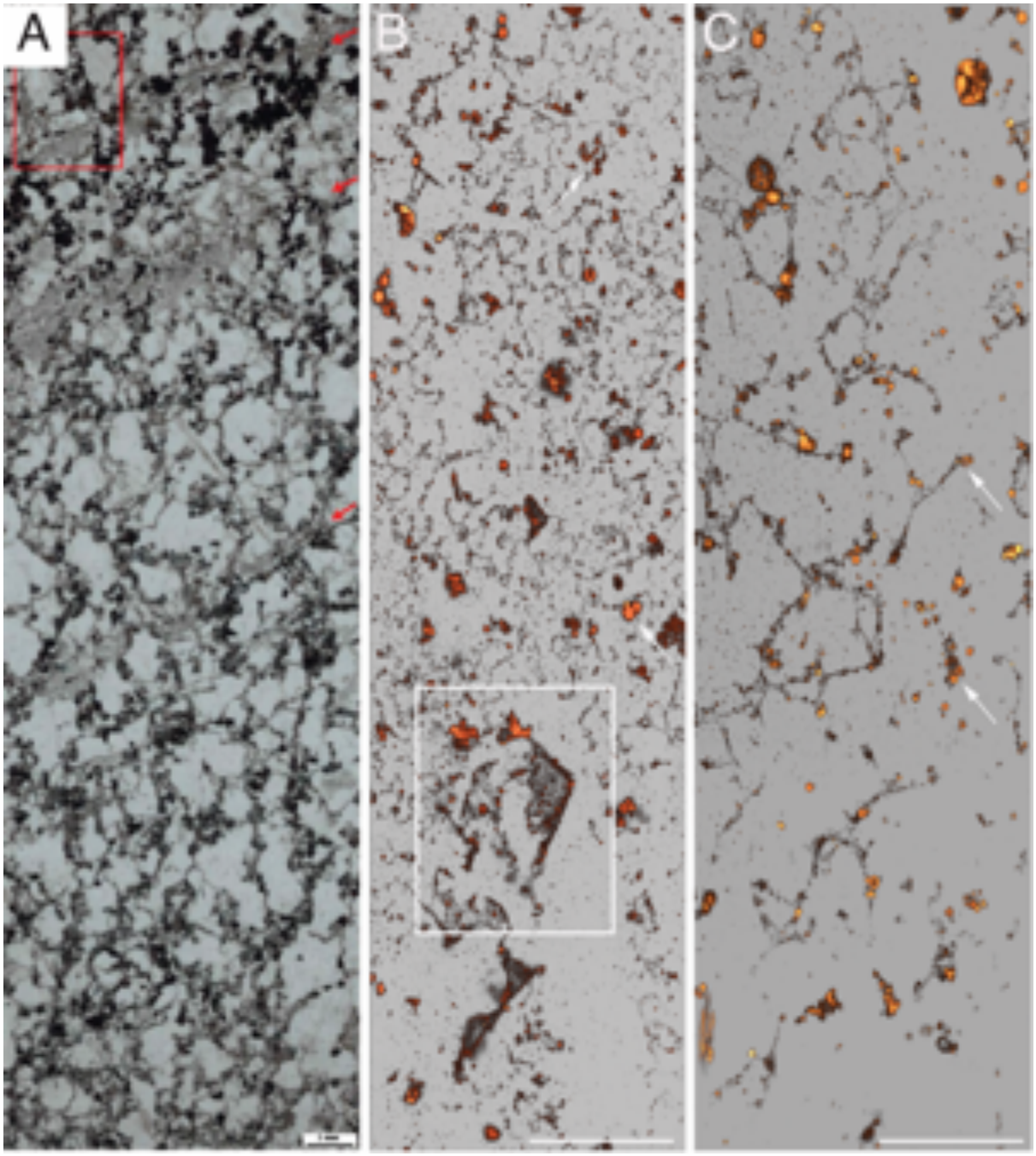

Fig. S26. Morphological comparison between honeycomb structures reported from Turee creek formations and *EM-P*.

Image A show tangled network of microfossil structures reported from Turee creek formation (originally published by Barlow *et al*., 2018) (22). Scale bar in images A is 2mm. Images B&C are morphologically analogous structures formed by *EM-P*. Cells in images D-F were stained with membrane stain, FM^{TM}5-95. Scale bars in images B&C are 50µm. Based on the

morphological resemblance we propose that Turee creek microfossils were leftover membrane debris of *EM-P*, rather than entangled network of filamentous microfossils. Boxed regions and arrows in images B&C points to spherical daughter cells attached to membrane debris.

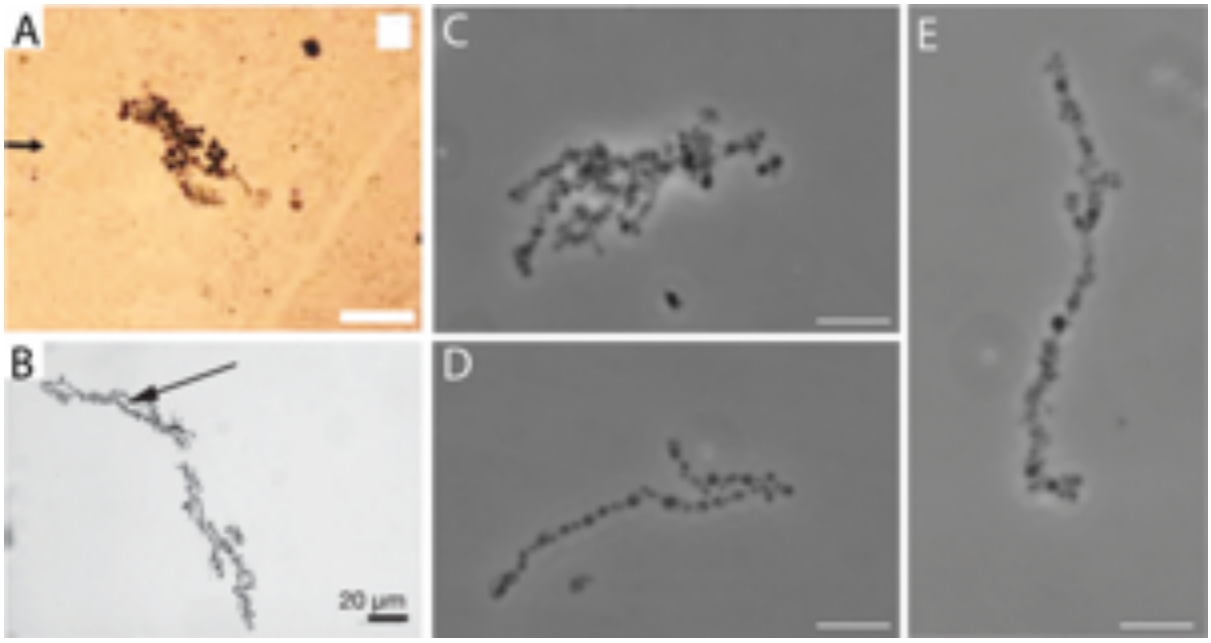

Fig. S27. Morphological comparison between Mount Grant and Moodies formation microfossils with *EM-P*.

Images A&B show microfossils reported from Mount Grant and Moodies formation (originally published by Javaux *et al*., 2010 & Sugitani *et al*., 2007) (29, 30). Scale bar in image A is 100µm. Images C-E are morphologically analogous *EM-P* daughter cells. Scale bars: 10µm (C-E).

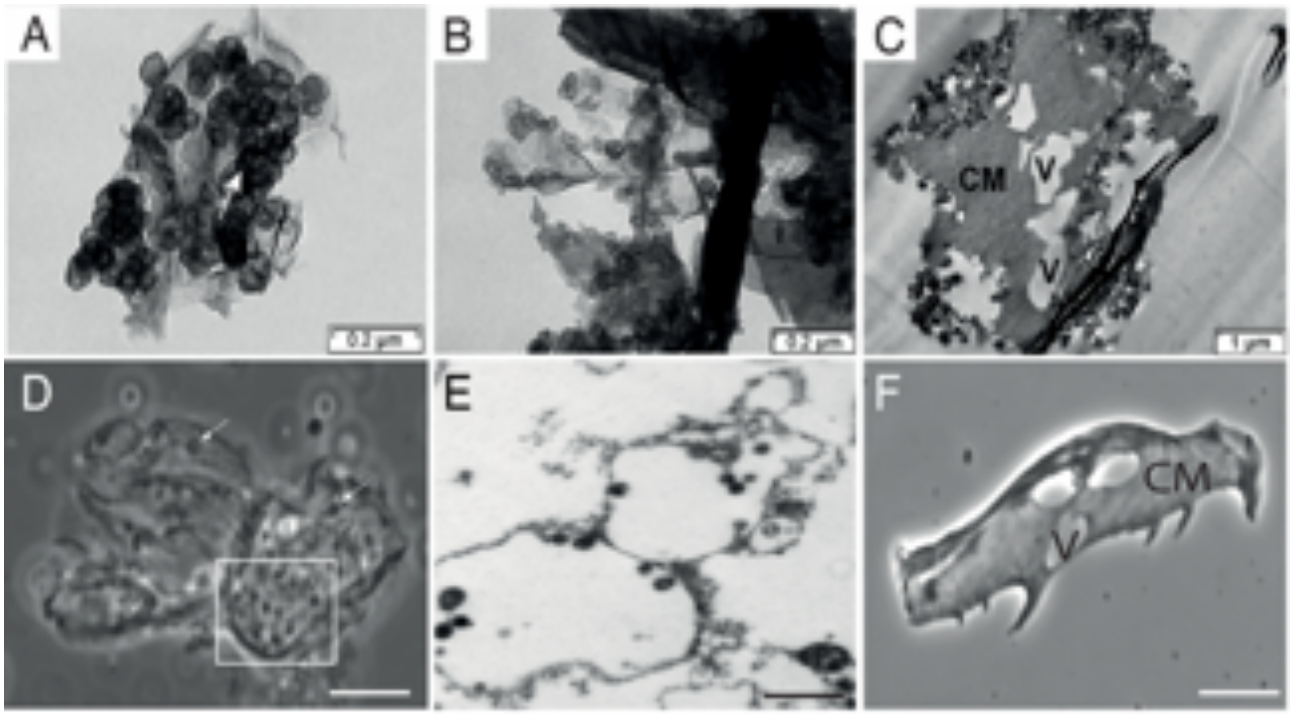

Fig. S28. Morphological comparison between Sulphur spring formation microfossils and *EM-P*.

Images A, B & C are organic structures reported from Sulphur spring formation (Duck *et al*., 2007) (31). Images D-F are Phase-contrast (D&F) and TEM (E) images of morphologically analogous *EM-P* daughter cells attached to membrane debris (D&E). Boxed region and arrows in image D points to the daughter cells within membrane debris. Movement of daughter cells attached to membrane debris can be seen in Movie S5. Images C & F shows membrane debris reported from Sulphur spring formation site and morphologically analogous debris observed in *EM-P* incubations. CM and V are abbreviations for cell membrane and vacuole respectively. Scale bars: 5μm (D & F) and 200nm (E).

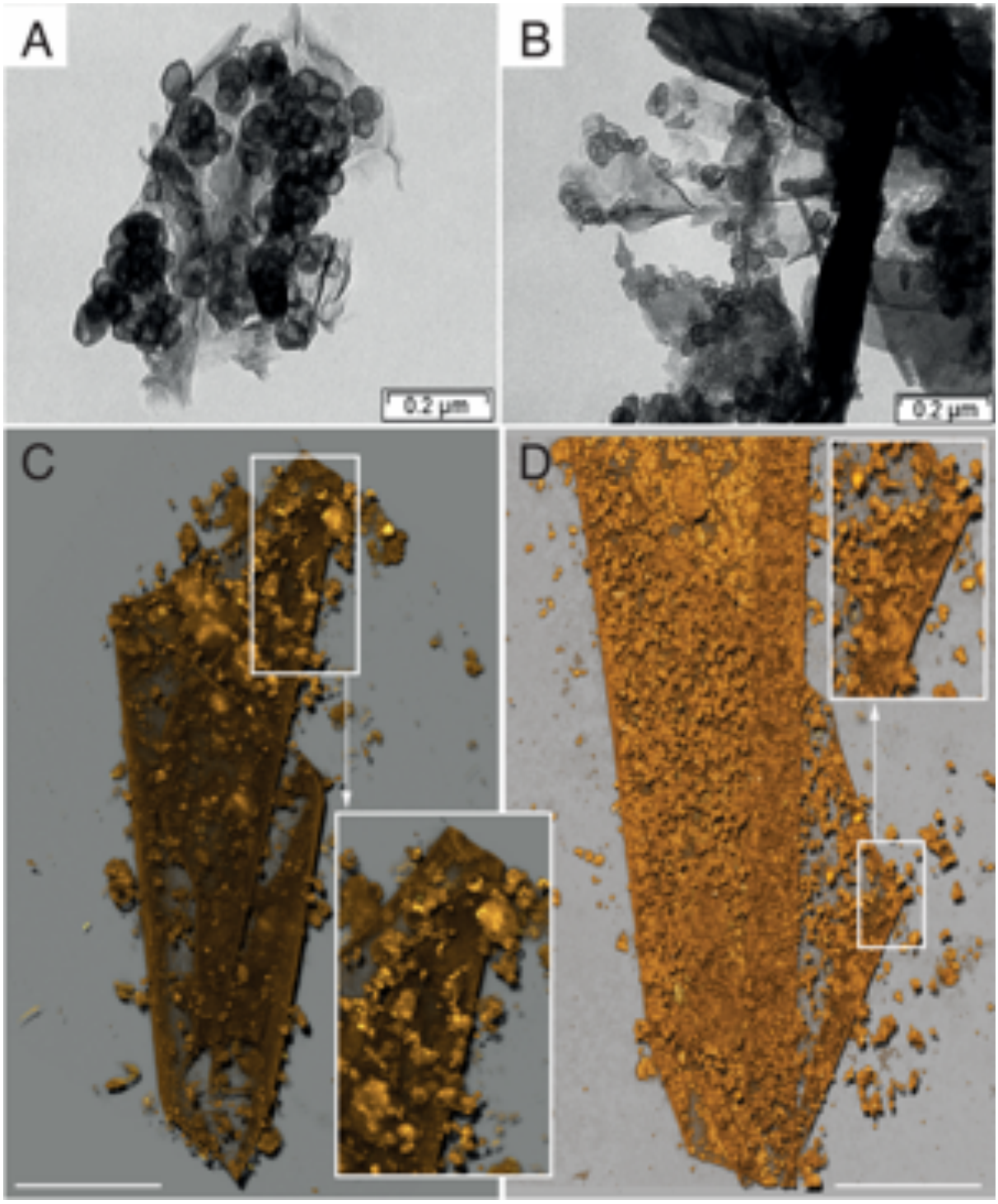

Fig. S29. Morphological comparison of Sulphur spring microfossils with *EM-P*

Images A & B are microfossils reported from Sulphur spring formation (Duck *et al*., 2007) (31). Images C & D are 3D-rendered STED microscope images of morphologically analogous *EM-P* daughter cells attached to membrane debris. Inset images in C&D show

magnified regions of membrane debris with daughter cells. Cells in images D-F were stained with membrane stain, FM^{TM}5-95 (yellow). Scale bars: 20µm (C & D).

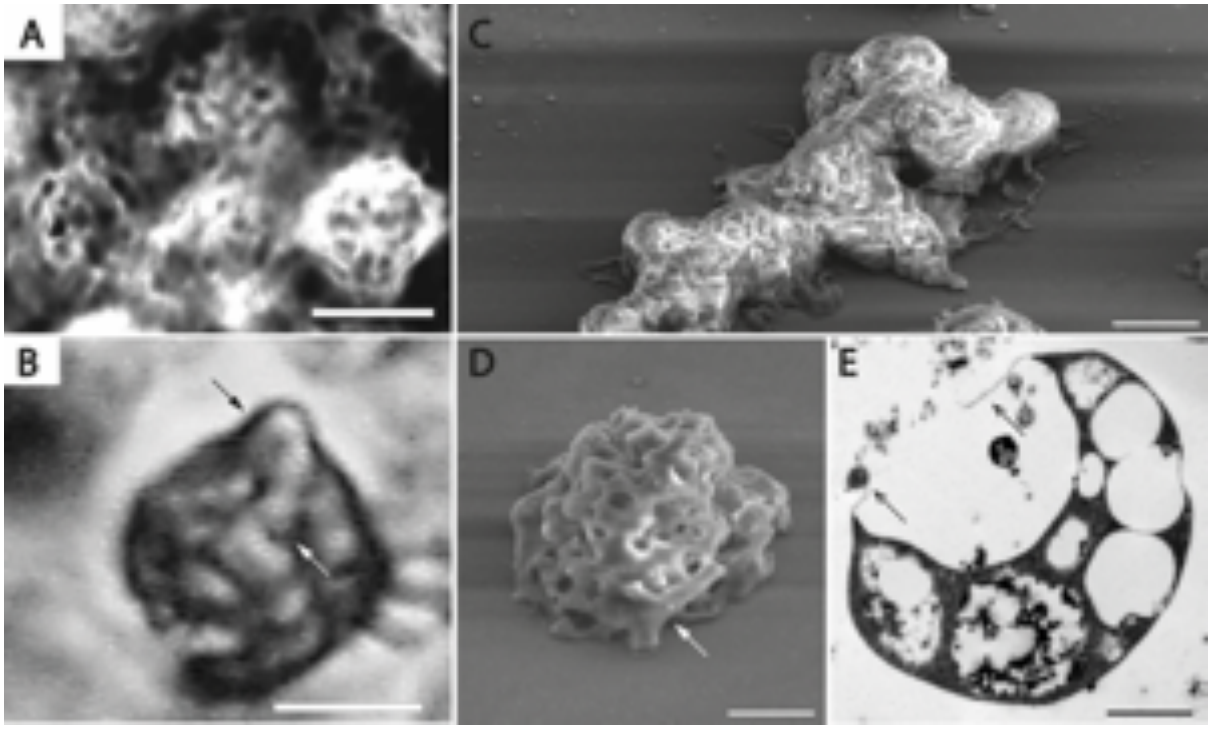

Fig. S30. Morphological comparison between *EM-P* and Kromberg formation microfossils.

Images A & B are microfossils reported from Kromberg formation (Kaźmierczak *et al.,* 2019) (32). Scale bar in images A & B are 10µm. Images C, D & E SEM and TEM images of morphologically analogous *EM-P's* cells. Scale bar in images C & D and E are 0.5µm and 200nm respectively. Arrows in images B & D points to similar surface texture of microfossils and *EM-P* cells.

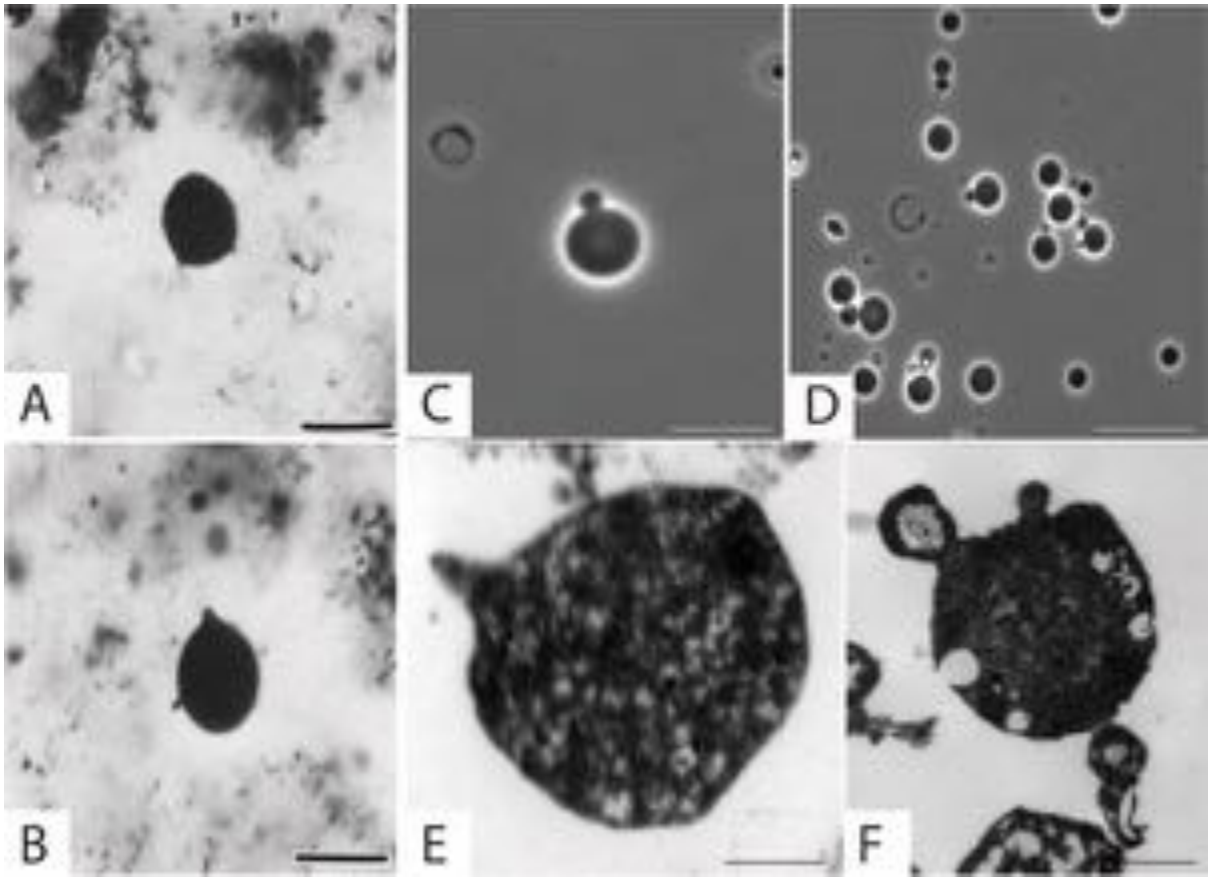

Fig. S31. Morphological comparison between North-Pole formation microfossils and *EM-P*.

Images A & B show spherical microfossils reported from North-Pole formation (Ueno *et al.,* 2006) (33). Images C & D are phase-contrast and TEM images of *EM-P* exhibiting morphological similarities with NMF microfossils. These cells represent first stage in the reproductive cycle of *EM-P* reproducing by formation of external daughter cells. Scale bar in images C & D and images E & F are 10μm and 500nm respectively.

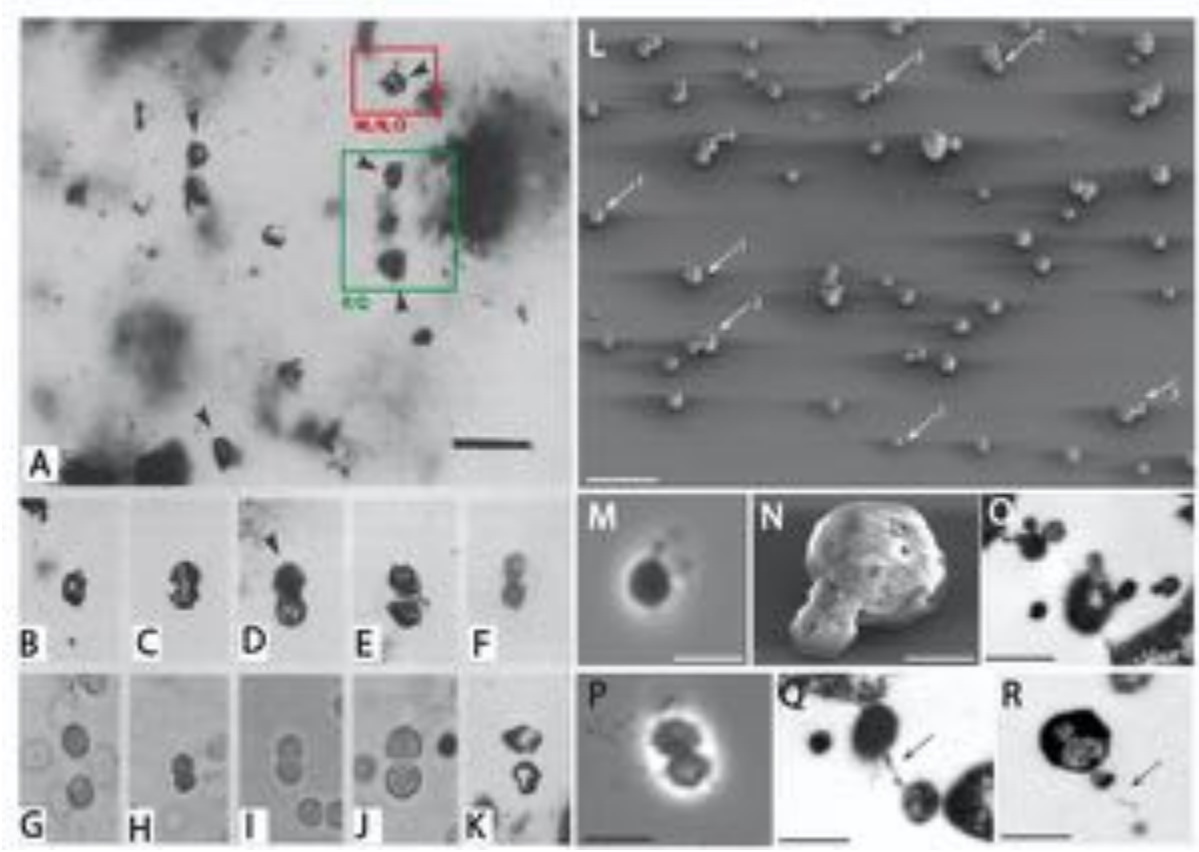

Fig. S32. Comparison of *EM-P* with Swartkoppie formation microfossils.

Images A-K are the images of Swartkoppie microfossils (Knoll *et al.,* 1977) (6). Images L-R are images of *EM-P* exhibiting morphological similarities with Swartkoppie microfossils. Image A shows cells with membrane overhangs (red box), cells in dyads (green box) and individual spherical cells (arrows). Morphologically analogous *EM-P* cells can be seen in images mentioned below the red and green boxes. Images M, N and O are phase-contrast, SEM and TEM images of cells with membrane extensions, like the microfossil cell shown within the red box. Images P-R shows sequence of stages involved in cell-division (Movie S14). Images B-F and G-K shows Swartkoppie microfossils reproducing by binary division. Morphologically similar *EM-P* cells were shown in image L (white arrows). Numbers next to the arrows indicate different stages of cells division.

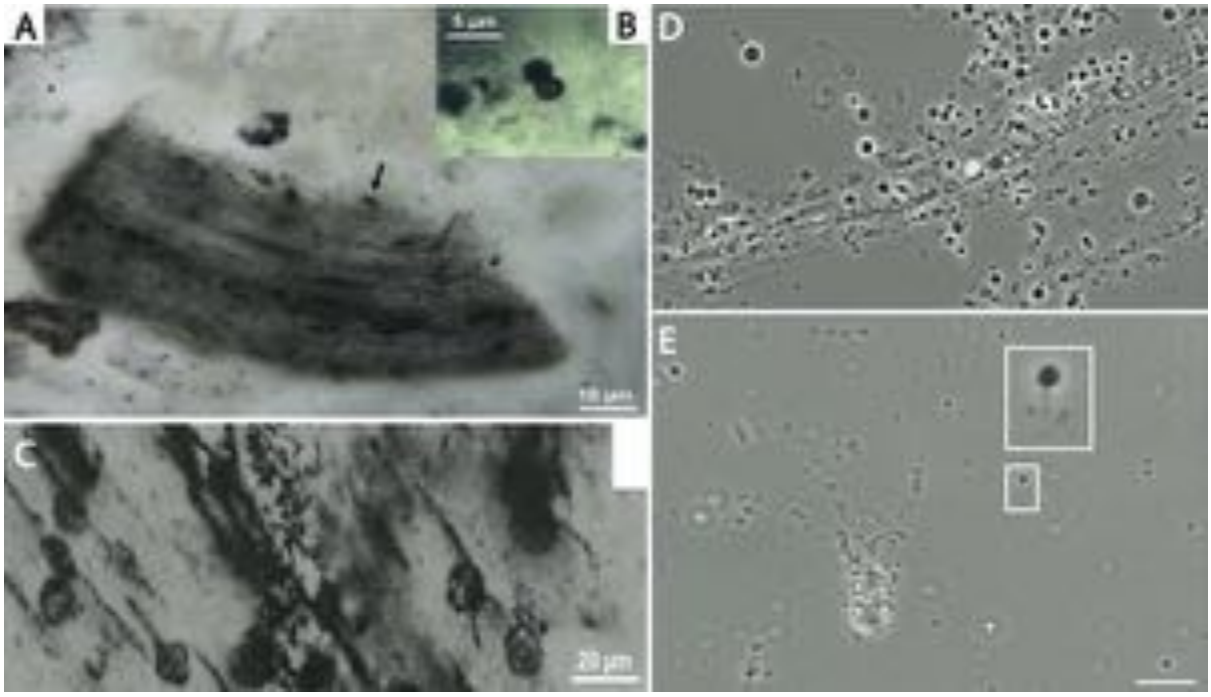

Fig. S33. Comparison of *EM-P* with Sheba formation microfossils.

Images A, B & C show spherical microfossils reported from Sheba formation (Hickman-lewis *et al.,* 2019) (34). Image A show aggregation of spherical microfossils within organic carbon clasts. Image B shows magnified image of spherical cells with filamentous extensions, that appears to be reproducing by binary division. Image C show spherical cells with unevenly distributed cytoplasm and filamentous extensions. Images D & E are morphologically analogous *EM-P* cells. Like Sheba formation microfossils *EM-P* cells formed aggregations that resemble clasts or organic carbon and have filamentous extensions. *EM-P* cells were also noticed to have uneven cytoplasm (fig. S9). Scale bars in image C is 10µm.

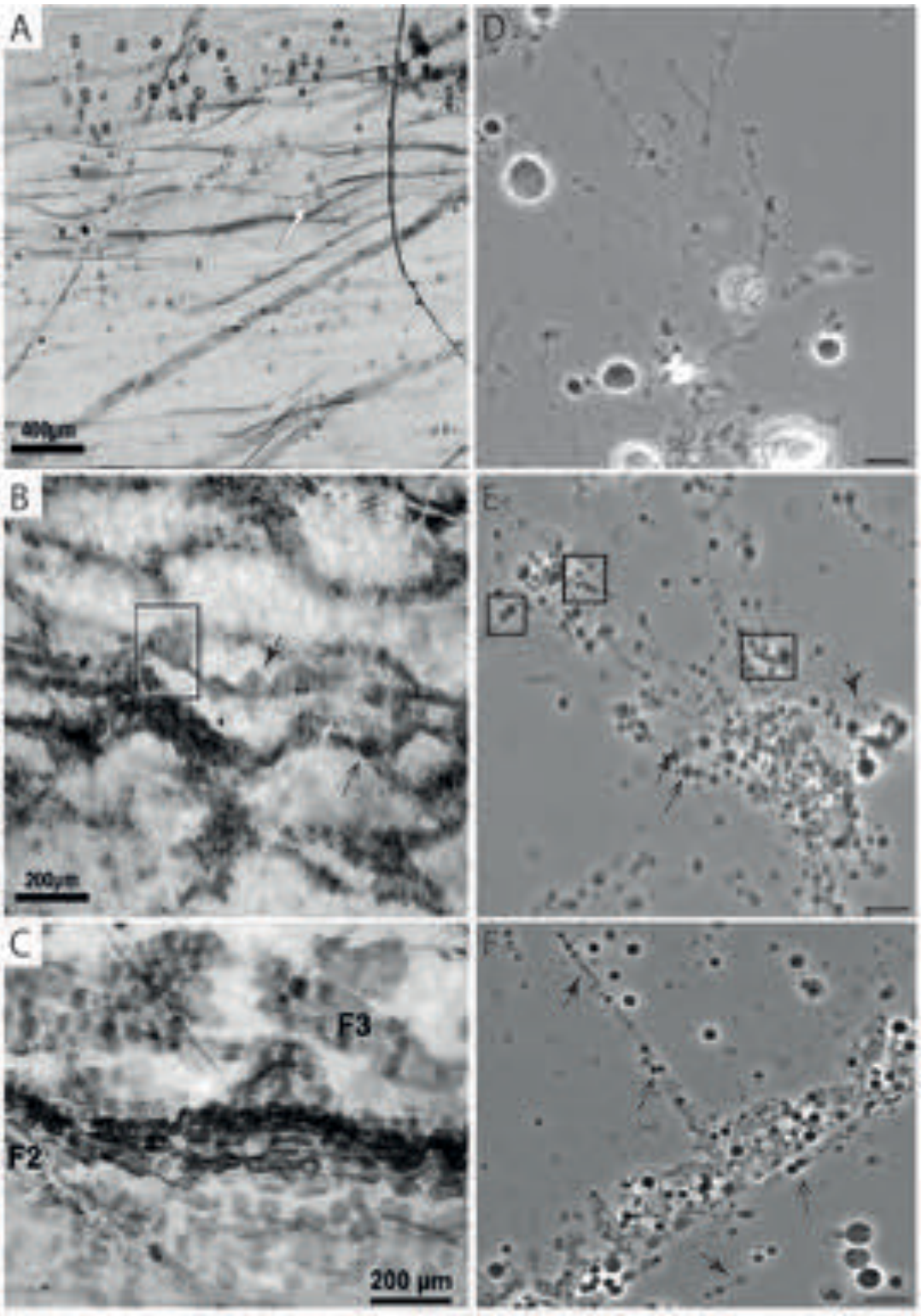

Fig. S34. Comparison of Cleaverville microfossils with *EM-P*

Images A-C are spherical microfossils reported from Cleaverville formations (Ueno *et al.,* 2006) (33). Images D-F are morphologically analogous *EM-P* cells. Scale bar in these images

D-F are 5µm. Open and closed arrows in all image's points to daughter cells with and devoid of organic carbon. Boxed regions within these images highlights the arrangement of daughter cells in pairs.

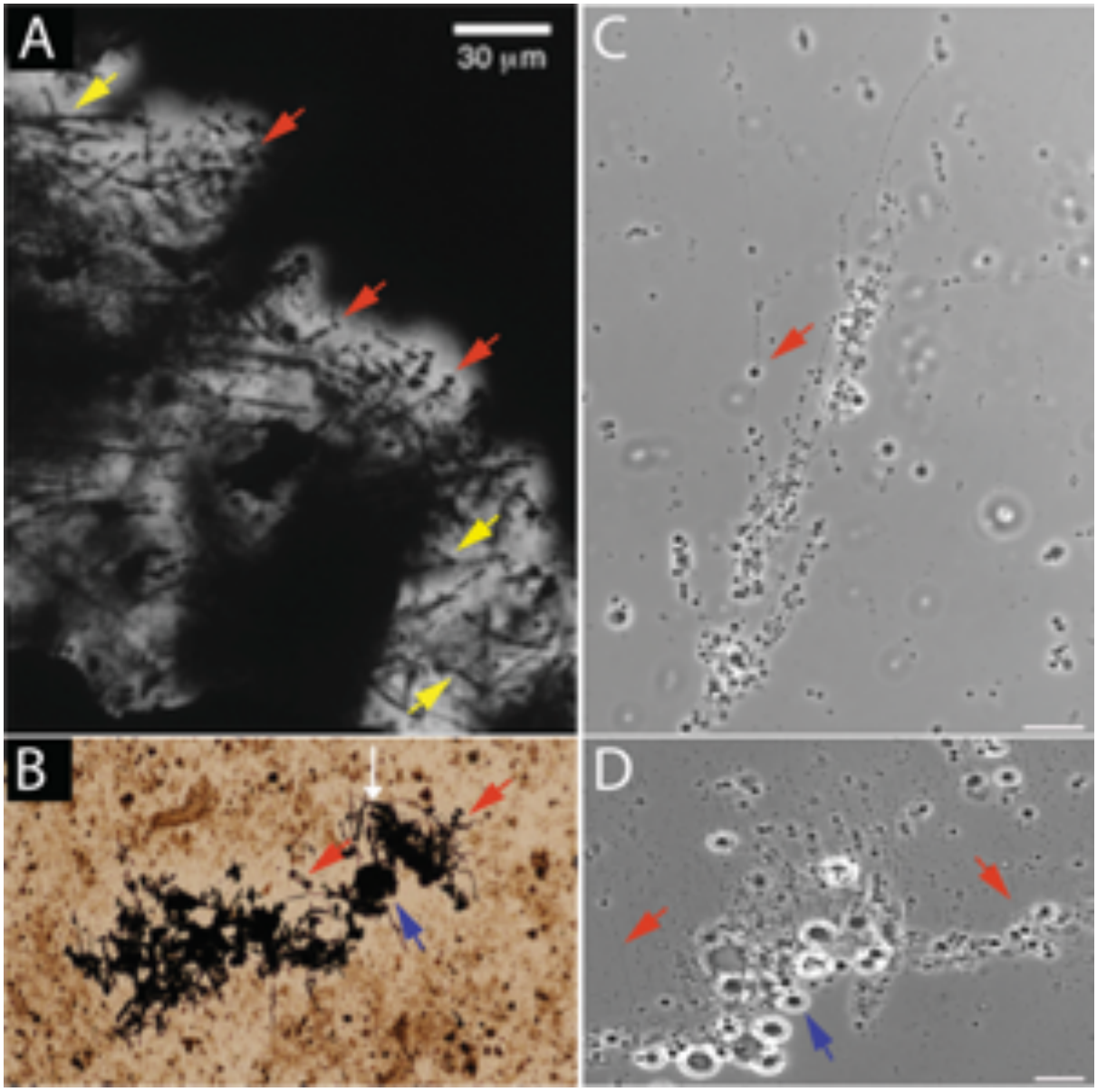

Fig. S35. Morphological comparison between *EM-P* and Sulphur spring formation microfossils

Images A & B are microfossils reported from Sulphur spring formations (Wacey *et al.,* 2014) (35). Red arrows in these images' points to filamentous structures with spherical inclusions.

Purple arrow in image B points to clusters of spherical organic structures from which filamentous structures appear to have originated. Images C & D are morphologically analogous *EM-P* cells. Similar to images A & B, arrows in these images points to filamentous structures with spherical daughter cells (red) and large spherical cells (purple) with filamentous extensions (image B). Scale bars in image C & D are 10µm.

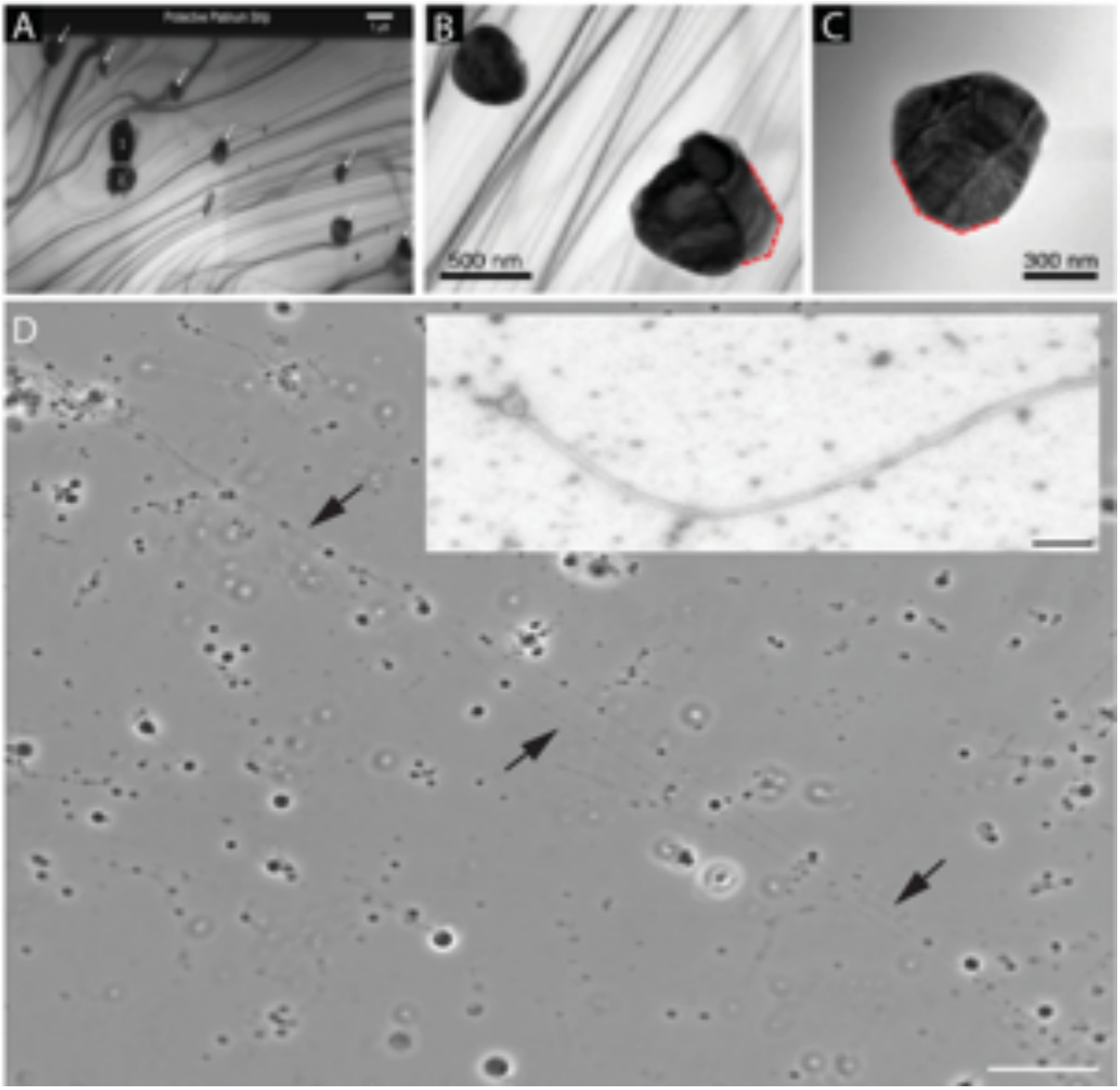

Fig. S36. Morphological comparison between *EM-P* and Sulphur spring formation. microfossils Images A-C are microfossils reported from Sulphur spring formations (Wacey *et al.,* 2014) (35). These microfossils have a filamentous morphology with spherical pyrite

rich inclusions. Image D shows filamentous structures formed by *EM-P*. Arrows in the image points to spherical daughter cells within the filaments. Inset image shows TEM image of such filaments. Scale bar in image C is 10μm and in the inset image is 1μm.

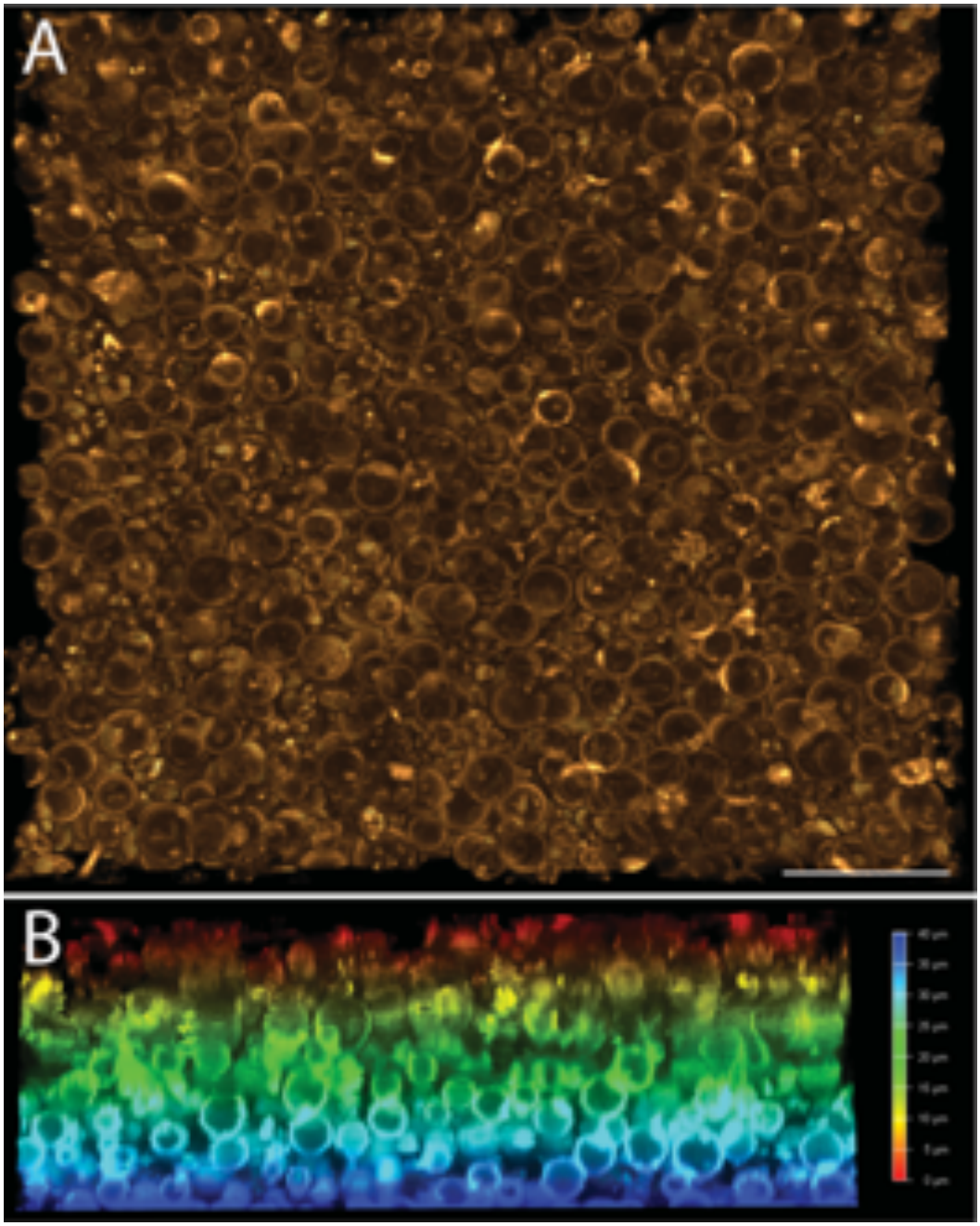

Fig. S37. Multilayered *EM-P* cells

Images A & B shows top and lateral view of *EM-P* cells growing in multiple-layers at the bottom of the chamber slide. Cells in above images were stained with membrane stain,

FM™5-95. Scale bar in the image A is 20µm. Cell-lysis and formation of membrane debris in such layered cells was shown in fig. S39.

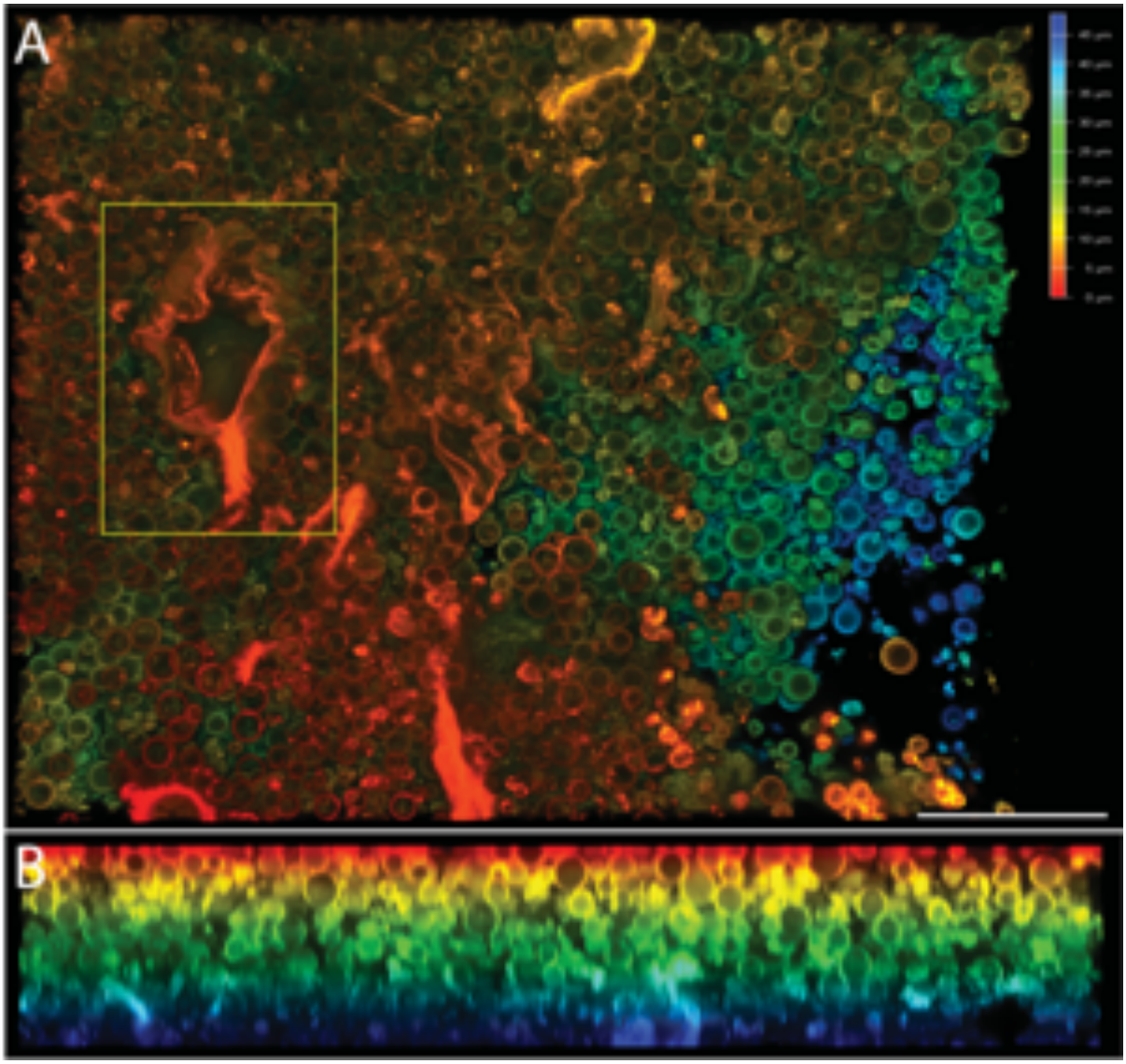

Fig. S38. Lysis and formation of membrane debris within multilayered *EM-P* cells. Images A & B shows top and lateral view of *EM-P* cells growing in multiple-layers at the bottom of the chamber slide. Cells in above images were stained with membrane stain, FM™5-95. Boxed region in image A shows the membrane debris that was being formed from lysis of cells. Scale bar in the image A is 20µm.

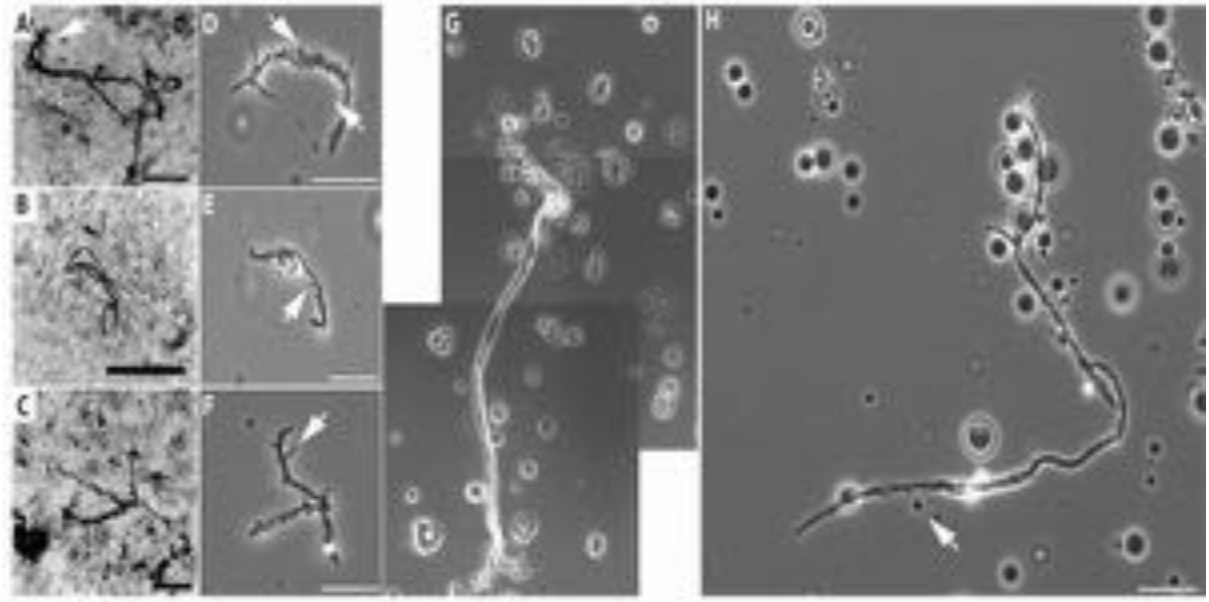

Fig. S39. Morphological comparison between *EM-P* and Mount Grant microfossils. Images A, B & C are organic structures reported from Mount Grant formation (Sugitani *et al.,* 2007) (29). The scale bar in images A-C are 20µm. Images D & H are morphologically analogous *EM-P's* membrane debris. Arrows in the images points to spherical inclusions attached to thread-like membrane debris. Membrane debris in images G & H, should have formed by lysis and collapse of either individual or cluster of large spherical cells of *EM-P* with hexagonal vesicles (fig. S27). Scale bars in images D-H are 10µm.

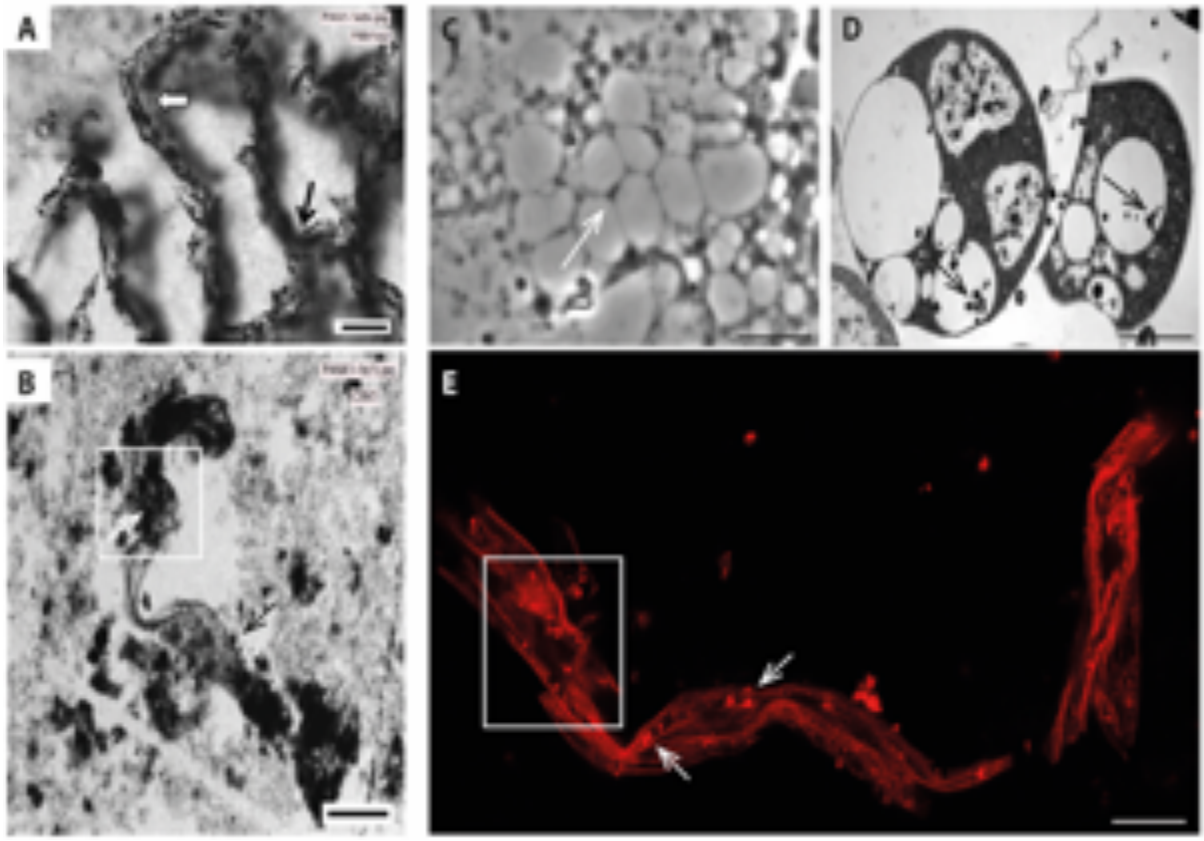

Fig. S40. Morphological comparison of SPF microfossils with *EM-P*.

Images A&B are organic structures reported from SPF (Sugitani *et al.,* 2013) (18). Scale bar in image A & B are 20µm & 50µm respectively. Images C-D are morphologically analogous *EM-P* cells or its membrane debris (E). Duel walled honeycomb like structures could be seen in both images A & C (white arrows). Black arrows in image A & D points to string of spherical daughter cells attached to walls of honeycomb. Boxed regions in images B & E shows similarities between film-like debris reported from SPF and membrane debris observed in *EM-P* incubations. Both these structures have spherical daughter cells with a membrane wrapping. Scale bar in image B is 10µm.

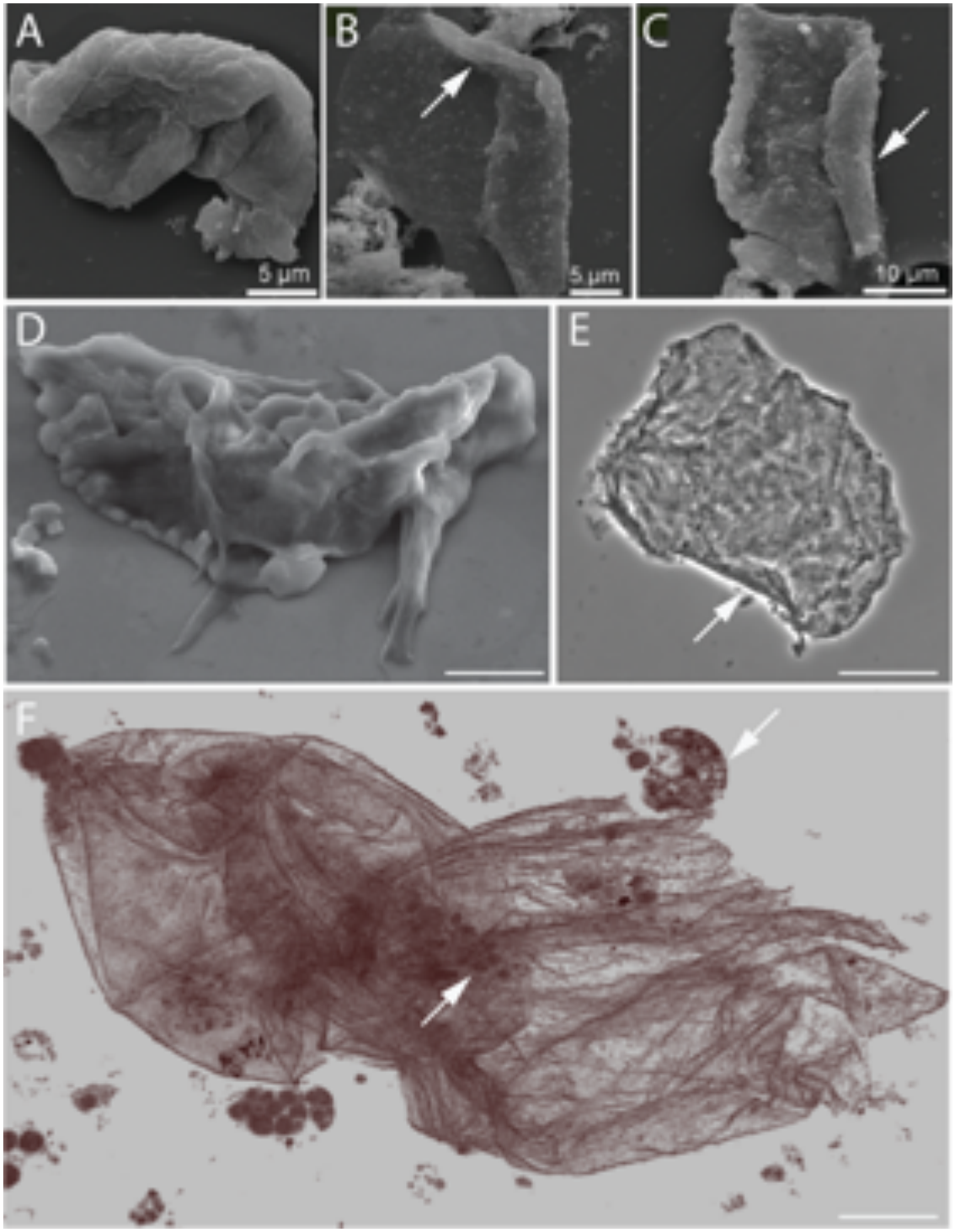

Fig. S41. Morphological comparison between *EM-P* membrane debris and SPF membrane debris.

Images A-C are organic structures reported from SPF formation (Delarue *et al.,* 2019) (17). These images show folded membrane like structures. Images D, E & F are SEM, phase-contrast and 3D-rendered STED images of morphologically analogous *EM-P's* membrane

debris. Arrows in image E points to bending of membrane at the edges, similar to what was observed in case of SPF organic structures. Arrows in image F points to spherical daughter cells of *EM-P* enclosed within the membrane debris. The scale bars in image D, E and F are 2µm, 10µm and 20µm.

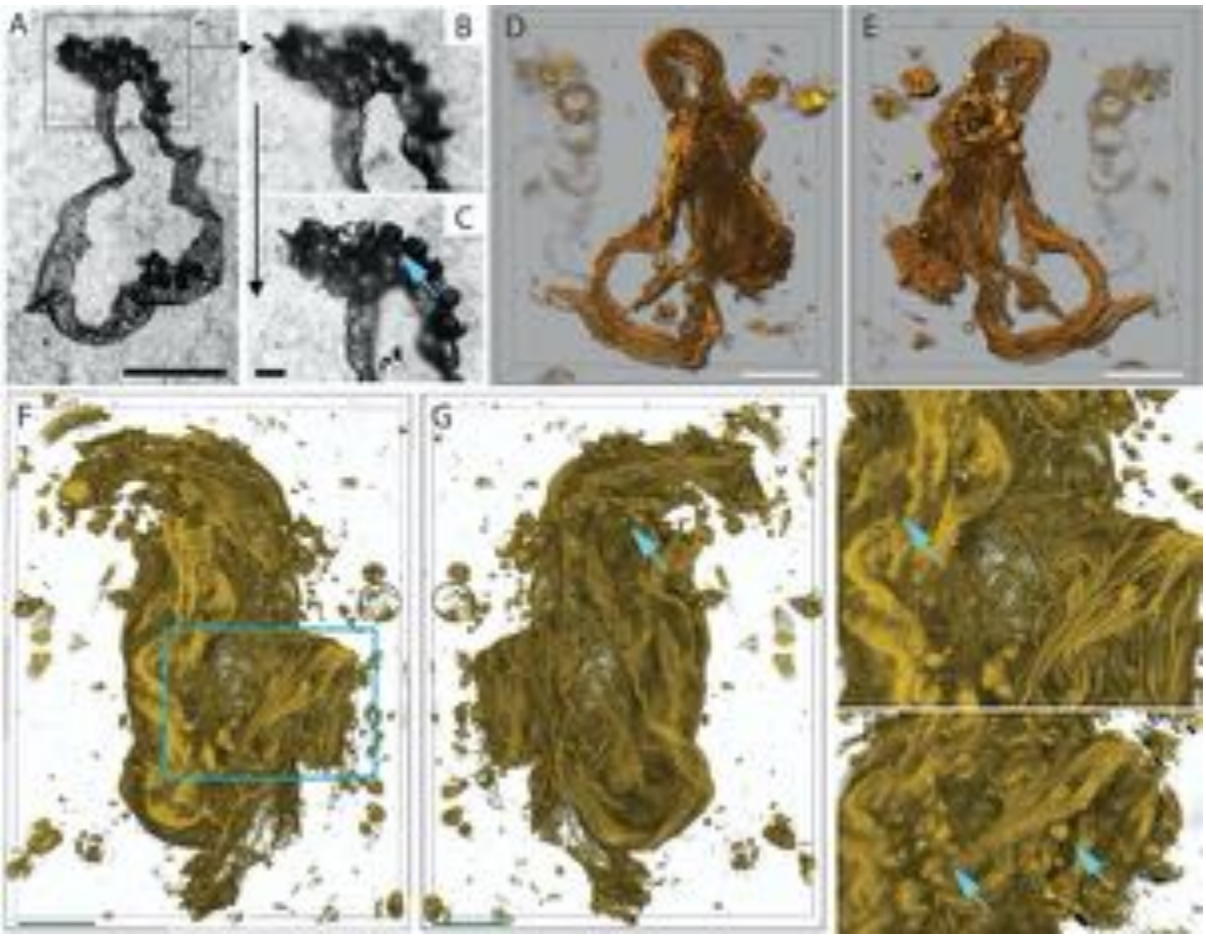

Fig. S42. Morphological comparison between *EM-P* and Goldsworth microfossils. Images A, B & C are organic structures reported from Goldsworthy formation (Sugitani *et al.,* 2007) (29). The scale bar in image A is 50µm. Images D & E are anterior and posterior views of morphologically analogous *EM-P* cells. Both images show film-like membrane with clusters of hollow spherical attachments (Cyan arrows). Images F-I shows flexible film-like

membrane debris of *EM-P* with similar spherical attachments. Scale bars in images F-I are 10μm.

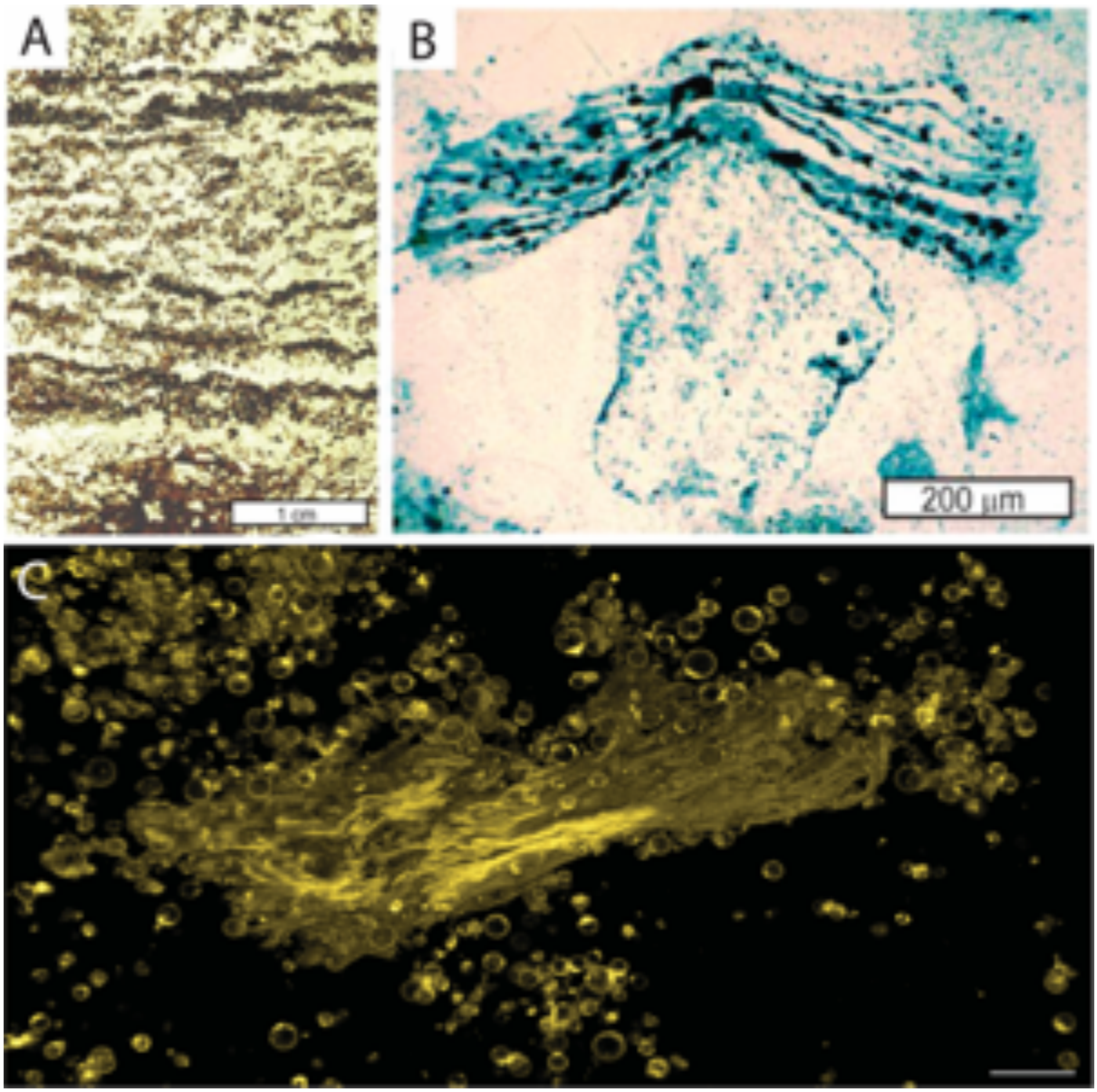

Fig. S43. Morphological comparison between *EM-P* and Farrel quarzite film-like structures.

Images A & B are organic structures reported from Farrel quarzite formation (Retallack *et al.,* 2016) (21). Both images show folded film-like membrane with spherical inclusions. Image C shows wrinkled membrane with spherical cells attached to it, similar in structures to Farrel quarzite microfossils. The scale bar in the image is 20μm.

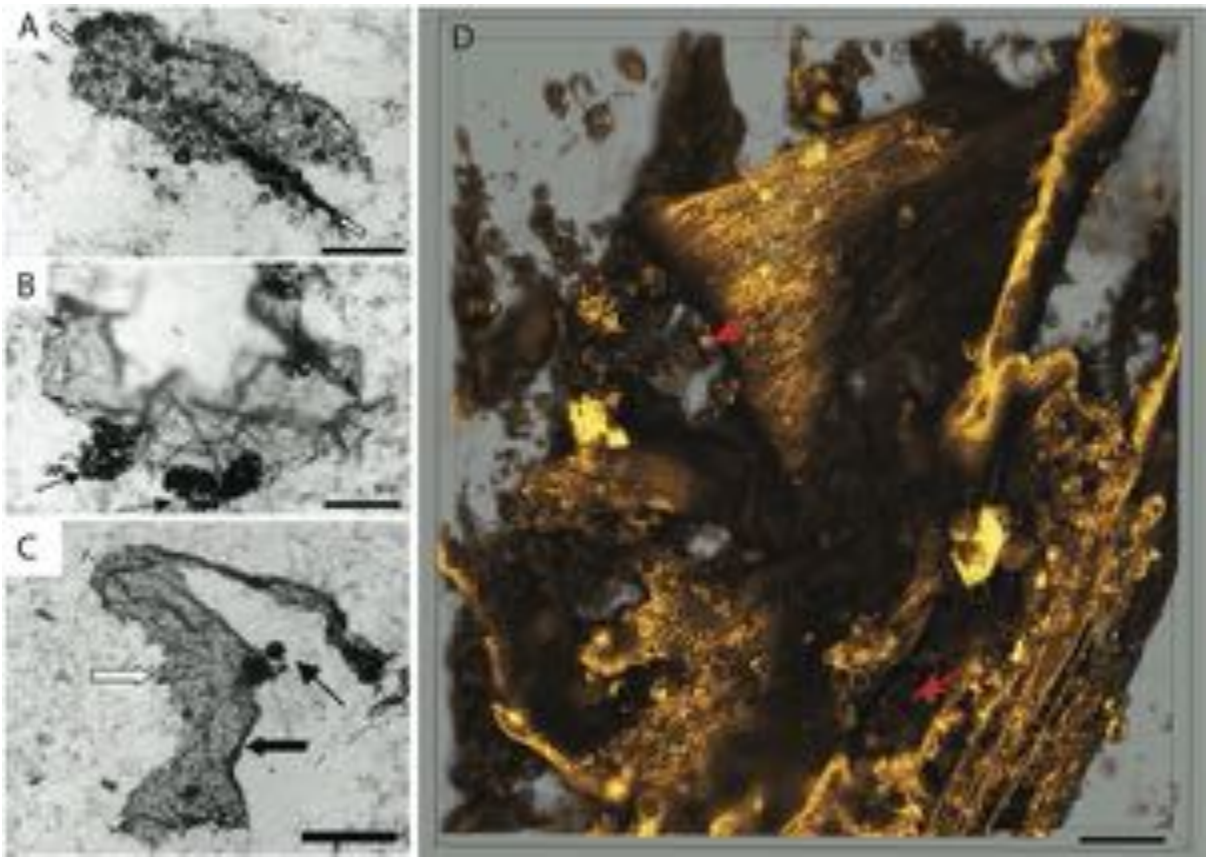

Fig. S44. Morphological comparison between *EM-P* and Goldsworth microfossils. Images A, B & C are organic structures reported from Goldsworth formation (Sugitani *et al.,* 2009) (29). The scale bar in image A-C are 50µm. Images D shows morphologically analogous film-like membrane debris observed in *EM-P* incubations. Arrows in images A-D points to either clusters or individual spherical structures attached to these film-like structures. Scale bar in image D is 10µm.

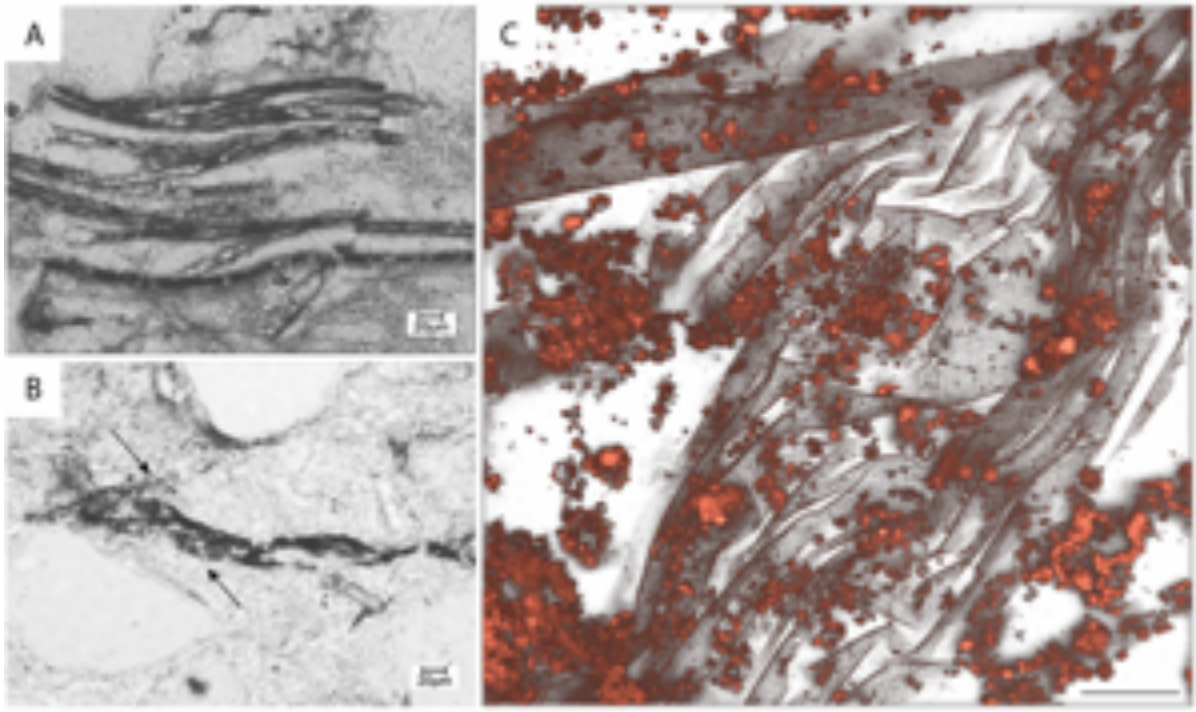

Fig. S45. Morphological comparison between *EM-P* and Moodies microfossils.

Images A & B are organic structures reported from Moodies formation (Kohler *et al.,* 2019) (12). Both images show folded film-like membrane with spherical inclusions (black arrows). Image C shows wrinkled membrane with spherical cells attached to it, similar in structures to Moodies microfossils. The scale bar in the image is 10µm.

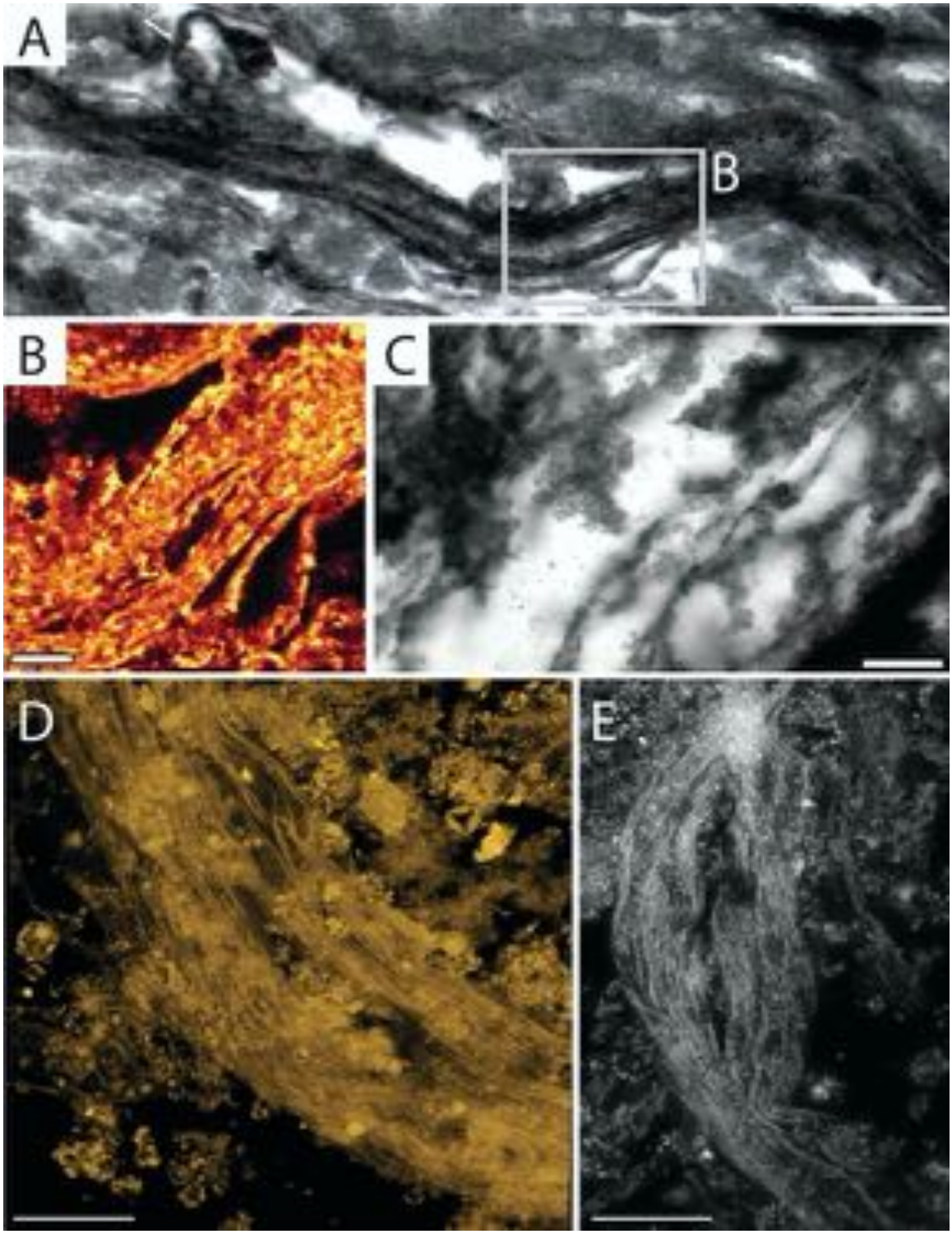

Fig. S46. Morphological comparison between *EM-P* and BRC microfossils.

Images A-C are organic structures reported from BRC formation (Hickman-Lewis *et al.,* 2016) (41). These images show folded over structures with spherical siderite structures attached to it. Image B is the magnified Raman microscope image of region within image A. Bright regions in Image B, indicates carbonaceous matter. The scale bar in these images are

20µm. Image C shows wrinkled *EM-P's* membrane with spherical cells attached to it, similar to BRC microfossils. The scale bar in the image is 20µm.

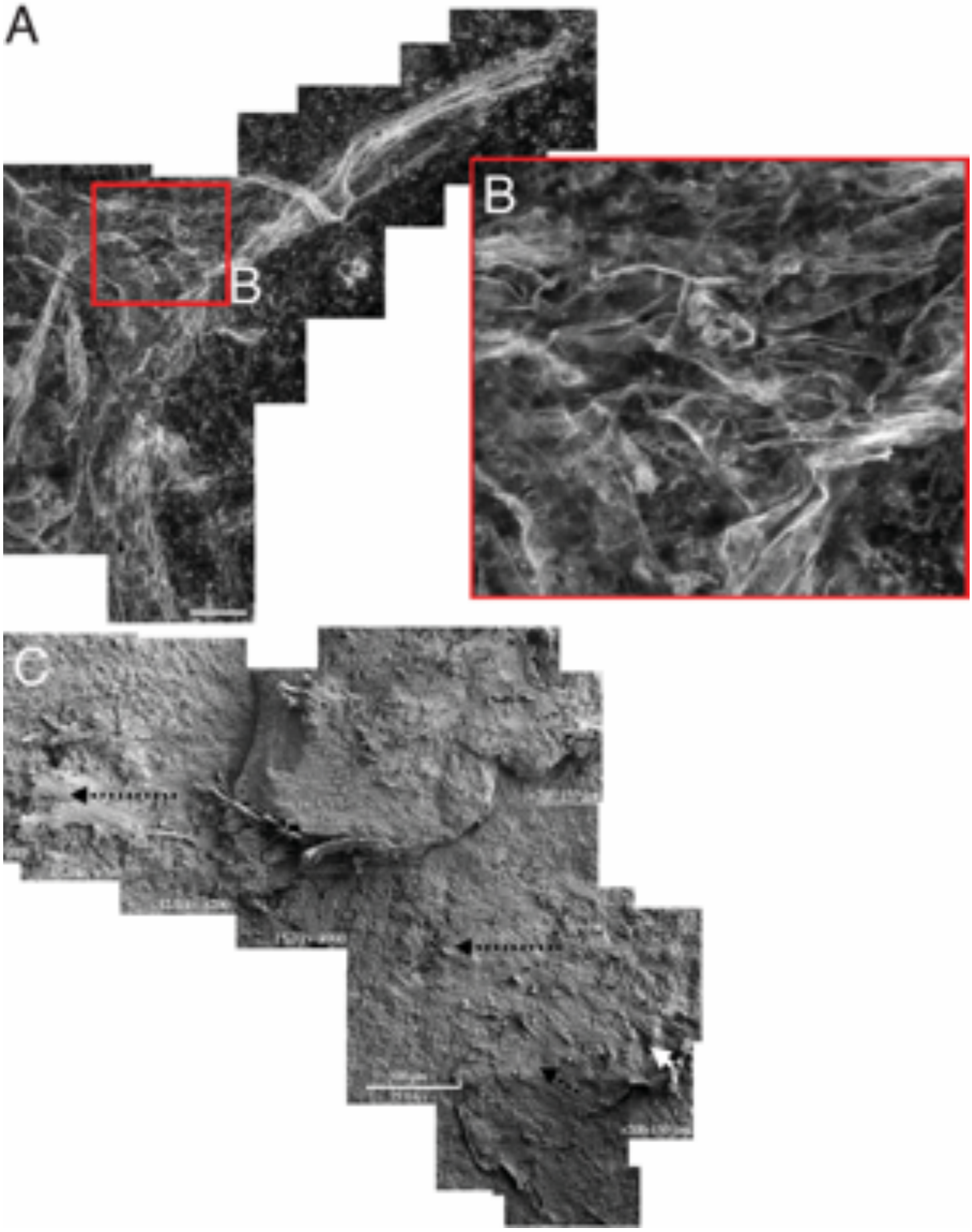

Fig. S47. Morphological comparison between *EM-P* membrane debris and BGB organic structures.

Images A shows a composite confocal images of *EM-P's* membrane debris. Image B is the magnified region of image A shown within the box. Scale bars in image A is 20µm. Image B is film-like organic structures reported from BGB formation (Westall *et al.,* 2006) (39).

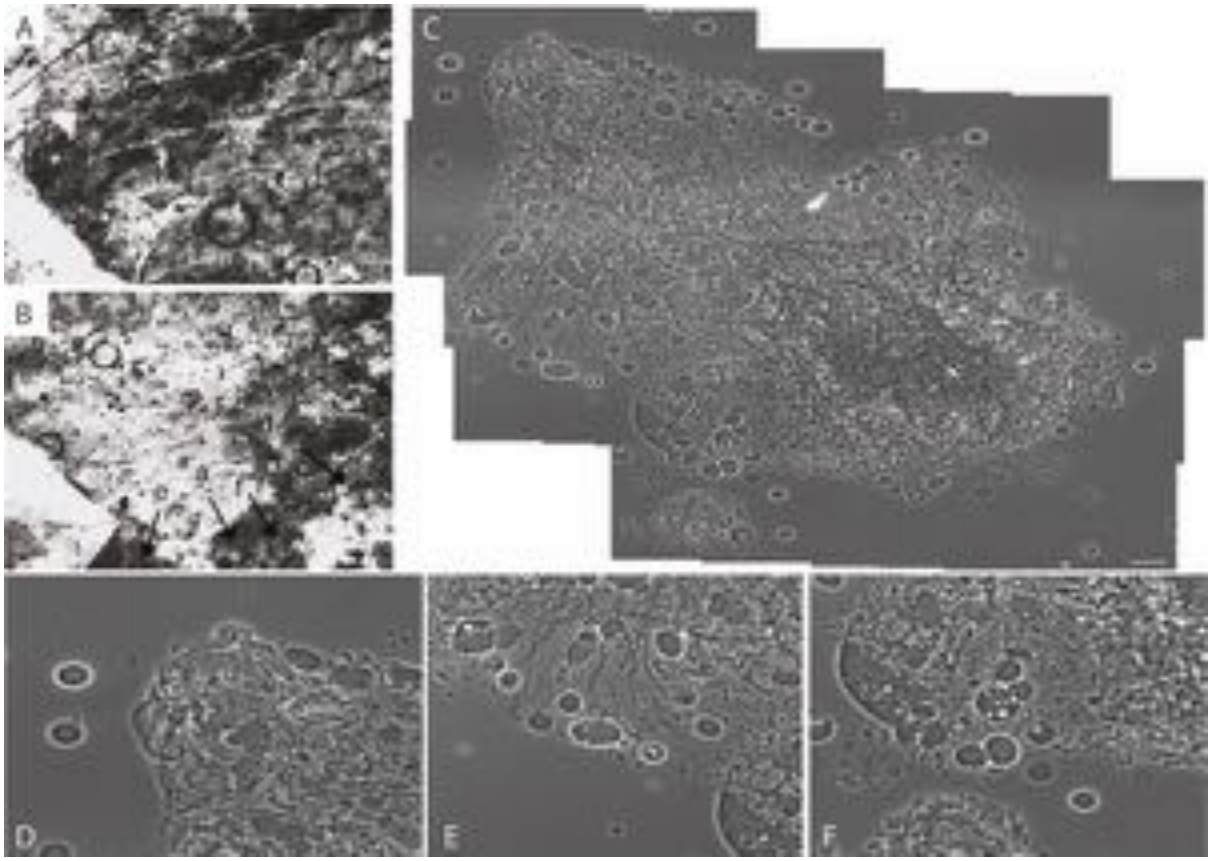

Fig. 48. Morphological comparison between *EM-P* and Chinaman creek microfossils. Images A & B are organic structures reported from Chinaman creek (Brasier *et al.,* 2005) (40). Images C composite image of morphologically analogous *EM-P* structures. Images D-F are magnified regions of image C. Scale bar in image C is 10µm. All the images show spherical structures with or devoid of organic carbon, enclosed in a film-like structure.

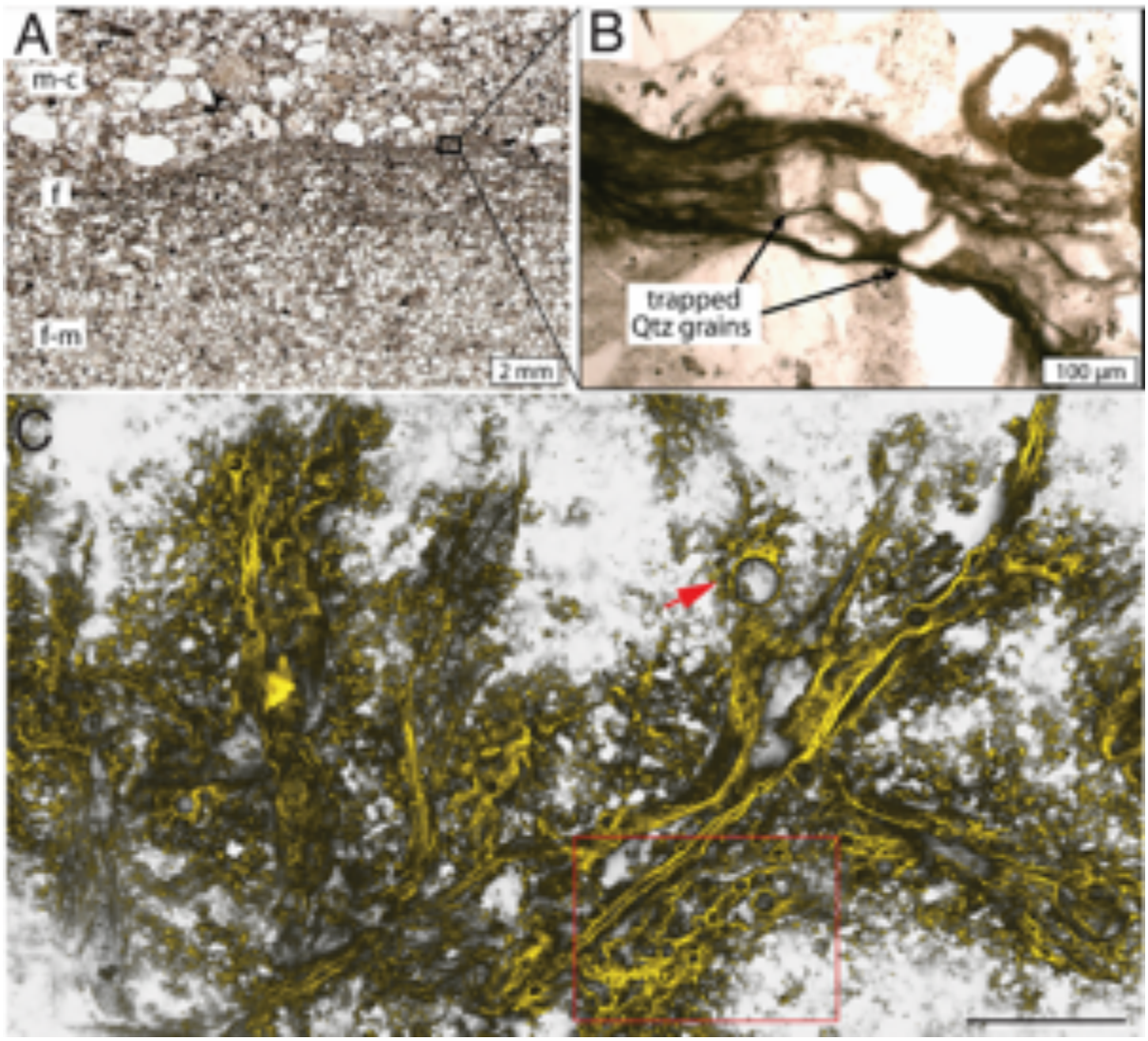

Fig. 49. Morphological comparison between laminated structures reported from Moodies group and structures formed by *EM-P*.

Images A&B are laminated structures reported from Moodies group (Homann *et al.,* 2015) (38). They show filamentous structures with lenticular gaps. These gaps were filled with quartz granules. Image C is a 3D rendered confocal image of *EM-P*'s membrane debris. Filamentous membrane debris bifurcating leading to the formation of spherical\lenticular gaps can be seen in several regions. Some spherical\lenticular gaps, were observed to be hollow (box) and some had honeycomb pattern within them (arrow), indicating the presence of large spherical *EM-P* cells with intracellular vesicles. 3D rendered STED microscope

image of individual spherical\lenticular gaps with and without *EM-P* cell debris were shown as fig. S51 and S52. Membranes were stained with Nile red and imaging was done using a STED microscope. Scale bar is 50µm.

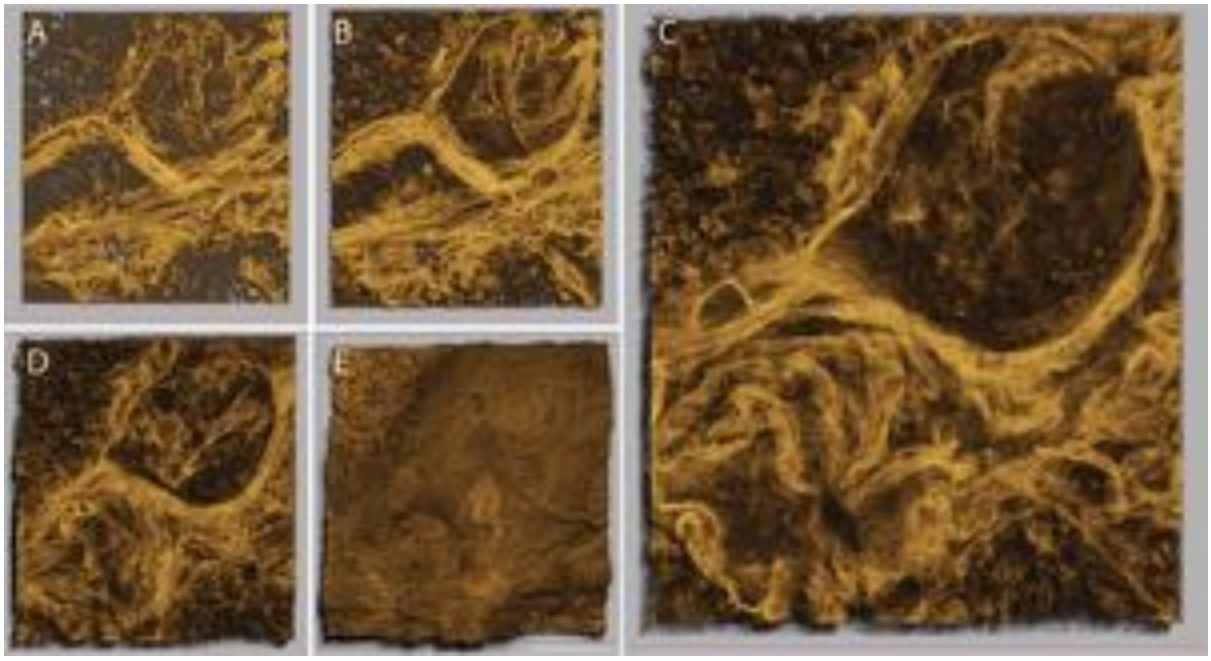

Fig. 50. Lenticular membrane debris of *EM-P*.

Images A-E show different layers of membrane debris from bottom (A) to the surface (E). Membranes were stained with Nile red and imaging was done using a point scanning microscope. Scale bars in image C is 20µm. Parallel layers of membrane debris can, like the ones reported from BRS formation can be seen in images A&B. Image C shows a large lenticular gap with honeycomb shaped imprint, which suggests past presence of a large lenticular *EM-P* cell at this location. Similar images were shown as fig. S56.

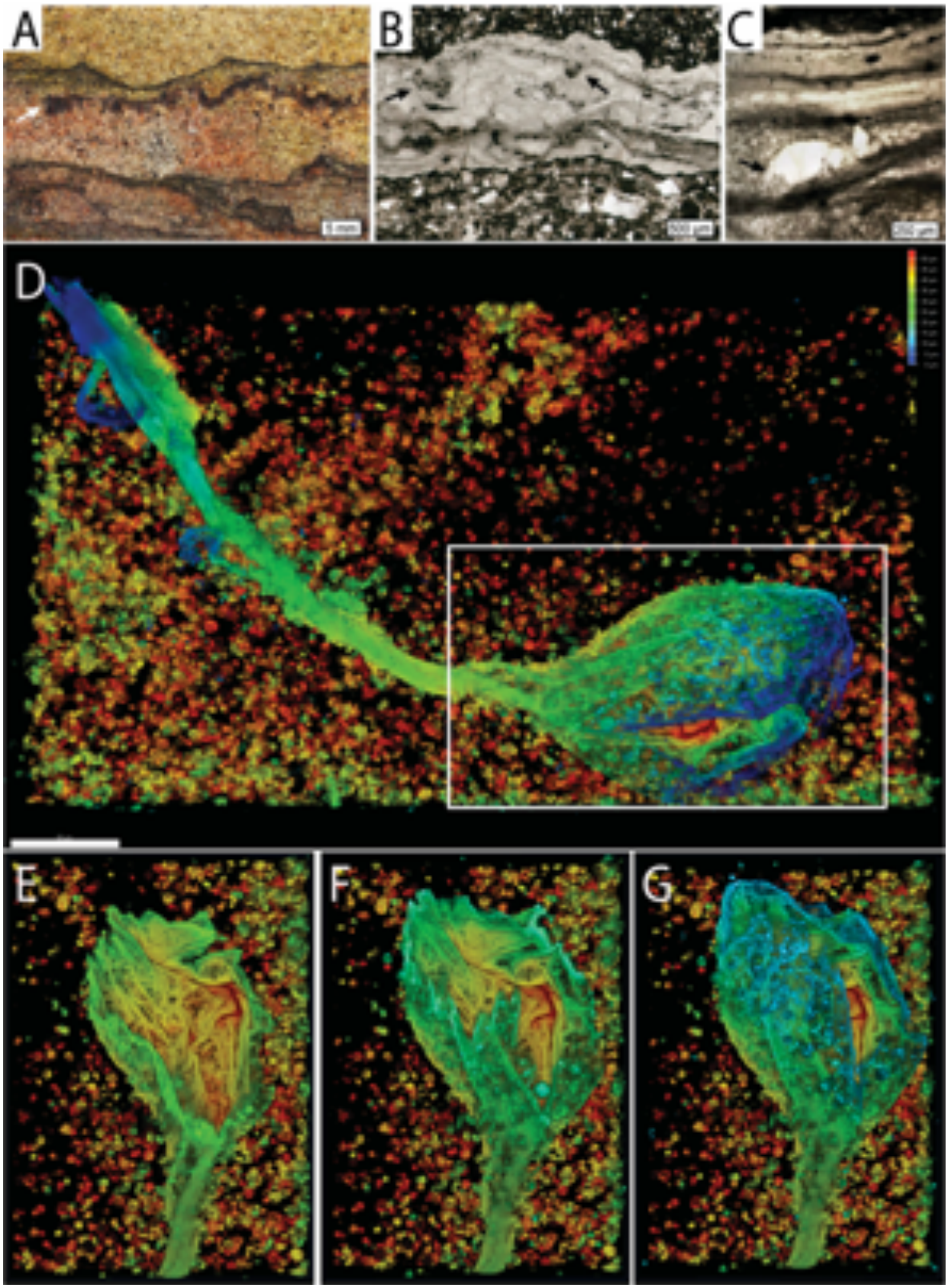

Fig. S51. Morphological comparison of Moodies laminations with *EM-P's* membrane debris.

Image A-C shows laminations reported from Moodies formations (Homann *et al.,* 2015) (38). Image D is 3D rendered image of *EM-P*'s membrane debris exhibiting hollow lenticular gaps. Images E-G show the hollow lenticular structure at different Z-axis positions. Membranes were stained with Nile red and imaging was done using STED microscope. Scale bar: 50µm.

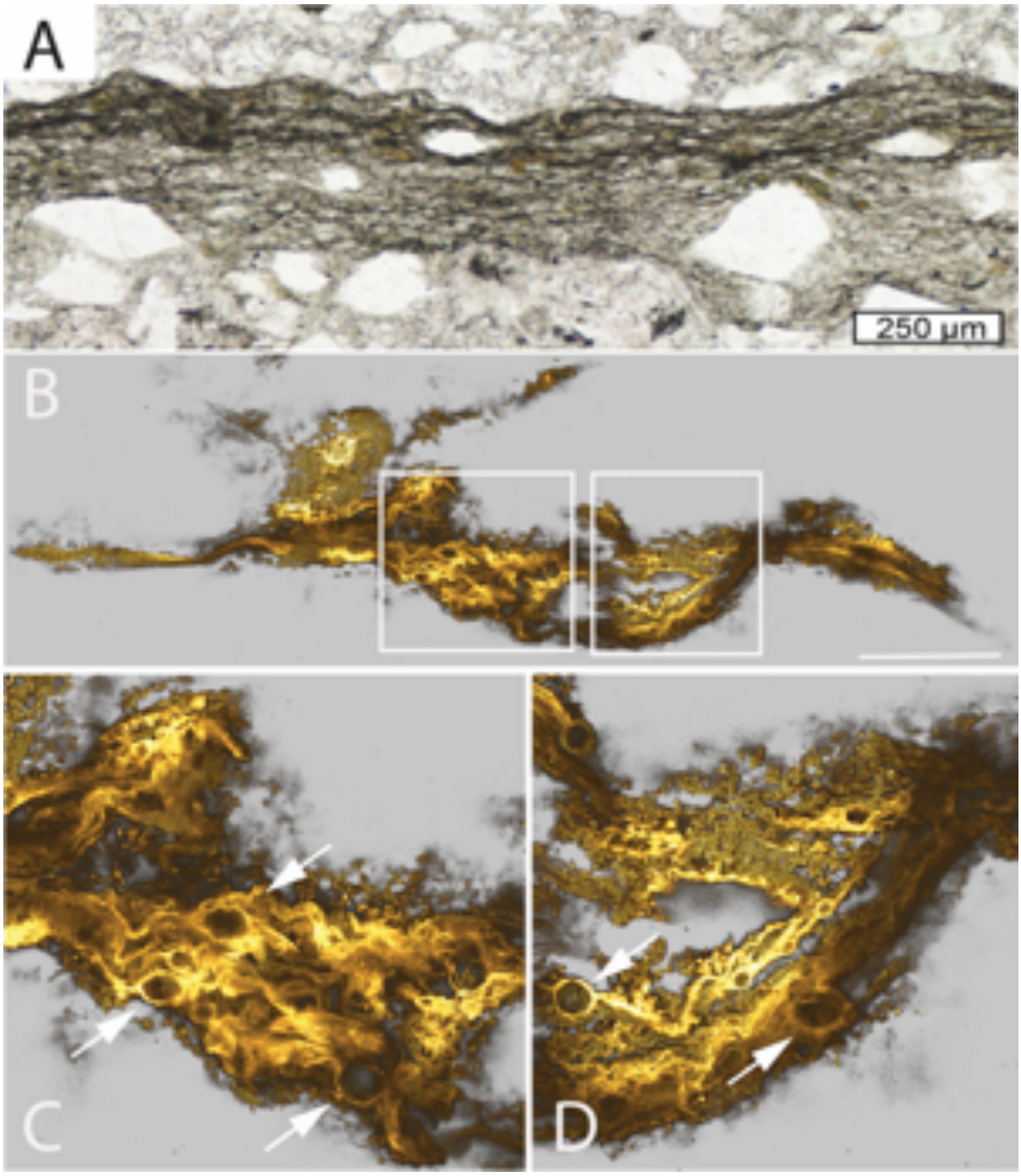

Fig. S52. Morphological comparison of Moodies laminations with *EM-P's* membrane debris.

Image A shows α-type laminations reported from Moodies formation (Homann *et al.,* 2015) (38). Image B is a 3D rendered confocal image of *EM-P*'s membrane debris. Images C&D are magnified regions of membrane debris shown in image B. Arrows in images C & D points to lenticular gaps within the membrane debris. Scale bar in image B is 20μm.

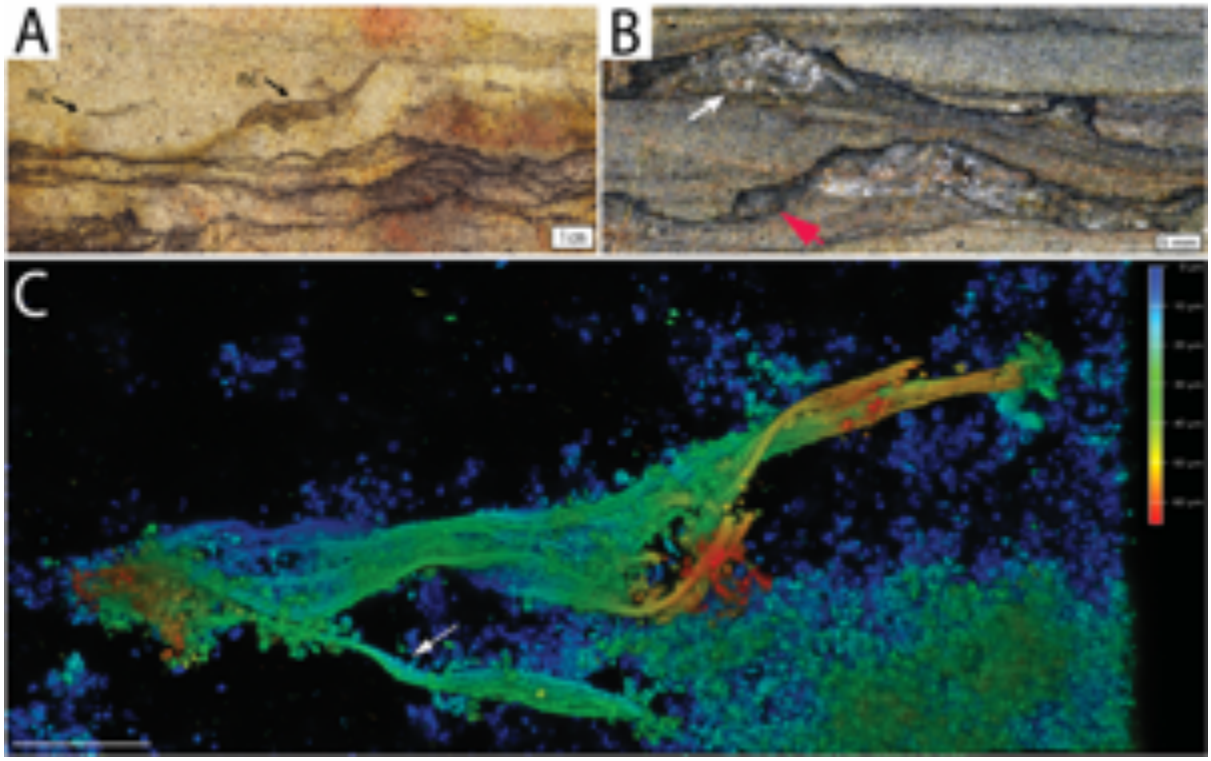

Fig. 53. Morphological comparison of *EM-P* Membrane debris with laminated structures.

Images A&B show bifurcating laminated structures reported from Moodies formation (originally published by Homann *et al.,* 2015). Image C is a 3D-rendered image of morphological analogous *EM-P*'s membrane debris. White arrows in image B points to hollow lenticular regions within the laminations, similar to the one observed in *EM-P* (Fig.

4,5&6). Arrows in images A & C points to bifurcation of membrane debris. Membranes were stained with Nile red and imaging was done using a point scanning microscope. Scale bar in image C is 50µm.

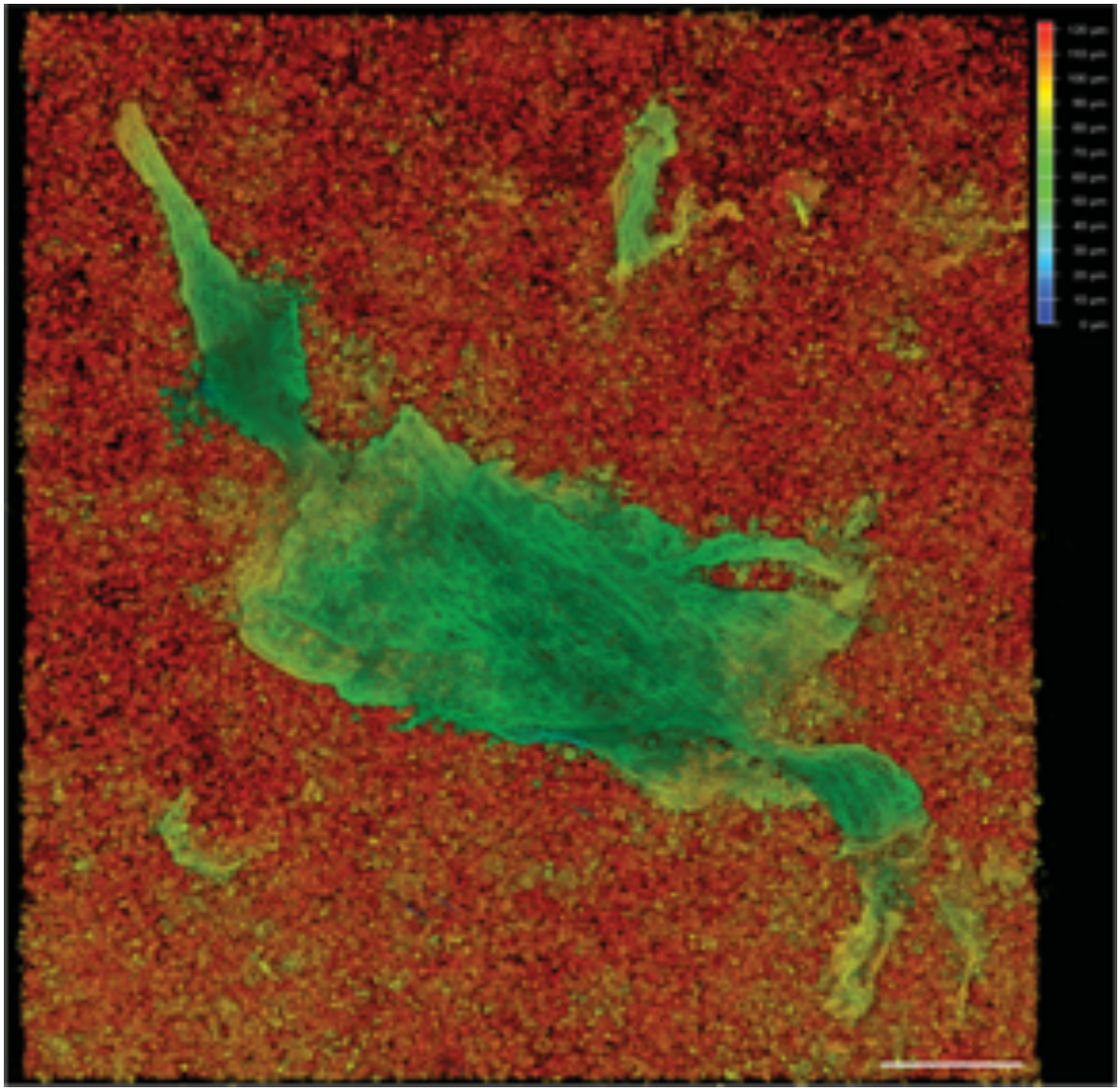

Fig. S54. Membrane debris of *EM-P*.

Image shows membrane debris of *EM-P* forming a layer over a mat of multilayered cells. Based on the morphological similarities with laminated structures, we presume, such structures were formed by a similar process. Lateral view of the image along with its

morphological comparison with α-type laminations reported from BRC was shown as fig. S54. Membranes were stained with Nile red and imaging was done using confocal microscope. Scale bar in image B is 100μm.

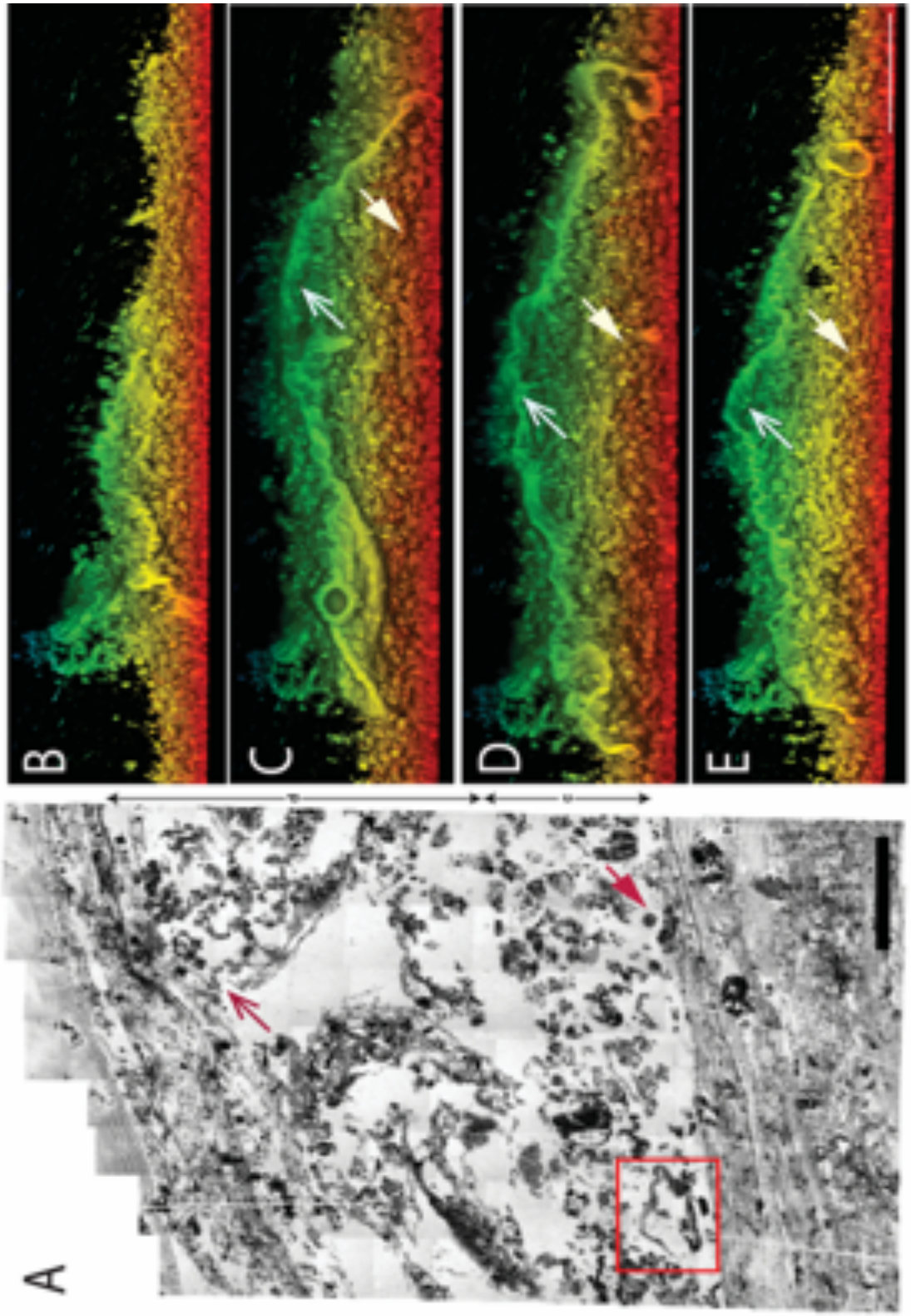

Fig. S55. Morphological comparison between BRC laminations and membrane debris of *EM-P*.

Image A shows α-type laminations reported from BRC (Tice *et al.,* 2009) (27). Two filamentous layers with hollow space between than can be seen in image A. The hollow space in-between is filled with filamentous membrane debris and spherical inclusions. Scale bar in image is 5mm. Images B-E show lateral sections of *EM-P* membrane debris shown in fig. S53. Scale bar in image B is 100μm. Open and closed arrows in all the images points to top layer of membrane enclosure and bottom cell-layer respectively. Hollow space in-between is filled with both membrane debris and spherical cells. We presume lysis of these cells could have produced membrane debris like the ones observed in image A. In support of this presumption, membrane debris very similar to β-type laminations (indicated by red box) was observed in *EM-P* batch cultures (shown in fig. S55-S59).

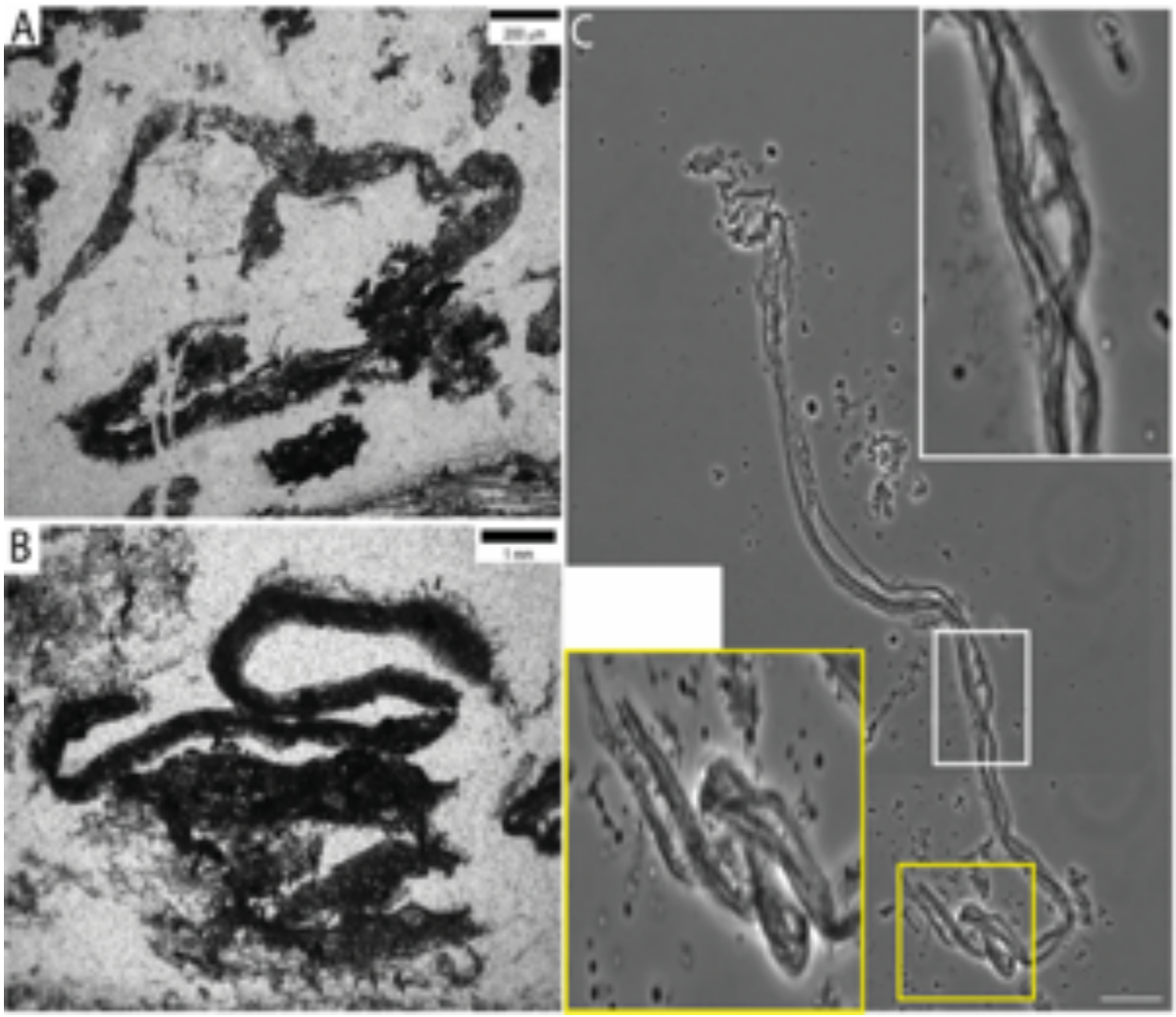

Fig. S56. Morphological comparison of BRC β-laminations with *EM-P's* membrane debris.

Images A & B show β-type laminations reported from BRC (Tice *et al.,* 2009) (27). These laminations are described as rolled-up or bundled filamentous structures. Image C shows morphologically analogous *EM-P's* membrane debris. Insets in image C are magnified regions of the debris showing bundled-up individual filamentous structures. Scale bars in image C is 10μm.

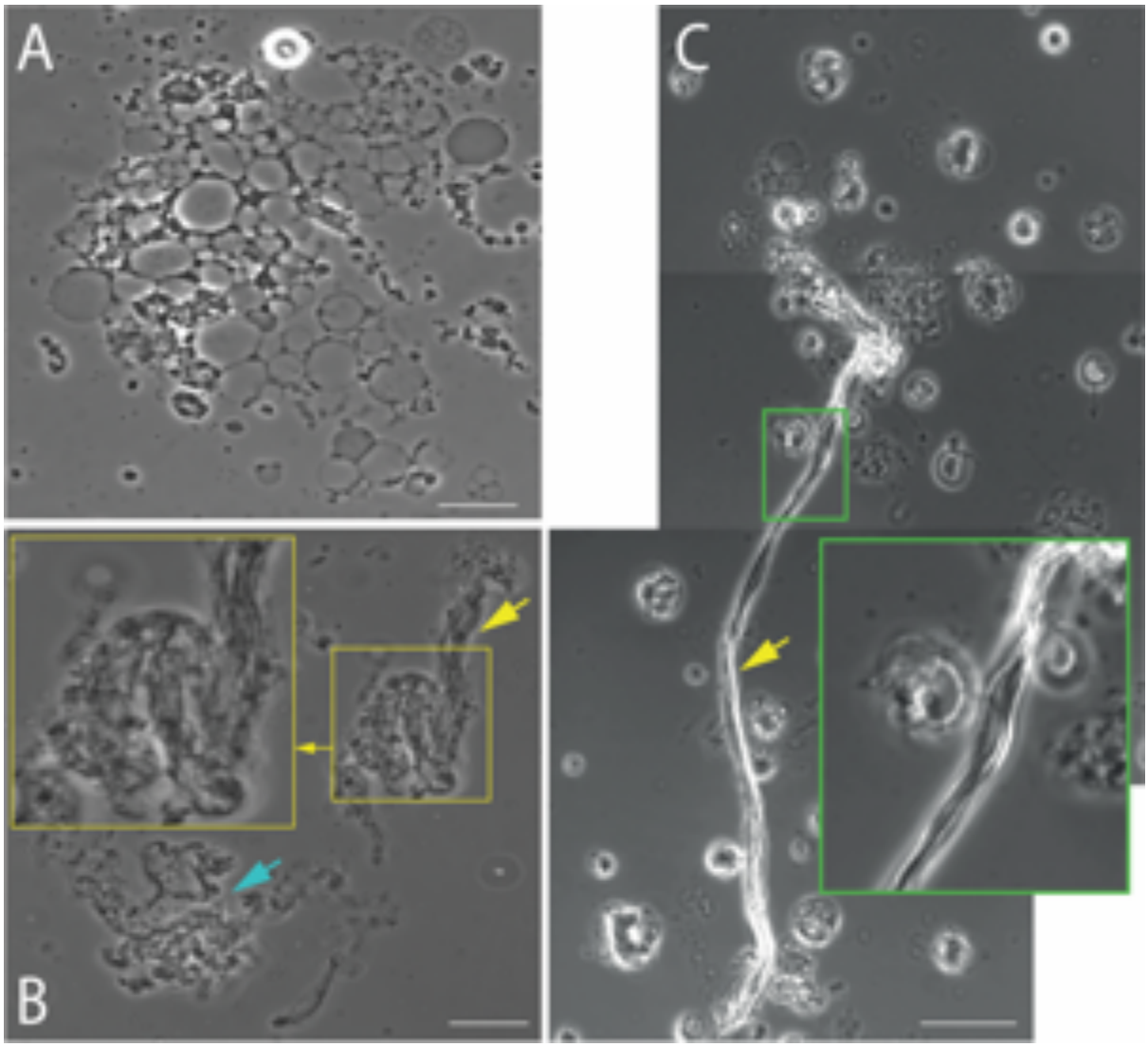

Fig. S57. Sequential stages involved in formation of β-laminations.

Images A-C shows steps involved in sequential transformation of membrane debris to β-type laminations. Image A show aggregation of vacuoles formed from lysis of large spherical *EM-P* cells. Image B shows collapsed membrane debris formed by lateral compression or deflation of such aggregations after release of daughter cells (Movie S10). Cyan and yellow arrows points to membrane debris and compressed membrane debris respectively. Inset in image B is the magnified region of compressed membrane debris. Image C shows structures similar to β-type laminations. Scale bars:10μm.

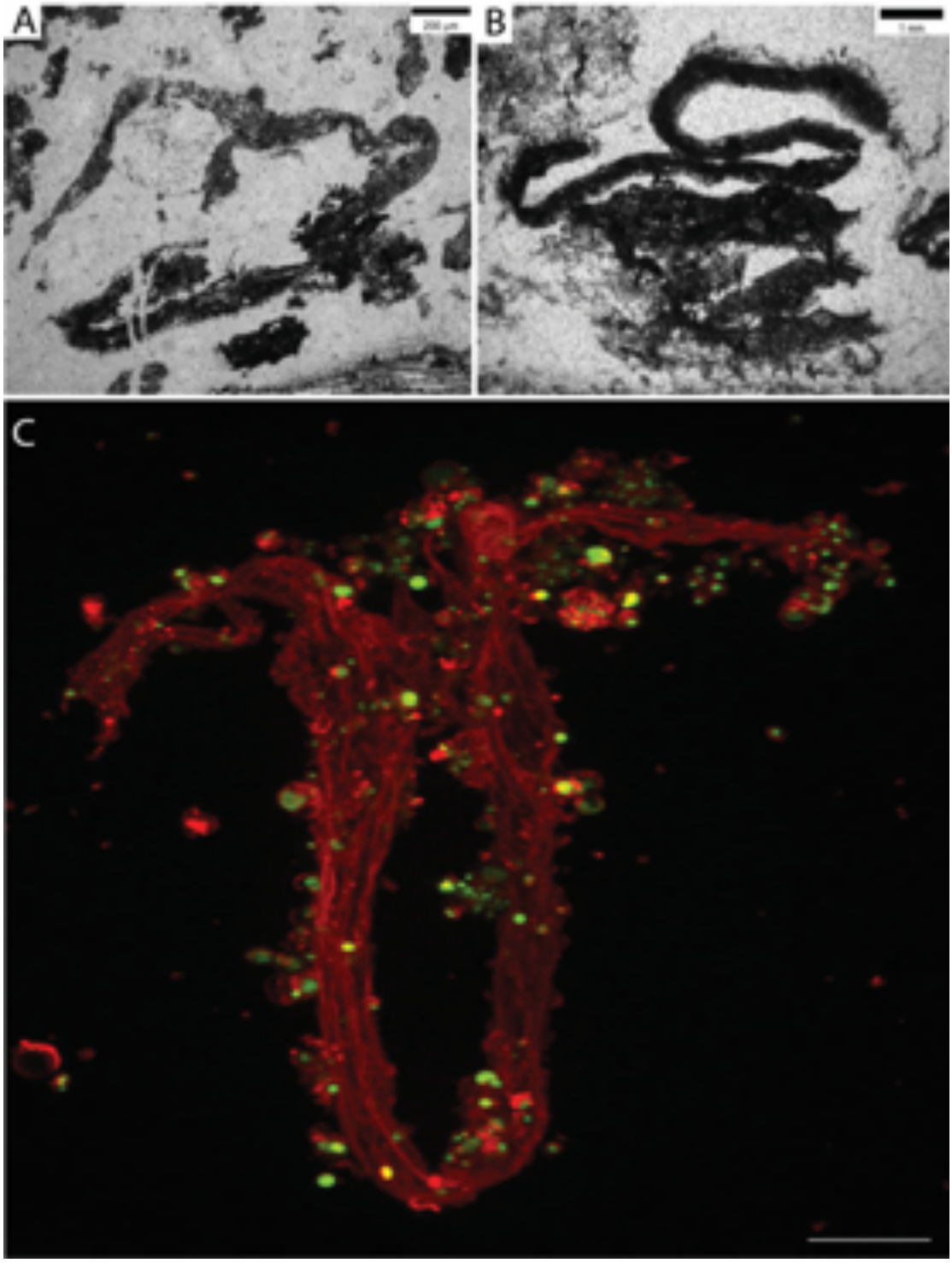

Fig. S58. Morphological comparison of BRC β-laminations with *EM-P's* membrane debris.

Images A & B show β-type laminations reported from BRC (Tice *et al.,* 2009) (27). Image C shows Super-resolution confocal image of morphologically analogous *EM-P's* membrane

debris. In the image membrane was stained with FM5-95 (red) and DNA is stained with PicoGreen (green). Scale bars in all images are 10μm.

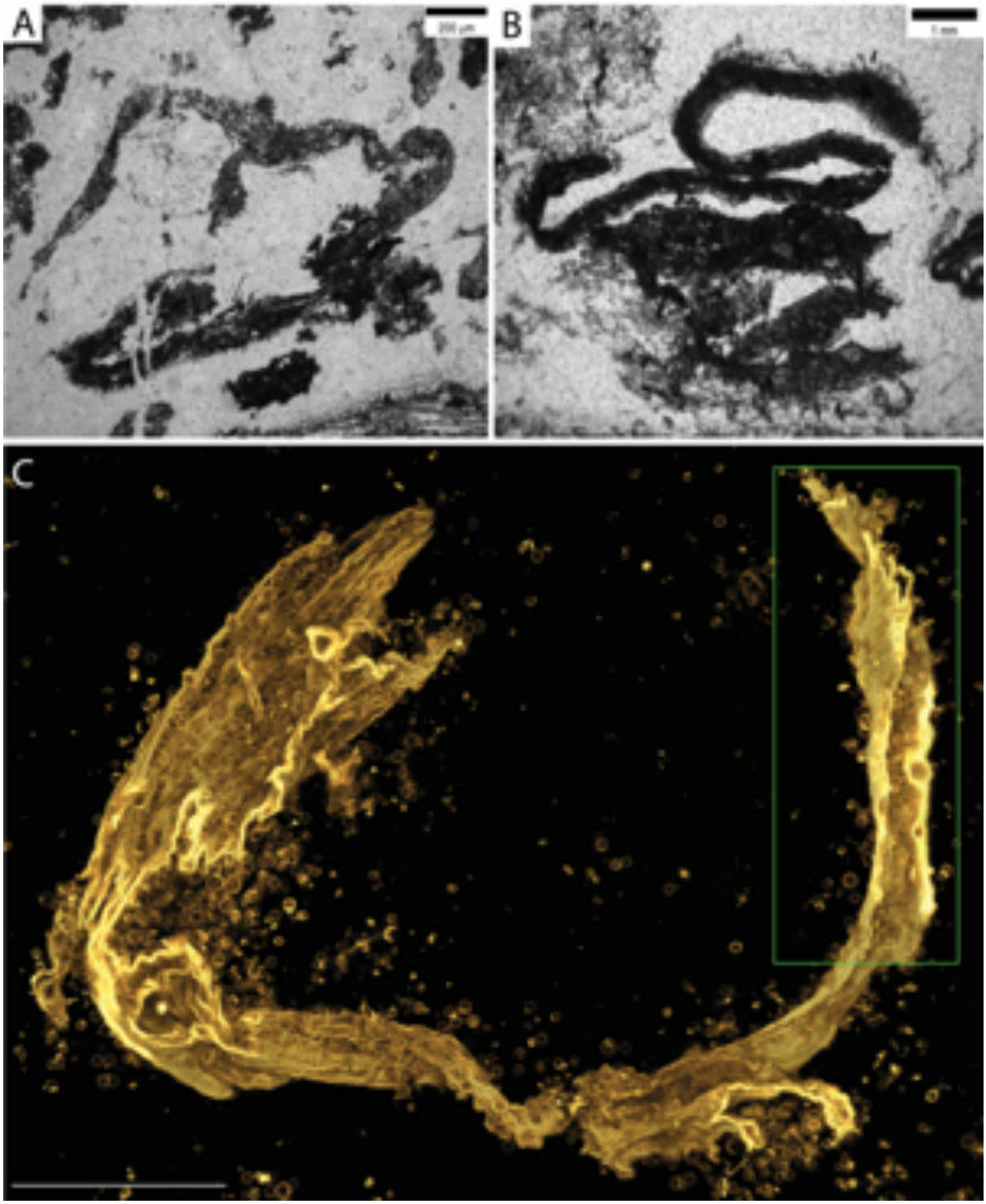

Fig. S59. Morphological comparison of BRC β-laminations with *EM-P's* membrane debris.

Images A & B show β-type laminations reported from BRC (Tice *et al.,* 2009) (27). Image C shows confocal image of morphologically analogous *EM-P's* membrane debris. In the image membrane was stained with Nile red. Boxed region in image C, highlights the membrane forming rolled-up structures, like described in case of BRC organic structures. Scale bars: 50μm.

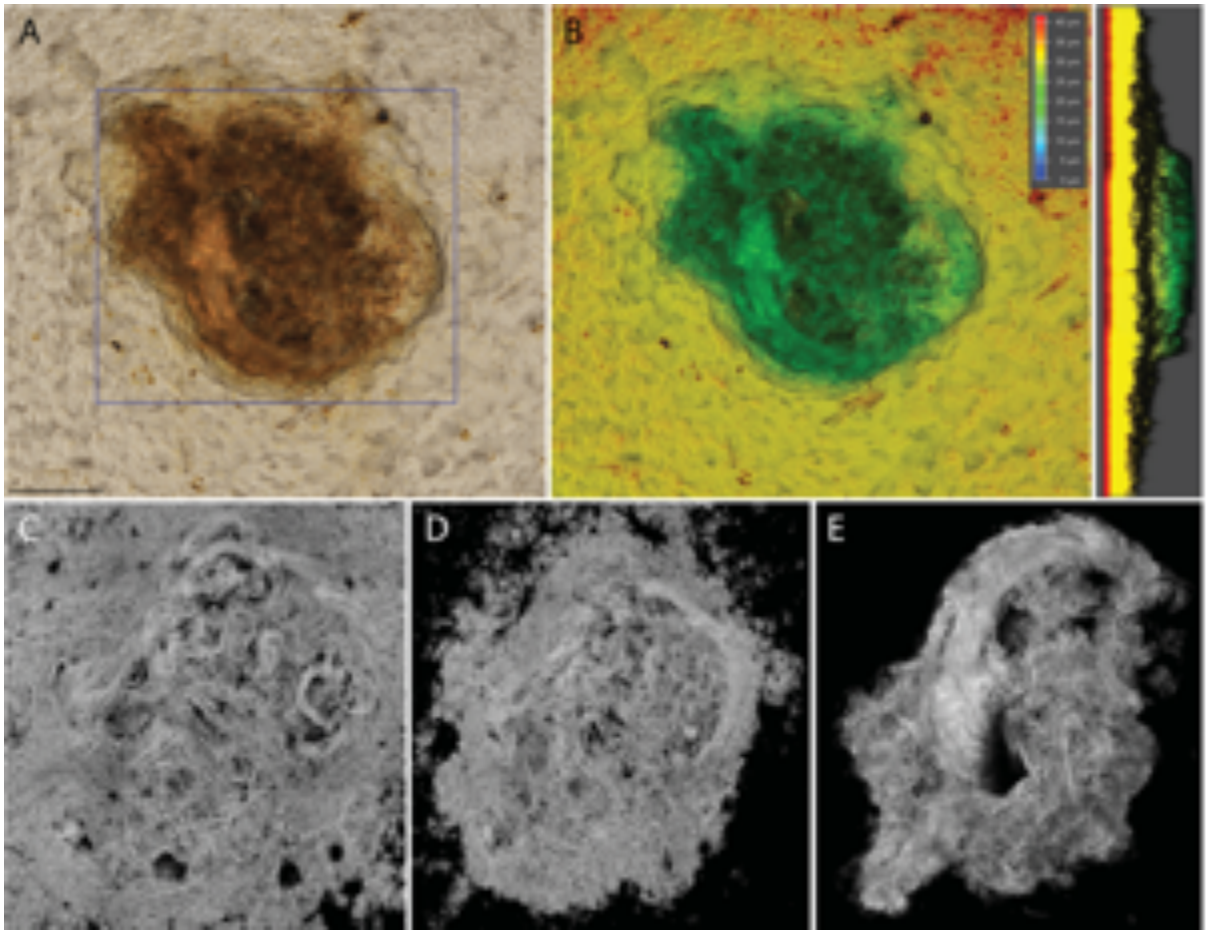

Fig. S60. swirl-like structures of *EM-P*'s membrane debris.

Images A-F shows a 3D-rendered confocal image of later stage membrane debris shown in fig. S52 & S53 as a result of complete cell lysis. This debris typically formed raised mound like structures. Images A&B show top view of such structures and Image C shows the side-view. Images C-E are images of such mounds at different depths (bottom to top). Formation

of swirls can be seen in images D & E. In the image membrane was stained with Nile red. Scale bar in the image A is 50µm. Morphological comparison of these structures with Archaean laminations was shown in fig. S61.

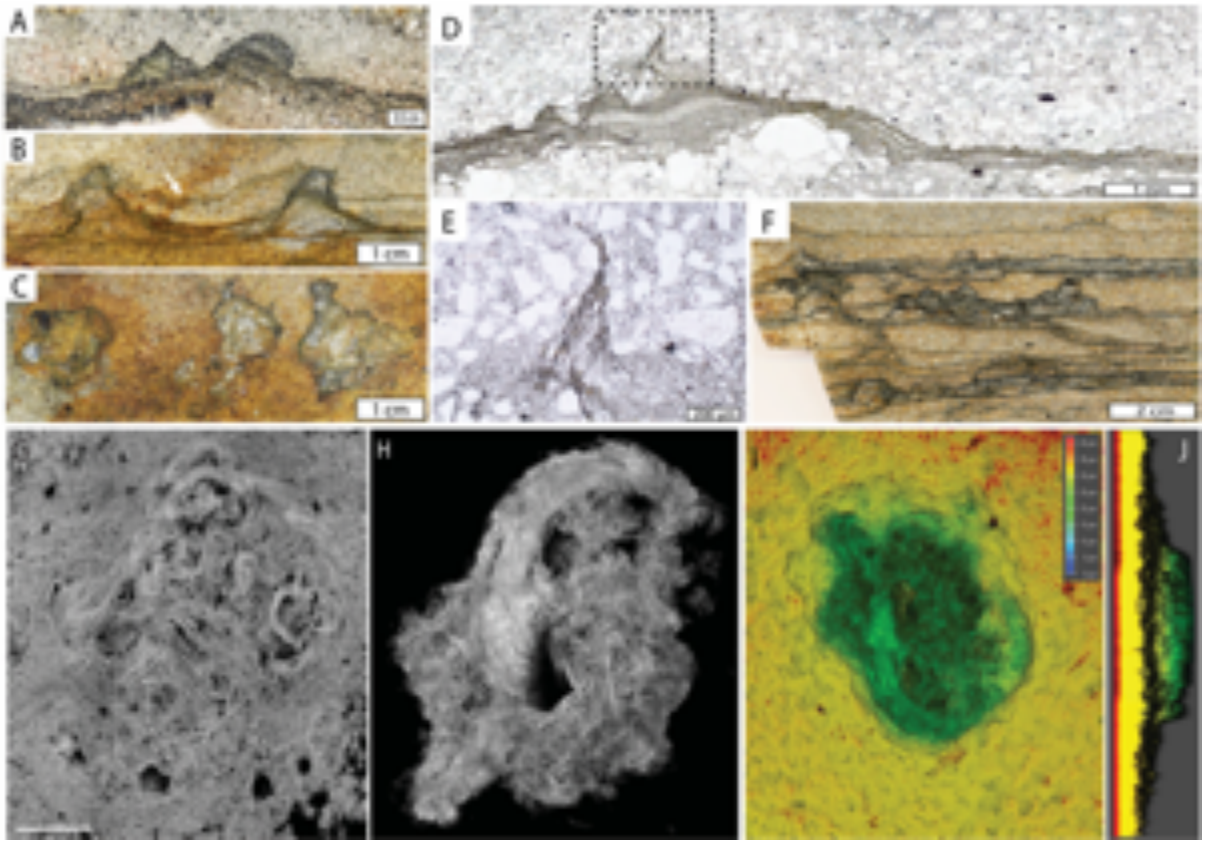

Fig. S61. Morphological comparison of Moodies laminations with *EM-P's* membrane debris.

Images A-F show raised mound like structures reported from Moodies formations (Homann *et al.,* 2015) (38). Image C shows top view of such mounds. These mounds were shown to have filamentous extensions at their peaks. Images G-I are morphologically analogous structures formed by *EM-P*. In the image membrane was stained with Nile red. Scale bar in the image A is 50µm.

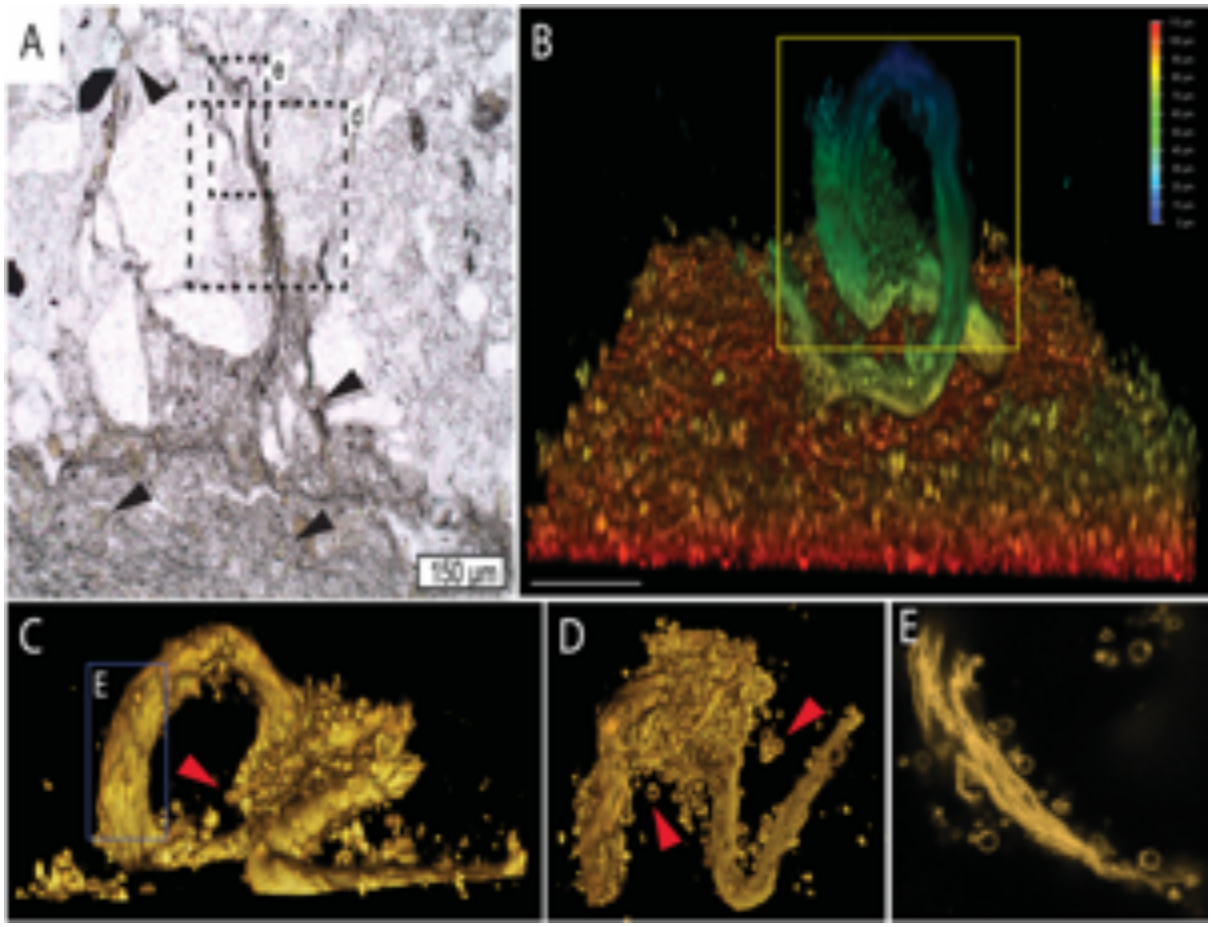

Fig. S62. Morphological comparison of BRC β-laminations with *EM-P's* membrane debris.

Images A show β-type laminations reported from Moodies formation (Homann *et al.,* 2015) (42). Laminations from Moodies formation were shown to form raised filamentous structures, like shown in image A. Arrows in the image points to spherical structures within the laminations. Images B-E shows 3D-rendered confocal images of morphologically analogous *EM-P's* membrane debris. Image B show filamentous membrane debris of *EM-P*, that rose above layers of spherical cells. Images C & D are close-up images of raised filamentous membrane debris of *EM-P* form different angle of viewing. Arrows in these images points to spherical cells that were attached to the membrane debris. Image E is a non-3D rendered

image showing individual strands of membrane within the debris. Scale bar in image B is 20µm.

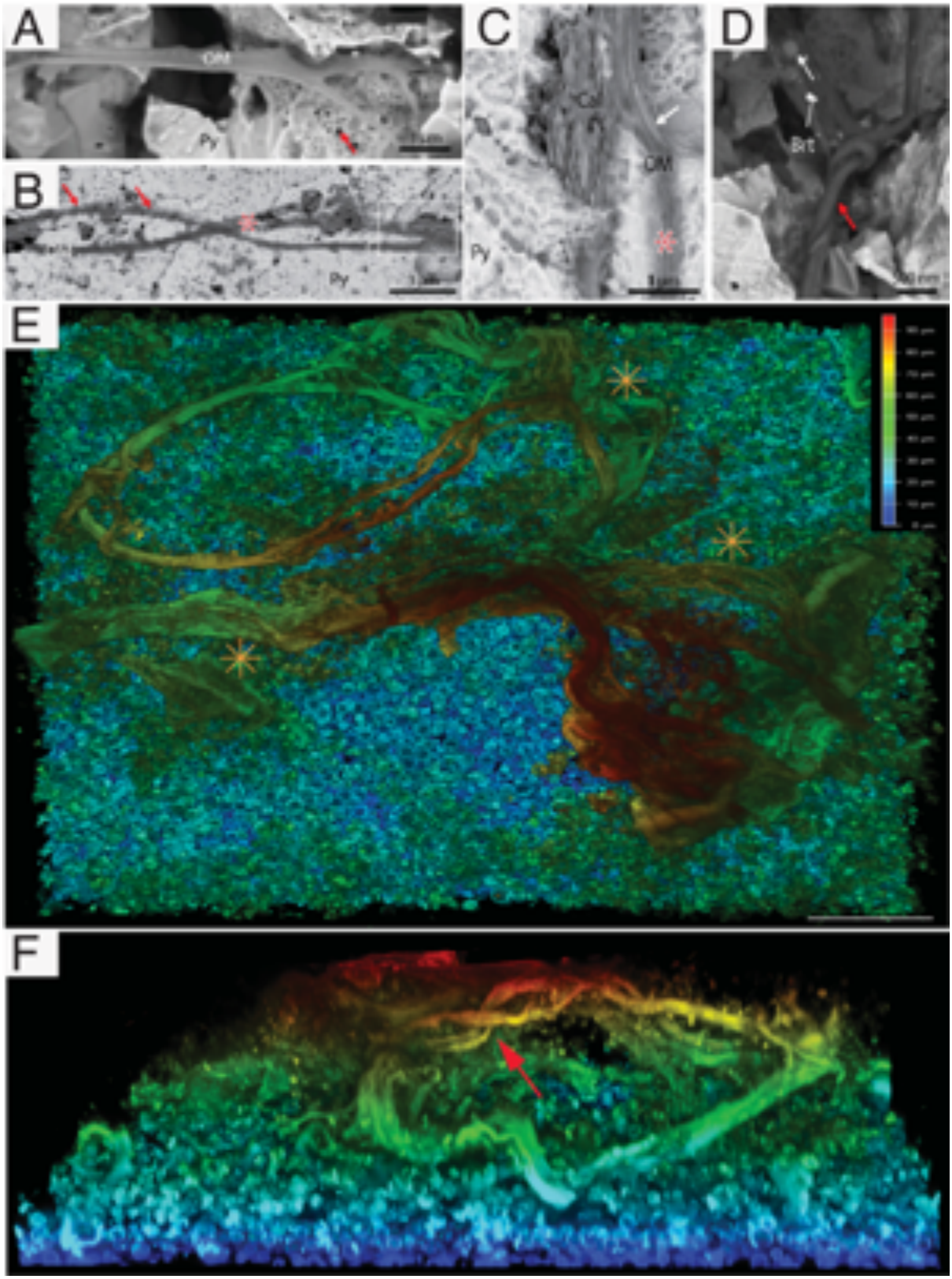

Fig. S63. Morphological comparison of Dresser formation laminations with *EM-P's* membrane debris.

Images A & B show β-type laminations reported from BRC (Tice *et al.,* 2009) (27). Images E & F are frontal and lateral view of morphologically analogous structures formed by *EM-P*. Arrows in these images points to helical structures observed both in microfossils and *EM-P*. Star signs in images B, C and E points to regions showing filamentous nature of the membrane debris. In the image membrane was stained with Nile red. Scale bars in image E is 50µm.

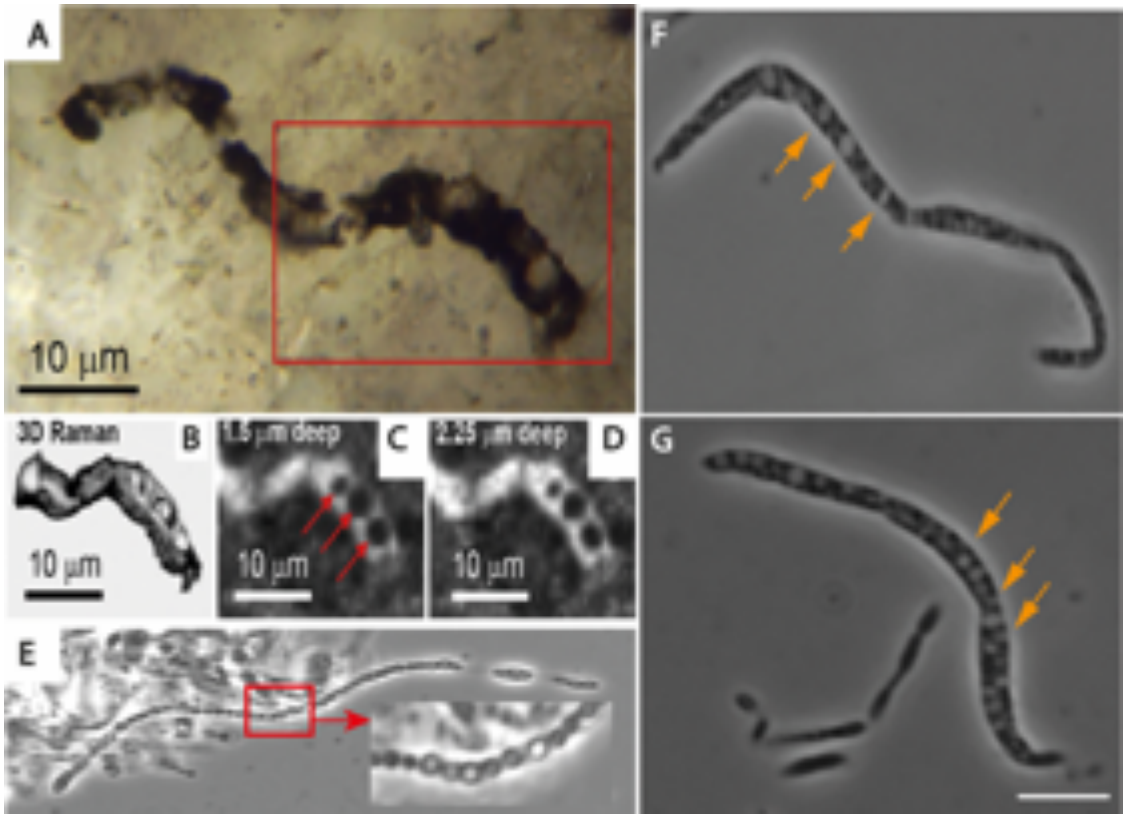

Fig. S64. Morphological comparison between *Primaevifilum amoenum* and *RS-P*.

Images A-D shows *Primaevifilum amoenum* (originally published by Schopf *et al.,* 2012 (53). Images E-G are morphologically analogous *RS-P* cells. Scale bars in image G is 10 µm. Arrows in all the images points to spherical regions of the filaments that are devoid of organic carbon. Inset in the image E is magnified region of the filament (red box).

Filamentous cell with spherical vacuoles in Image E is an early growth stage morphotype of *RS-P* cell.

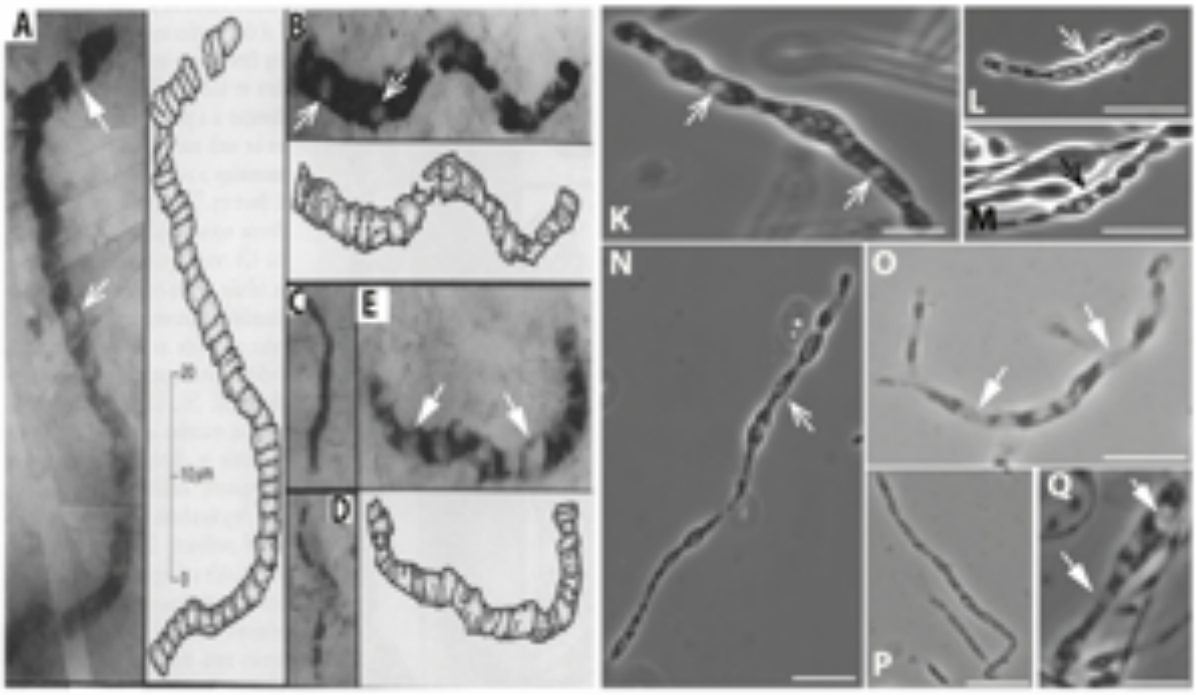

Fig. S65. Morphological comparison between *Primaevifilum amoenum* and *RS-P*: Images A-E shows *Primaevifilum amoenum* (originally published by Schopf *et al.,* 1993) (1). Images K-Q are morphologically analogous *RS-P* cells. Scale bars in all images are 10 µm. Closed and open arrows in images points to polygonal or spherical regions of the filaments that are devoid of organic carbon.

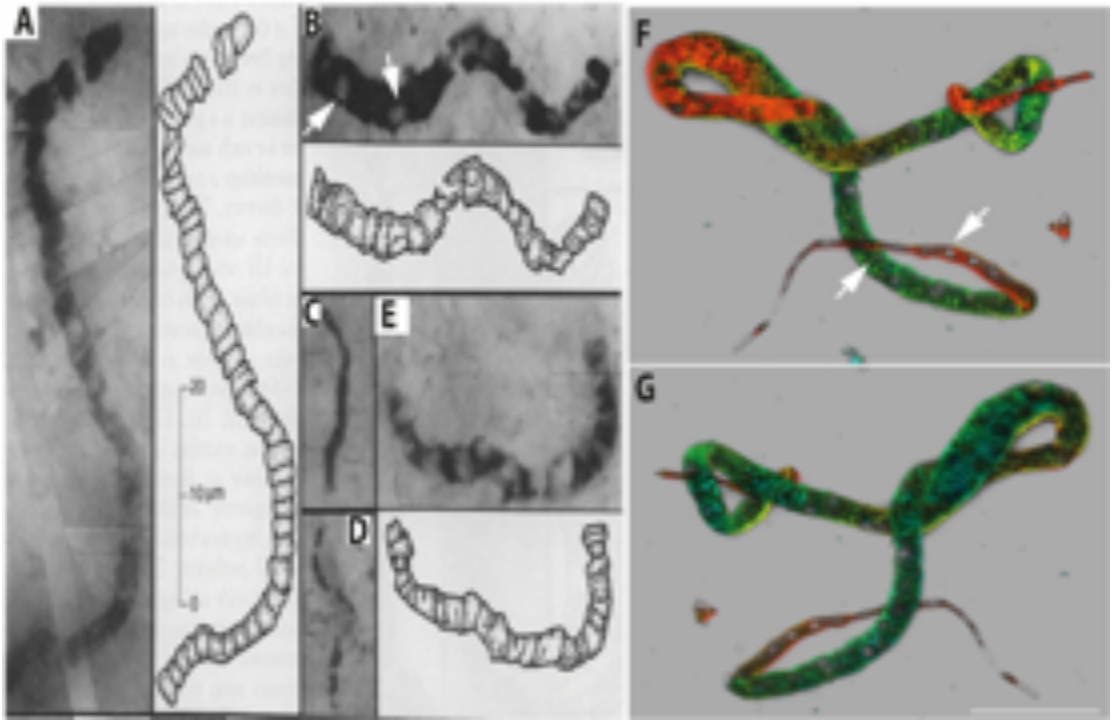

Fig. S66. Morphological comparison between *Primaevifilum amoenum* and *RS-P*.

Images A-E shows *Primaevifilum amoenum* (originally published by Schopf *et al.,* 1993) (1). Images F & G are 3D-rendered STED images of morphologically analogous *RS-P* cells. Scale bars in all images are 10 µm. Arrows in images points to spherical regions of the filaments that are devoid of organic carbon. Long filamentous cells of *RS-P* were often noticed to form twisted structures. Similar morphotypes of *RS-P* exhibiting bending in right angles or twisting were also shown in fig. S74-S76.

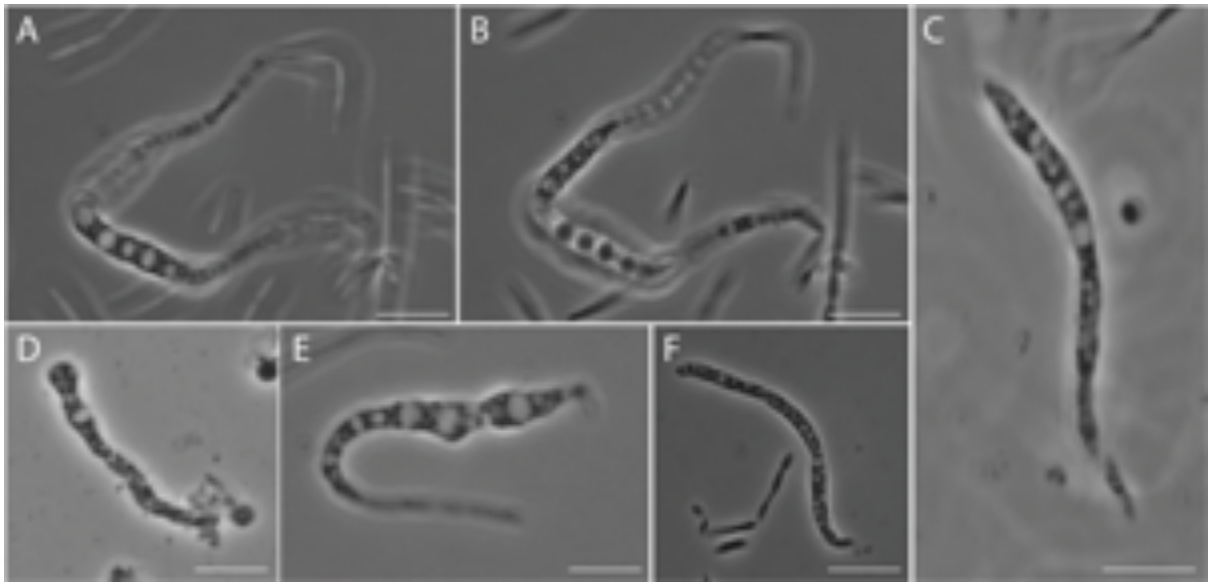

Fig. S67. ***RS-P morphotypes resembling P.amoenum.***

A-F are bright-field images of *RS-P* exhibiting morphological similarities with *P.amoenum*. Scale bars in all images are 10 µm. A&B are images of the same cell at different focal planes. All these cells exhibit distinctive morphological features of *P.amoenum,* filamentous cells with hollow spherical vacuoles.

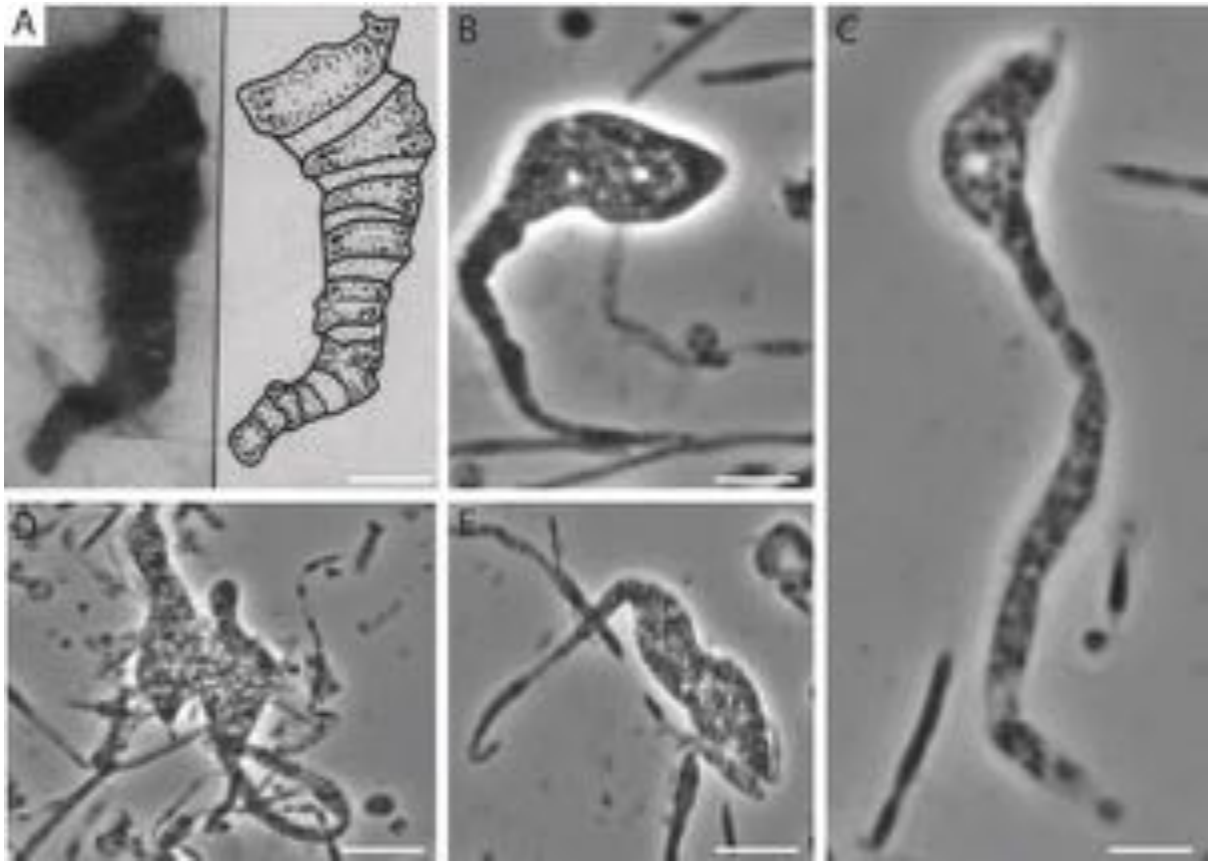

Fig. S68. Morphological comparison between *Primaevifilum attenuatum* and *RS-P*.

Images A shows filamentous microfossil, *P.attenuatum* (originally published by Schopf et al., 1993) (1). Images B-F are analogous morphotypes of *RS-P*. Scale bars all images are 10 µm. P.attenuatum is described as croissant shaped microfossil exhibiting attenuation of its trichomes. Images B-E are morphologically analogous *RS-P* cells. In-comparison to microfossils, *RS-P* also exhibited swollen/lenticular cells with equatorial overhangs.

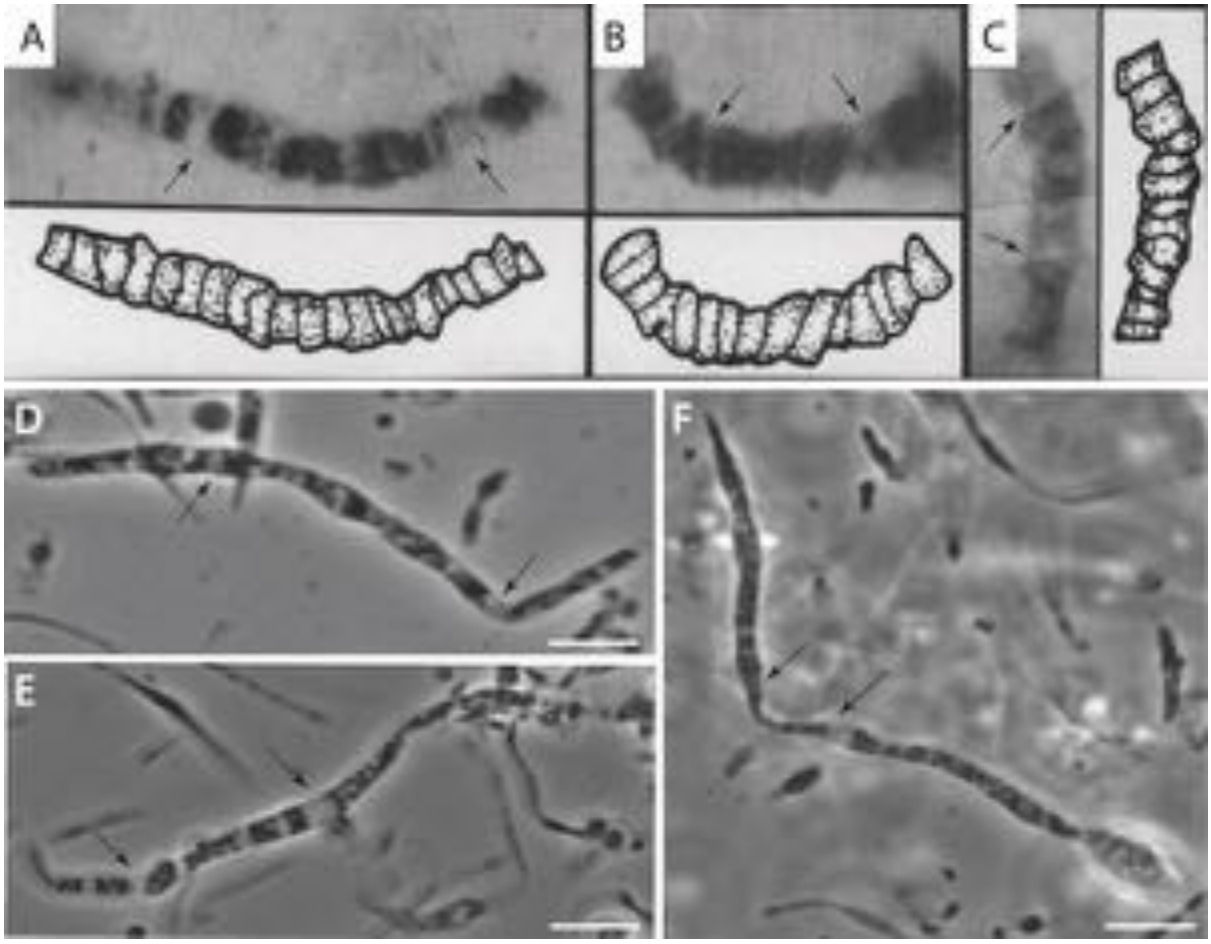

Fig. S69. Morphological comparison between *Primaevifilum delicatum* and *RS-P.*

Images A-C shows filamentous microfossil, *P.delicatum* (originally published by Schopf et al., 1993) (1). Images D-E are morphologically analogous *RS-P cells.* Scale bars in these images are 10 µm. *P.delicatum* is described as cylindrical filamentous microfossils exhibiting a banded pattern, similar to the banded pattern observed in *RS-P* (arrows).

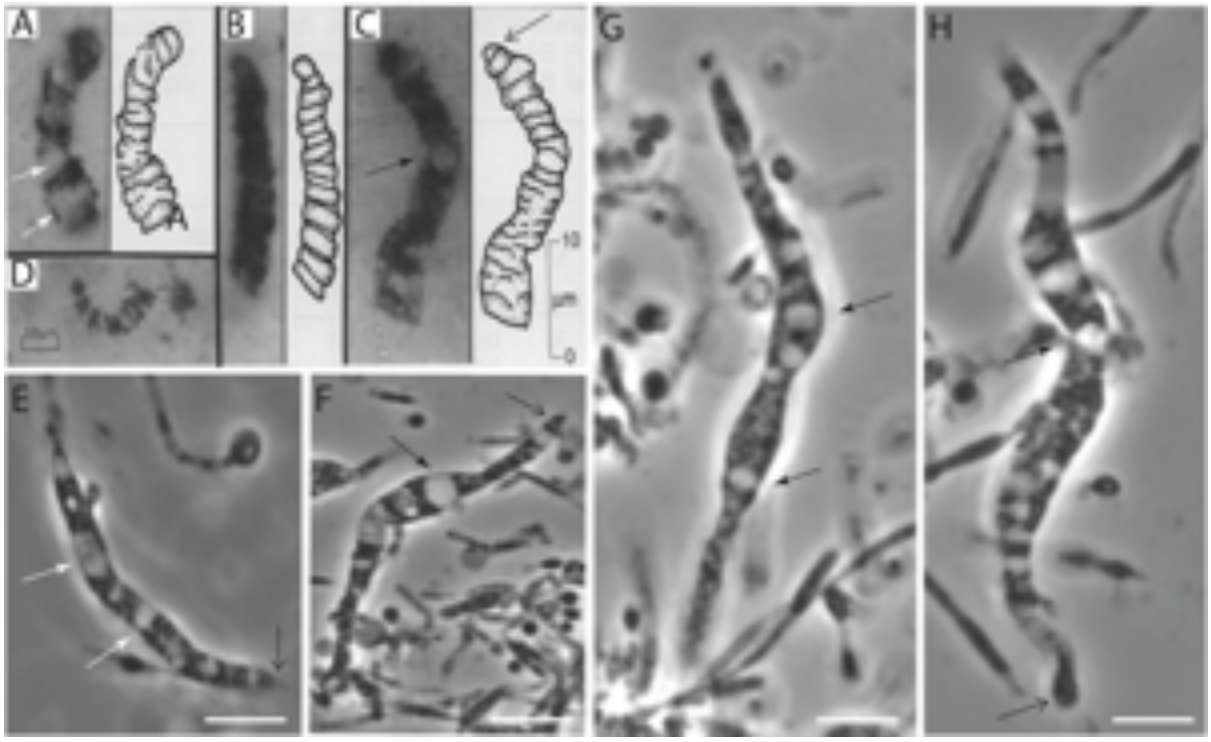

Fig. S70. Morphological comparison between *Archaeotrichion septatum* and *RS-P.*

Images A-D depicts filamentous microfossil, *A.septatum* (originally published by Schopf et al., 1993) (1). Images E-H are morphologically analogous *RS-P* cells. Scale bars in these images are 10 µm. *A.septatum* is described as filamentous microfossils exhibiting a banded pattern and rounded terminal. Open black arrows in images E & H points to similar structures in *RS-P*. White arrows in all image's points to rectangular hollow regions and closed black arrows points to similar spherical regions.

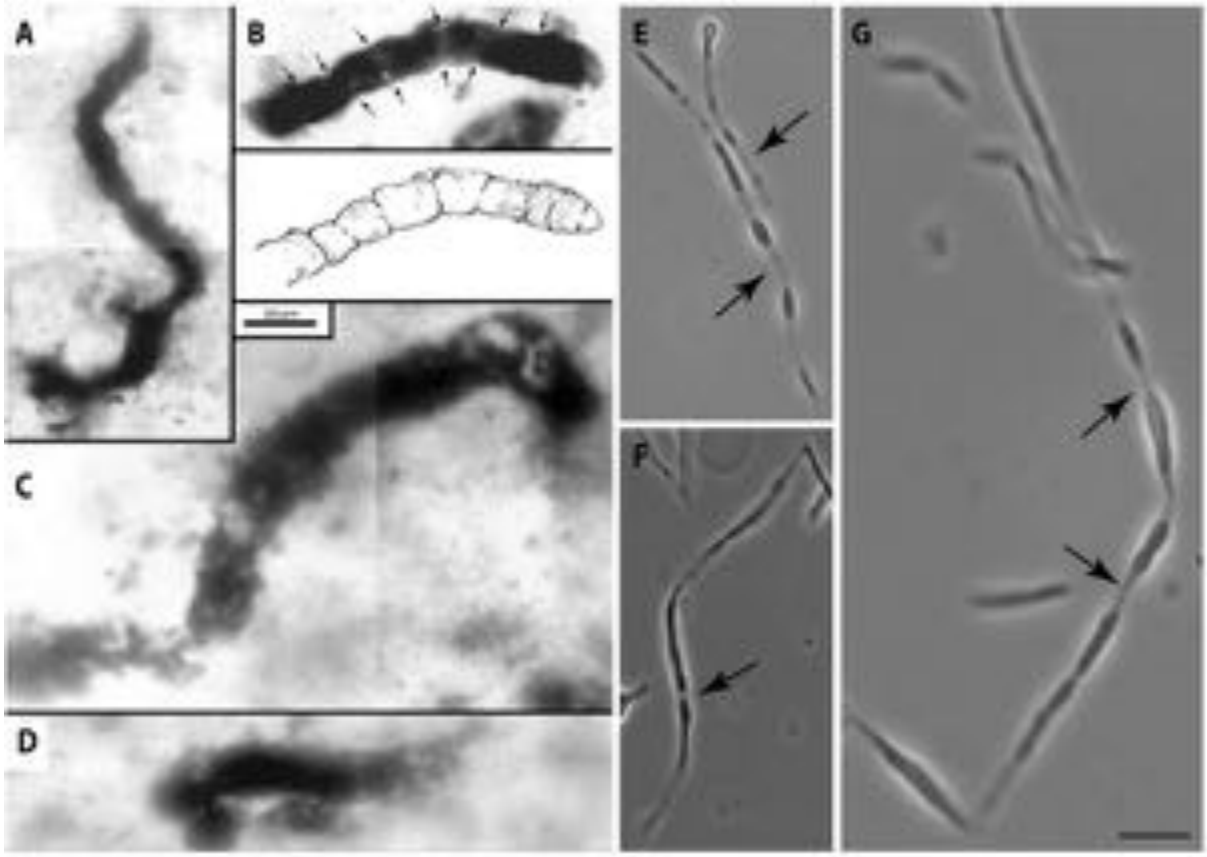

Fig. S71. Morphological comparison between North pole filamentous microfossils and *RS-P*.

A-D are the images of North Pole microfossils (originally published by Ueno *et al.,* 2001) (43). Images E-G show morphologically analogous *RS-P* cells. Scale bar in image G is 10µm. Arrows in all the images points to hollow regions of the filament that were devoid of organic carbon (cytoplasm).

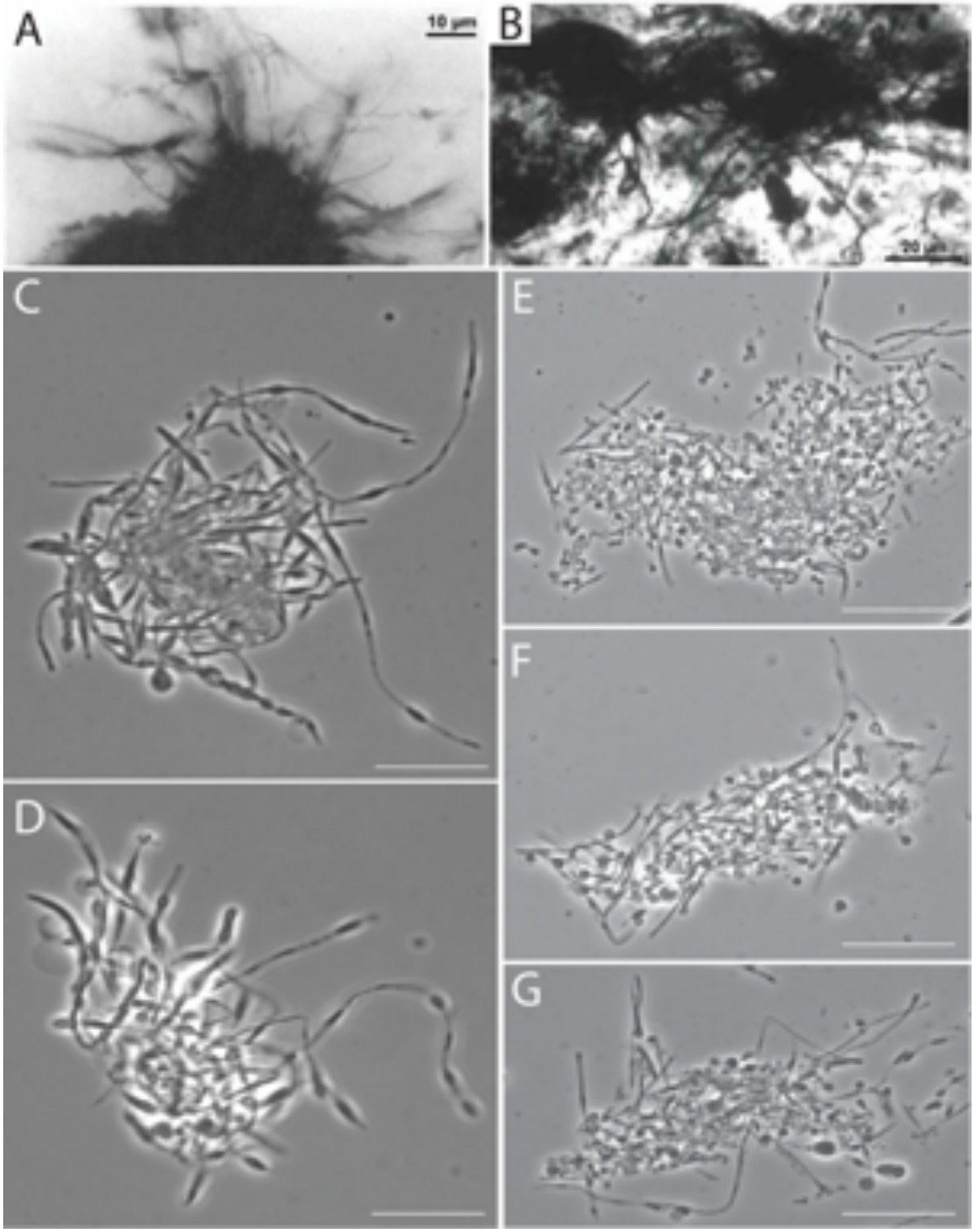

Fig. S72. Morphological comparison between Sulphur spring filamentous microfossils and *RS-P*.

A & B are images of filamentous microfossils reported from Sulphur spring formations (originally published by Rasmusssn *et al.,* 2000) (1). Images C-G show morphologically analogous *RS-P* cells. Scale bars in images C-G are 10µm.

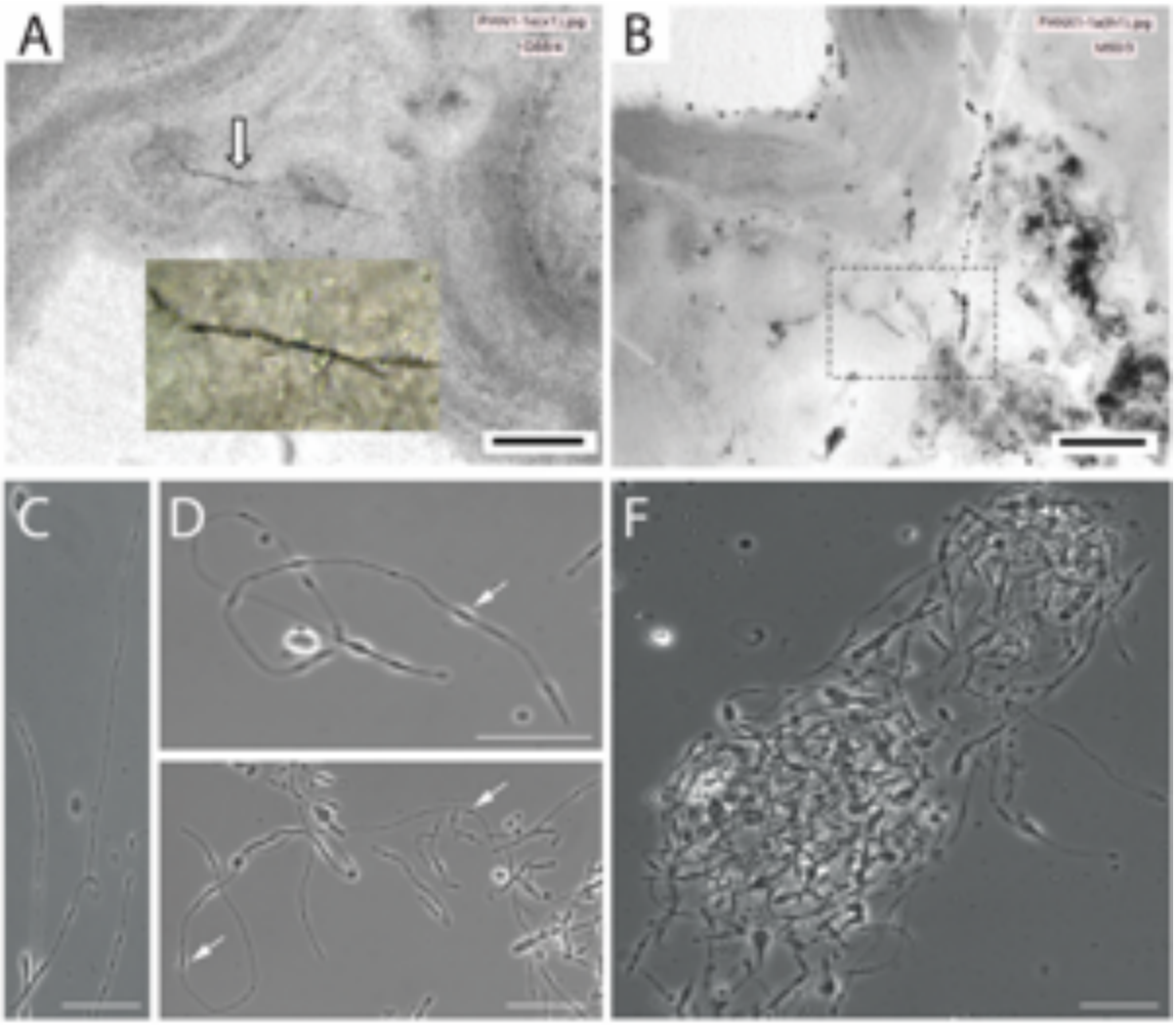

Fig. S73. Morphological comparison between tubular SPF microfossils and *RS-P*.

A & B are the images of filamentous SPF microfossils (originally published by Sugitani *et al.,* 2013) (18). Scale bars in image A & B are 50µm. Images C-F show morphologically analogous *RS-P* cells. Scale bars in images C-F are 10µm. Arrows in all the images points to regions of the filament that appear to be swollen (blistered appearance). Sequential stages involved in transformation of these swollen regions into lenticular cells is shown as fig. S78.

Image F shows clumps of entangled filaments. Similar clumps of entangled filaments were also reported from SPF formations and can be seen in image B.

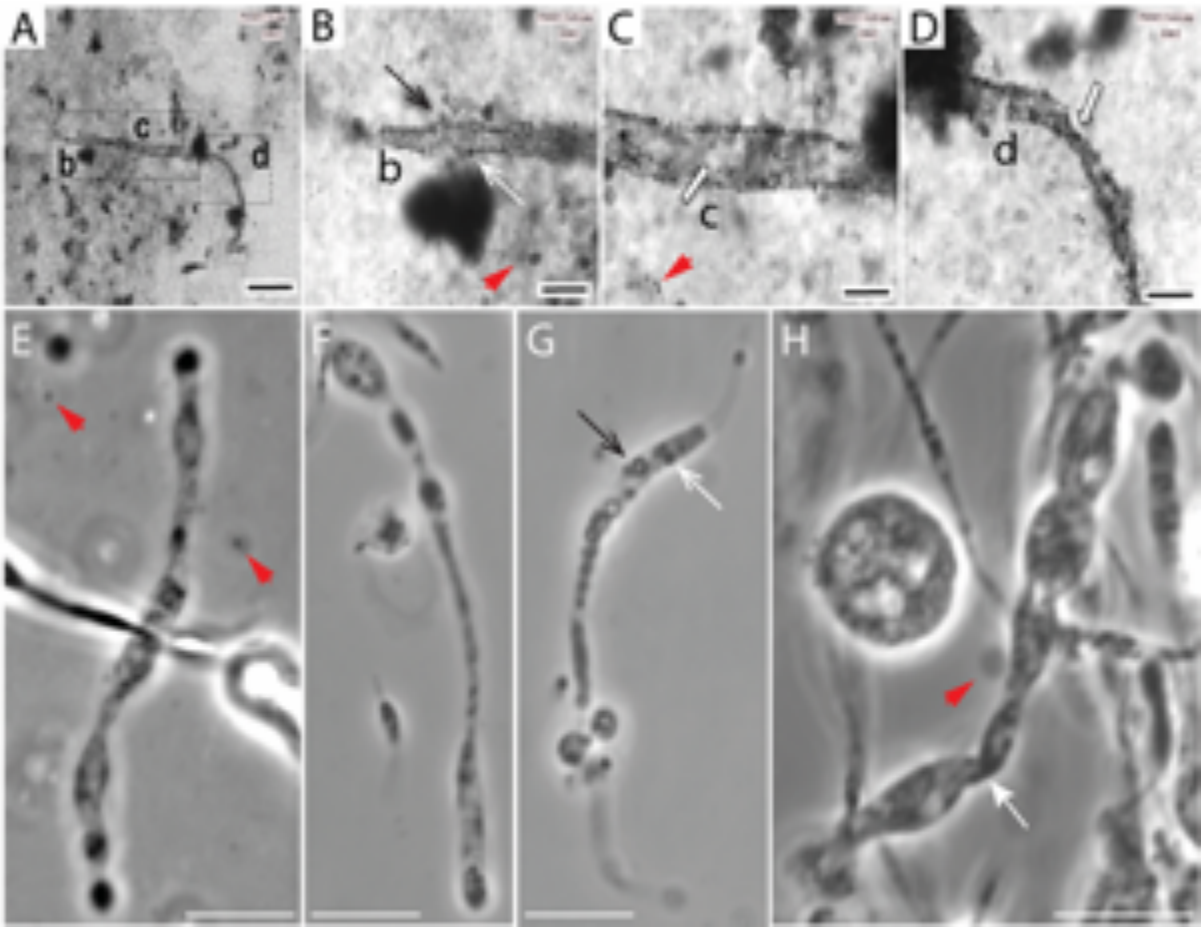

Fig. S74. Morphological comparison between tubular SPF microfossils and *RS-P*. Images A-D show tubular microfossils reported from SPF site (originally published by Sugitani *et al.,* 2013) (18). Image A shows a tubular microfossil from SPF. Images C-D are magnified images of different regions of the filament. Scale bar in image A and image B-D are 50µm and 20 µm respectively. Images E-H show morphologically analogous late growth stage *RS-P* cells. Scale bar in these images are 10µm. Sequential stages involved in formation of these cells is shown as fig. S78. Open white and black arrows points to intracellular spherical inclusions with and devoid of organic carbon. Red arrowheads points to structures

that were similar spherical structures that were out of the cell. Closed white arrow in image H points to bending of the filamentous cell similar to SPF microfossil shown in image D.

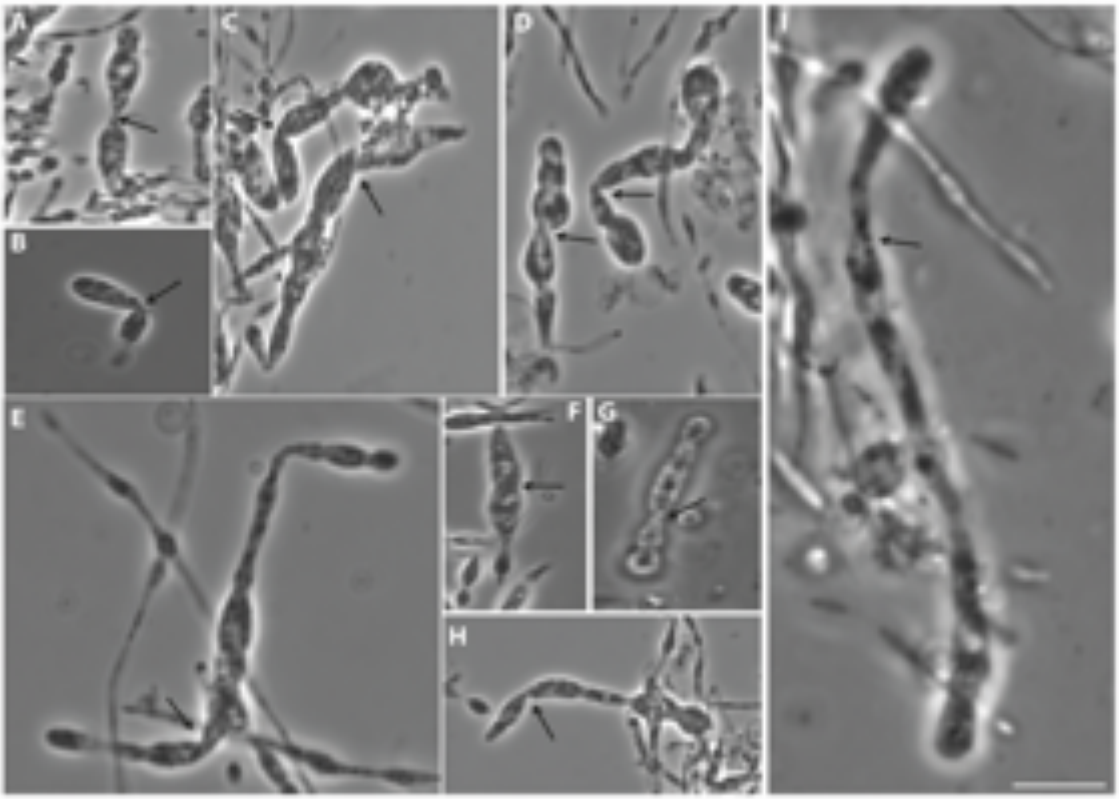

Fig. S75. Twisting of tubular *RS-P* cells.

Images A-H show tubular *RS-P* cells. scale bar in image I is 5µm. Arrows in images points to Regions of the filament that underwent twisting or bending.

Fig. S76. Aggregates of *RS-P* cells exhibiting different morphologies.

Images A show3D rendered STED-microscope image of *RS-P* cell aggregate. Scale bars in these images are 20µm. Magnified images of cells within boxed regions were shown as image B & C. Image B shows *RS-P* cells resembling thick tubular microfossils reported from

SPF (fig. S74) and Image C shows filamentous *RS-P* cells that underwent twisting and bending, similar to microfossils reported from Apex chert formation (fig. S74&75).

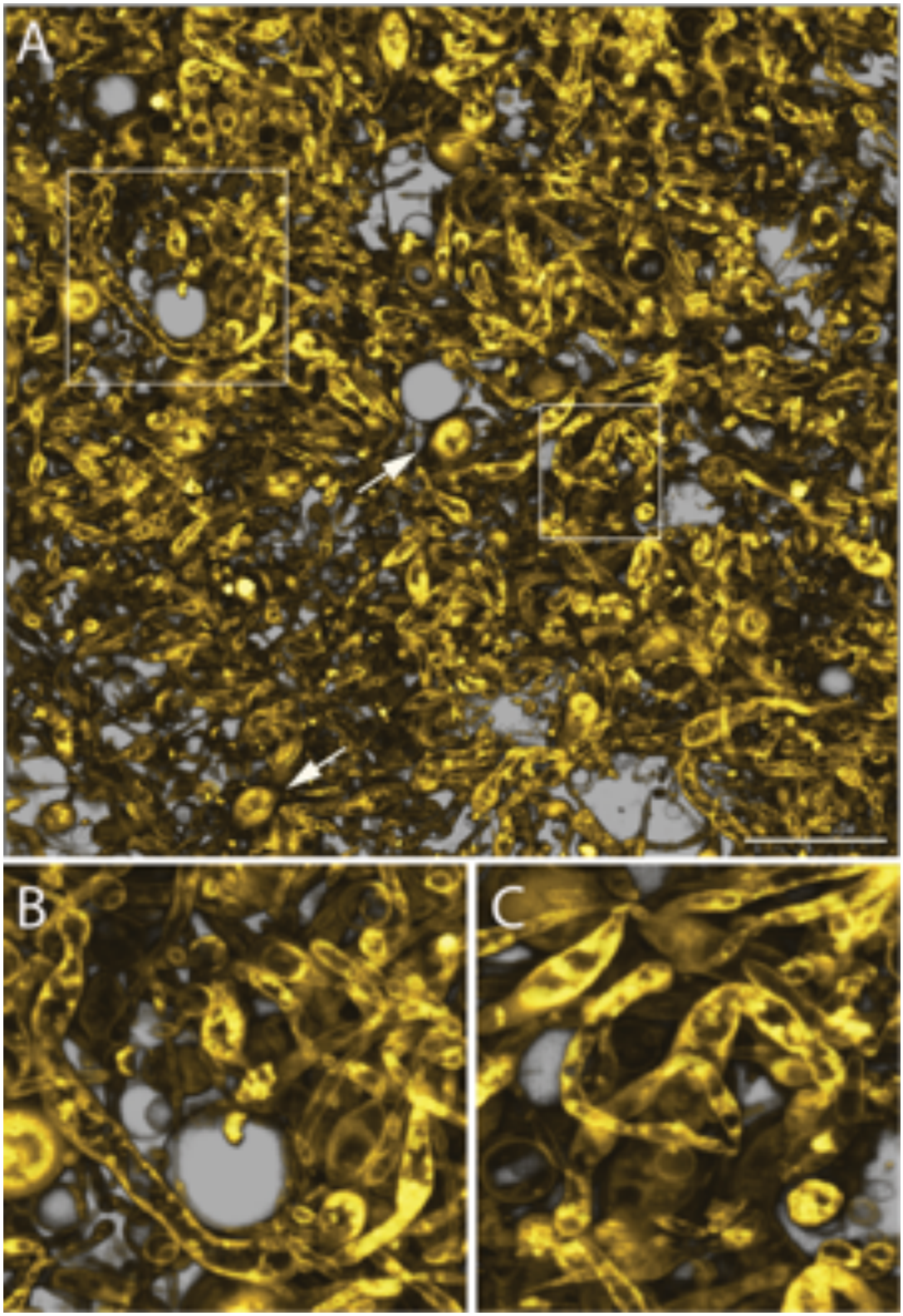

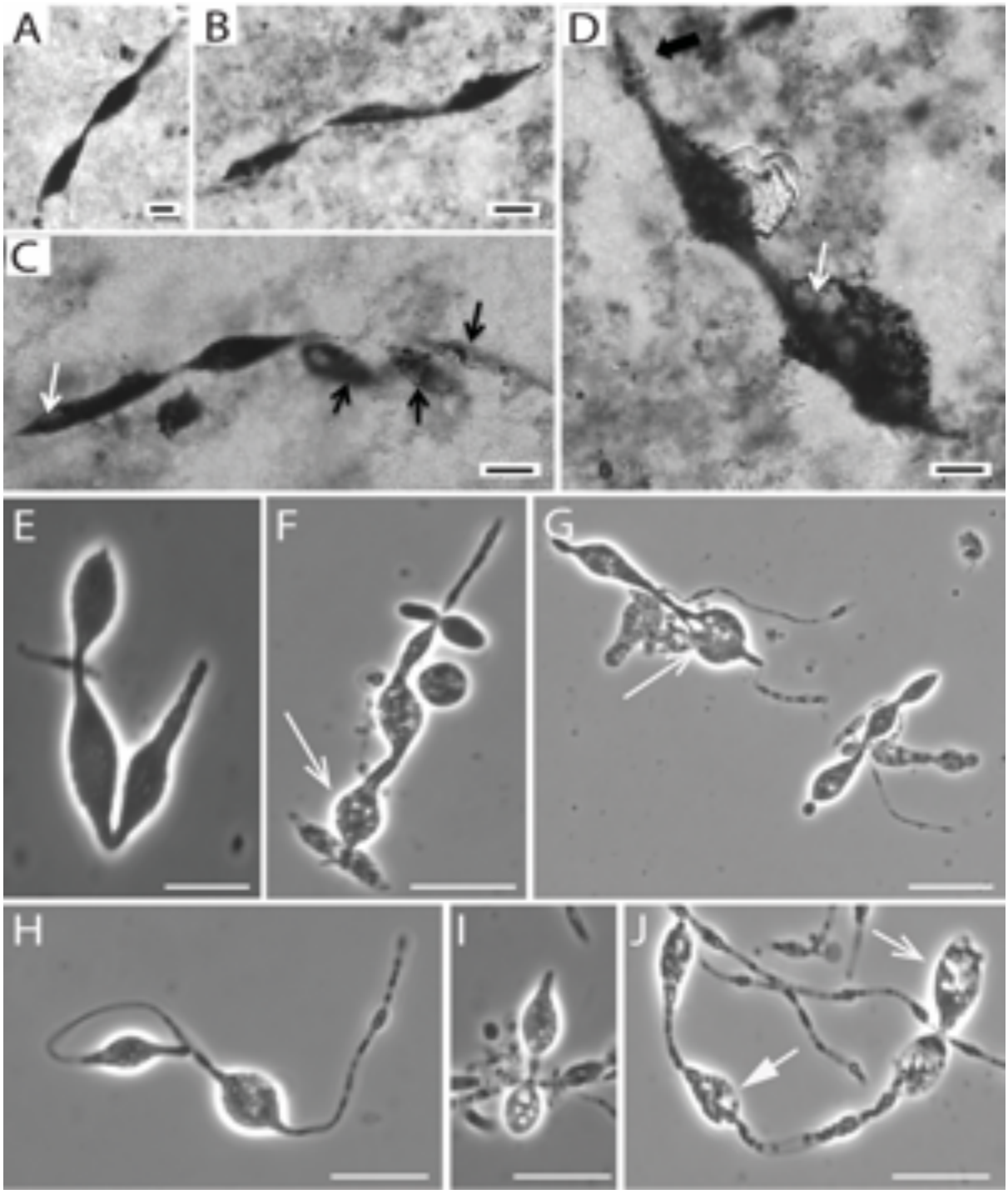

Fig. S77. Morphological comparison between lenticular SPF microfossils and *RS-P.*

Images A-D show lenticular microfossils reported from SPF site (originally published by Sugitani *et al.,* 2013) (18). Scale bar in images A-D are 10µm. Images E-J are

morphologically analogous *RS-P* cells, from different growth stages. Scale bar in images E-J are 10µm. Arrow in image D points to voids within the lenticular cells. Closer inspection of cells in image D also shows presence of reticulate structures and spherical inclusions within the cell. *RS-P* cells exhibiting similar intracellular voids can be seen in images F, G I and J (open arrows). Spherical inclusions within the cell can be seen in image J (closed arrows).

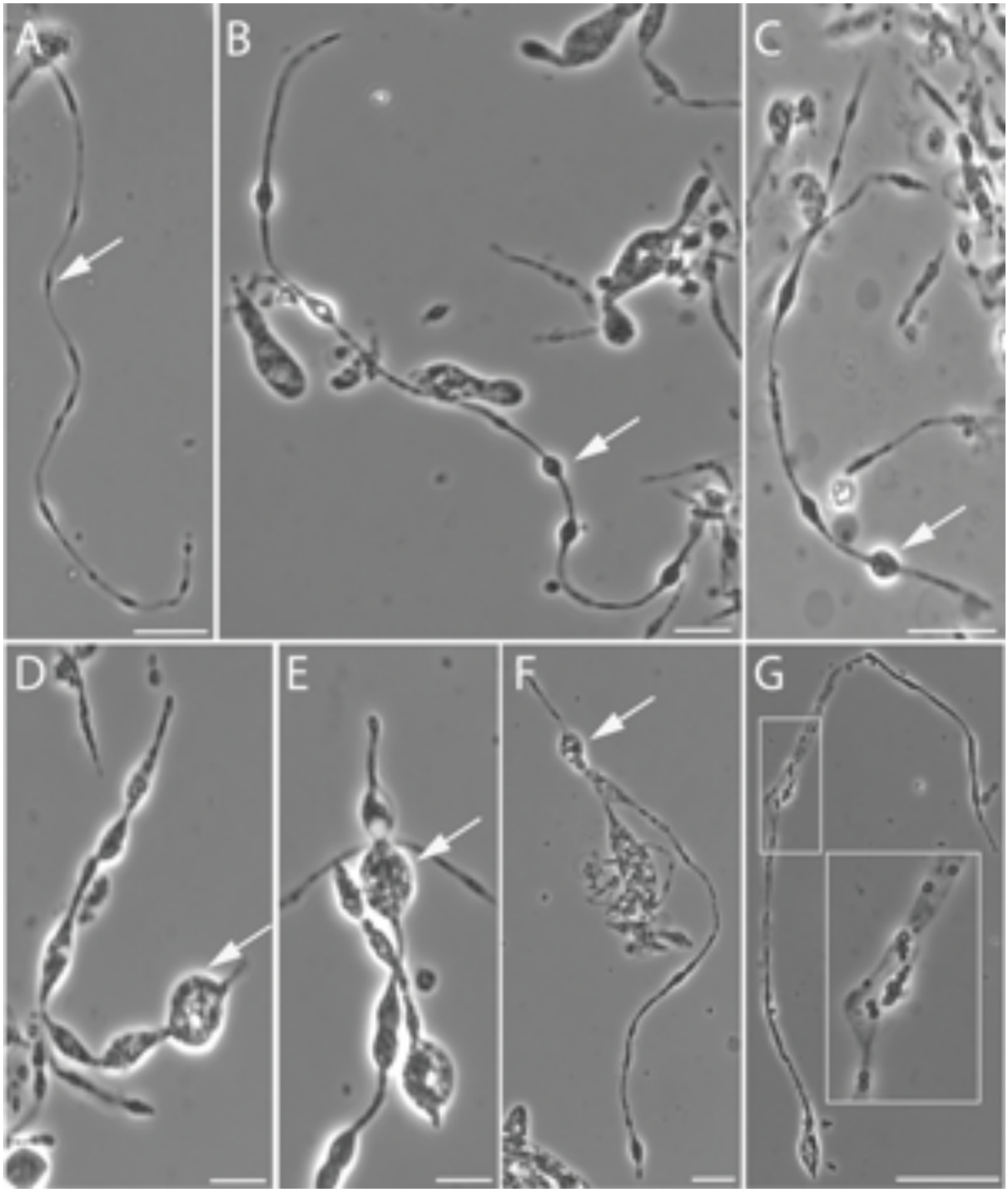

Fig. S78. Life cycle and transformation of blisters to lenticular structures.

Images A-G are phase-contrast images showing sequential morphological transformation of *RS-P* over the course of its growth. Arrows in all the images point to gradual growth of blister within the filaments into lenticular structures. Over time these lenticular structures transformed from having uniformly distributed cytoplasm to having reticulate structures

within them. Inset image in G show the magnified region of filament which is hollow and contain spherical inclusions. Scale bars in these images are 10µm.

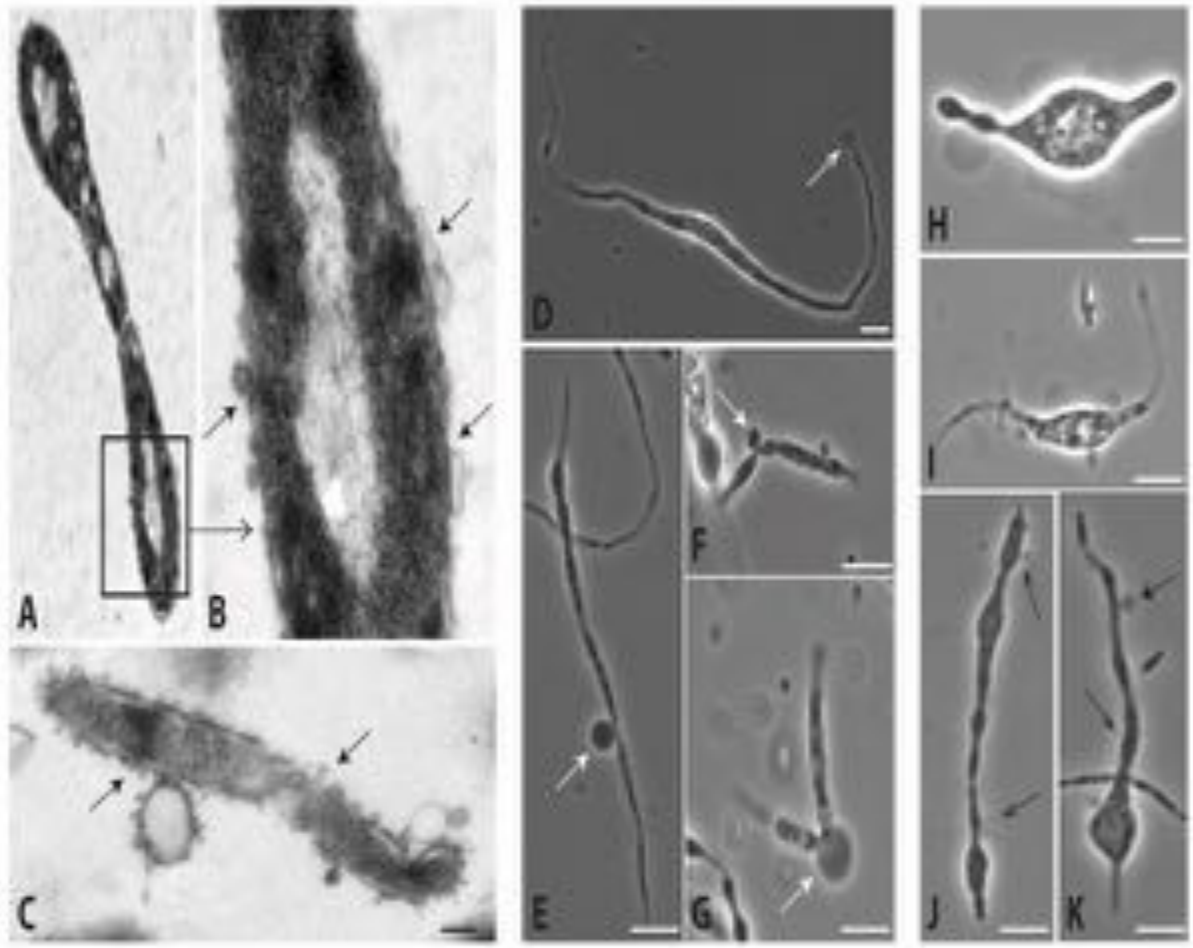

Fig. S79. Outer membrane vesicle (OMV) formation in *RS-P*.

A, B & C are TEM images of *RS-P* showing OMV in hour-glass shaped cells (A&B) observed during early or late growth stages (scale bar is 0.5µm). D-G are filamentous morphotypes of *RS-P* with central (E, F & G, closed arrows) or terminal (D, open arrows) OMV's. Bending or even breakage of filaments was observed as these OMV's grew larger (G). H & I are lenticular morphotypes of *RS-P* with OMV's. J & K are *RS-P* morphotypes with OMV's observed during early growth stages. Two types of OMV's were observed in *RS-P*, spherical (E) and faintly visible filamentous (J & K) (Can be seen clearly in Movie S9).

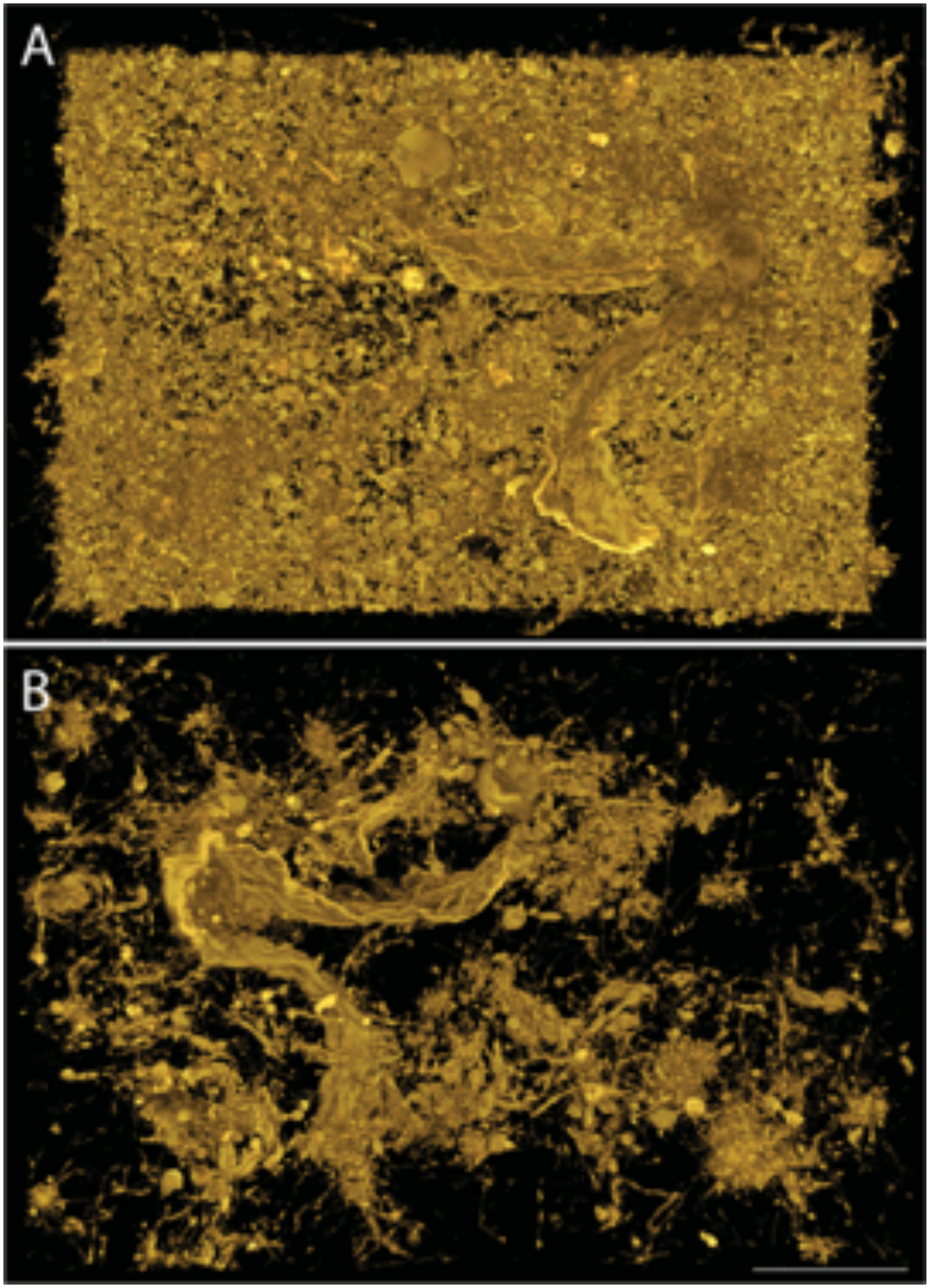

Fig. S80. Membrane debris formation in *RS-P*.

Images A & B show formation of membrane debris within large aggregations of *RS-P* cells. Image B is the posterior view of cropped (along the Z-axis) image A, to better visualise the texture of membrane debris. Scale bar in image B is 10µm.

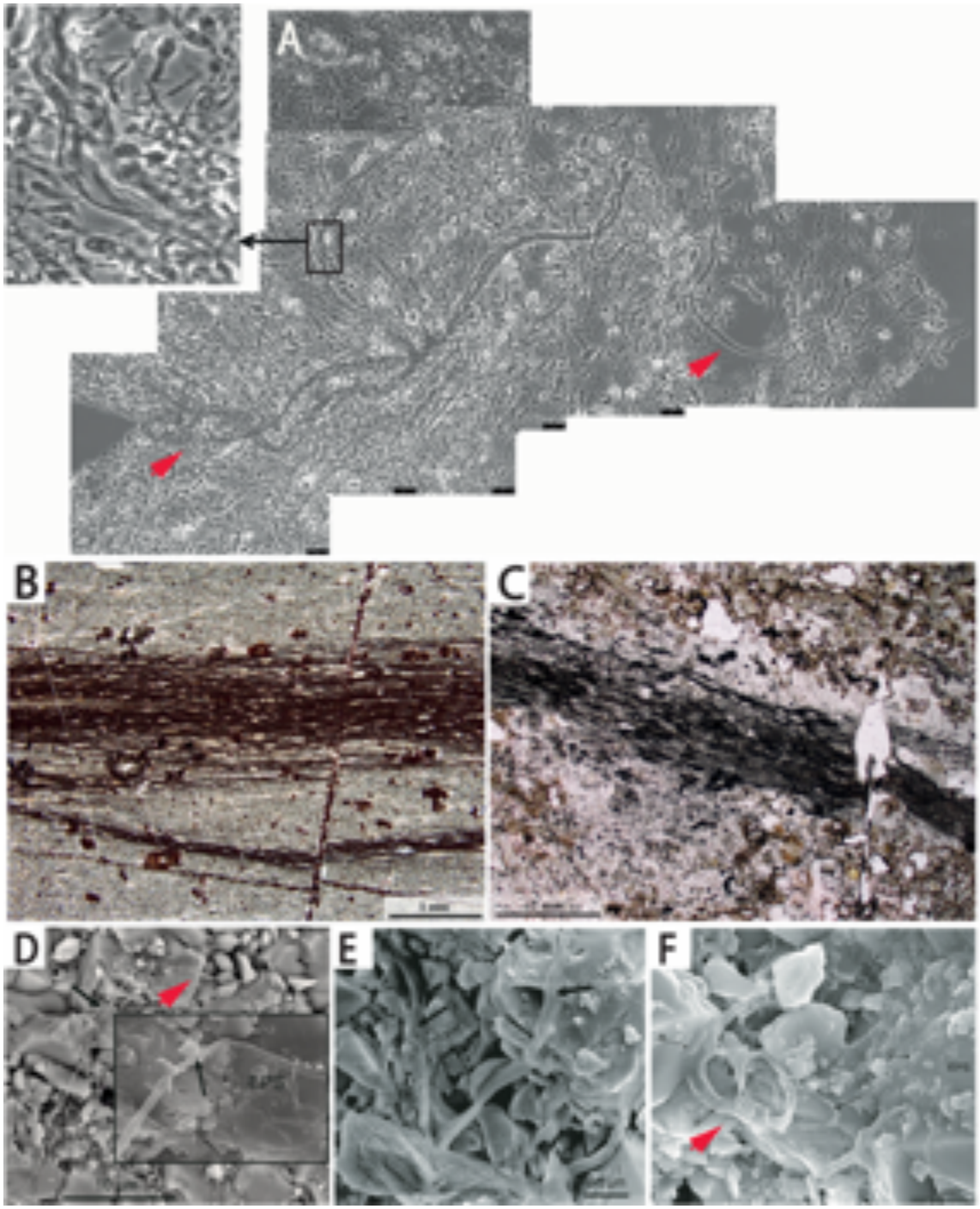

Fig. S81. Comparison of filamentous membrane debris *RS-P* with organic structures reported from BGB and Kitty's Gap Chert.

Image A is composite image of filamentous membrane debris formed by *RS-P*. Images B&C were organic structures reported from BGB (originally published by Hickman-Lewis *et al.,* 2018) (48). Images D-F were organic structures reported from Kitty's Gap Chert (originally

published by Westall *et al.,* 2006) (47). Images B & C lamination like structures. Images D-F are SEM images of similar structures from Kitty's Gap Chert. Black arrows in image E shows fibrous nature of these structures (along with red arrows in these images). The magnified region of image A shows similar nature of *RS-P* membrane debris. Arrows in images A and F points to similar twisting and bending it these structures. Scale bars in image A are 10µm.

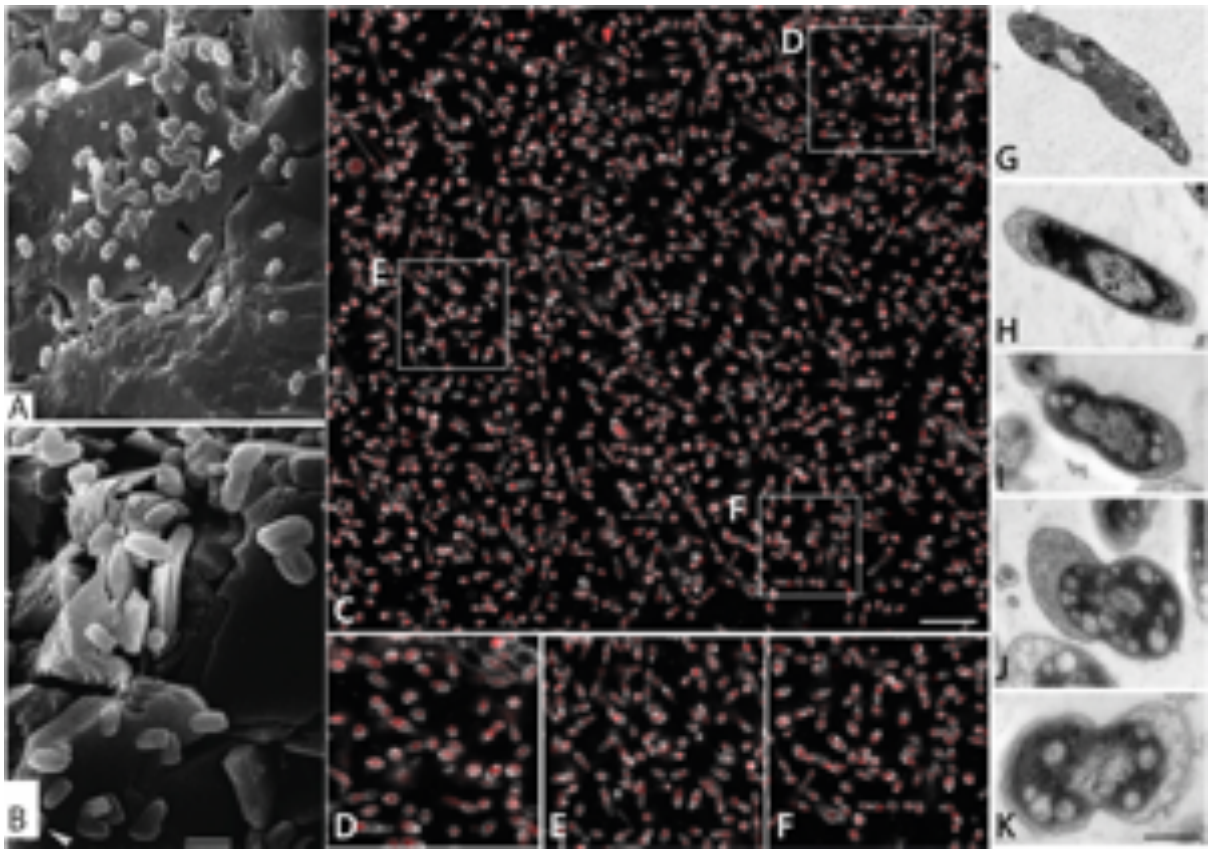

Fig. S82. Morphological comparison of BGB microfossils with *RS-P*.

Images A & B are rice grain-like microfossils reported from BGB formations (originally published by Westall *et al.,* 2001) (20). Images B - K are STED (C-F) and TEM (G-K) images of morphologically analogous *RS-P* cells. The scale bar in images C and K are 5µm & 0.5µm respectively. Images D-F are magnified regions of image C. Membrane was stained white and DNA red, in these images. These images show the last growth stage of *RS-P*, when

long filamentous *RS-P* cells were fragmented into smaller daughter cells. Images G-K are TEM images of such daughter cells. Remnants of the fission process can be seen as membrane overhangs in these images.

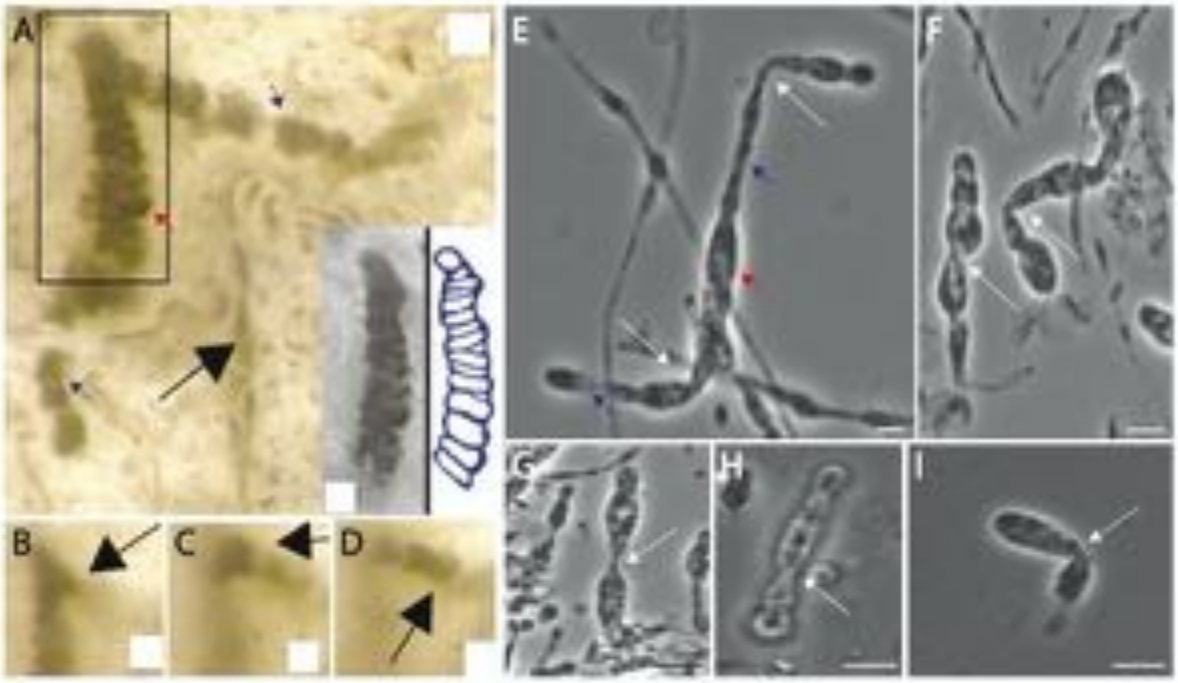

Fig. S83. Comparison of filamentous Apex chert microfossils with *RS-P*.

Images A-D are filamentous microfossils reported from Apex chert (originally published by Wacey *et al.,* 2016) (11). Images E-I show morphologically analogous tubular *RS-P* cells. scale bar in these images are 5µm. White arrows in images points to regions of the filament that underwent twisting or bending. Blue & red arrows points to regions of the filaments with and devoid of organic carbon, giving it a banded appearance.

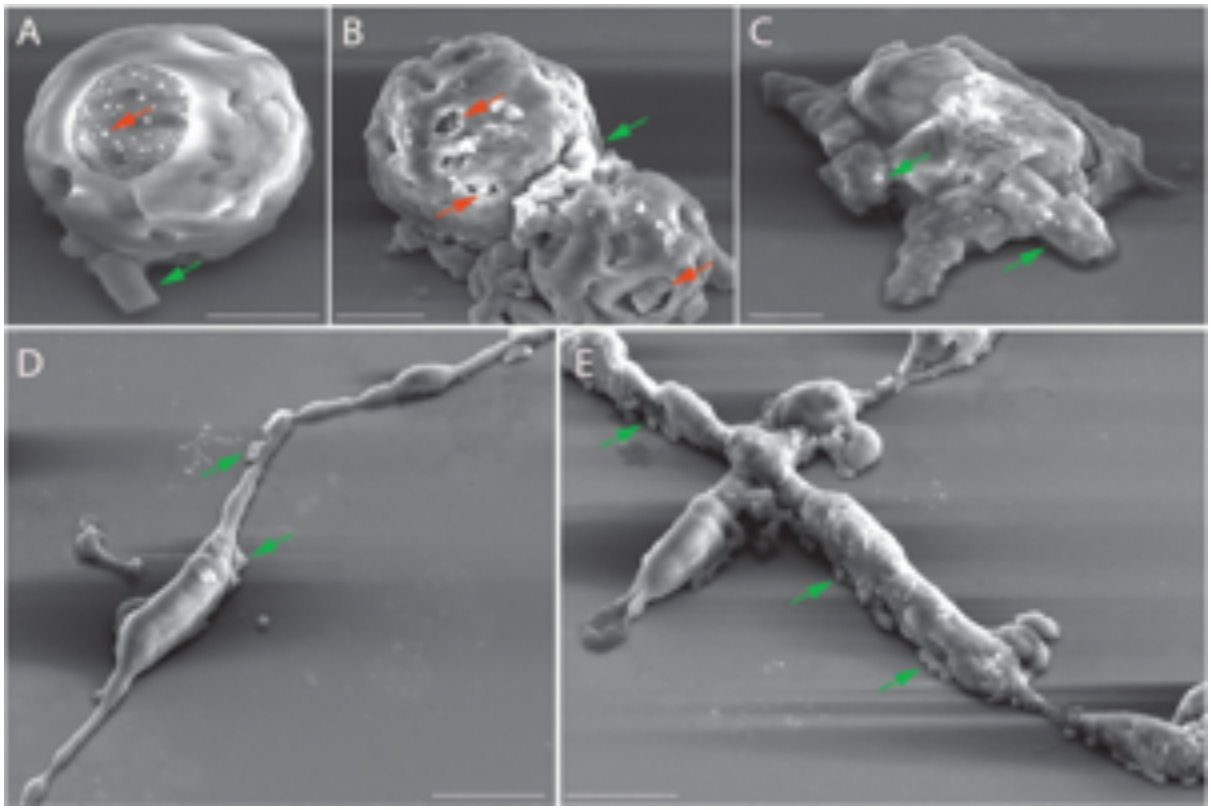

Fig. S84. Association of salt with bacterial protoplasts.

Images A-E are SEM images of *EM-P* (A-C) and *RS-P* (D & E). Images A-C show early (A), mid (B) and late (C) growth stage cells of *EM-P*. Arrows in all these images points to salt crystals on the surface of the cells. Red arrows in particular points to salt crystals within the outer membrane invaginations. Scale bars in all the images are 2µm.

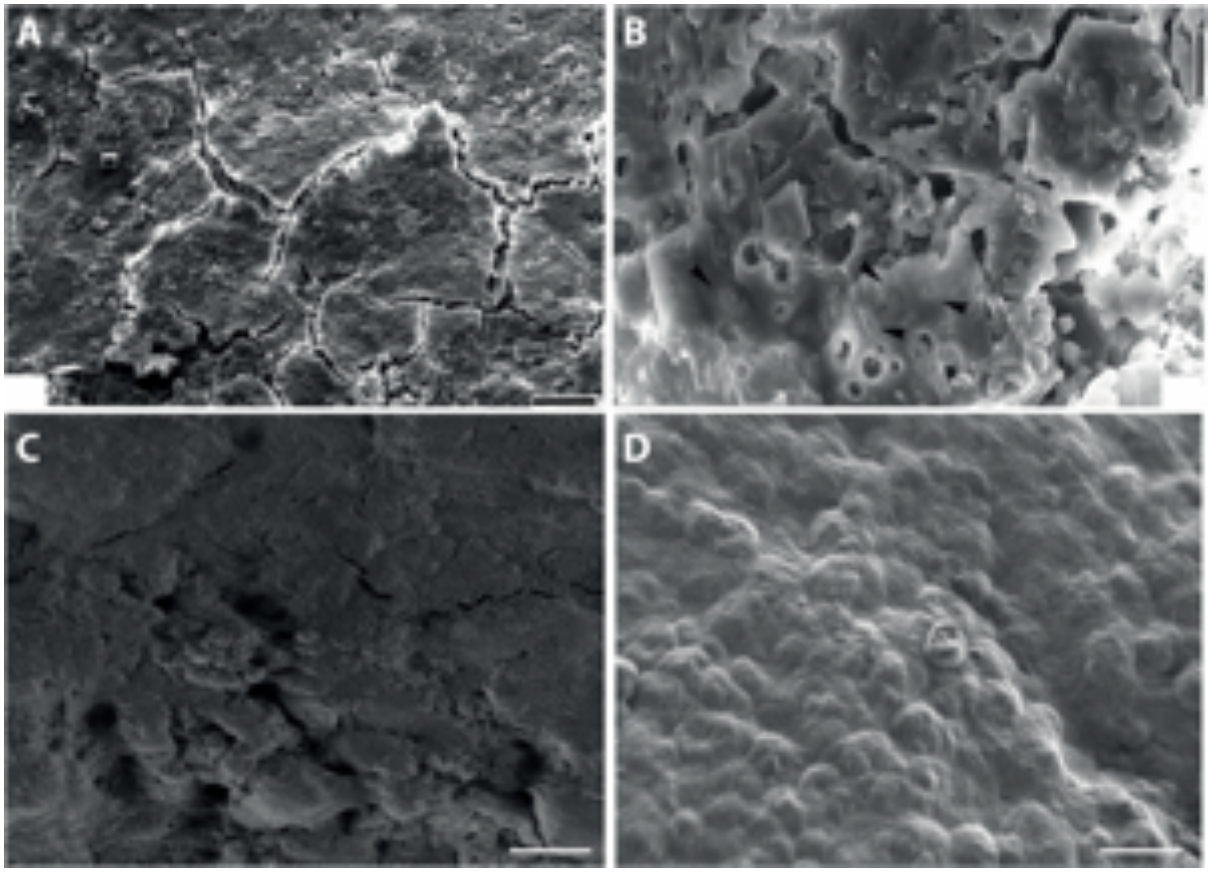

Fig. S85. Morphological comparison of Kromberg microfossils with *EM-P*.

Images A & B show mineral encrusted microbial mats (A) and spherical microfossils (B) within these encrusted mats reported from Kromberg formation (originally published by Westall *et al.,* 2001) (20). Scale bars in images A & B are 20µm. C & D show SEM images of morphologically analogous salt encrusted *EM-P* cells after 30 months of incubation. Elemental composition of such microbial mats and individual cell morphologies are shown in fig. S86. Scale bars in images C & D are 2µm.

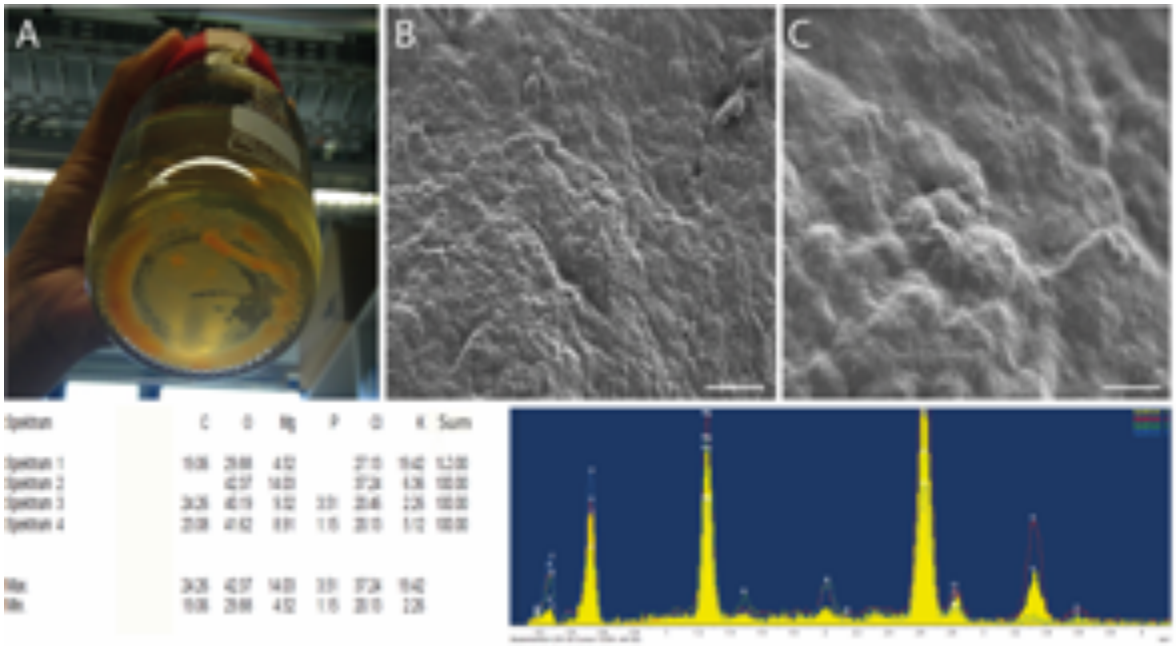

Fig. S86. Chemical nature of *EM-P*'s crust.

Images A show 30-month-old *EM-P* culture at the bottom of the bottle. Over the course of incubation, *EM-P* biofilm transformed into brittle wafer due to encrustation with salt. Images B & C show SEM images of *EM-P*. Scale bars in these images are 2µm. Elemental composition of solidified mat is shown below the images (determined by SEM-EDX).

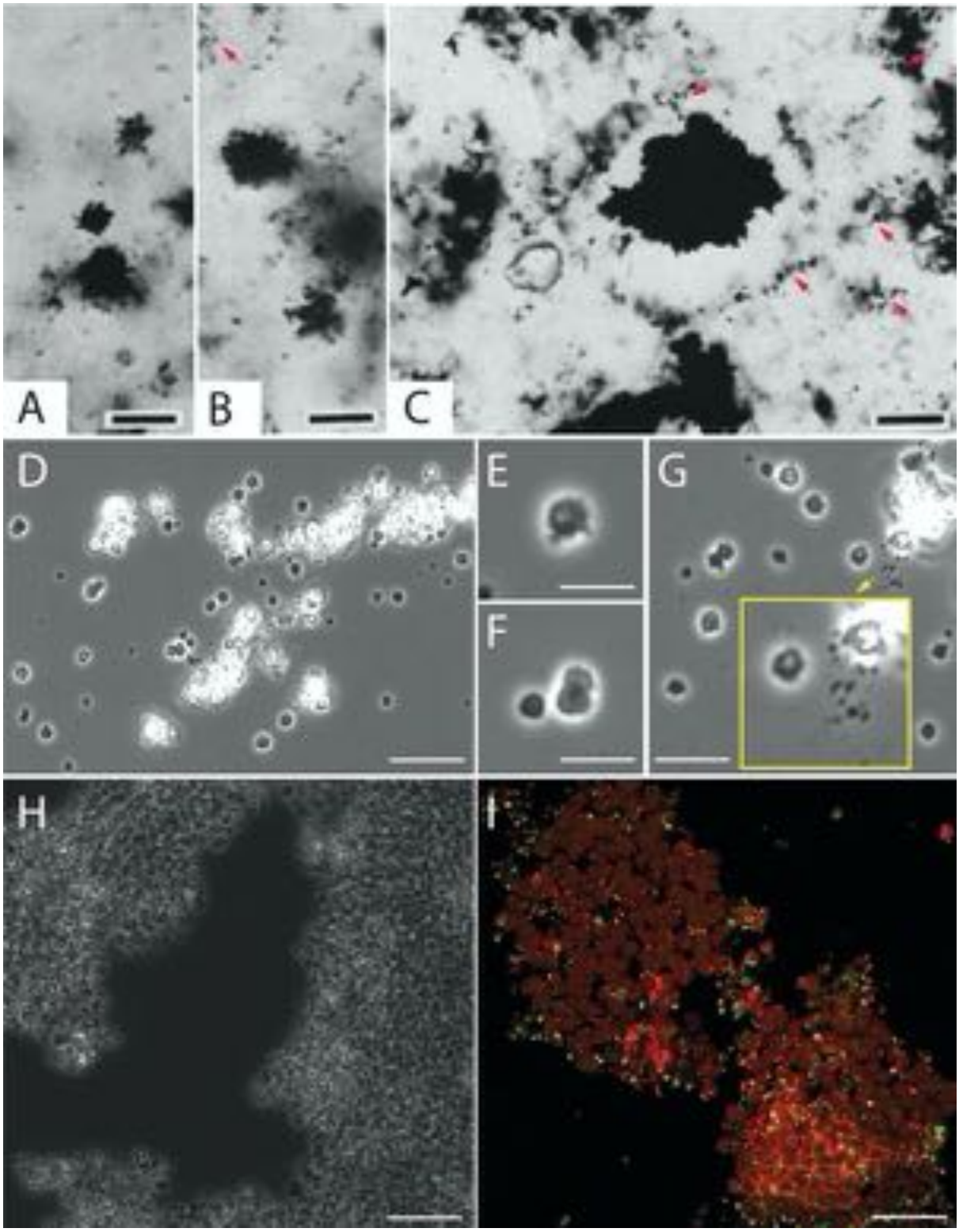

Fig. S87. Morphological comparison of North-Pole microfossils with *EM-P.*

Images A-C show spherical microfossils with stellate projections reported from North-Pole formation (originally published by Buick *et al.,* 1990) (19). Scale bars in images A-C are

100µm. D-I are phase-contrast (D-H) and super-resolution confocal (I) images of morphologically analogous *EM-P* cells. Like microfossils, *EM-P* cells revived from the above-described crust formation formed stellate structures at cell periphery. Arrows in images C & G points to filamentous string of daughter cells extending out of cell clumps. Image I show salt encrusted *EM-P* cells, that were stained with Picogreen (for DNA, green) and Nile red (membrane, red). Scale bars in images A-C are 10µm.

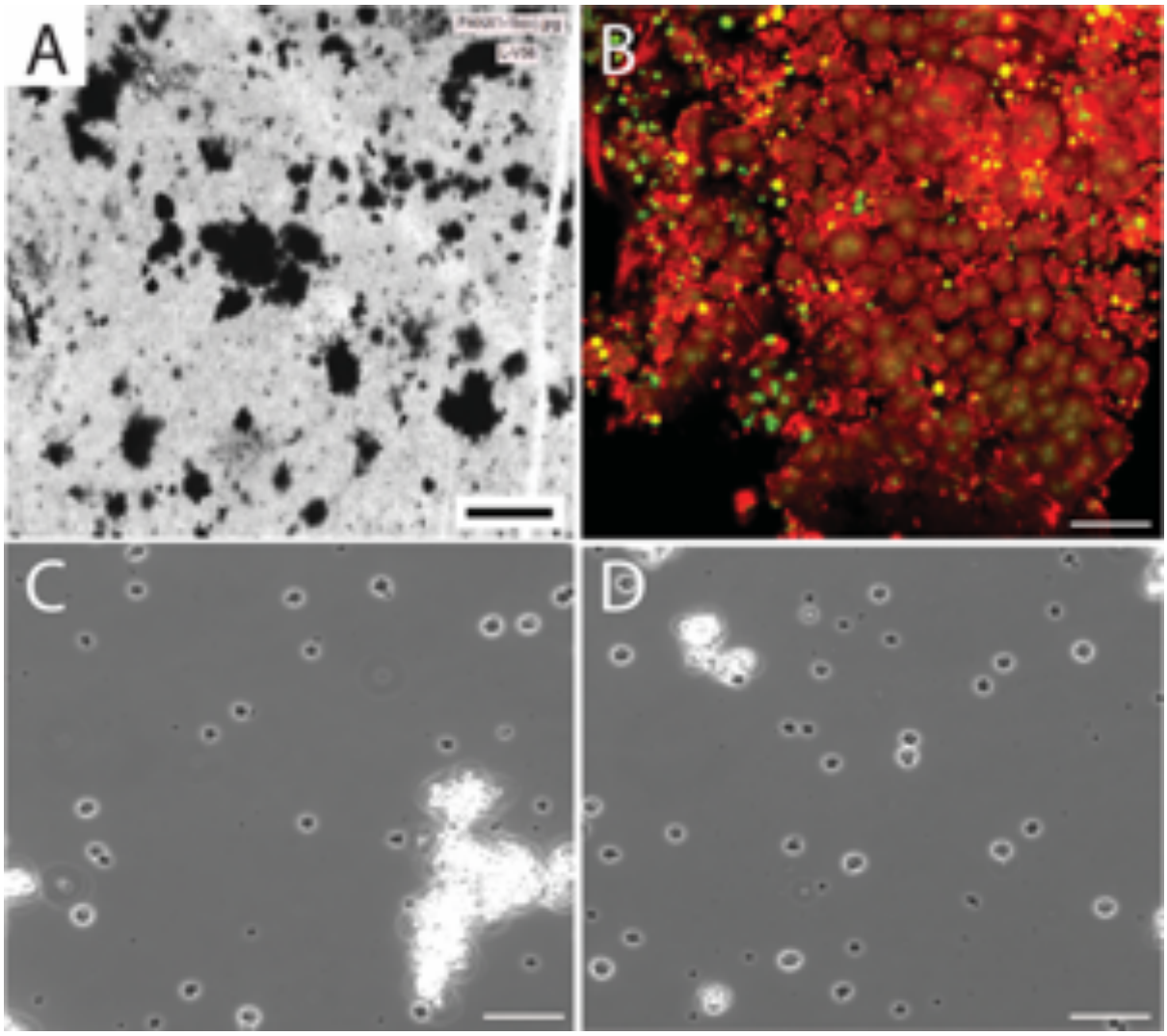

Fig. S88. Morphological comparison of SPF microfossils with *EM-P*.

Images A show spherical microfossils with stellate projections reported from SPF (originally published by Sugitani *et al.,* 2013) (18). Scale bar in image A is 200µm. B-D are spinning-

disk confocal (B, stained as described above in fig. S87) and phase-contrast (C & D) images of morphologically analogous *EM-P* cells. Like microfossils, *EM-P* cells revived from the above-described crust formation formed stellate structures at cell periphery. Scale bars in images B-D are 10µm.

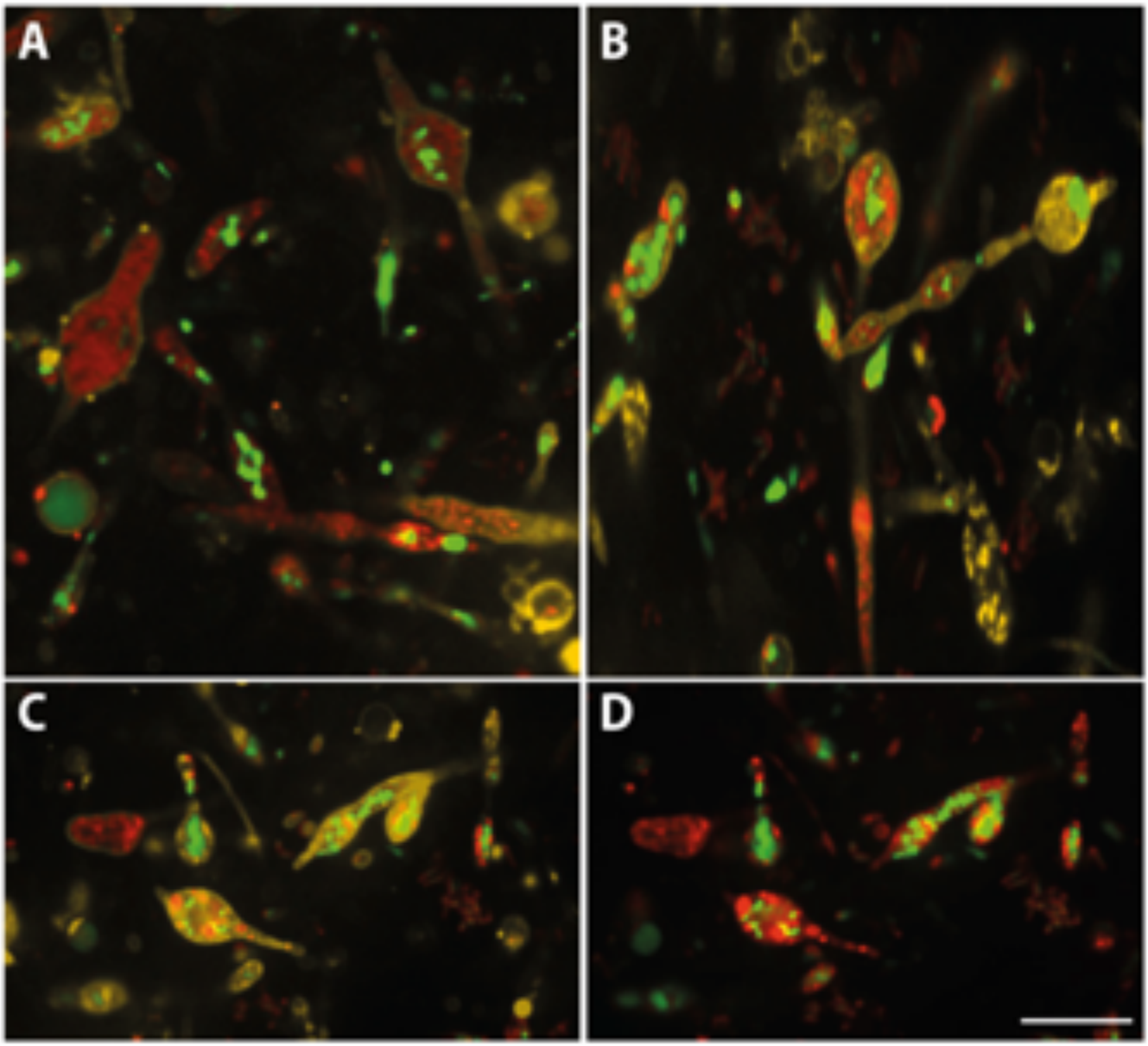

Fig. 89. Confocal microscope images of *RS-P*

Images A-D are filamentous morphotypes of *RS-P*. Cells in these images are stained with membrane dye FM™5-95 (Yellow), FAST™ Dil (Red) specific for lipid disordered (L_d) membrane and DAPI, specific for DNA (Green). Boxed regions within the images show cells

that spherical invaginations within the cell were composed of unsaturated fatty acids, compared to the saturated fatty acids at the cell periphery. Scale bars in images B-D are 10μm.

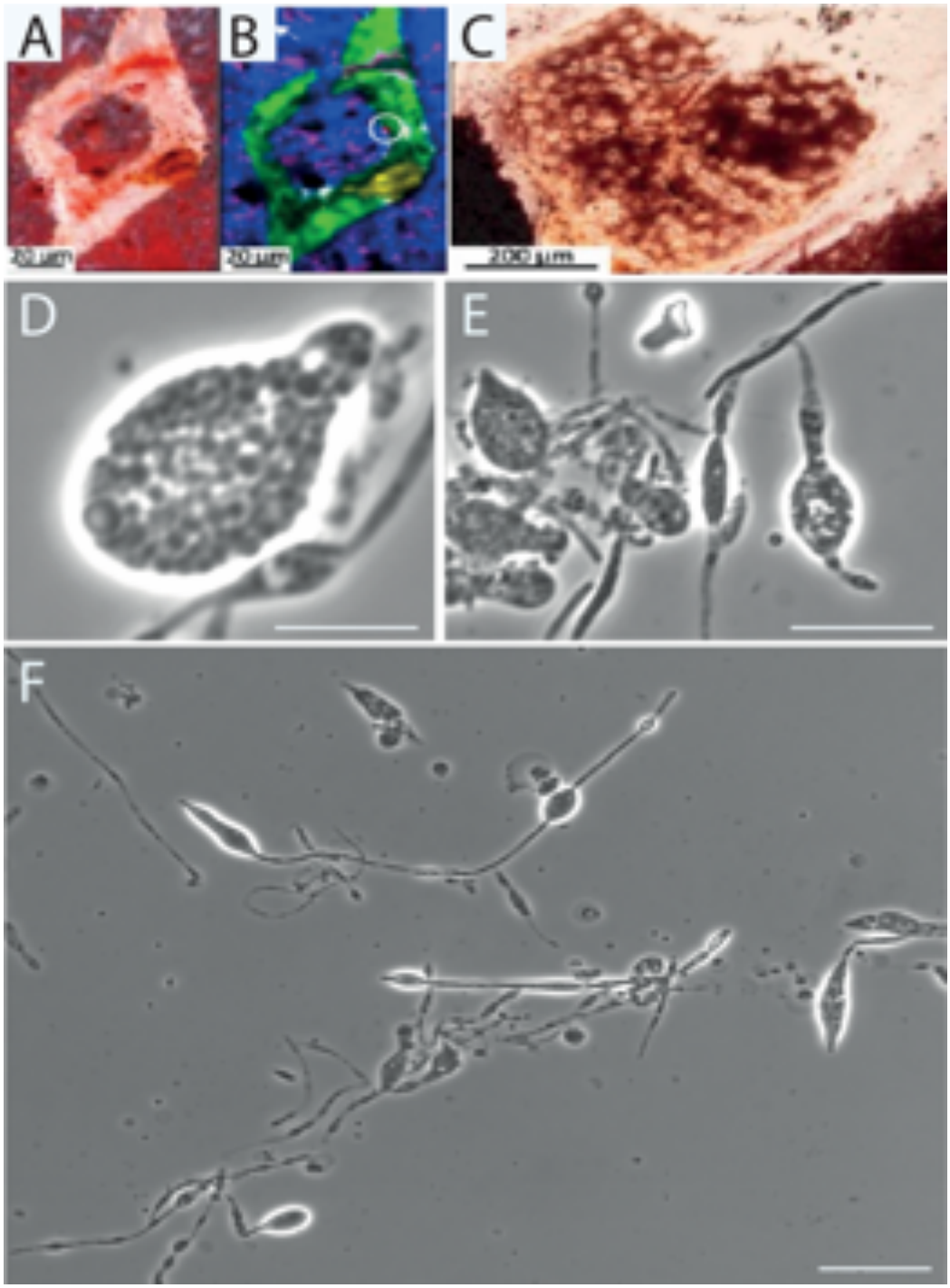

Fig. S90. Morphological comparison of *RS-P* with organic structures reported from granular iron formations.

Images A-C are organic structures reported from granular iron formations (originally published by Dodd *et al.,* 2018) (76). Image C show magnified region of lenticular cell with granular interiors. Images D-F are morphologically analogous *RS-P* cells. Similar granular structures can be seen in *RS-P* (D-F). Scale bars in images D & E are 10µm.

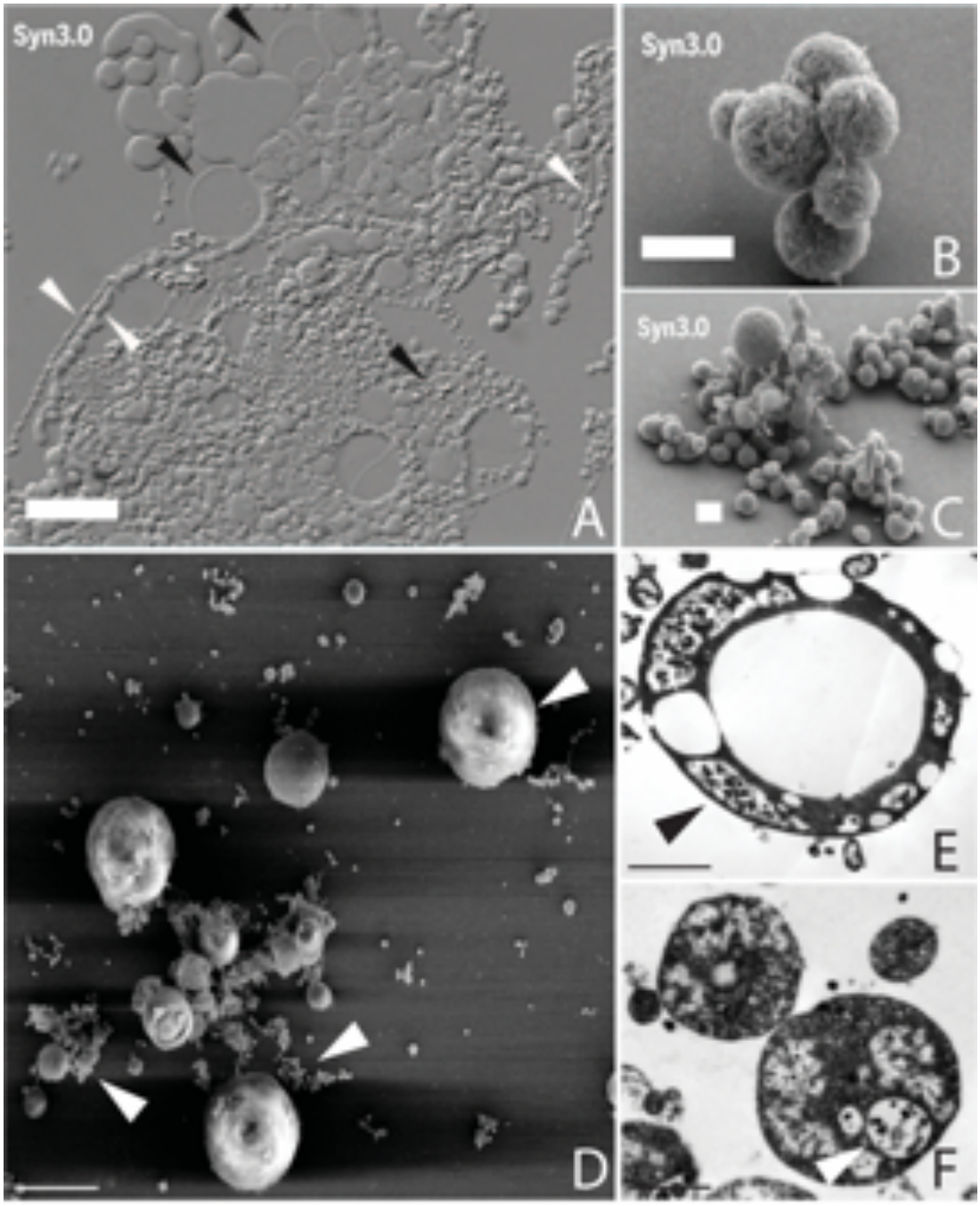

Fig. S91. Morphological comparison of *EM-P* with Syn3.0.

Images A, B & C show Syn3.0. White and black arrows in these images' points to segmented filaments and large intracellular vesicles (originally published by Hutchison *et al.,* 2016) (82). Scale bars in images A and B & C are 10µm and 1µm respectively. Images D, E & F show morphologically analogous *EM-P* cells. Arrows in image A points to large spherical

cells with a string or external daughter cells, similar to the segmented filaments observed in Syn3.0. Images E & F are TEM images of *EM-P* showing intracellular vesicles and daughter cells within the vesicle. Similar cells can be seen among Syn3.0 (pointed by black arrow in the bottom right part of image A). Scale bars in images D and E & F are 2μm and 0.5μm respectively.

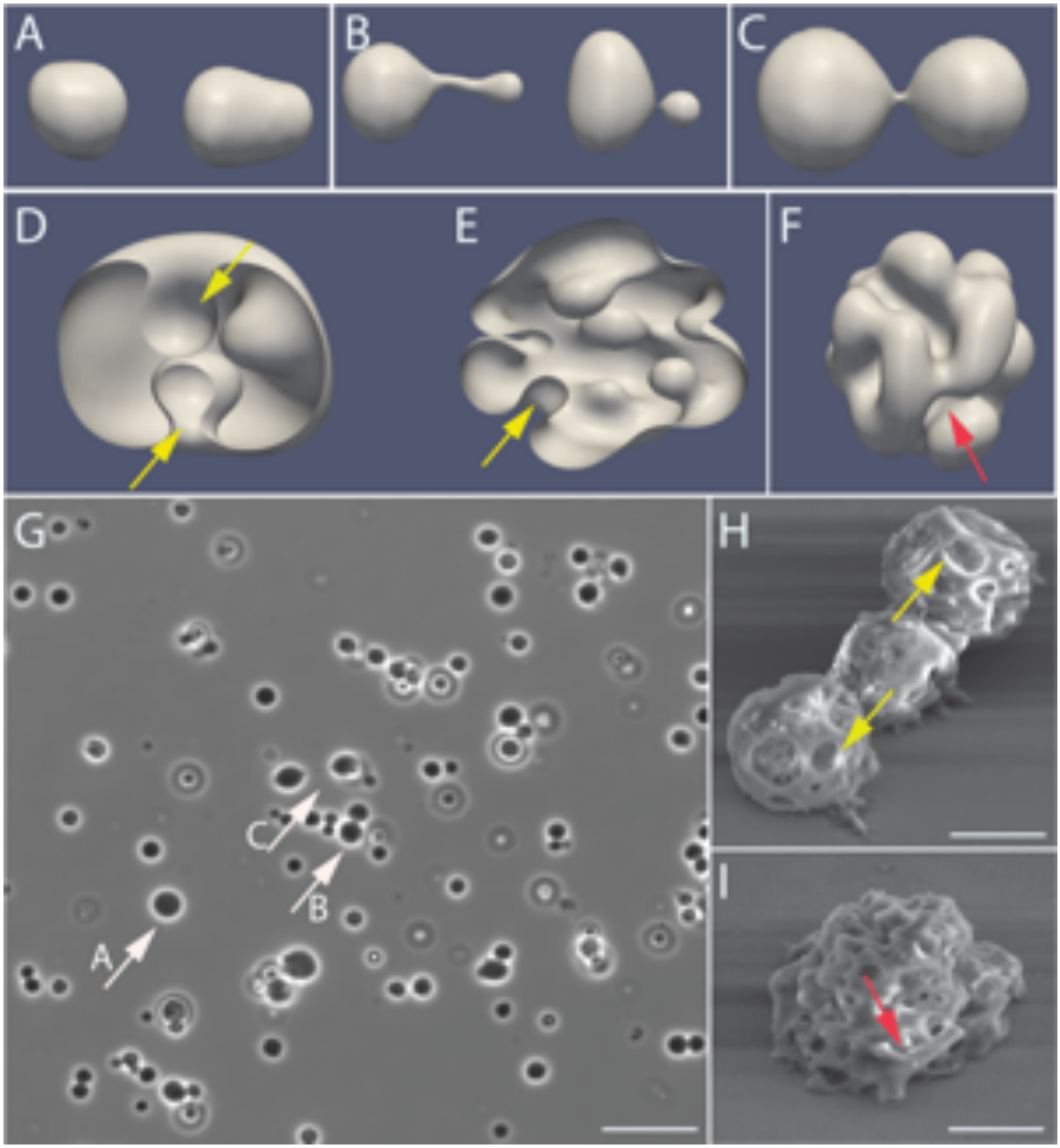

Fig. S92. Morphological comparison of *EM-P* with protocell morphologies from computer simulations.

Images A-F show cellular morphologies that were a result of numerical simulations (originally published by Ruiz-Herrero *et al.,* 2019) (83). Images G-I are morphologically analogous *EM-P* cells. Arrows in image G points to cells that were morphologically analogous to cells shown in images A-C (as the letters next to the arrows). Yellow arrows in

images D, E & H points to invaginations on cells surface. Red arrows in image F & I points to similar folding pattern observed in both *EM-P* and the ones predicted by numerical simulations. Such pattern of folding was predicted to have formed when rate of increase in cytoplasmic content of the cell is out paced by rate of phospholipid synthesis. Scale bars: in 10μm (G) and 0.5μm (H&I) respectively.

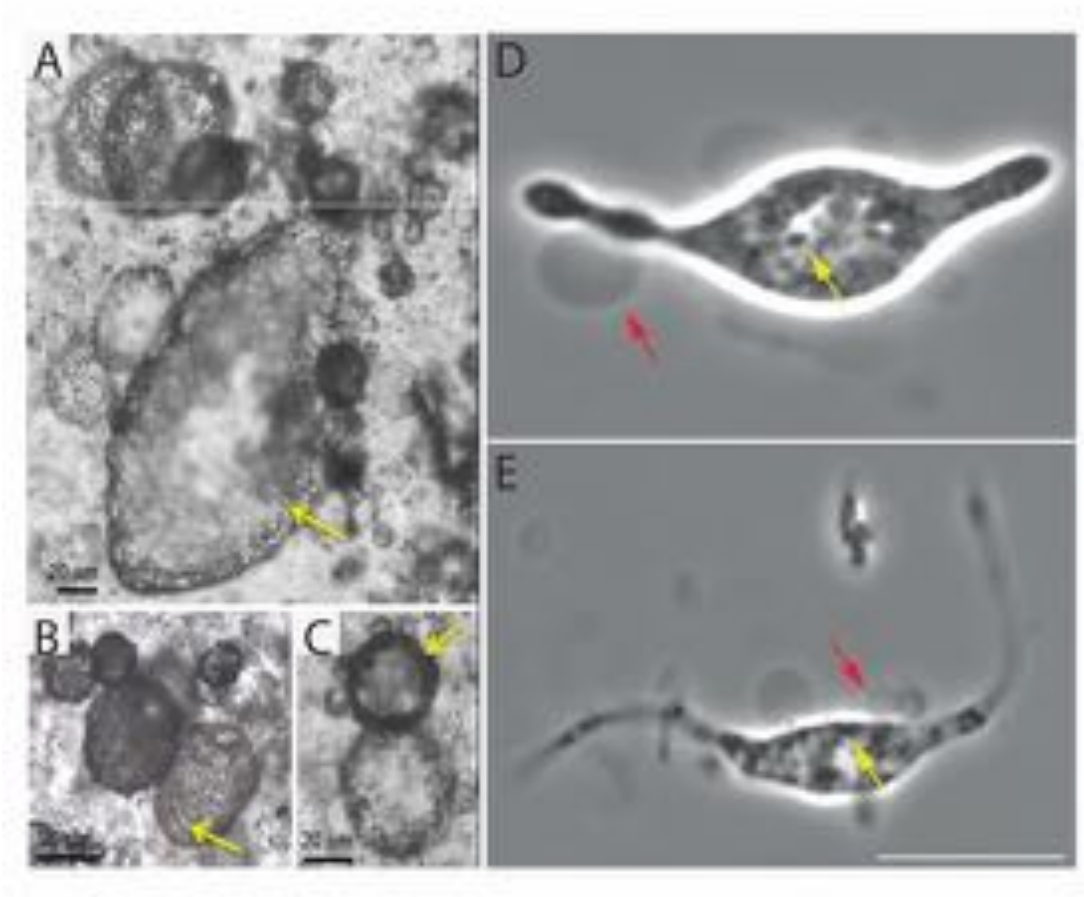

Fig. S93. Morphological comparison of elliptical organic structures from SPF with *RS-P*

Images A-C are elliptical organic structures reported from SPF (originally published by Wacey *et al.,* 2018) (49). These cells were characterised by granular Fe(III)-mineral interiors (Yellow arrows in image A). Red arrows in these images points to hollow spherical structures attached to the surface of these elliptical structures. Similar spherical structures with or devoid of organic carbon could also be seen in images A-C. Images C & D are morphologically analogous *RS-P* cells. Like microfossils, these cells were elliptical in shape

with granular interiors (yellow arrows). Red arrows in these images points to membrane vesicles that were largely devoid of organic carbon, similar to the ones reported from SPF. Similar OMV's with organic carbon can be seen in Fig. 8. Yellow arrows in image B points to intracellular lath like structures, comparison of these structure with *RS-P* was shown in fig. S94-S96. Scale bars: 10µm (D & E).

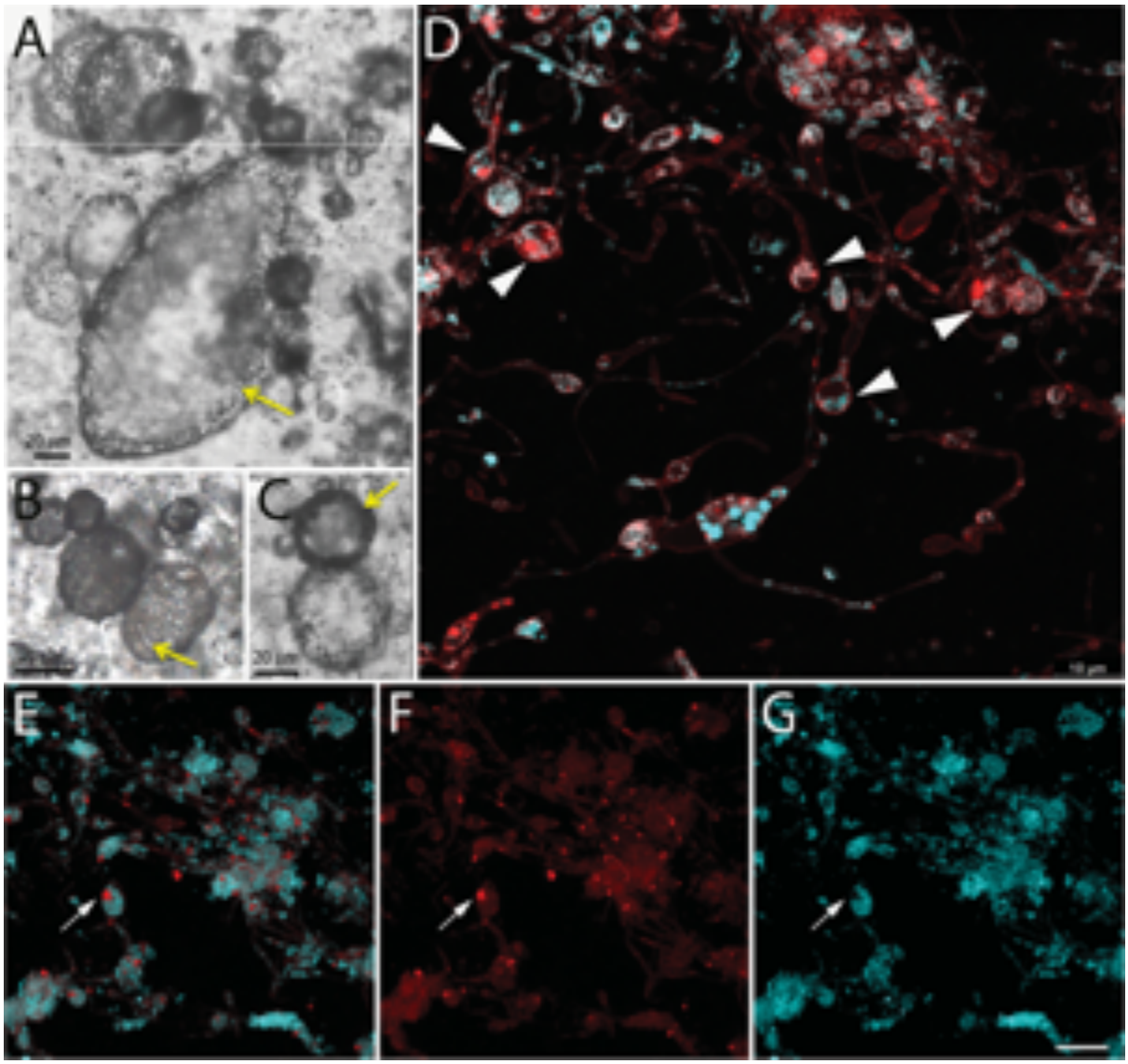

Fig. S94. Comparison of elliptical organic structures from SPF and *RS-P*.

Images A-C are elliptical organic structures reported from SPF (originally published by Wacey *et al.,* 2018) (49). Images D-G are morphologically analogous *RS-P* cells. Arrows in

image D points to elliptical cells with granular interiors. Cells in images D-G are stained with universal membrane (red) and lipid disordered (L_d) membrane specific (cyan) stains. Images E-G show overlay and images with individual stains. Arrows in these images' points to structures similar to lath like structures creating gaps in the distribution of intracellular granules. *RS-P* cells with lath-like structures were shown in fig. S95 &S96. Scale bar: 10µm (G).

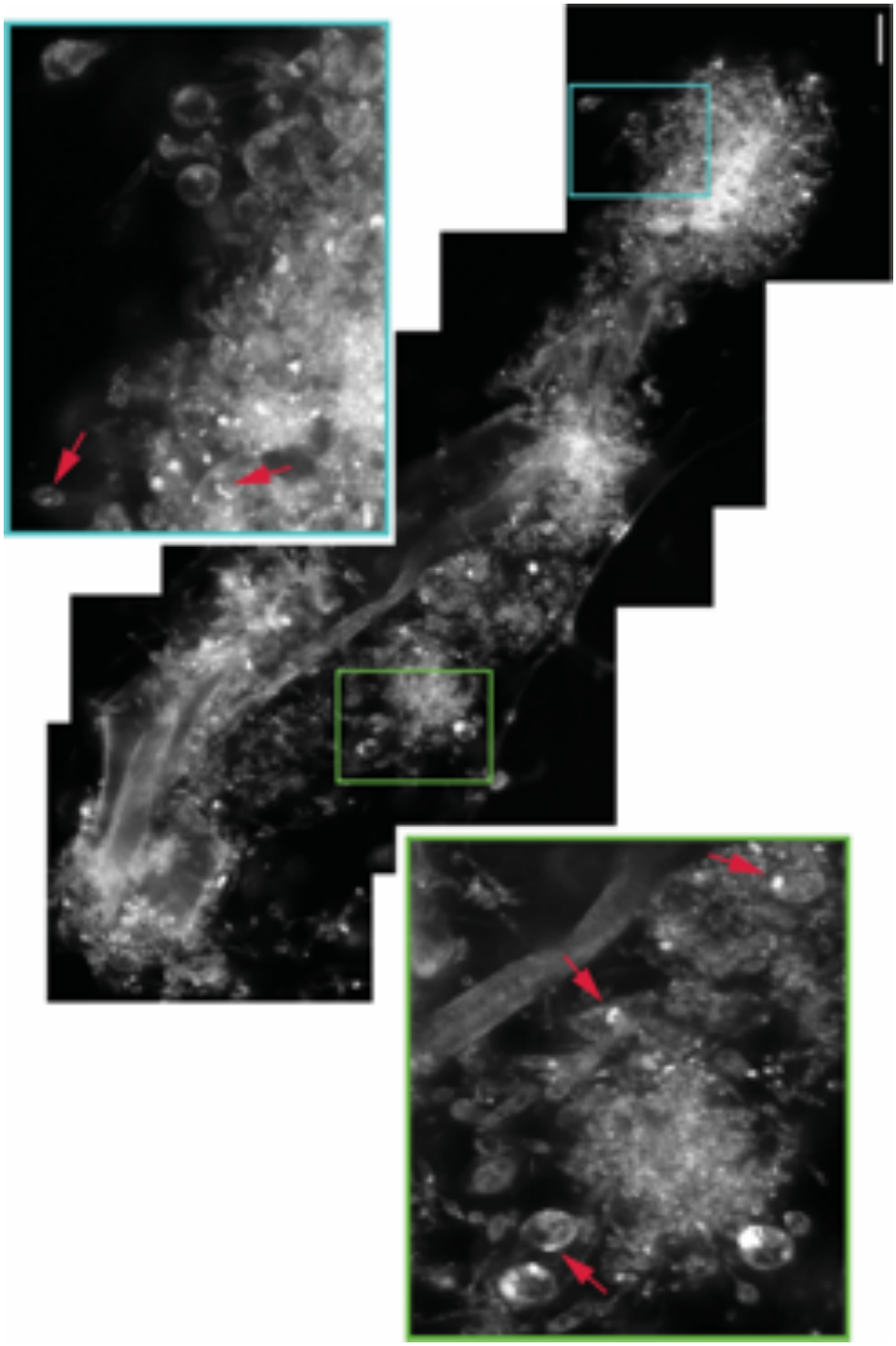

Fig. S95. Late growth stage *RS-P* cells

Image shows late growth stage *RS-P* cells with both granular and lath-like (red arrows) interiors. Images B&C are magnified regions within green and blue boxes. Cells in these

images are stained with membrane dye FM™5-95 and imaged using a STED microscope. Scale bar: 10μm.

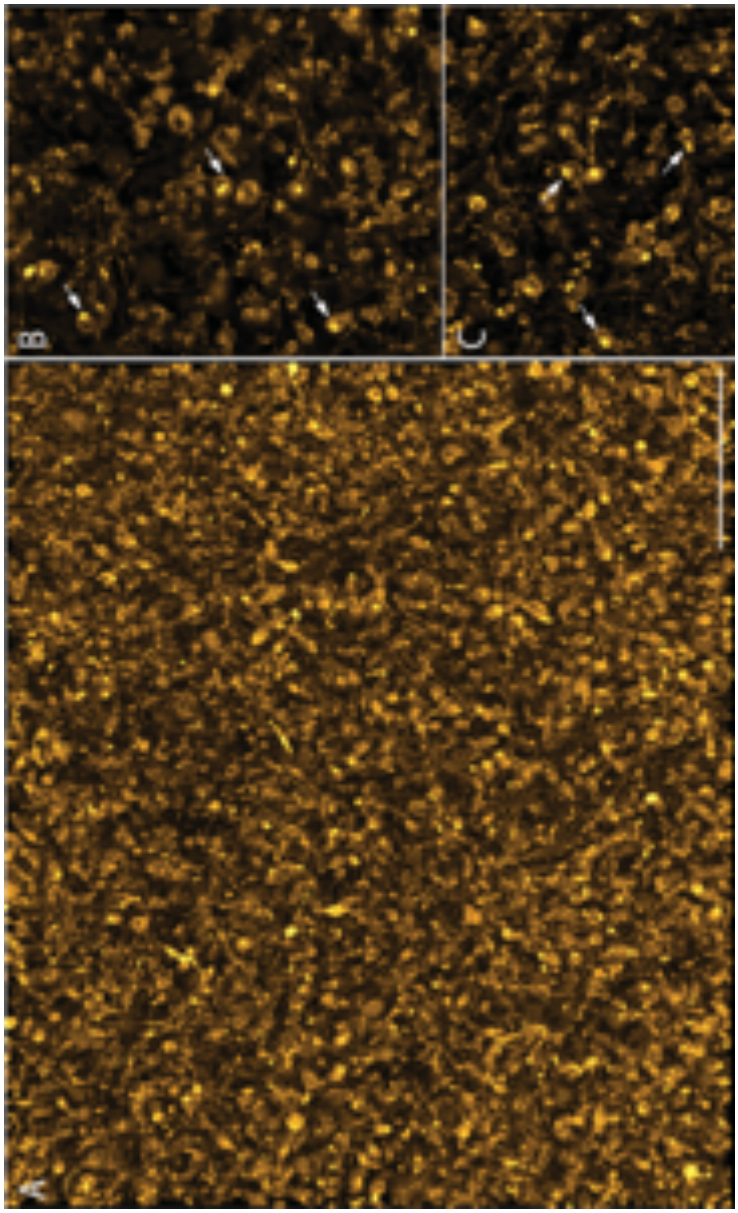

Fig. S96. *RS-P* cell aggregates

A shows 3D rendered image of mid growth stage *RS-P* cells growing as densely packed microbial mat. Images B & C show magnified regions of the cell aggrigations. Arrows in these images point to different morphotypes of lath-like structures. Cells in these images are

stained with membrane dye FM™5-95 and imaged using a STED microscope. Scale bar: 10µm.

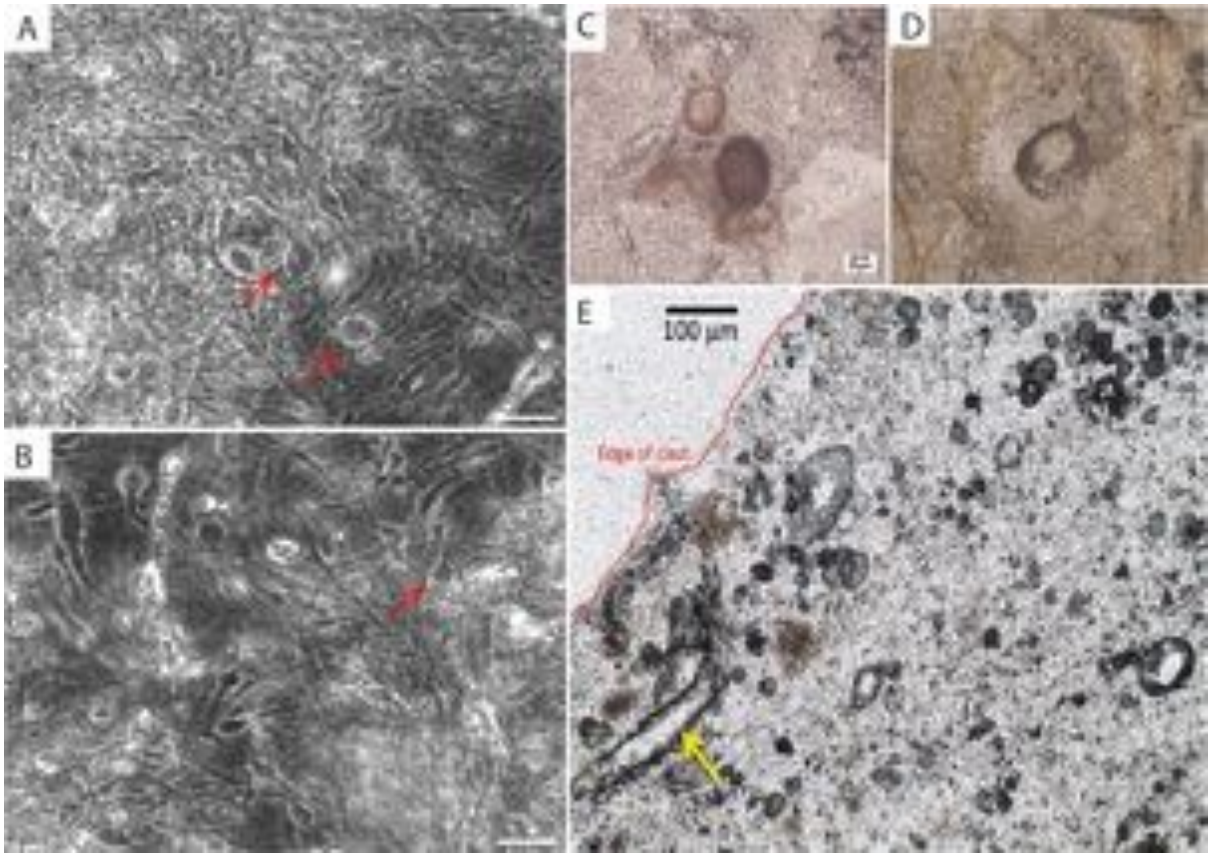

Fig. S97. Comparison of linear strands of *RS-P* morphotypes with elliptical structures from SPF.

Images A & B are phase-contrast images of *RS-P* cells enclosed in a film-like membrane debris. Arrows in the image's points to lenticular cells with granular interiors beneath the membrane. Images C & D are morphologically analogous organic structures reported from Moodies formations (originally published by Köhler *et al.,* 2019) (12). Image E shows morphologically analogous organic structures reported from SPF (originally published by Wacey *et al.,* 2018) (49). Scale bars: 10µm (A and B).

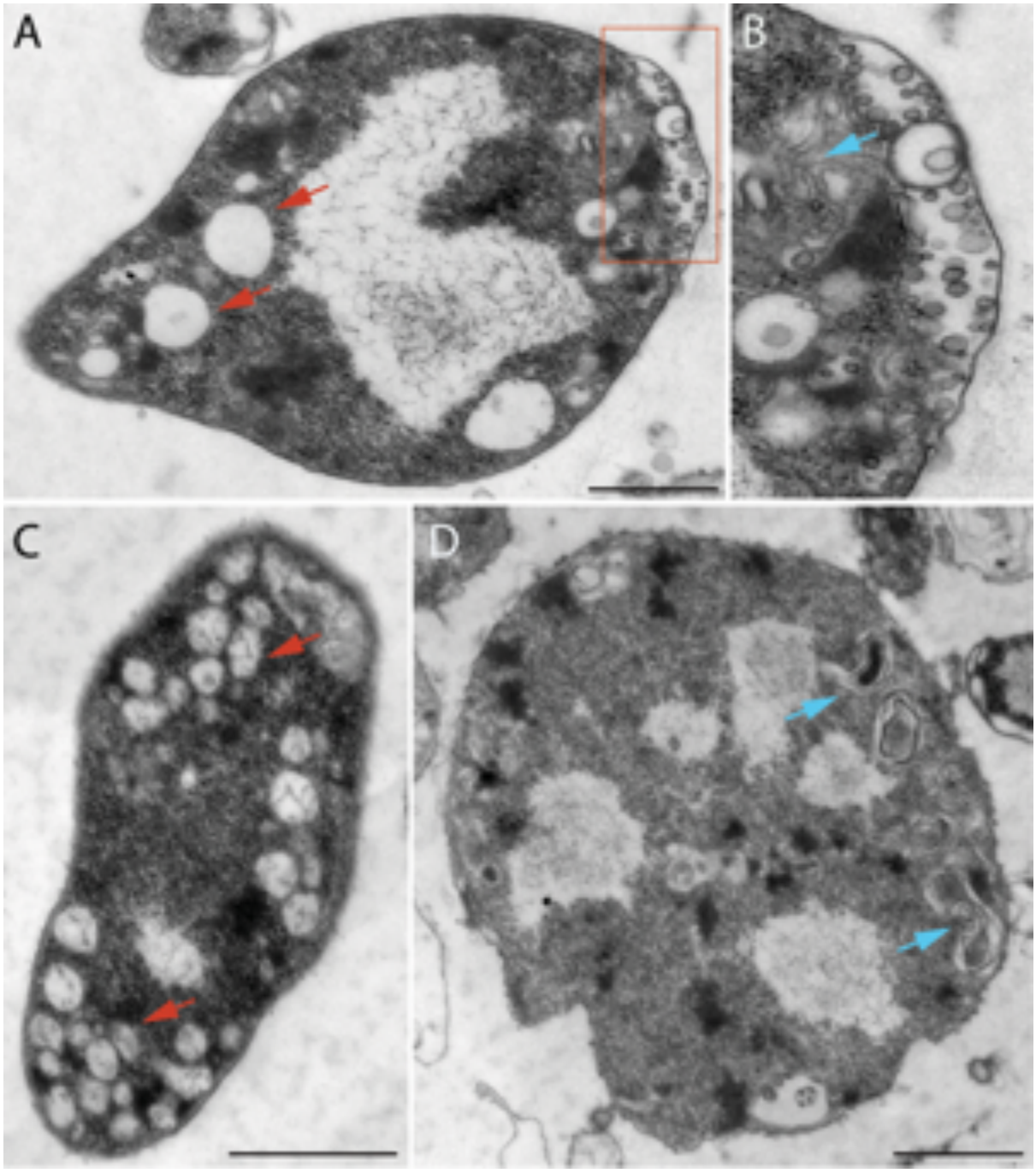

Fig. S98. Intracellular membrane vesicles in *RS-P*.

Image A show TEM images lenticular *RS-P* cell with intracellular membrane vesicles. Image B shows magnified region of image A (within the box). These vesicles are formed by membrane invagination of outer cell membrane (B). Invagination of outer membrane happened either into the cell like shown in image A or out of the cell, like shown in fig. S93

& Fig. 8. Image D shows multilamellar filamentous vesicles (cyan arrows). We presume that these vesicles should have formed lath-like structures reported from some microfossil sites like Dresser formation (fig. S93). Scale bar: 0.5μm.

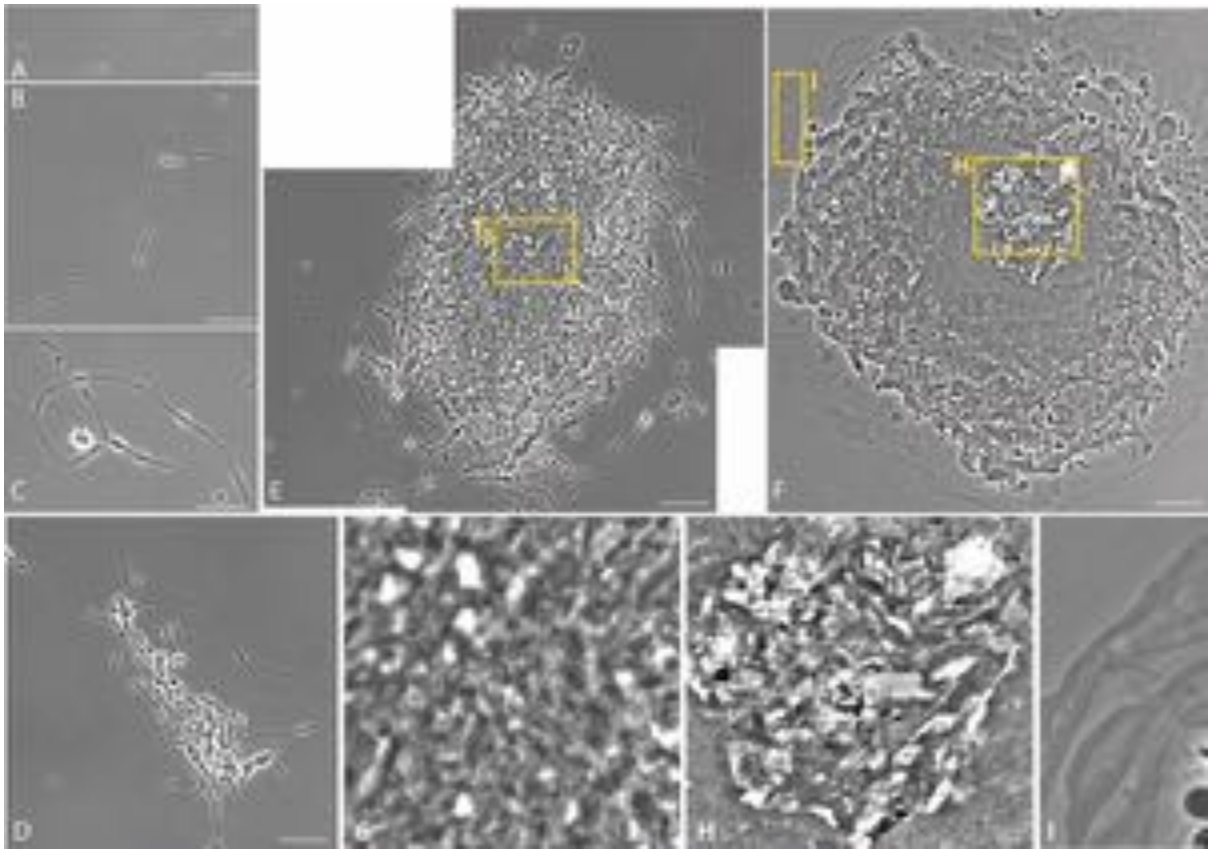

Fig. S99. Sequential stages involved in of film-like membrane debris in *RS-P* incubations

Images A-E are phase-contrast images of early growth stages (2-4 days from inoculation) *RS-P*. In this stage most *RS-P* cells were in the form of long filamentous cells with blistered appearance (yellow arrows). Image-E shows mid-growth stage *RS-P* cells (4-8 days from inoculation), in which filaments cells entangled with one another and formed large clumps. Individual cells can be seen in the periphery of these clumps. The boxed region in Image-E (magnified and shown as Image-G), shows that these regions of the clumps, that lack

distinguishable individual cells. Image-F shows an example of late growth stages (8-15 days from inoculation) *RS-P.* In such aggregations, distinct individual cells were restricted to the periphery. Membrane debris formed at the centre of these structures transformed into a film-like structure (magnified and shown as Image-H) and excess membrane transformed into filamentous lipid vesicles and extruded from the core to the periphery of the colony (magnified and shown as Image-I). TEM and 3D-rendered STED images of these clumps are shown as fig. S100 and fig. S101 respectively. Scale bars: 10µm.

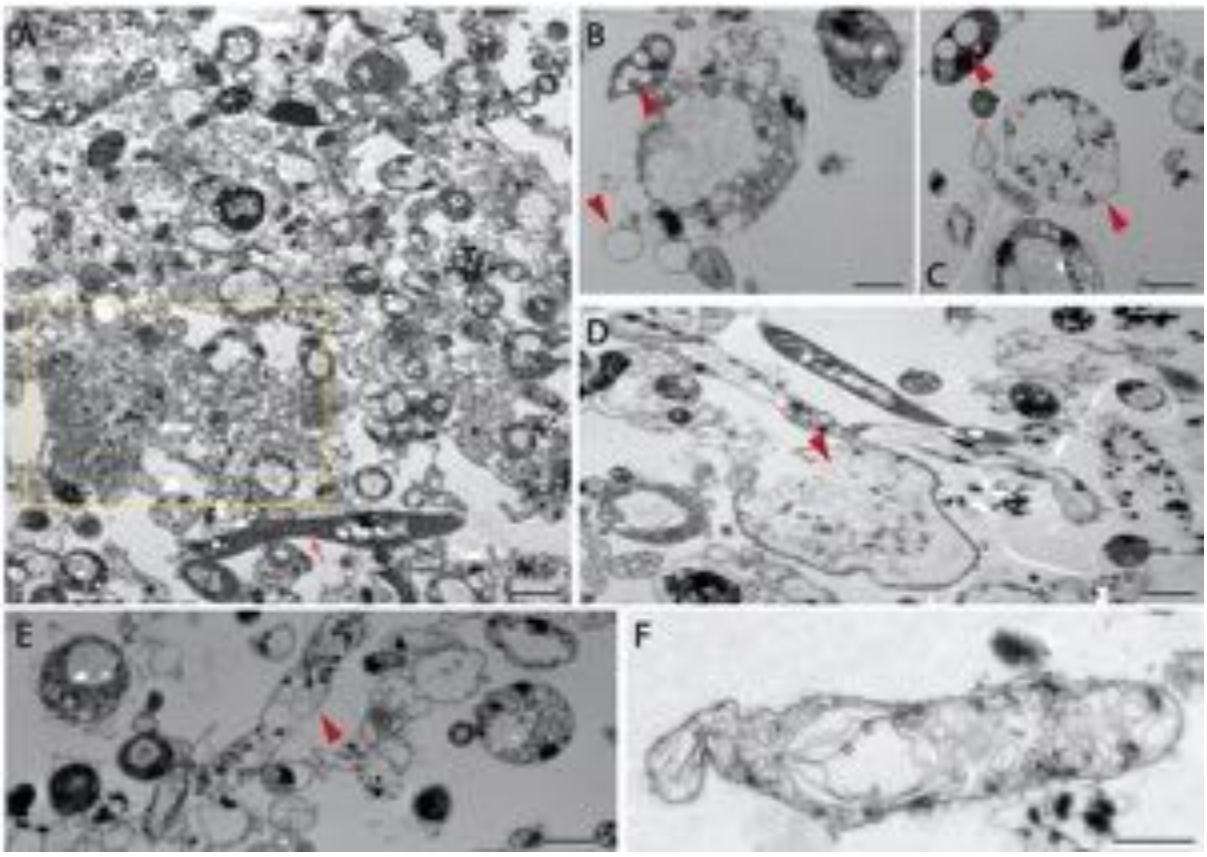

Fig. S100. TEM images of late growth stage *RS-P* cells.

Images A-F depicts late growth stage *RS-P* cells that were mostly depleted in their cytoplasmic content and instead contain hollow intracellular membrane vesicles. Boxed region in Image-A highlights the fusion of individual cell to forms film-like membrane

debris, similar to what was shown in fig. S99 & S101. Red arrow (open) points to a filamentous *RS-P* cell with cytoplasm (typical example of early growth stage morphotype of *RS-P*). Image-F depicts filamentous *RS-P* cell depleted in its cytoplasmic content (typical example of late growth stage morphotype of *RS-P*). Images B-E depicts the intermediary growth stage morphotype of *RS-P.* Red arrows (closed) in these images' points to hollow intracellular membrane vesicles of different sizes. Scale bars: 100nm.

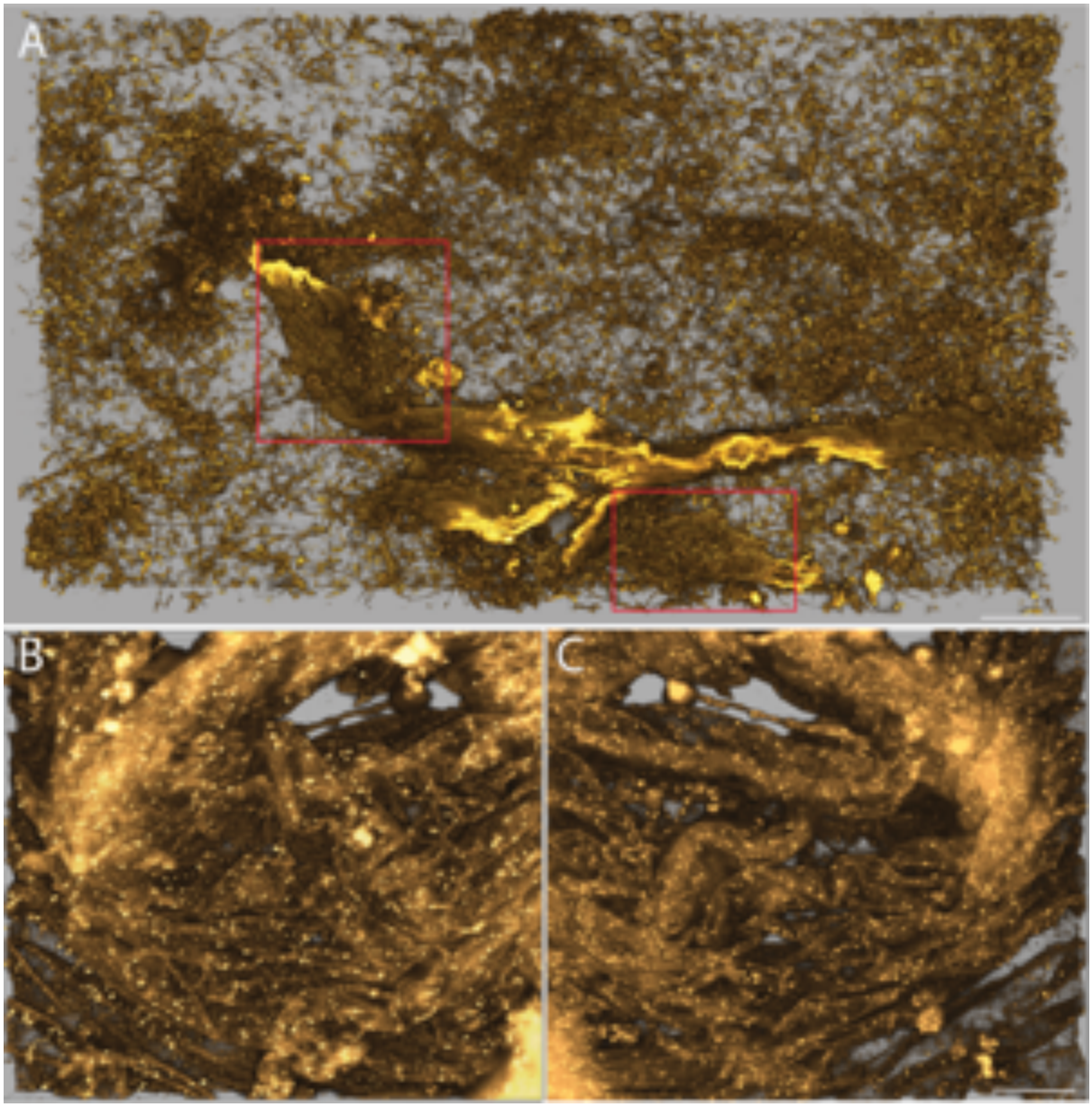

Fig. S101. 3D-rendered STED images of late growth stage *RS-P* cells with membrane debris.

Image A thin filamentous *RS-P* cells observed during the late growth-stages. All *RS-P* morphologies can be seen in the image, thin filamentous, thick tubular, lenticular cells along with hollow outer membrane vesicles and membrane debris (boxed regions). Images B&C shows anterior and posterior view of film-like membrane debris observed in *RS-P*. The

granular structures associated with the membrane debris were the intracellular membrane vesicles, that were shown in fig. S98 and fig. S100. Scale bar: 50µm (A) and 10µm (C).

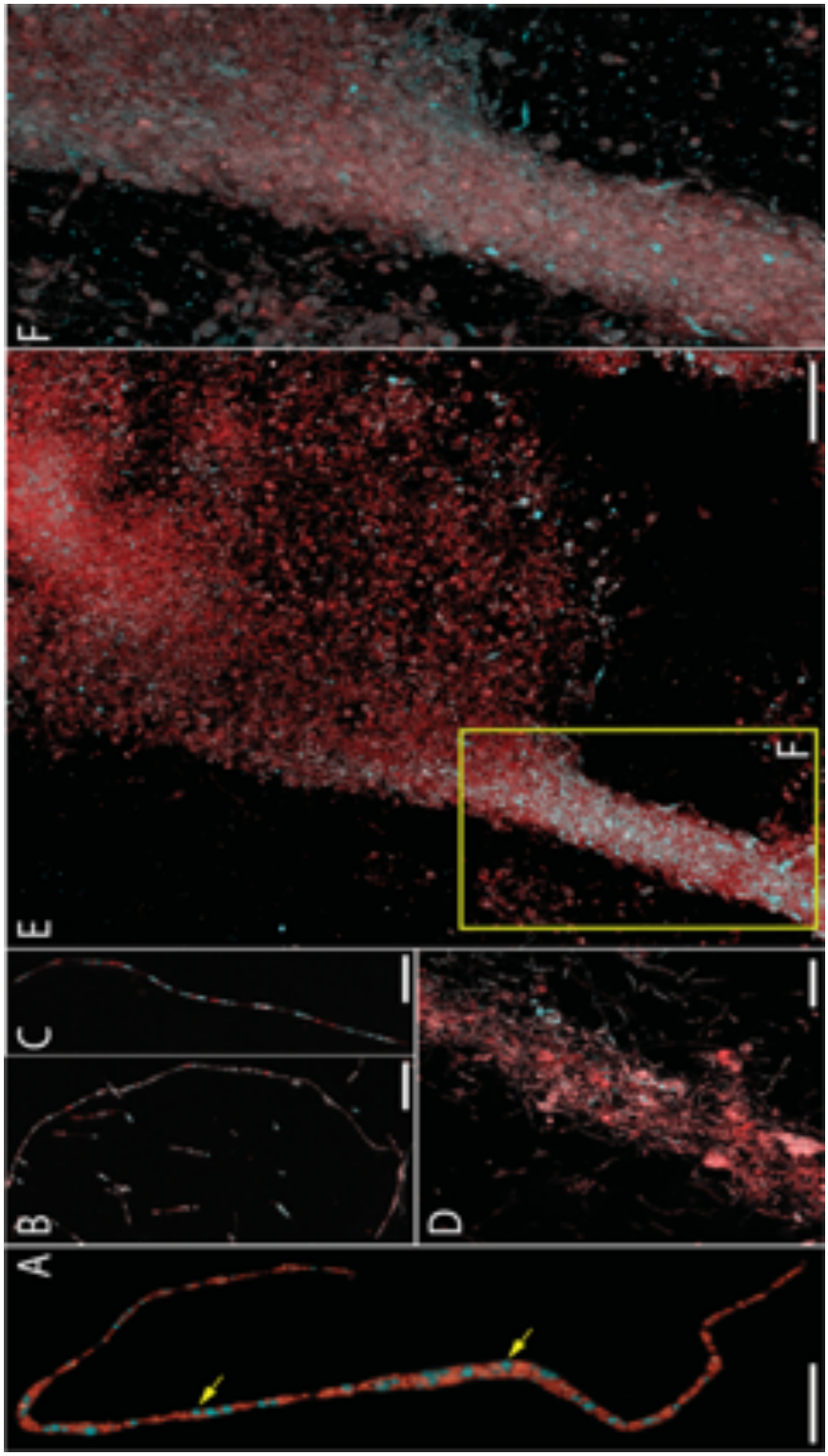

Fig. S102. Sequential stages involved in transformation of *RS-P* into volcanic glass-like membrane debris.

Images A-C are filamentous morphotypes of *RS-P*. Cells in these images are stained with membrane dye FM^{TM}5-95 (red) and stain specific for lipid disordered (L_d) membrane (cyan). Over the course of our incubation these cells entangled with each other to form linear clumps (D-E). Image E shows the ongoing process of such clumping. Image F is the magnified image boxed region in image E. Lysis of cells within the clumps led to formation of membrane debris, like shown in fig. S101. Intracellular L_d rich membrane vesicles formed granular structures that were attached to the membrane debris. Subsequent morphological transformations of such membrane debris into volcanic glass like structures are shown in fig. S103 & S104. Scale bars: 10µm (E-I).

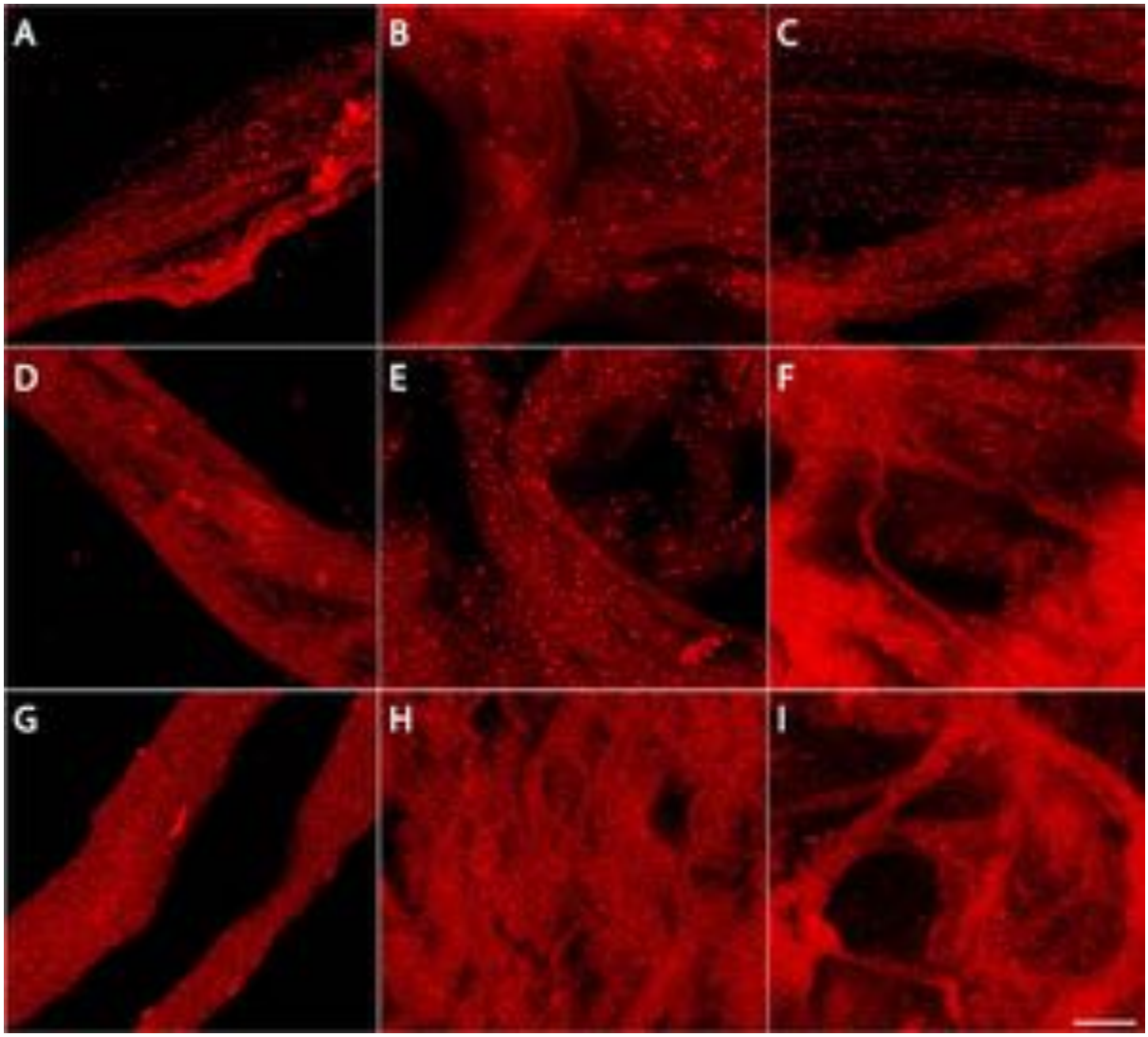

Fig. S103. Sequential stages involved in transformation of *RS-P* into volcanic glass-like membrane debris.

Images A-I are STED microscope images of *RS-P*'s membrane debris. Images A, D & G shows stages in transformation of fibrous strands of membrane into linear clumps of membrane debris without distinctive individual membrane strands. Images B, E & H and C, F & I show similar transformation of thread like membrane debris either into fabric or spun thread like structures. Granular structures associated with fibrous membrane debris were intracellular membrane vesicles shown in fig. S97, S99 and fig. S101A. Comparison of these

structures with SPF formation organic structures was presented as fig. S104. Membrane debris in these images are stained with Nile red. Scale bar: 10µm (I).

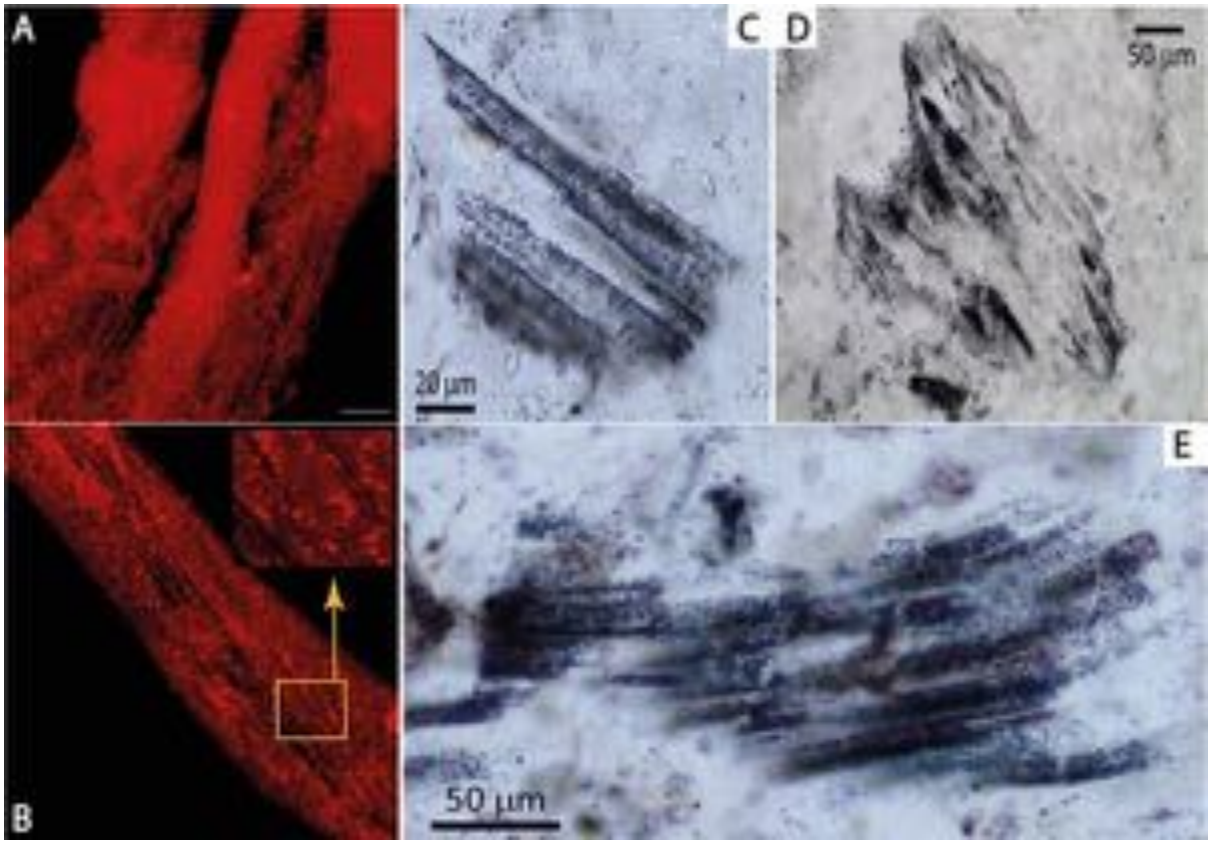

Fig. S104. Comparison of linear strands of *RS-P* membrane debris and SPF organic structures.

Images A & B are fibrous membrane debris produced by *RS-P*. Insert in image B shows magnified region of membrane debris, showing spherical/granular structures associated with membrane debris. Membrane debris in these images are stained with nile red. Images C-E are morphologically analogous organic structures reported from SPF site (originally published by Wacey *et al.,* 2018) (49). Like *RS-P*, these structures were composed of long strands of membrane debris with spherical structures associated with it. Like in *RS-P*, we presume these spherical structures were tiny intracellular vacuoles (fig. S102). Scale bar: 10µm (A).

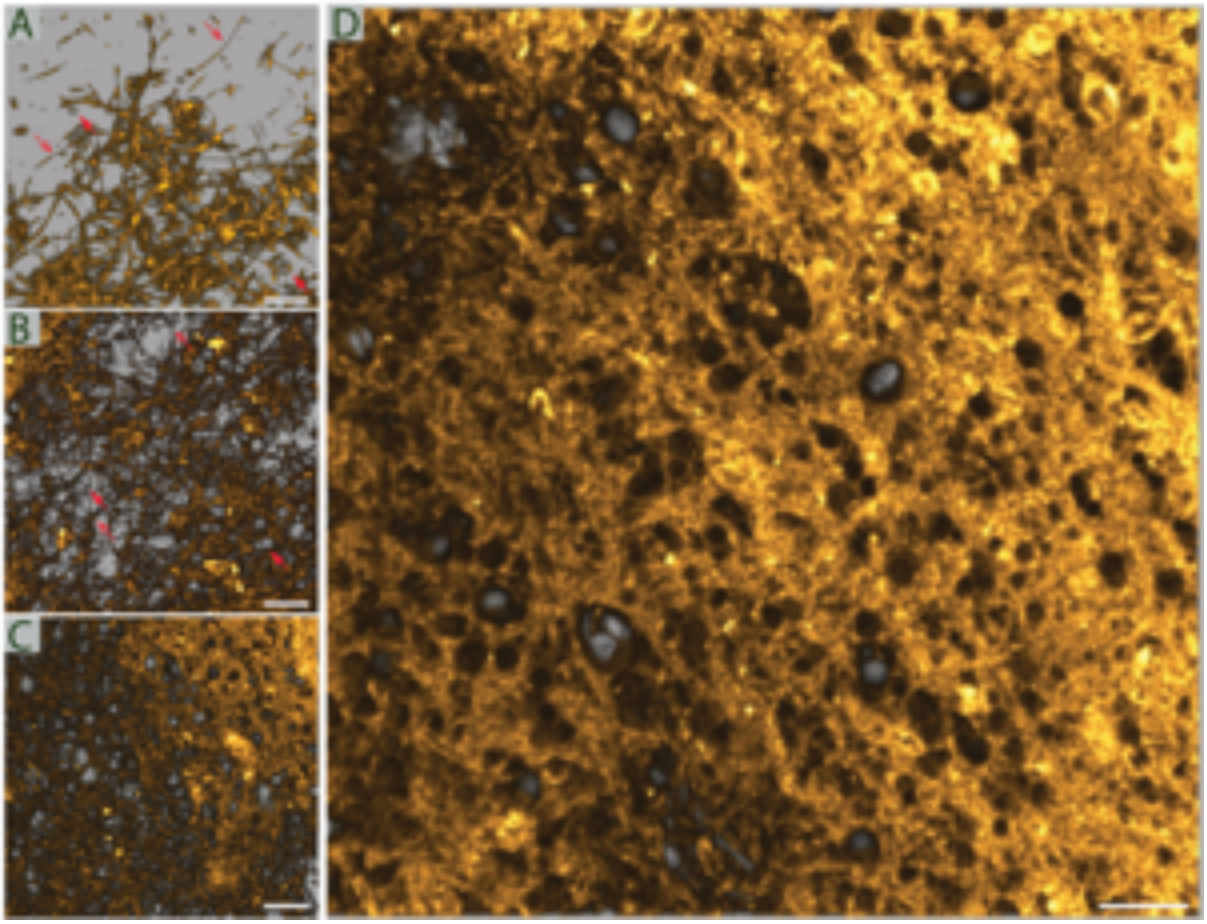

Fig. S105. Sequential morphological transformation of *RS-P* leading to formation of pumice like structures.

Image A shows *RS-P* cells from an early growth stage. Open and closed arrows in these images' points to filamentous *RS-P* cells and outer membrane vesicles respectively. Formation of these vesicles was also shown in Fig. 8 and S93. Images B-D shows gradual increase in *RS-P* cell numbers leading to an increase in cell densities and tighter packing of cells. Image D shows largely un-distinguishable filamentous cells and hollow outer membrane vesicles in-between. These *RS-P* cell mats gradually transformed into pumice like structures (shown in fig. S106). Scale bar: 10µm.

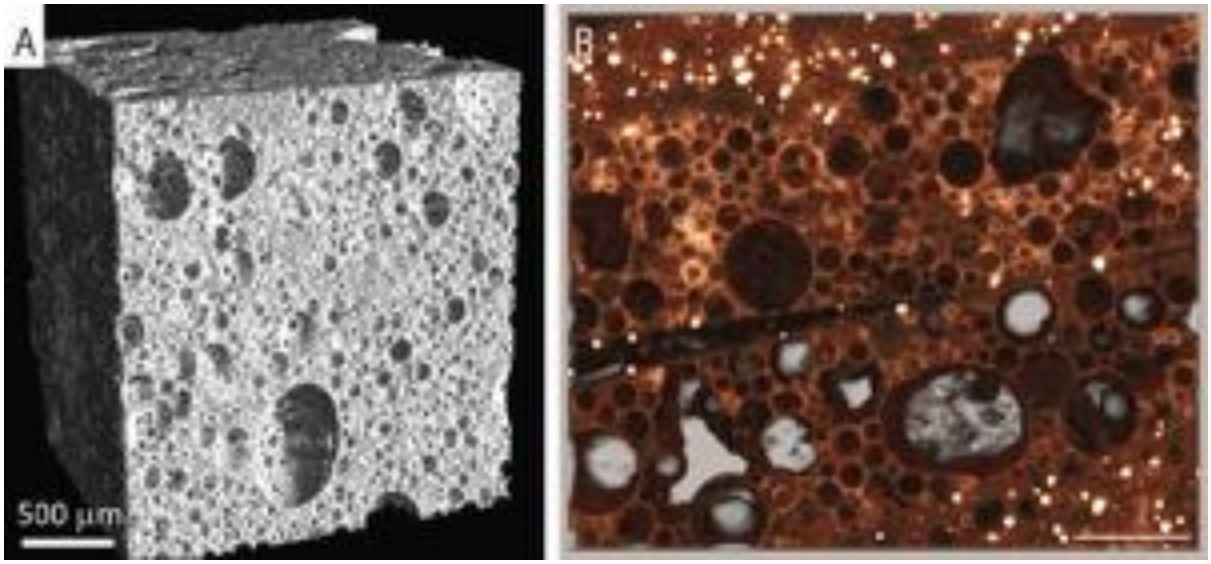

Fig. S106. Comparison of *RS-P* colony morphologies with volcanic pumice.

Image A shows volcanic pumice (originally published by Wacey *et al.,* 2018) (49). Image B is the 3D-rendered image of *RS-P* membrane debris similar in appearance to pumice. Hollow spherical structures within membrane debris were OMV's of *RS-P*. Scale bar: 5µm (B).

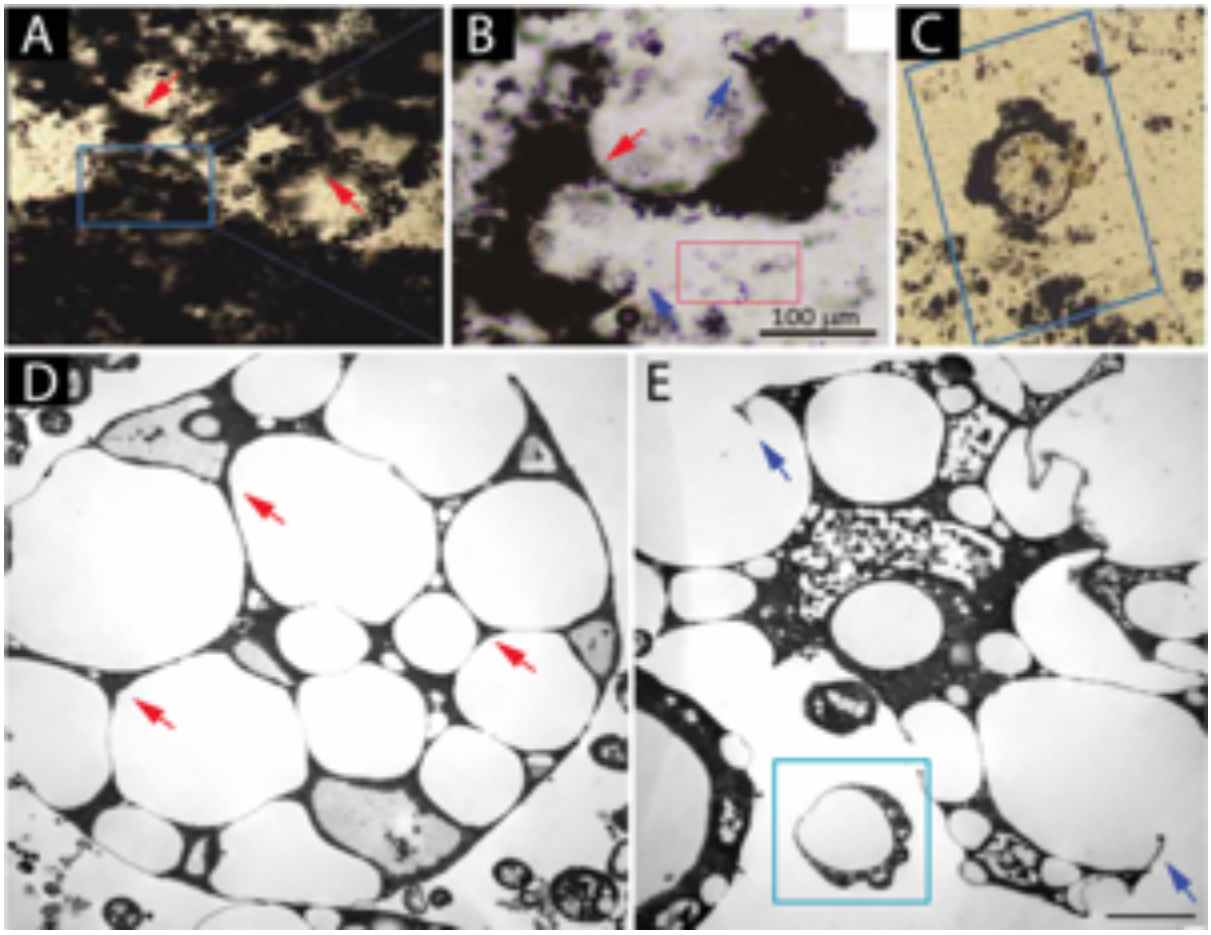

Fig. S107. Morphological comparison of Dresser formation spherical microfossils with *EM-P*.

Images A-C were aggregations of spherical microfossils reported from Dresser formation (originally published by Wacey *et al.,* 2018) (10). D&E are TEM images of morphologically analogous *EM-P* cells. Image A shows hollow spherical aggregations that were devoid of organic carbon. Similar *EM-P* cells were shown in image D. Red arrows in this image points to Y-shaped junctions with organic carbon. Such *EM-P* cells over the course of their growth underwent membrane rupture to release daughter cells (image E, purple arrows). The process of lysis and dispersion of these cells was shown in Image E. Morphology of these *EM-P* cells were very similar to the organic structures reported from Dresser formation (Image B). Like *EM-P* cells, presence of daughter cells can also be seen in close proximity (red box). Image C

shows an isolated spherical structure, with inner spherical inclusions with presumed thick and uneven cell wall. Morphologically analogous *EM-P* cell can be seen in Image E (Cyan box). Movie S4, shows similar structures with spherical inclusions (daughter cells). Scale bar: 200nm (E).

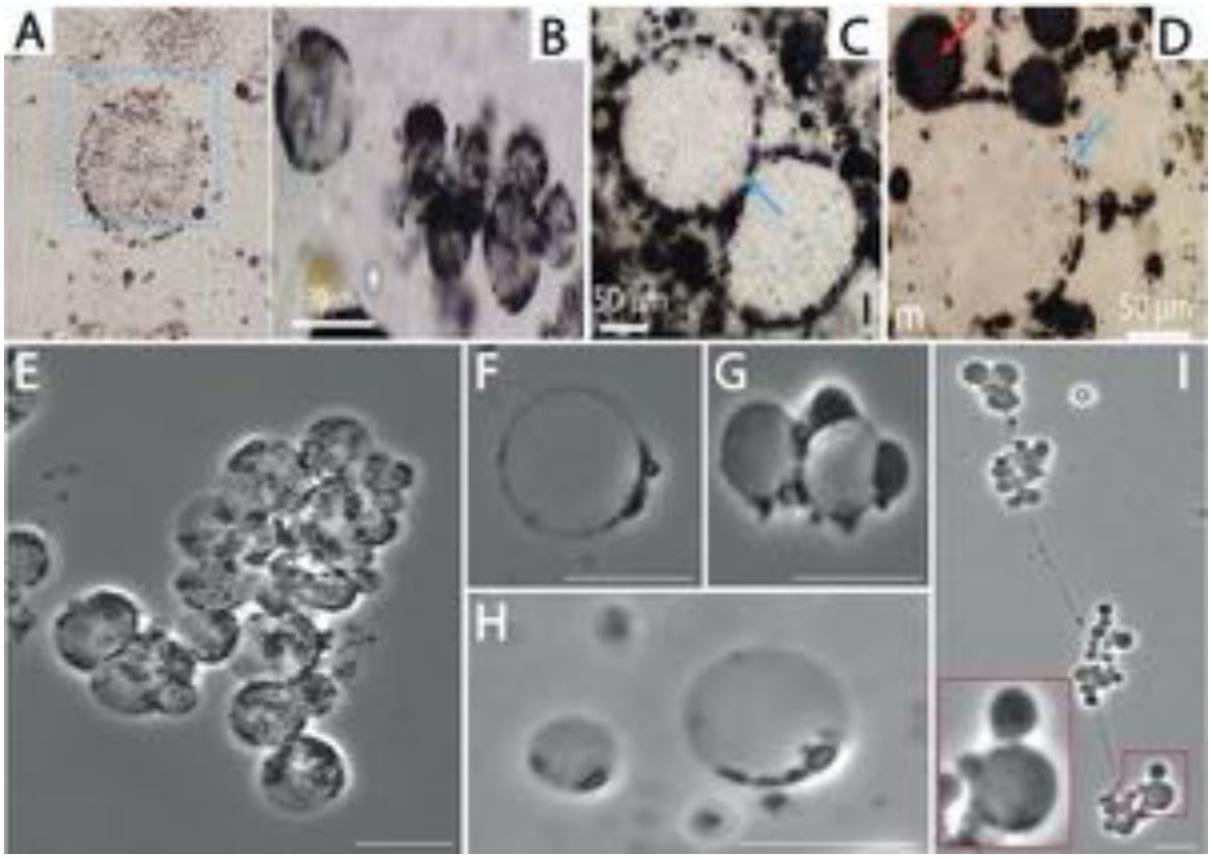

Fig. S108. Morphological comparison of Dresser formation spherical microfossils with *EM-P*.

Images A-D were aggregations of spherical microfossils reported from Dresser formation (originally published by Wacey *et al.,* 2018) (10). E-I are images of morphologically analogous structures observed from *EM-P*. Blue arrows in images C&D points to cells with discontinuous cell walls. Similar cell boundary features can be seen in *EM-P* (E-H). Sequential stages involved in the formation of such *EM-P* cells was shown in fig. S109 &

S110. Red arrows in image D points to cells with cytoplasm that were attached to the hollow spherical cells. Morphologically analogous *EM-P* cells were shown in image G. Scale bars 10μm (E-I).

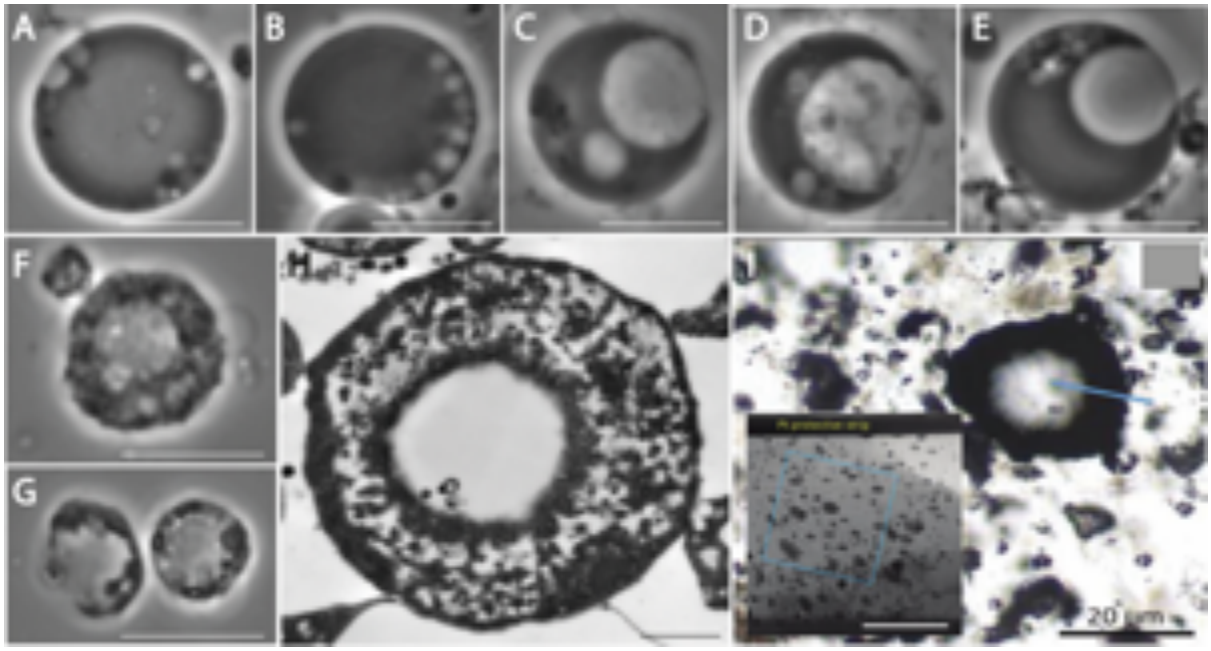

Fig. S109. Sequence of morphological transformations leading to formation of *EM-P* cell having an appearance of a thick cell wall.

Images A-G shows the sequential morphological transformations of *EM-P* cells with one large central vacuole and multiple smaller vacuoles. Over the course of its growth smaller vacuoles were squeezed between cell and vacuole membrane (F-G), leading to the appearance of a pours cell wall. Images F-G and H are phase-contrast and TEM images of such *EM-P* cells. Image I show spherical microfossil reported from Dresser formation (originally published by Wacey *et al.,* 2018) (10). Insert in the image I is TEM image of region indicated by blue line. The porous nature of this region is similar to *EM-P* cell shown in image H. Scale bars in images A-G and H are 10μm and 200nm respectively. Scale bar: 500nm.

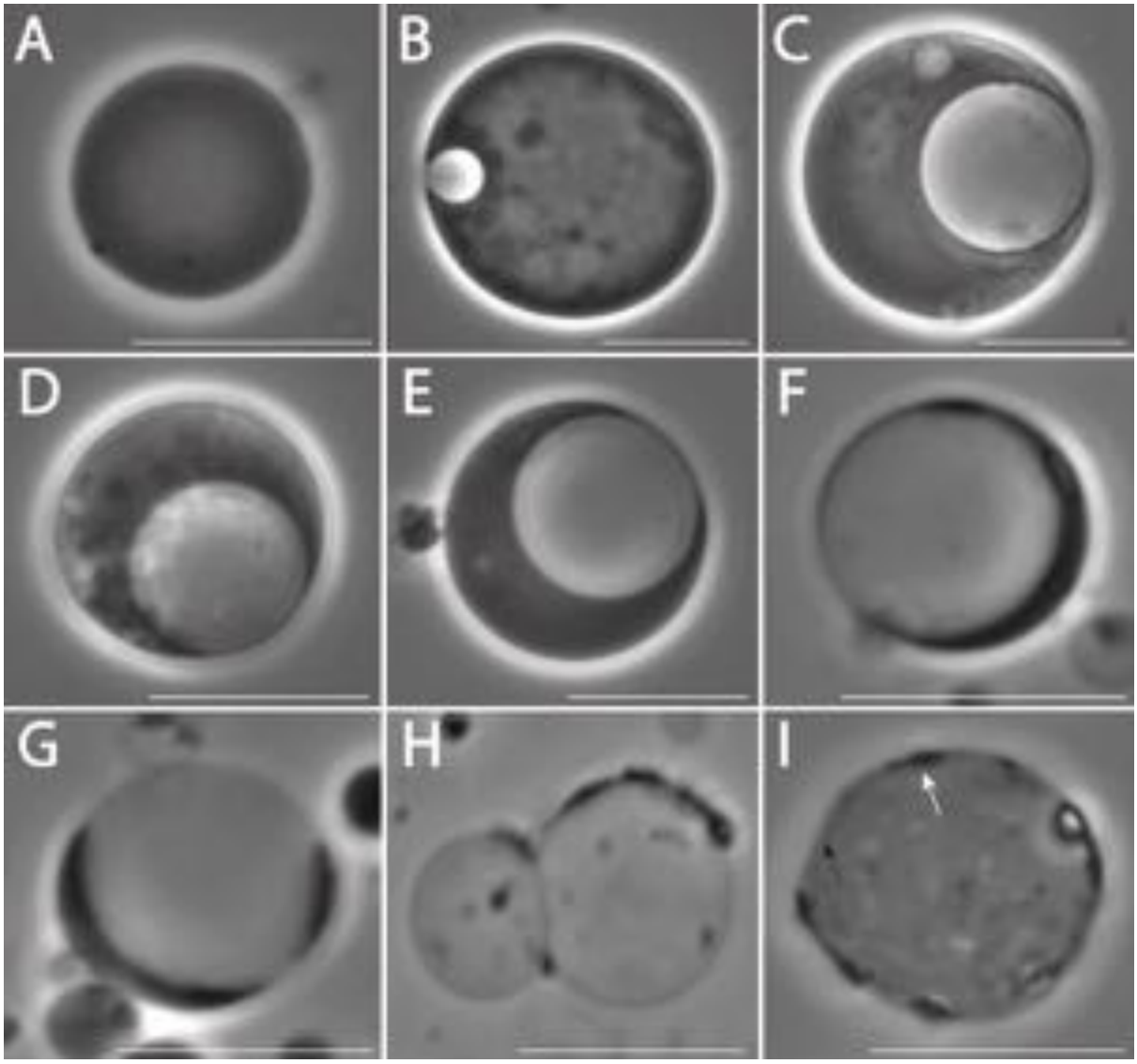

Fig. S110. Sequential morphological transformation of *EM-P* cells with cytoplasm to hollow vacuoles.

Images A-I phase-contrast images of *EM-P*. In sequence they show, formation (B) and increase in size of intracellular vacuole (B-G). Over the course of its growth, cytoplasm from the parent cell is transferred into the daughter cells in the vacuole (barely visible tiny spherical structures in the vacuole) which led to gradual depletion of cytoplasmic volume and a gradual increase in vesicle volume. In their late growth stages, presence of cytoplasm is restricted to periphery of the cell as discontinuous patches (H&I). Scale bars: 10µm.

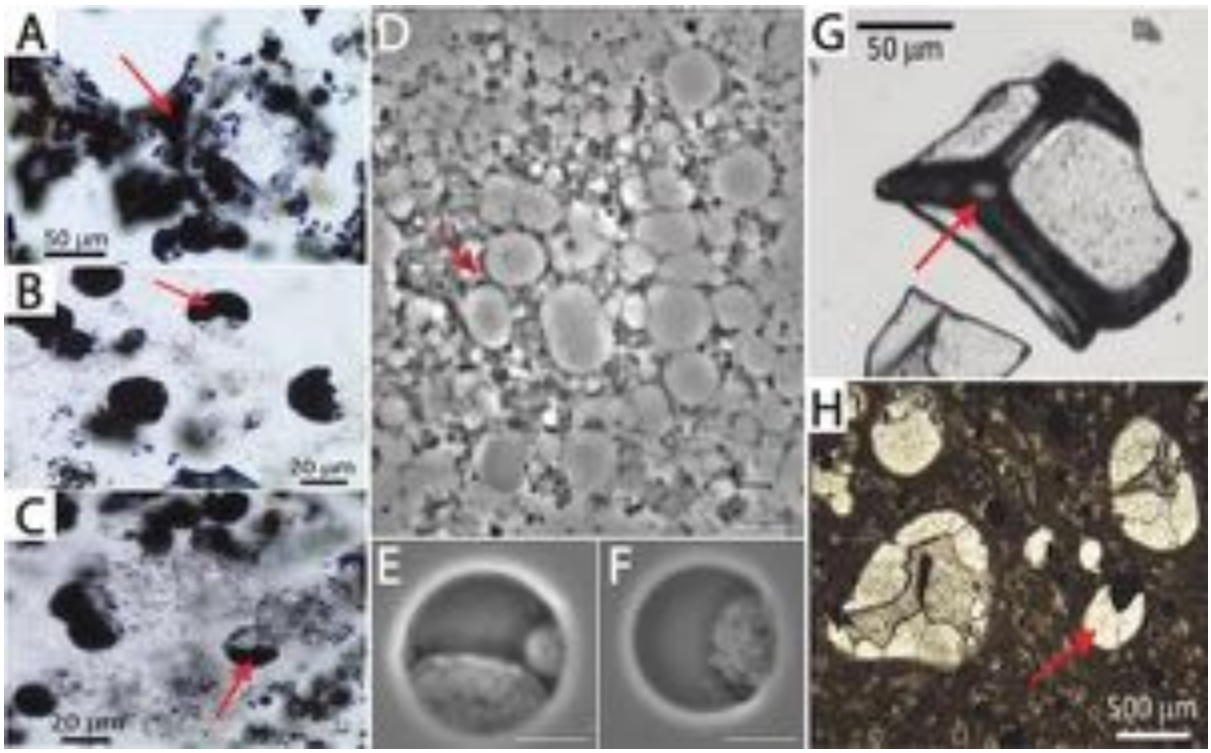

Fig. S111. Morphological comparison organic structures reported from Dresser formation with *EM-P*.

Images A-C were spherical microfossils reported from Dresser formation (originally published by Wacey *et al.,* 2018) (10). Images D-F are morphologically analogous structures observed from *EM-P*. Images G-H were images of volcanic glass (originally published by Wacey *et al.,* 2018) (10). Red arrows in Image A points to the intersection between three hollow spherical structures, resembling volcanic glass (G). Similar spherical structures devoid of organic carbon and Y-shaped junctions that were rich in organic carbon can be seen in *EM-P* (Image D, red arrow). Images B & C shows cells that were partially depleted in organic carbon (red arrows), similar to structures reported from volcanic glass. Analogous morphotypes of *EM-P* were shown in images E & F. Scale bars 10µm(D-F).

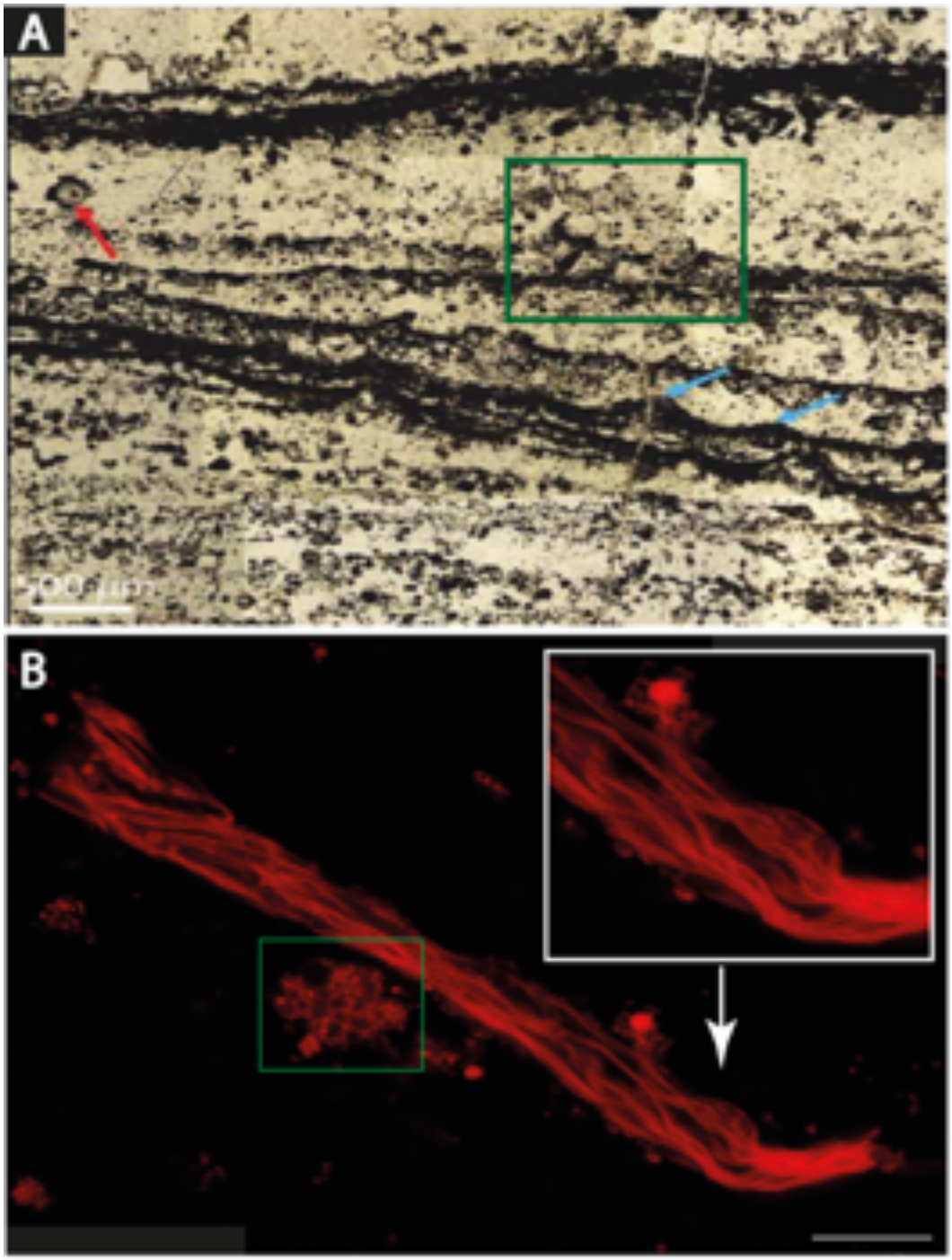

Fig. S112. Morphological comparison organic structures reported from Dresser formation with *EM-P*.

Image A show organic structures reported from Dresser formation (originally published by Wacey *et al.,* 2018) (10). It shows wavy filamentous structures with individual (red arrow) or aggregations (green box) of hollow spherical inclusions. Image B is the membrane debris

formed by lysis of *EM-P*, which is analogous in its morphology to organic structures reported from Dresser formation. Regions within the green box shows similar clusters of hollow spherical cluster of vacuoles. Insert in image B is the magnified region of the membrane debris, showing its wavy pattern. Numerous spherical structures resembling *EM-P* daughter cells can also be seen associated with membrane debris. *EM-P* cell resembling the individual spherical structure (red arrow in image A) was shown in fig. S108E. Cells and membrane debris in image B was stained with membrane stain, FM™5-95 (red). Scale bar: 10µm (B).

Supplementary Table

Sample	DELTA 13/12C V-PDB ‰
Triptic Soya Broth	-19.38 (0.29)
EM-P	-23.71 (0.24)
13:0	-29.24 (1.24)
i14:0	-27.24 (0.14)
a14:0	-18.20 (1.39)
i15:0	-29.49 (0.67)
a16:0	-30.8 (0.24)
16:1 ω-7	-38.25 (0.70)
17:0	-30.85 (1.28)

Table 1: Table show $\delta^{13}C$ of growth media, biomass and fatty acids V-PDB ‰ of *EM-P*.

Sample	DELTA 13/12C V-PDB ‰
Nutrient Broth	-15.39 (0.21)
RS-P	-18.14 (0.91)
13:0	-28,40 (0.57)
14:0	-27.98 (2.24)
a15:0	-28.36 (0.74)
15:0	-16,24 (0.72)
16:1 ω-5	-41.35 (2.54)
a17:0	-22.53 (0.31)
17:0	-23.58 (1.79)
18:0	-25.13 (1.72)
20:1 ω-9	-35.43 (0.05)

Table 2: Table show $\delta^{13}C$ of growth media, biomass and fatty acids V-PDB ‰ of *RS-P*.

Supplementary movie

Movie S1-3. Movies shows sequential stages involved in *EM-P* cell lysis and release of intracellular vacuoles containing daughter cells. Scale bar in the movie is 5µm.

Movie S4. Movie shows ongoing process by which vesicles underwent lysis to release of daughter cells. Scale bar in the movie is 10µm.

Movie S5. Movie shows large aggregations of intracellular vacuoles with or without daughter cells. Such aggregations were frequently observed in the late-stationary growth phase of *EM-P*. Scale bar in the movie is 10µm.

Movie S6. Movie shows layered membrane debris of *EM-P* forming hollow lenticular structures. Such structures should have formed by random folding of membrane debris as no indication of trapped cells, was observed in these structures. Scale bar in the movie is 20µm.

Movie S7. Movie shows a layer of *EM-P* cells and membrane debris that was formed over this layer. Several spherical cells can be seen attached to the membrane debris and in the free space between the cell layer and wavy membrane. Membrane debris was often noticed to have lenticular folding pattern. Scale bar in the movie is 100µm.

Movie 8. Movie shows a tubular *RS-P* cell with cell interiors largely devoid of organic carbon, similar to SPF microfossils. Spherical organic structures can be seen moving within the filament. Scale bar in the movie is 5µm.

Movie S9. Movie show *RS-P* cells with filamentous and spherical outer membrane vesicles. Scale bar in the movie is 10μm.